Tampere University

TOMMI VARIS

Approaches for Linking the High Kinetic Thermal Spray Process, Residual Stresses and Coating Performance by Utilizing In-situ Monitoring

Tampere University Dissertations 365

Tampere University Dissertations 365

TOMMI VARIS

Approaches for Linking the High Kinetic Thermal Spray Process, Residual Stresses and Coating Performance by Utilizing In-situ Monitoring

ACADEMIC DISSERTATION
To be presented, with the permission of
the Faculty of Engineering and Natural Sciences
of Tampere University,
for public discussion in the auditorium K1702
of the Konetalo building, Korkeakoulunkatu 6, Tampere,
on 15 January 2021, at 12 o'clock.

ACADEMIC DISSERTATION
Tampere University, Faculty of Engineering and Natural Sciences
Finland

Responsible supervisor and Custos	Professor Petri Vuoristo Tampere University Finland	
Supervisor	Professor Sanjay Sampath Stony Brook University USA	
Pre-examiners	Doctor Jiří Matějíček Institute of Plasma Physics Czech Republic	Professor Reijo Lappalainen University of Eastern Finland Finland
Opponent	Doctor Jiří Matějíček Institute of Plasma Physics Czech Republic	Professor Hanlin Liao University of Technology of Belfort-Montbeliard France

The originality of this thesis has been checked using the Turnitin OriginalityCheck service.

Cover design: Roihu Inc.

ISBN 978-952-03-1825-3 (print)
ISBN 978-952-03-1826-0 (pdf)
ISSN 2489-9860 (print)
ISSN 2490-0028 (pdf)
http://urn.fi/URN:ISBN:978-952-03-1826-0

PunaMusta Oy – Yliopistopaino
Joensuu 2021

PREFACE

The work was carried out in the Material Science and Environmental Engineering unit at Tampere University (Tampere, Finland) and VTT Technical Research Center Ltd. (Espoo, Finland). The research was mostly funded by the Finnish Funding Agency for Technology and Innovation (Tekes, currently Business Finland) under various research projects. This work was also partly funded by the FIMECC Hybrid materials public-private program. In addition, this work was also supported by the K.F. and Maria Dunderberg Foundation and Technology Industries of Finland Centennial Foundation.

I would like to thank my co-workers at VTT and Tampere University for their help, and willingness to share their expertise throughout the project. I would especially like to thank my former co-workers at VTT: Tomi Suhonen, M.Sc, Kimmo Ruusuvuori, B.Eng., Mr. Markku Lindberg, Dr. Erja Turunen, Mrs Seija Kivi, Mika Jokipii, B.Eng., and Dr Arash Ghabchi for the productive and enjoyable working atmosphere during the project. I would also like to express my gratitude to my colleagues Dr. Jarkko Kiilakoski, Ville Matikainen, M.Sc., Dr. Jussi Laurila, Henna Niemelä-Anttonen, M.Sc., Dr. Heli Koivuluoto, Mr. Mikko Kylmälahti, Mr. Anssi Metsähonkala and Mr. Jarkko Lehti, the thermal spraying research and staff of the laboratory at Tampere University, for all the help and shared experiences. I am also grateful to have such good collaboration with great co-authors in my articles. In particular, I would like to thank Prof. Sanjay Sampath of the University of Stony Brook in the USA for the ideas and tools which he introduced to me. He gave me the opportunity to ignite this whole study during my visits at the Center for Thermal Spray Research (CTSR). Also, I would like to acknowledge my co-workers at CTSR including Dr. Alfredo Valarezo, Dr. Brian Choi, and Dr. Gopal Dwivedi.

Most of all, I am grateful to my supervisor, Prof. Petri Vuoristo, who first provided an opportunity to carry out this work and then gently pushed me to complete the work. His guidance and comments were highly appreciated. I would also like to thank Prof. Vuoristo for the friendly encouragement and understanding I received when I was going through some of the most difficult stages of my personal life during this project.

I am grateful to have had the support and understanding of my family and friends. In particular, I would like to thank my son, Tatu, who has given me great support and who showed me that if the targets are set high and you work hard you will inevitably achieve good things.

Tommi Varis

11.12.2020

Vantaa, Finland

ABSTRACT

Thermally sprayed hardmetal coatings have been successfully used in many critical applications including hydraulic cylinders, landing gear, paper machine rolls, ball and gate valves, and several other parts, which require wear resistance. Currently, due to variations in the spray processes, feedstock material, and spray parameters, there might exist a wide range of properties for the same coating material. Perhaps the most important factor for the coating properties is the feedstock powder and its quality. The size distribution of the powder needs to be suitable for the process; in addition to this the particle density, carbide size, and powder homogeneity affect the properties of the coating. Furthermore, the coating properties for a selected powder are related to the particle state, more precisely the particle thermal and kinetic energy at the impact. Today, the particle state can be monitored by in-situ diagnostics with devices that measure the temperature (T) and velocity (v) of the particles during flight. The particle state can be further linked to the coating properties and performance by so-called process mapping methodology. At present, many thermal spray processes and equipment exist, each having their own specific characteristics of particle temperature and velocity. For example, the newest thermal spray processes, such as High Velocity Air Fuel (HVAF), provides about a 1000 °C lower flame temperature and 30-40% higher particle velocity compared to more conventional High Velocity Oxygen Fuel (HVOF) thermal spray processes. HVAF thus produces very dense coating structures and reduces the brittleness caused by excessive particle heating.

Coating formation also induces stresses caused by the rapid solidification of the spray droplets (quenching) and thermal mismatch stresses during cooling. The thermal history will have a major impact on the residual stresses and it may influence the performance of the coating by affecting the mechanical properties of the coating as well. In high-kinetic-energy thermal spray processes, e.g. the HVOF, High-Pressure High Velocity Oxygen Fuel (HP-HVOF), HVAF, and cold spray (CS) processes, the compressive stress component also known as peening stress, intensifies during the manufacturing process. Peening stresses act on the substrate or on the previously deposited layer.

Insufficient attention has been paid so far to the factors arising from the manufacturing process. Thus the effect of the thermal history and residual stresses on the properties of coatings is largely unknown. Moreover, there is generally a lack of knowledge on the property variation in coatings produced by various devices from the same material, as coating properties are managed largely by the trial and error approach. Consequently, insufficient understanding and/or information on the relationship between the manufacturing process and coating properties makes it significantly more difficult to set property targets for the applications.

This work focuses on the approaches to provide a link between process-structure-property correlations in high kinetic thermal spraying by utilizing in-situ monitoring tools, which enable reliable manufacturing of thermal spray coating. These tools include inflight particle temperature and velocity measurements and an in-situ coating property sensor (ICP). The ICP measures the substrate curvature during spraying, enabling the monitoring of information on the coating formation process and residual stresses. First, the role of gas flows and process conditions on the particle state was evaluated by mapping the particle temperature and velocity resulting from different conditions and how they are linked to coating properties. Further, the in-situ curvature technique and progressive deposition model of Tsui and Clyne [1,2] were used in order to understand how thermal spray processes and parameters affect the residual stresses of coatings made by the HVOF, HP-HVOF, HVAF, and CS processes. Materials focused on in relation to HVOF and HVAF were WC-CoCr and Cr_3C_2-NiCr, whereas Al, Ti, and Cu were used in the CS case. Studies showed that high compressive residual stresses controlled by the particle molten state, velocity, and substrate temperature can develop in high kinetic thermal sprayed carbide coatings. The role of compressive stresses proved to be significant for the cavitation erosion resistance and fatigue life performance of the coatings. It was shown that the residual stress of cold spray coatings, mostly controlled by impact pressure and thus in most cases developing into compressive stress, may develop into tensile stress in conditions with low impact pressure and relatively high thermal energy.

TIIVISTELMÄ

Termisesti ruiskutettuja kovametallipinnoitteita on käytetty menestyksekkäästi monissa kriittisissä sovelluksissa, kuten hydraulisylinterit, laskutelineet, paperikoneen telat, pallo- ja porttiventtiilit sekä useat muut kulumiskestävyyttä vaativat osat. Nykyisin ruiskutusprosessien, pinnoitusjauheiden ja ruiskutusparametrien vaihtelusta johtuen samalle pinnoitemateriaalille voidaan aikaansaada erilaisia ominaisuuksia. Ehkä tärkein tekijä pinnoiteominaisuuksien kannalta on jauhe ja sen laatu. Jauheen kokojakauman on oltava sopiva prosessille ja tämän lisäksi tiiveys, karbidikoko ja jauheen homogeenisuus vaikuttavat pinnoitteen ominaisuuksiin. Lisäksi valitulla jauheella saavutettuihin pinnoiteominaisuuksiin vaikuttaa ruiskutettavien partikkeleiden tila. Tarkemmin ottaen partikkeleiden lämpöenergia ja kineettinen energia törmäyshetkellä. Partikkeleiden tilaa voidaan tarkkailla suoraan partikkelivirrasta mittaamalla niiden lämpötilaa (T) ja nopeutta (v) lennon aikana ja linkittää prosessin olosuhteet pinnoiteominaisuuksiin ns. "process mapping"-menetelmää hyödyntämällä. Nykyisin on käytössä useita eri termisen ruiskutuksen prosesseja, joista jokainen voi tuottaa partikkeleille hieman erilaisen lämpötilan ja nopeuden. Tämän takia samalla pinnoitusmateriaalille voidaan saada eri prosesseilla suhteellisen laaja kirjo erilaisia ominaisuuksia. Esimerkiksi uusimmat termisen ruiskutuksen prosessit, kuten HVAF, tarjoaa noin 1000 °C matalamman liekin lämpötilan ja 30 – 40 % suuremman partikkelinopeuden tavanomaisempiin HVOF ruiskutusprosesseihin verrattuna. Tämän takia ne tuottavat erittäin tiiviitä pinnoiterakenteita, joilla ei kuitenkaan ole partikkeleiden liiallisesta kuumenemisesta aiheutuvia negatiivisia ominaisuuksia kuten haurautta.

Pinnoitteen muodostumisprosessi saa aina aikaan pinnoitteeseen jännityksiä, jotka ovat seurausta partikkeleiden nopeasta jäähtymisestä ja mahdollisesta alustan ja pinnoitemateriaalin lämpölaajenemiserosta. Partikkeleiden ja alustan lämpöhistoria vaikuttaa merkittävästi jäännösjännityksiin mikä voi vaikuttaa myös pinnoitteen suorituskykyyn ja pinnoitteen mekaanisiin ominaisuuksiin. Esimerkiksi korkean partikkeleiden kineettisen energian omaavilla termisen ruiskutuksen prosesseilla kuten HVOF, HVAF ja kylmäruiskutus saadaan valmistusprosessin aikana syntymään partikkeleiden iskeytymisestä johtuva puristusjännitystila. Partikkeleiden

iskeytymisestä syntyvä iskuenergia aiheuttaa puristusjännityksiä joko alustaan tai aiemmin ruiskutettuun kerrokseen.

Usein valmistusprosessista johtuvien tekijöiden hallintaan on kiinnitetty riittämätöntä huomiota, joten lämpöhistorian ja jäännösjännitysten vaikutusta pinnoitteiden ominaisuuksiin ei suurelta osin tunneta. Lisäksi eri laitteilla samasta materiaalista valmistettujen pinnoitteiden ominaisuuksien vaihtelusta ei ole systemaattisesti kerättyä tietoa. Pinnoitteiden ominaisuuksia hallitaan suurelta osin yritys ja erehdys -lähestymistavalla, minkä vuoksi ei saada riittävää ymmärrystä valmistusprosessin ja pinnoiteominaisuuksien välisestä riippuvuussuhteesta. Tämä voi jopa haitata merkittävästi eri sovelluksille asetettavia riittävän tarkkoja ominaisuusvaatimuksia.

Tässä työssä hyödynnetään prosessin aikaisia diagnostiikkatyökaluja, joita käyttämällä voidaan linkittää korkeakineettisten ruiskutuprosessien prosessiolosuhteet pinnoiterakenteeseen ja pinnoiterakenne pinnoiteominaisuuksiin. Näihin työkaluihin kuuluvat partikkeleiden lämpötilan ja nopeuden mittaukseen käytettävät diagnostiikkalaitteet sekä ruiskutuksen aikainen pinnoiteominaisuuksien mittauslaite (ICP), joka tarkkailee substraatin käyristymistä mahdollistaen pinnoitteen muodostumisprosessin monitoroinnin ja jäännösjännitysten määrittämisen. Hyödyntämällä prosessin aikaista monitorointia saadaan pinnoitteiden valmistusprosessista tietoa, joka auttaa ymmärtämään prosessin ja pinnoiteominaisuuksien välistä vuorovaikutusta. Kaasuvirtausten ja prosessiolosuhteiden vaikutusta partikkeleiden tilaan arvioitiin kartoittamalla hiukkasten lämpötilaa ja nopeutta erilaisilla prosessisäädöillä, minkä jälkeen selvitettiin millaisia pinnoiteominaisuuksia ja erityisesti jännitystiloja eri prosessiolosuhteet tuottivat. Jännitysten määrittämiseen käytettiin Tsuin ja Clynen analyyttista laskentamallia ja selvitettiin kuinka HVOF–, HP-HVOF–, HVAF– ja kylmäruiskutusprosessit ja niiden ruiskutusparametrit vaikuttavat pinnoitteiden jäännösjännityksiin. HVOF– ja HVAF– prosessissa tutkittiin WC-CoCr - ja Cr_3C_2-NiCr –pinnoitteita ja kylmäruiskutuksessa Al, Ti ja Cu pinnoitteita. Tutkimukset osoittavat, että korkeakineettisillä termisen ruiskutuksen prosesseilla saadaan partikkeleiden sulamisastetta, nopeutta ja substraatin lämpötilaa säätämällä merkittäviä puristusjännityksiä omaavia karbidipinnoitteita. Puristusjännitysten merkitys osoittautui tärkeäksi pinnoitteiden kavitaatioeroosionkestävyyttä ja väsymiskestävyyttä parantavaksi tekijäksi. Osoitettiin myös, että kylmäruiskutuspinnoitteiden jäännösjännitykset, joihin tyypillisesti vaikuttaa iskuenergian määrä ja sen vaikutuksesta muodostuva puristusjännitys, voivat kehittyä myös vetojännityksiksi olosuhteissa, joissa on alhainen iskuenergia ja suhteellisen korkea prosessilämpötila.

CONTENTS

ABBREVIATIONS

a&s	Agglomerated and sintered
Al	Aluminum
Co	Cobalt
Cr	Chromium
Cr_3C_2	Orthorhombic chromium carbide
Cr_7C_3	Orthorhombic chromium carbide
$Cr_{23}C_6$	Cubic chromium carbide
CS	Cold spray
CTE	Coefficient of thermal expansion
Cu	Copper
DE	Deposition efficiency
HP-HVOF	High-Pressure High Velocity Oxygen Fuel
HVAF	High Velocity Air Fuel
HVOF	High Velocity Oxygen Fuel
HV	Vickers hardness value and load in kilograms
ICP-sensor	Integrated coating property sensor
KIC	Fracture toughness
Ni	Nickel
O/F ratio	Oxygen/fuel ratio
SEM	Scanning electron microscopy
T	Temperature
Ti	Titanium
v	Velocity
XRD	X-ray diffraction
W	Tungsten
WC	Hexagonal tungsten monocarbide
W_2C	Hexagonal tungsten hemicarbide

ORIGINAL PUBLICATIONS

Publication I T. Varis, T. Suhonen, A. Ghabchi, A. Valarezo, S. Sampath, X. Liu, and S.-P. Hannula, "Formation mechanisms, structure, and properties of HVOF-sprayed WC-CoCr coatings: An approach toward process maps," Journal of Thermal Spray Technology, vol 23, No. 6, pp. 1009-1018, Aug. 2014.

Publication II T. Suhonen, T. Varis, S. Dosta, M. Torrell, J.M. Guilemany, "Residual stress development in cold sprayed Al, Cu and Ti coatings," Acta Materialia, vol 61, pp. 6329–6337, Aug. 2013.

Publication III T. Varis, T. Suhonen, M. Jokipii, P. Vuoristo, "Influence of powder properties on residual stresses formed in high-pressure liquid fuel HVOF sprayed WC-CoCr coatings," Surface & Coatings Technology, vol 388, 9 p., Mar. 2020.

Publication IV T. Varis, T. Suhonen, J. Laakso, M. Jokipii, P. Vuoristo, "Evaluation of residual stresses and their influence on cavitation erosion resistance of high kinetic HVOF and HVAF-sprayed WC-CoCr coatings," Journal of Thermal Spray Technology, May 2020.

Publication V T. Varis, T. Suhonen, O. Calonius, J. Čuban, M. Pietola, "Optimization of HVOF Cr_3C_2-NiCr coating for increased fatigue performance," Surface & Coatings Technology, vol 305, pp. 123 – 131, Aug. 2016.

Author's contribution

The publications were prepared in close cooperation with the other authors. The following describes the contribution of the author and co-authors in the scientific publications as agreed with the co-authors.

Publication 1: The author designed and planned the experimental procedures with the co-authors (T. Suhonen, A. Ghabchi, A. Valarezo, S. Sampath) and later conducted the coating preparation, particle diagnostics, curvature data collection,

and coordinated the structural characterizations (performed by X. Liu) and wear testing studies. Furthermore, the author gathered all the data for the publication, wrote the majority of the manuscript together with T. Suhonen and A Valarezo, and later revised it with the co-authors.

Publication 2: The author participated in the deposition parameter design together with T. Suhonen, S. Dosta, and M. Torell for the coating preparation carried out at the University of Barcelona (CPT) in Spain. The author attended the spray sessions and curvature data collection. Later he was responsible for the residual stress calculations and some parts of the text revision work with the co-authors.

Publication 3: The coatings were deposited by M. Jokipii in the thermal spray laboratory at VTT in Espoo, Finland. The author designed the spray parameter selections and participated in the spraying sessions. Moreover, the author coordinated the metallographic and wear testing studies. The author was also responsible for the curvature measurements, spray particle diagnostics, and utilization of the analytical model for residual stress calculations. The first manuscript draft and revision of the article was made by the author.

Publication 4: The coatings were deposited by M. Jokipii in the thermal spray laboratory at VTT in Espoo, Finland, in the sessions according to the experimental design made by the author and T. Suhonen. The author also conducted the particle diagnostics, residual stress calculations, and wear testing studies. Coating characterization prior to and after the wear tests were performed by J. Laakso. The author wrote the first draft of the manuscript and later revised it with the co-authors.

Publication 5: The author deposited the coatings together with research staff in the thermal spray laboratory at VTT, in Espoo, Finland. The author participated in the design of the experiment and coating parameter selection together with T. Suhonen. Residual stress optimization and determination were done by the author. Fatigue testing was performed by O. Calonius and J. Čuban at Aalto University, in Espoo, Finland. The author conducted all the analysis of the fatigue surfaces. The author wrote the first draft of the manuscript, which was further supplemented by the co-authors.

1 INTRODUCTION

1.1 Background of the research

The extraordinary flexibility of thermal spraying with respect to materials and versatility with respect to geometry will make thermal spraying a useful solution for wear and corrosion challenges. Thermal spray technology has been used successfully in aircraft landing gear [3–5], bearing journals and shafts, valves and pumps in the process industry, hydraulic cylinders in the offshore and automotive industries, and calender rollers in a paper machine, etc. [6,7]

Thermally sprayed microstructure is unique. Thermally sprayed coatings are generated from the impingement of many heated and accelerated individual particles, which form a lamellar structure. In techniques like High Velocity Oxygen Fuel (HVOF), High-Pressure High Velocity Oxygen Fuel (HP-HVOF), Cold spray (CS), High Velocity Air Fuel (HVAF), and Warm Spray (WS), the feedstock material, i.e., the powder in these processes, is fed into the flame and within milliseconds is heated up to molten or semi molten stage and accelerated up to 1100 m/s. Upon impact to the substrate, particles form lamellae, which are rapidly cooled to the substrate temperature cooling rate of approximately 10^6 C/s. The CS process differs from the other processes in that the particles are in solid state during flight and their adhesion to the substrate is based on the energy produced by plastic. Currently there exist many thermal spray processes, each having their own specific principles and characteristics of particle temperature (T) and velocity (v). The latest thermal spray processes, such as HVAF and CS, provide lower particle temperature and higher velocity and produce very dense coating structures, due to the high kinetic energy. There is much potential foreseen for the new high kinetic thermal spray processes due to the fact that the low temperature of the processes will lead to very low oxide content in metallic materials and high velocity in many cases will lead to denser structures, compared to conventional spray processes. [6–8]

The tendency toward lower particle temperatures has changed the particle deposition from molten particle impact to semi molten or solid particle impact. For microstructure manipulation and process optimization, it is essential to understand

the effect of the particle conditions, impact conditions, and particle quenching on the formation of lamellae interfaces, on the coating microstructure and further on the properties. It is well known that the lamellae of thermally sprayed coatings are not perfectly bonded [9]. Several studies have shown that the lamellae interfaces are critical as they offer routes for chlorine diffusion or for penetration of liquid corrosive media through the coating, for instance [10–12]. Lamellae interfaces also affect the mechanical properties of the coating and their quality is therefore critical for the wear resistance of thermally sprayed coatings.

Due to the special nature of thermal spraying processes they produce residual stresses in the coating. Residual stresses in a thermally sprayed coating cannot be completely avoided but their magnitude can be affected by the spray parameters, substrate temperature, and powder properties. The magnitude and direction of residual stresses are of great importance in coating damage or degradation processes as they are superposed with external loads occurring in the components. It is reasonable to assume that many coating properties, such as adhesion, wear resistance, fatigue properties, and even corrosion performance are dependent on the existing residual stresses in the coating. However, the residual stresses are relatively seldom linked to the wear properties and mechanical properties of the coatings. One clear challenge is that the adjustment of spray parameters influences both the coating properties and residual stresses, and thus their interaction might be difficult to estimate. In this study the strategy was to harmonize the coating fabrication procedure in terms of sample size and robot manipulation in order to reliably study the effect of adjusting other spray parameters which have an influence, e.g., the particle temperature and velocity, and thus the coating properties and residual stresses. Data was collected during the deposition process that can be used for scientific review of the coating formation process. By using the on-line particle sensor, particle in flight conditions (T and v) can be monitored. In addition, by using the in-situ curvature monitoring technique, direct measurements of the particle impact, quenching, and thermal history can be recorded. The curvature technique also allows the determination of the residual stresses in the coating. In-situ monitoring can be utilized to collect direct measurements from the spray process and in that way it allows the relationship to be identified between the processing, structure, properties, and performance of the coatings.

1.2 Aim of the work

In this work, the focus is on the understanding of the residual stresses that are formed in the high kinetic thermal spray processes, especially the conventional HVOF, HP-HVOF, HVAF, and CS processes. First, the goal is to understand the magnitude of residual stresses generated by different processes, how thermal spray process parameters affect them, and how they can be controlled, influenced, and optimized. Second, the objective is to develop concepts which help in determining the residual stresses by utilizing in-situ monitoring tools. Further, the concepts of optimizing the coating process and development of property maps for thermally sprayed coatings are considered in order to understand how the coating deposition parameters are related to the coating properties, especially wear performance, for example. The main motivation was to understand the effect of processing, particularly particle kinetic energy and thermal history, on the residual stress state and mechanical response of the coatings under mechanical loading and to consider the effect of the stress state on coating performance against wear and fatigue life. Through deep scientific knowledge of the spray particle interaction and thus the ability to control and optimize the performance of thermal sprayed coatings, many still unresolved issues in new demanding applications may be solved. Examples include corrosion and wear prevention in numerous applications in energy production or the process industry, which in the future will require the understanding of the coating and component damage tolerance and the ability to integrate the coatings as a part of the mechanical design of the components.

1.3 Research questions

This work aims to answer the following research questions:

i. What are the most feasible approaches for assessing stresses via curvature monitoring?

ii. How do different spraying processes, such as HVOF, HP-HVOF, HVAF, and CS, and the particle state they produce, affect the mechanical properties and stress states of the coatings, and how can they be controlled, influenced, and optimized?

iii. How do residual stresses influence the mechanical response and wear performance of the coating?

iv. In what way do the properties of the powder affect the residual stresses?

Table 1 clarifies the content and scientific contribution of Publications I - V and indicates in which publication the research questions of this dissertation are discussed.

Table 1. Scientific contribution of Publications I - V and their relationship to the research questions.

Publication	Contribution	Research question
Publication 1 "Formation mechanisms, structure, and properties of HVOF-sprayed WC-CoCr coatings: An approach toward process maps"	Addresses the utilization of process mapping concept and process adjustment strategy to develop various particle conditions in HVOF spraying. The relations of process – particle condition - microstructure properties of WC-CoCr coatings are presented.	ii iii
Publication 2 "Residual stress development in cold sprayed Al, Cu and Ti coatings"	Covers the studies of curvature development in cold sprayed Al, Ti, and Cu coatings using the in-situ curvature method. It is one of the first papers to show tensile residual stresses in cold spraying.	ii
Publication 3 " Influence of powder properties on residual stresses formed in high-pressure liquid fuel HVOF sprayed WC-CoCr coatings"	Studies the critical influence of variation in powder particle density and size distribution of WC-CoCr powder on the residual stresses in coatings. The study shows the importance of powder properties on the coating quality, formation of residual stresses, and deposition efficiency.	i iv
Publication 4 "Evaluation of residual stresses and their influence on cavitation erosion resistance of high kinetic HVOF and HVAF-sprayed WC-CoCr coatings"	Studies the residual stress control of various thermal spray processes: HVOF, HP-HVOF, and HVAF, and demonstrates the method of utilizing in-situ curvature and temperature data for the calculation of through thickness residual stresses in WC-CoCr coatings. The effect of highly compressive residual stresses on the cavitation resistance is discussed.	i ii iii iv
Publication 5 "Optimization of HVOF Cr3C2-NiCr coating for increased fatigue performance "	The publication deals with the fatigue performance of HP HVOF sprayed Cr3C2-NiCr coating. It first demonstrates the process mapping methodology for parameter optimization in order to prepare high compressive residual stress in the coating and then shows the improved fatigue life resulting from the compressive stress state.	ii iii

2 HIGH KINETIC THERMAL SPRAYING

Thermal spraying refers to a coating process in which the coating material, usually in the form of powder or wire, is completely or partially melted and accelerated by a rapid gas flow to the pre-treated surface to produce a coating [7,8]. Currently there exist many thermal spray processes, each having their specific principles and characteristics of flame temperature and velocity, as shown in Fig. 1 [6,7,13,14]. High kinetic thermal spray processes and their manipulation are introduced in the following chapters.

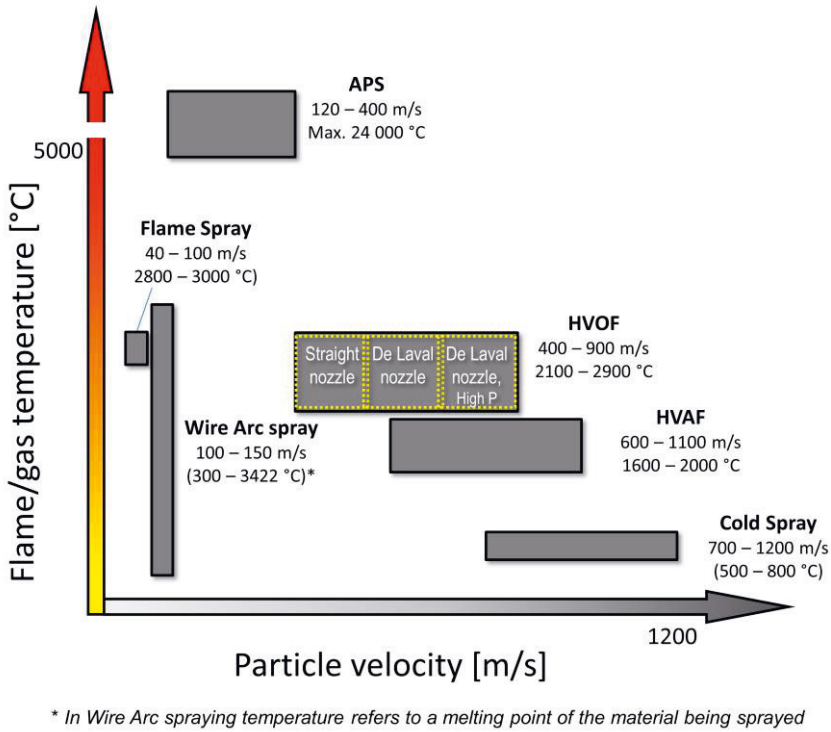

Figure 1. Classification of thermal spray processes in accordance with particle velocity and flame temperature based on references [6,7,13,14].

2.1 Principle of high kinetic thermal spraying processes

In thermal spray technology, coating properties are often directly related to the temperature-velocity characteristics of the spraying equipment. The newest thermal spray processes, such as HVAF, provide lower particle temperature and higher velocity compared to more conventional HVOF thermal spray processes and thus produce very dense coating structures [6,15]. Fig. 2 shows the principle of Kermetico Inc's HVAF equipment as well as the characteristic gas velocities and temperatures. The new generation HVAF guns such as AK07 from Kermetico Inc. and M3 from Uniquecoat Technologies LLC have a relatively large combustion chamber followed by a deLaval nozzle. In the process, several thousands of liters/min of compressed air and several hundreds of liters/min of propane fuel gas are fed through the nozzle to ensure high particle velocities. A lot of potential is foreseen for the new high kinetic thermal spray processes since the low temperature and catalytic burning in the processes lead to very low oxide content in metallic materials. In addition, high velocity contributes to the formation of denser coating structures compared to the coatings sprayed with conventional HVOF methods. The tendency toward lower temperature has changed the particle deposition from molten particle impact to semi molten or solid particle impact.

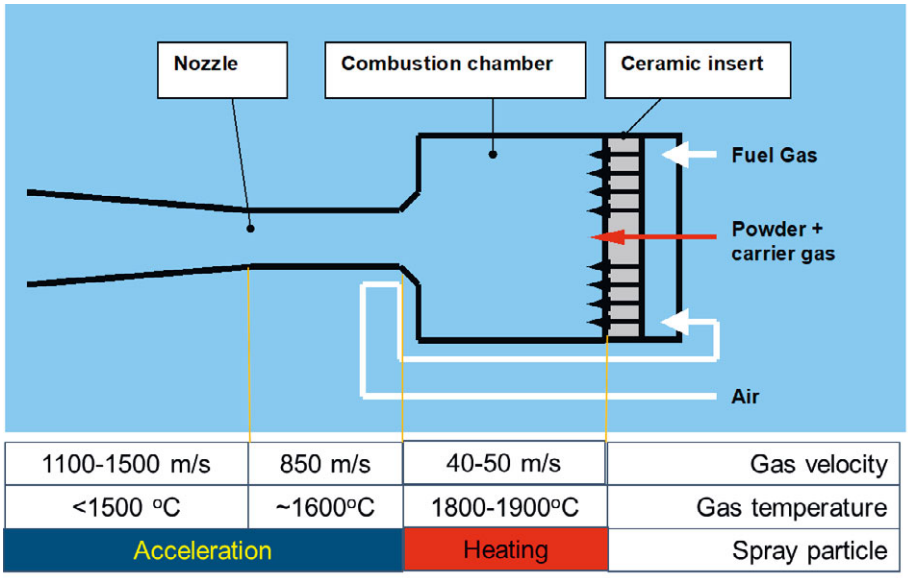

Figure 2. Schematic diagram of Kermetico HVAF gun and its typical gas temperatures and velocities in different sections of the gun. Source: Kermetico; www.Kermetico.com

In HVOF processes (Fig. 3) the heat is generated from the combustion of fuel, typically hydrogen, propane, propylene, kerosene, or ethylene, with oxygen in the combustion chamber of the spray gun. The combustion gases are at high pressure (3-15 bar) in the combustion chamber, from which they are ejected through the nozzle and accelerated to supersonic velocities. In HVOF processes, the maximum gas temperatures in the combustion chamber are approximately 3000 ºC, whereas in the HVAF process, the combustion of the fuel gas, propane or propylene, with compressed air, lowers the flame temperature by approximately 1000 ºC compared to HVOF. The powder is introduced radially into the nozzle or axially into the combustion chamber. Within milliseconds it is heated up to the molten or semi molten stage and accelerated up to 1200 m/s toward the substrate. During the impact on the substrate it is rapidly cooled to the substrate temperature at the rate of 10^6 ºC/s. The flame temperatures are high enough to oxidize metallic material or to cause other unwanted effects in hardmetal coatings. For example, in the case of WC-Co coatings, such effects are carbon loss and dissolution of carbides in the matrix. Therefore, excessive heating of powder during flight may have a negative influence on the properties of hardmetal and metal coatings. However, due to the high particle velocity in high kinetic thermal spray processes, the dwell times (time above melting temperature) for the particles are relatively short, which is why the adverse changes, e.g., carbon loss and carbide dissolution in WC–Co(Cr), can be kept low. In other words, the effects they cause are relatively small if attention is paid to the selection of powder and adjustment of the spray parameters to control them. In the HVAF process, the flame temperature is even lower than it is for the HVOF process, which often has positive effects on the coating properties. HVAF-sprayed metallic and hardmetal coatings have better properties, as a result of a higher amount of retained carbide phases and a lower level of oxidation. This results in higher ductility and may improve wear resistance as well. However, the properties of the sprayed materials are strongly related to the process and processing, thus careful attention to the processing and optimization of the parameters is required. [6,8,16]

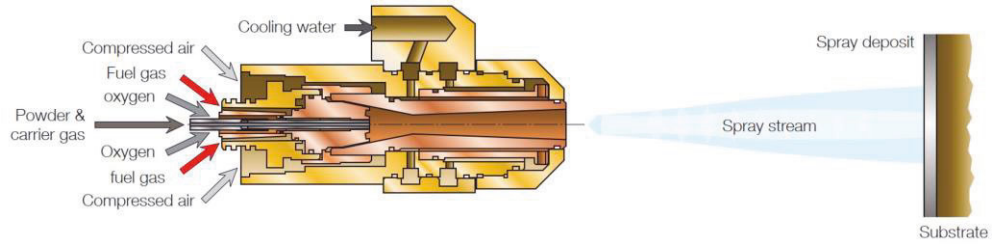

Figure 3. Cross-sectional view of a DJ Hybrid HVOF gun. Source: Oerlikon Metco, www.oerlikon.com/metco/en/products-services/coating-equipment/thermal-spray/systems/hvof/diamond-jet/.

The CS process (shown in Fig. 4) was invented in the late 1990s. It is, in theory, a very simple system in which particles are accelerated in a high velocity gas stream. High-velocity gas stream is produced by generating a high-pressure gas to a combustion chamber and allowing the gas to expand through a converging-diverging nozzle. By increasing the temperature and pressure of the gas before expansion, a CS gas temperature from 400 to 1200 ºC can be high enough to exceed the material dependent critical velocity, which makes deposition upon the particle impact possible. The major benefit of cold sprayed coatings is that they are pure, i.e., free of oxides, and noticeably dense. In the CS process, the applicable materials were initially limited to soft metals such as copper, iron, aluminum, nickel, titanium, and their alloys. However, it remains very challenging for CS to form coatings with cermet powders such as WC-Co. The reason is believed to be the lack of deformability of the powder at the low temperature. Nevertheless, the recent development of cold spray systems [18] has increased the ability of CS to process harder materials like WC-Co with a higher matrix content. [19–23]

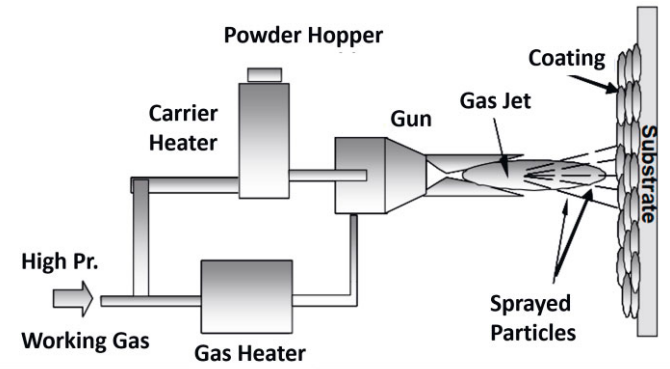

Figure 4. Schematic presentation of the cold spray process [24].

2.2 Process parameter manipulation, control, and optimization

There are several parameters in high kinetic thermal spraying, which have an effect on the deposit formation and hence coating properties. The differences are the biggest between coating processes like first generation HVOF, HP-HVOF, and HVAF. Furthermore, each coating device may have different hardware setups, which significantly affects the coating formation. This variability in the devices makes the comparison of the results often very complex.[14]

After the spray device, fuel gas, and gun configuration has been selected, there are still several parameters that influence the microstructure of the coatings and thus the properties. Perhaps the most important is the powder, which needs to have a suitable particle size distribution for the process. For the optimization of the coating microstructure and properties, important controllable factors in the high kinetic process are particle temperature, velocity, and melting state. The fluid dynamics play a major role in influencing the particle temperature and velocity. The schematic presentation of the interactions in thermal spray high velocity processes are shown in Fig. 5.

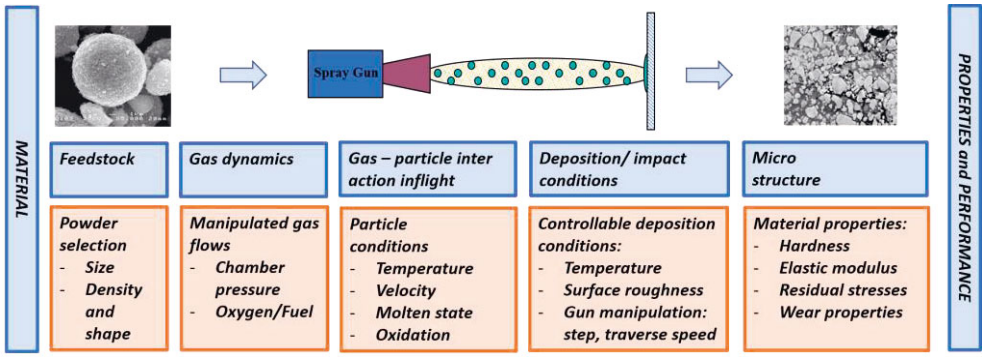

Figure 5. The route from the material to performance in thermal spraying via the physical interactions during the process.

Heat is generated from the combustion of gaseous or liquid fuel at high pressure. The temperature of the flame is primarily dependent on the characteristics of the selected fuel, which determines the maximum flame temperature, heat of combustion, and heat transfer. Flame temperature is expressed by the adiabatic flame temperature, which shows the maximum flame temperature without any losses to cooling, for example. Adiabatic flame temperatures of various fuels with different Oxygen-to-Fuel (O/F) ratios are shown in Fig. 6. The adiabatic flame temperature

is dependent on the O/F ratio. The flame temperature reaches its maximum close to the stoichiometric ratio, which means that an optimal amount of oxidizer is present for complete burning. If there is an excess amount of oxidizer or fuel the remaining unburned components will make the flame cooler. This allows the fine tuning of the flame temperature of the process. Notably, the maximum adiabatic flame temperatures are not reached at the stoichiometric ratio (λ=1) but at slightly fuel rich ratios. The reason for this is that not only oxidation reactions but also dissociation reactions occur when burning hydrocarbon fuels. Consequently, in addition to CO_2, a minor amount of CO is formed, and the heat loss caused by the formation of CO can be compensated by excess fuel. [16,25]

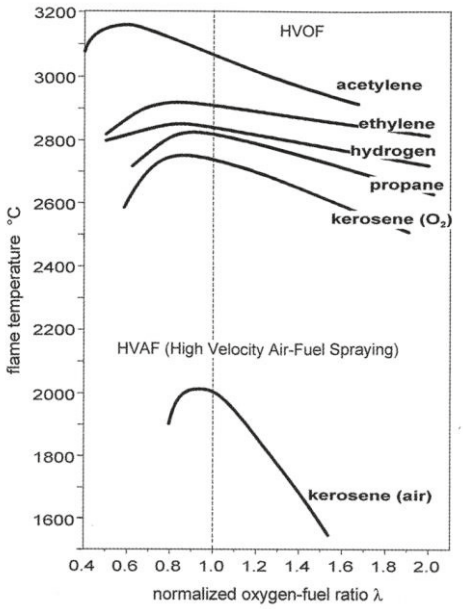

Figure 6. Maximum adiabatic flame temperatures of various fuels as a function of O / F ratio [16].

With respect to the gas dynamics, the basic design principle of all HVOF torches is based on compressible fluid flow through either a converging-straight or converging-diverging nozzle. In a converging-straight nozzle, the cross-sectional area of the nozzle decreases after the combustion chamber and remains unchanged throughout the converging part, whereas in a converging-diverging (or de Laval) nozzle the area increases after the converging part toward the exit. Converging-straight nozzles have a velocity limitation of Mach 1 [25,26]. To achieve higher velocities the nozzle must be designed as a de Laval nozzle. At the nozzle throat the converging flow reaches

supersonic velocity and increases more at the diverging part due to the pressure drop for the current constant mass flow. Most of the newer, third generation, HVOF torches use a converging-diverging nozzle geometry. Their area ratio between the throat and nozzle exit determines the maximum Mach number of the gases exiting the nozzle. Typically, the nozzles are designed so that the area ratio produces a design Mach number of between 2 to 5.

In thermal spraying, the interest is in the particle velocity and temperature (and melting stage) at impact, since these have the most significant influence on coating quality. It has been shown that one straightforward way to control the velocity of sprayed particles is to adjust the chamber pressure using the amount of gas flow through the nozzle. Particle temperature can be adjusted by adjusting the balance of fuel gases, i.e., the O/F ratio. With the control of these two variables, the chamber pressure and O/F ratio, travel is possible in the T-v space horizontally and vertically. In order to manipulate the particle temperature and velocity, an understanding of the gas-particle interaction is essential. Regarding the maximum mass flow through the nozzle, it is dependent on the chamber pressure and accelerating force for the particles, known as drag force ($\rho_g {v_g}^2$), which is known to be dependent only on the chamber pressure (P), Mach number (M), and specific heat ratio (γ): $\rho_g {v_g}^2 = \gamma M^2 P$. Therefore, particle velocity can be controlled by adjusting the chamber pressure by the total volume of the gas flow. [27–31]

Thermal spraying is a process in which the particle state affects the coating properties. It is understandable that coating properties are not only determined by the selected material, but also by the selected spray process and selected parameters. Coating formation is a complex process and influenced by several factors, as shown in Fig. 5, thus there is a clear need for a science-based approach to control the process-property-performance linkages. Process mapping methodology provides a science-based approach to design, assess, and optimize high performance coatings as it simply visualizes the relation of different process adjustments on the particle's in-flight state and further on the properties. The process mapping concept is implemented in two stages. First, the availability of particle monitoring via process sensors, which can measure the particle T and v, have enabled mapping of the in-flight particle state with various spray parameters. This presentation is called the first order process map. Second, measuring the coating properties prepared from various particle conditions allows the mapping of mechanical properties or wear resistances in the T-v space. Property maps in the T-v space are called second order maps. Systematic application of the process mapping concept allows understanding of the process-property interaction for various coating materials. [32–37]

3 RESIDUAL STRESSES IN THERMAL SPRAYING

In thermal spraying, a particle stream of 6-12 mm spot size is continuously sprayed in 3-10 mm steps over the work piece to be coated until the desired thickness has been reached. The spray stream consists of various sizes (depending on the size distribution) of hot particles. These particles have a certain temperature and velocity and melting ratio typical of spray process and tuned by selected spray parameters and spraying distance. Coating quality such as microstructure, density, and lamellae adhesion are mainly influenced by these particle related factors. Residual stresses, which are inevitably formed during thermal spraying processing, depend strongly on the spraying parameters. The resulting stress states are affected not only by the temperature and velocity of the particles but also by the temperature of the substrate and the coefficients of thermal expansion (CTE) of the materials. The thermal power of the spray gun used strongly affects the temperature history of the substrate as well as such factors as pitch, spray distance, external cooling, and how frequently spray passes were made. The origins of residual stresses, shown in Fig. 7, from the manufacturing of the coating are known as a) quenching stress, b) coefficient of thermal expansion (CTE) mismatch stress, and c) peening stress.

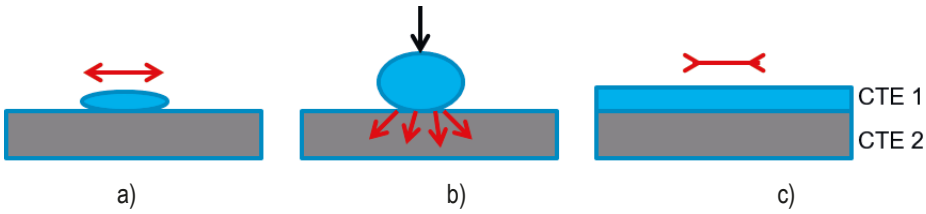

Figure 7. Sketch of the mechanisms of generation of different stress components in thermal spraying. a) Quenching Stress from the individual particle cooling – tensile, b) Peening Stress from the particle impact – compressive, c) CTE Mismatch Stress during coating and substrate cool down – tensile/compressive.

3.1 Quenching stress

Quenching stresses originate from the rapid solidification and contraction of the impacted spray particles, when they cool down to a substrate temperature. The interconnected lamellae shrink due to cooling, but the bonding forces between the other droplets tend to prevent shrinkage. As a result, tensile stress, which is also called quenching stress, is created on the lamellae. Quenching stresses are micro stresses by nature, which influence across the whole coating structure through the contact points of the lamellae. Thus, at micro level the coating may exhibit large local variations in stress levels. Quenching stress can be calculated by (1) [38]:

$$\sigma_q = \alpha_c E_c (T_m - T_s) \quad (1)$$

where α_c is the CTE of the coating, E_c is the elastic modulus of the coating, and T_m and T_s are the melting temperature and substrate temperature, respectively. Theoretical maximum values of quenching stress would in many cases lead to quenching stresses of over 2 GPa. However, in practice, the quenching stresses are significantly lower because they are relaxed by different relaxation mechanisms such as microcracking, creep, lamella slipping, and yielding. Quenching stresses can be controlled to a small extent by the substrate temperature, but its magnitude is more influenced by the level of adhesion between the lamellae. The better the adhesion, the higher the quenching stresses that may develop. [38,39]

3.2 Peening stress

Peening stresses are known to be caused by the high-velocity impacts of particles resulting in the plastic deformation of the substrate and/or previously deposited coating layers. The magnitude of peening stresses is related to the impact energy of the particles, $E_{kin}=1/2\ mv^2$. Particle mass can be expressed by volume and density $m = 4/3\pi r^3 \cdot \varrho$. This shows that the peening effect of the particles is related to the velocity (v) and mass (m) of the particles [40]. Peening contributes to a different extent for different materials. Very high peening stresses can result in materials that are more susceptible to plastic deformation compared to materials with brittle behavior [41]. Peening stresses are generated by the impact of individual particles with different sizes and velocities, and therefore the range and magnitude of the stress field resulting from each particle varies. This results in a relatively complex

stress. However, the force balance of the substrate deposit is well maintained, which allows the experimental comparison of different conditions using the curvature method [42]. This requires the approximation that the peening stresses are applied across the entire width of each layer. In practice, the magnitude and variation of the stresses due to peening during the deposition process are not well known. Some estimation of the thickness of the stress field has been proposed by Bansal et al. [43]. They estimated by finite element modeling that the size of 20–38 μm AISI 316 particle impact in HVOF spraying induces compressive stresses up to a depth of 30 μm in the coating. Moreover, further complexity in peening stress estimation comes from the fact that some material will stick and some bounce off, which generates a thermal spike in the material associated with its plastic deformation. [43,44]

3.3 Thermal mismatch stress

The sources of thermal mismatch or CTE mismatch stresses are the material mismatch between the coating and the substrate in the post-deposition cooling stage. If the CTE of the substrate is higher than that of the coating it tends to contract more and result in a compressive residual stress in the coating. This is a typical situation for coatings, which in many cases have a lower CTE than the steel substrate. Approximately, the stress arising from CTE mismatch can be estimated from the resulting misfit strains by (2) [45]:

$$\sigma_{th} = \frac{E_c}{1-\nu_c}[CTE_c(T_r) - CTE_s(T_r)] \cdot \Delta T \quad (2)$$

From this it is evident that thermal mismatch stress is influenced by the CTE of the substrate and coating material and can be effectively controlled by the substrate temperature during the coating process.

3.4 Measurement techniques of residual stresses

Residual stresses of coatings can be measured by several non-destructive or destructive methods. Non-destructive methods include X-ray diffraction, neutron diffraction, and Raman spectroscopy. Destructive methods include layer removal techniques and the hole drilling method. In addition, several computational techniques are available for residual stress estimation. These methods have their own

characteristics, which affect the residual stress values obtained [41,46]. Diffraction techniques are based on the measurement of changes in lattice spacing caused by residual stresses. It is compared to the known lattice constants of the current phase and transferred to residual stresses by the elastic modulus of that phase. The methods can measure residual stresses locally from different phases in the material provided that the lattice parameters and elastic modulus of the current phase are known, which is not often the case in thermal spraying. In thermal spraying, processing-induced compositional changes are common and there is also a possibility of the occurrence of amorphous phases in thermal spraying due to rapid quenching. Thus, the X-ray diffraction method reveals the micro stresses in the coating, which may be balanced on the microlevel between different phases and may not transfer macroscopically over the whole coating structure. One limitation of common laboratory X-ray equipment is that its penetration depth is only several micrometers and through thickness profiles cannot be determined without utilizing a layer removal technique, thus losing the non-destructive nature of the method. High energy X-ray and neutron diffraction methods have a much deeper penetration depth and enable through thickness presentation. However, neither of these are considered to be easily available and they are also expensive. Through thickness residual stress profiles are commonly determined by layer removal and hole drilling. These methods use strain gages for measuring the macro strain release in the structure caused by material removal. The accuracy of layer removal and the hole drilling method are dependent on the kinds of calibration coefficients used for the coatings, and often these calibration coefficients of the inhomogeneous coatings do not exist. Furthermore, layer removal may produce misleading results if layer removal causes plastic deformation or cracking in the coating. [1,2,41,46–58]

Substrate-coating curvature monitoring is a specific non-destructive method, in which the bending of the coated strip is measured. Controlled bending in curvature methods requires spraying the coating on a specific type of substrate strip. Therefore, it is used mainly for comparative analysis on the effect of different spray parameters on the residual stresses. The measurement of curvature and temperature in-situ as proposed by Kuroda et al. [38] and Matejicek et al. [59] can track the origin of all residual stresses arising from deposition stresses, i.e., quenching and peening, and post deposition stresses, i.e., CTE mismatch. The strip curvature can be further transferred to average coating macro stresses by the Stoney (3) [47] or Brenner and Senderoff (4) [48] equations,

$$\sigma_c = \frac{E_s' \, t_s^2 \, d\kappa}{6 d t_c} \tag{3}$$

$$\sigma_c = \frac{E_s' t_s(t_s + \beta^{1.25} dt_c)\, d\kappa}{6 dt_c};\ \beta = \frac{E_c'}{E_s'} \quad (4)$$

where E_c' and E_s' are the effective Young's modulus of the coating and substrate, t_c and t_s are the thickness of coating and substrate, and $d\kappa$ is the curvature.

In order to predict the residual stress distribution in a progressively deposited coating, an analytical model based on the balance of a misfit strain was presented by Tsui and Clyne [2]. The details of this procedure and the equations are presented in section 5.3 "Residual stress evaluation". Tsui and Clyne added the deposition stress calculation to post deposition thermal mismatch models. In their model, the quenching stress from each deposition layer causes constant stress and after each new layer, the force and momentum are balanced between the underlying spray layers and substrate. Thus, the quenching effect of each coating layer lowers the quenching stress of the underlying layers. They did not present the calculation of quenching stress. However, the quenching stress, which is the input value for the model, can be determined by an in-situ curvature monitoring device as well as temperatures for the thermal mismatch calculations. Other parameters needed for residual stress distributions with the analytical model are the elastic properties of the materials, specimen dimensions, and thicknesses. The Tsui and Clyne model was developed to predict tensile quenching stresses, whereby the generation of quenching stress of each new layer can be limited to the layer thickness. If the model is used for predicting the peening stresses, the thickness of the peening action is not exactly known. It should be further noted that in calculations based on curvature measurements, the residual stresses are thought to be evenly distributed throughout each layer, which naturally significantly lowers the peak stresses that may be present in the thermally sprayed coating. In reality, quenching and peening stresses cause significantly higher local stress concentrations than the calculations show. [2,41,46]

3.5 Residual stresses in thermally sprayed coatings

The majority of residual stress studies on thermally sprayed coatings focus on the area of thermal barrier and wear resistance in WC-Co/CoCr and Cr_3C_2-NiCr coatings. By reviewing the literature of the residual stresses in coatings produced by high kinetic processes (HVOF and HVAF), it is evident that the variation in the obtained results of residual stresses in WC-Co/CoCr coatings is significant. For example, Bolelli et al. [60] reported tensile stress of approximately 1000 MPa

measured by the X-ray method in a WC-CoCr coating sprayed using DJ Hybrid HVOF. Smith et al. [61] reported a -1000 MPa compressive stress by the curvature method for the same material sprayed using the JP5000 HVOF process. As shown in the earlier chapters, the formation of stresses in thermally sprayed coating is relatively complex and affected by many factors. Particle conditions (velocity, temperature, and melting degree) upon impact determine whether quenching stresses or peening stresses dominate at the deposition stage. The material temperature history of the substrate together with the CTE differences between the substrate and coating material determine the post deposition residual stresses. However, relaxation of the stresses by cracking, creeping, and lamella slipping [38] may be activated, causing the measured stresses not to depend directly on the above-mentioned factors. Furthermore, different residual stress measurement methods may give different residual stress levels. Therefore, it is natural that variation in spray processes, powders, and temperature histories may produce a wide variety of residual stresses.

The majority of residual stress studies on high kinetic sprayed coatings have been done for HVOF-sprayed WC-Co and WC-CoCr coatings. With respect to residual stresses in HVOF-sprayed WC-CoCr coatings, the method used for residual stress determination has been layer removal, X-ray diffraction (XRD), hole drilling, and the curvature method. McGrann et al. [62] used the layer removal method to determine residual stresses in JetKote II HVOF-sprayed WC-17Co coatings. Coatings were sprayed using various parameters on mild steel or aluminum substrates in order to modify the residual stress state. In the case of steel substrate, they reported compressive residual stress states of -124 MPa to -365 MPa in the coatings; when they used aluminum substrate having a higher CTE they measured even higher stresses, reaching -80 MPa, -500 MPa, and -760 MPa in the WC-17Co depending on the parameters. Oladijo [63] used the X-ray diffraction method and Venter [64] used neutron diffraction measurement in a study in which they altered the compressive post deposition stresses in JP-5000-sprayed WC-17Co coatings by varying the substrate CTE. It is noteworthy that JP-5000 uses kerosene fuel and the powder is fed radially on the nozzle. Table 2 shows the average compressive residual stress in the coatings with both methods. Santana [65] also showed compressive residual stresses in JP-5000 WC-17Co coating. Stresses in the coating according to XRD ranged from -183 MPa to -220 MPa. Luo et al. [66] also showed -120 to -350 MPa compressive stresses for CJS, which is kerosene HVOF with radial powder feeding and uses hydrogen stabilization to lower the flame temperature compared to JP-5000. Although the majority of XRD residual stress measurements were

performed on high pressure kerosene fuel systems, which produce mainly compressive stresses, it is evident that if the particles are heated, more tensile residual stresses can be generated in the coating, as shown by Pina et al. [67]. They studied the residual stresses in WC-12Co coatings by XRD and measured 160 MPa of tensile residual stress in the coating surface. The coating in this case was sprayed with CDS-100 HVOF (from Plasma Technik AG), which is a relatively high temperature, first generation HVOF system.

Table 2. The effect of various substrate CTEs on residual stresses of JP-5000 sprayed WC-Co coatings. [63,64]

Substrate	CTE (10^{-6}/C)	Residual Stress (Neutron diff.)	Residual Stress (X-ray)
Al	23	-378 MPa	-224 MPa
α-Brass	19	-48 MPa	-149 MPa
Stainless steel	17		-93 MPa
Mild steel	11	-35 MPa	
Super invar	1.2	70 MPa	-79 MPa

The literature highlights a few aspects that need to be considered when looking at stress results measured by the XRD method. The first aspect is that typically only the residual stress of the WC phase is determined by XRD [63,65]. The matrix and carbide phase may have a different CTE and their thermal mismatch during contraction may lead to significant local residual stresses. A lower CTE for WC compared to cobalt for example leads to compressive stresses in WC, as measured by Larson and Oden [68] for sintered WC-Co. Secondly, the penetration depth of typical laboratory scale X-rays is only a few micrometers and always measures the surface [69]. However, the residual stresses of the coatings are not uniform in terms of through thickness. Often, for example if the WC-Co coting is on top of steel, the CTE of the coating is lower than that of the substrate, which produces compressive stresses during post-deposition cooling. On the other hand, the quenching stresses, which are tensile, dominate the deposition stage. As a result, compressive stresses are higher near the substrate interface and shift toward tensile as the coating thickness increases [50]. Stokes and Looney [70] also showed that quenching effects became smaller as the coating thickness increased up to 1 mm. Therefore, the thickness coating is an important factor to observe when comparing the residual stresses of coatings. Furthermore, Pina et al. [71] showed in their study that the external loading of coated structure do not necessarily transfer the strains to the lattice level of coating. They bent various coated beams and measured the stresses by XRD and strain gauges from the top of coatings and for some of the materials

could not detect the relation between the XRD stress and mechanically applied stress. They stated that the observed phenomenon of coating behavior is due to the coating structure, in which the opening of pores and microcracks and the sliding between lamellae allow the transfer of externally applied strains in the macroscale. X-ray diffraction operates on a smaller scale than the strains imposed by external loading. In contrast, strain gages, shown in Fig. 8, glued on the coating surface, correspond to strains integrated over their underlying surface and add the effects of the strain of dense material to the strains due to cracks, porosity, and lamella sliding. Therefore, they state that the magnitude of the strains recorded by strain gages is higher than that observed by X-ray diffraction. Thus, it is clear, that this specific structure of the coating must be understood, when evaluating its stress states by different methods. XRD method measures the local stresses in the lamellae and depend on the microscale lattice strains and Young's modulus in the lamellae whereas the methods based on measuring elongation or deflection such as curvature and the layer removal method based on strain gages depend on the macroscale strains and Young's modulus of the larger coating volume. It is noteworthy that when coating density and lamellae adhesion improve, the stresses measured by the different methods converge.

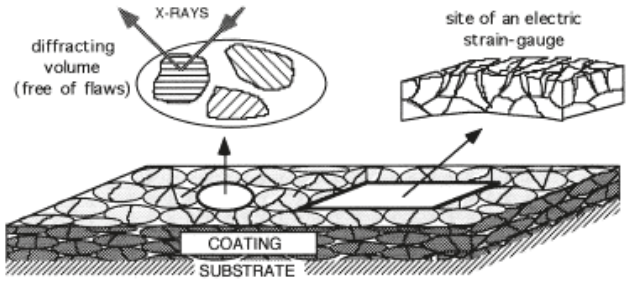

Figure 8. A schematic of the different volume scales of the material covered by X-rays and electric strain gages [71].

A relatively good understanding of the effect of coating processes on the residual stresses of HVOF-sprayed WC-Co and Cr_3C_2-NiCr coatings is gained from the curvature studies of Smith et al., Lamana et al., and Vackel et al, listed in Table 3. They used an ICP device to measure curvature and average residual stress in the coating [61,72,73]. Generally, the DJ Hybrid HVOF process produces tensile residual or slight compressive stresses, whereas the JP 5000 produces higher compressive residual stresses. However, it is evident that variation is relatively wide depending on the spraying parameters. Smith et al. [61] showed the variation of WC-

CoCr sprayed by JP5000 to be 14 to -1081 MPa. Vackel et. al [73] showed that pushing the gas flows higher in the DJ Hybrid process can produce relatively high compressive residual stress with that torch as well. From the study of Lamana et al. [72], it is evident that with the same parameters WC-12Co has the tendency for slightly higher compressive stress compared to WC-17Co.

What is noticeable is that relatively few studies have been carried out for residual stresses in Cr_3C_2-NiCr coatings. One of the few studies was the work of Smith et al., who showed strong parameter dependency on the residual stresses of Cr_3C_2-NiCr as well [61]. Also, residual stresses of HVAF-sprayed coatings have been reported only in a few studies. They highlight that a colder and higher velocity process than HVOF shifts the residual stresses toward compressive stress. Kumar et al. [74] showed compressive stress by XRD ranging from -360 to -500 MPa in a HVAF (AK-06)-sprayed WC-CoCr coating. Bolelli [75] reported approximately zero residual stress in HVAF (M3) sprayed WC-CoCr coating.

Table 3. Curvature residual stresses of various carbide-based hardmetal coatings sprayed by various processes and parameters.

Authors	Coating Material	Process	Residual Stress (Stoney)
Lamana, Pukasiewicz and Sampath, 2018 [72]	WC-12Co	HVOF DJ Hybrid 2600	-46
	WC-12Co	HVOF JP 5000	-434
	WC-17Co	HVOF DJ Hybrid 2600	-16
	WC-17Co	HVOF JP 5000	-388
Smith et al., 2020 [61]	WC-12Co	HVOF DJ Hybrid 2600	-61, -151
	WC-12Co	HVOF JP 5000	-432
	WC-10Co4Cr	HVOF JP 5000	14.3, -71, -1081
Vackel and Sampath, 2017 [4]	WC-CoCr	HVOF DJ Hybrid 2600	-645, ±0
Smith et al., 2020 [61]	Cr_3C_2-NiCr	HVOF DJ Hybrid 2600	57, -126
		HVOF JP 5000	-432

Regarding cold sprayed coatings, Luzin et al. [76] studied cold sprayed (Kinetic Metallization) Al and Cu coatings by neutron diffraction and the Tsui and Clyne fitting and measured compressive residual stresses in both materials. In aluminum, approximately -9 MPa of compressive stress was measured, whereas residual stress in Cu was -45 to -81 MPa. Aluminum showed minimal shock hardening compared to Cu due to its low impact energy. Luzin et al. stated that the deposition stage stresses play a major role in residual stress development in cold spraying and that thermal effects do not play a notable role in changing the distribution. The residual stresses in the material are determined by dynamic flow stress, which is the stress required to continue the plastic deformation in the material, and impact pressure.

They stated that the higher impact energy of Cu, despite its higher dynamic flow stress, leads to a significantly higher plastic strain and compressive stress in copper than in aluminum [76]. Spencer et al. also followed the approach of Tsui and Clyne's progressive model to evaluate residual stresses in aluminum coatings sprayed by the Kinetic Metallization and CGT Kinetiks 4000 systems [77]. Coatings were sprayed on magnesium alloy. The residual stress in aluminum coatings sprayed by the Kinetic Metallization system was -17 - -21 MPa, whereas the CGT system reached -76 MPa stresses in the aluminum. They concluded that the residual stress profiles were dominated by the peening process and that the thermal mismatch stresses were minimal. However, at higher processing temperatures, the thermal mismatch stresses became notable. Ghelichi et al. [78] pointed out that favorable compressive stresses may relax considerably due to the process gas temperature from the cold spray to induce a negative annealing effect in the coating and substrate. This effect was clearly observed by means of experiments on samples previously grit blasted and then submitted to the cold spray process without using powder.

4 WEAR PROPERTIES OF THERMALLY SPRAYED WC-COCR AND CR_3C_2-NICR COATINGS

Mechanical wear can be described as the gradual removal or deformation of a material. The severity of the wear depends on the intensity of the mechanical contact force that takes place between the surfaces and the relative speed of the counterparts. It is important to note that wear is not a material property, but a system response. Many different wear modes have been identified such as adhesive, abrasive, fretting, cavitation erosion, and impact wear. The wear mode defines a situation which has relatively similar conditions in the interrelationship of the counterparts. The physical mechanisms of material removal are still not well defined [79]. Generally, it may be thought that the mechanism is the detachment or physical separation of material particles from the surface, starting with the breakdown of the surface or subsurface material structure as a result of loading from a moving counterpart. Local plastic deformation resulting in grooving, crack initiation, and crack growth destroys the surface and results in wear particle formation and accumulation of wear. In abrasive and adhesive wear relatively high contact loads are most likely to causes severe plastic deformation at the surface and cause severe wear. Fatigue wear is often mild wear as it requires crack growth by continuously repeating loading induces the plastic deformation and contributes to crack initiation and growth under the contact area. Plastic deformation around an asperity, also in light contact, has been thought to play an important role in fatigue wear [80]. Cavitation erosion wear and erosion wear may also take place as the fatigue erosion mechanism. [79–83]

The wear resistance of materials is usually dependent on a complex combination of fracture toughness and hardness. For most materials, an increase in hardness results in a decrease in toughness. A good combination of toughness and hardness is sought by combining the ductility of a metallic phase and the hardness of a hard phase in a so-called metal matrix composite (MMC). One example of such a successful material is WC-Co hardmetal, which is traditionally produced by liquid phase sintering. The high wetting and adhesion between the WC hard phase and Co matrix are advantageous for the properties of WC-Co. Good cohesion is explained first by the good wetting of liquid Co on WC, and second, the strong bonding forces between metallic Co and W. Bonding between hard phases was found to be strongly

related to the dissolution of carbide in the matrix resulting in a nucleated zone [84]. Hardmetals, such as WC-Co(Cr) and Cr_3C_2-NiCr are also the most important group of materials processed by thermal spraying [85]. When the hardness and toughness of HVOF-sprayed WC-Co were investigated, it was found that the WC-Co coatings by HVOF were rather brittle, regardless of the Co content. It was clarified that significant dissolution of WC into the Co binder phase takes place when the Co binder phase is molten during spraying and there is not enough time available on the substrate for the dissolved tungsten and carbon to fully precipitate back and form carbides [86–88].

4.1 Properties of thermally sprayed hardmetal coatings

The microstructure, which is formed by thermal spray processing is unique compared to microstructures by other processing methods. Thermal sprayed coatings are generated from the impingement of many heated and accelerated individual splats, which form a lamellar structure from the rapidly quenching particles. The lamella boundaries are always the weak links in thermally sprayed coatings and are responsible for the reduced tensile strength and elastic modulus of thermal sprayed coatings. The reduction in the properties can be 10% – 60% compared to the properties of wrought material having a similar phase composition [8]. The imperfectness of lamellar cohesion has hindered the performance of thermally sprayed coatings in many applications. For example, weak lamella boundaries in wear applications can cause increased wear due to lamella detachment. Recently however, higher velocity HVOF or HVAF processes have led to an improvement in coating density and in the cohesive properties of the lamella, hence improving the overall mechanical properties of the coatings.

The variation in the mechanical properties of the WC-Co(Cr) and Cr_3C_2-NiCr coatings has also been presented as related to the microstructural changes arising from oxidation (carbide loss) and carbide dissolution in a matrix. The mechanism of compositional changes in WC-Co coatings is well described and shown in Fig. 9. There are two mechanisms for WC-CoCr coatings that change the coating microstructure and can be detected from the microstructure: a) carbon loss reactions and b) dissolution of carbide in the liquid matrix. Carbon loss occurs via the direct oxidation of the carbide which causes the formation of W_2C, or via the oxidation of dissolved carbon from the liquid. Dissolution of WC into the Co binder phase takes place when the Co binder phase is molten during spraying. Molten Co dissolves the

WC grains, the carbon and tungsten content of the matrix increases, and the relative size of the carbides decreases. During cooling, the Co(Cr) matrix becomes supersaturated from W and C resulting in the formation of W_2C on the surface of the original WC. During slow cooling, the precipitation of eta carbide, Co_6W_6C, phases occurs in the Co-rich matrix. Usually, the cooling rate is so high that equilibrium cannot be reached and amorphous or nanocrystalline W-rich phases may occur. [86,89]

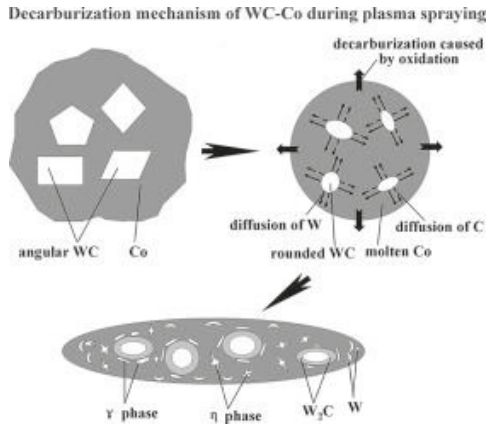

Figure 9. Schematic description of decarburization process in WC-Co powders during flight. (a) In the original WC-Co powder, the WC particles embedded in the Co matrix are sharp and irregular, b) the particle after in-flight stage showing diffusion-controlled carbon loss and W dissolution, and (c) the splat after coating formation and quenching shows carbon loss and W and C dissolution induced phases such as W_2C and eta phase.[90]

In the HVOF spraying of Cr_3C_2-NiCr, the decarburization during spraying results in the formation of Cr_7C_3 and $Cr_{23}C_6$. Cr_7C_3 is observed typically around original Cr_3C_2 carbides and is associated with the overheating of powder particles during spraying. The $Cr_{23}C_6$ carbide occurs in nanosized particles in the matrix as a result of carbide dissolution. In addition, in Cr_3C_2-NiCr coating, Cr_2O_3 thin oxide skins may be found at the lamella boundaries. Neither of these has been shown to have a prominent effect on the brittleness of the coating. It may be that more of the coating properties are influenced by carbide bounce-off, especially when sprayed using the HVAF process [91,92]. [93,94]

Despite the decarburization, the properties of WC-Co(Cr) and Cr_3C_2-NiCr materials are not necessarily degraded during spraying, and coatings in general are known to represent the most wear-resistant material applied by using thermal spray processes. Further, many studies have shown that due to the colder flame, the

carbide dissolution and oxidation is lesser in the HVAF process than in the HVOF process, which has a positive effect on the ductility of the coating. However, process optimization by in-situ monitoring of the particle state and linking it to mechanical properties and wear performance enables further improvement of coatings for their desired properties. It should also be said that the temperature and velocity of the particles substantially influence the stress states of the coating, a topic on which there is little information in the literature.

4.2 Effect of residual stresses on the wear properties of thermally sprayed hardmetal coatings

Compressive residual stresses have proven beneficial against several wear modes such as abrasion, adhesion, erosion, fretting, and cavitation erosion [95–98]. In many cases, stresses are generated on the surface of the components by machining or other post-treatment processes such as shot peening. In some cases, the wear itself may induce a hardening mechanism and generate compressive stresses. Garbar et al. [97] showed that compressive residual stresses, which were initiated by the abrasive wear process itself, increased the abrasive wear resistance of steels. Steels were heat treated in various heat treatment stages and wear resistance increased even if the material had already been treated to its maximum hardness. However, it is ambiguous whether the improvement in abrasion resistance is affected by the increase in hardness or the residual stress state. Concerning thermally sprayed coating, the residual stresses are generated from the coating manufacturing process and have an effect throughout the whole coating, not only on the surface. Further, the stresses influence the surface layer of the substrate. Although residual stresses are an inevitable part of thermally sprayed coatings, their effect on wear resistance has been investigated only in relatively few studies. Most of the publications address abrasive erosion and cavitation wear. It is characteristic of the studies on the relation of residual stresses and the wear of thermally sprayed coatings that it is often unclear how much the stress state influences the wear resistance. This is because when the stress state changes due to altering the spray parameters, other coating properties such as hardness and toughness often change as well, which makes it difficult to draw conclusions. Moreover, the residual stress states may be generated from many different sources, leading to stress states at different micro or macro levels. Inhomogeneous stress states may have an unpredictable effect on the wear resistance

against various wear mechanisms. Therefore, in many cases, the effect of residual stresses is only generally stated, but mechanistic examination is lacking.

Oladijo et al. [63,99] identified the correlation of the abrasion wear resistance and residual stresses of WC-Co coatings (Fig. 10). The residual stresses of the coatings were altered by spraying onto the substrates with various CTEs. However, the use of different substrates also resulted in different hardnesses and there was also a correlation between abrasive wear resistance and hardness. Maiti et al. [100] showed that abrasion wear resistance in the ASTM G-65 rubber wheel test and erosion resistance in ASTM G-76 improved as an increased amount of coating thickness was ground. The increased ground thickness contributed to increased compressive residual stress, which they combined with good abrasion and erosion resistance. They also mentioned that surfaces were work-hardened due to the grinding process, which may explain the increased wear performance as well. When studying the adhesive pin-on disc wear test, Luo et al. concluded that high compressive residual stress increases the wear resistance, while high tensile stress decreases the wear resistance [66]. They increased the compressive residual stresses in the coating surface by adding more spray layers. [63,66,99,101,102]

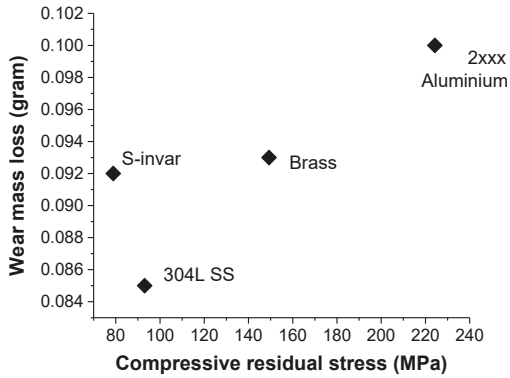

Figure 10. Effect of compressive stress on the abrasion resistance of WC-Co coatings on different substrates [63].

In cavitation erosion, damage is caused by the continuous formation and collapse of cavitation bubbles that generate a high impulsive load of high intensity. Each individual load generates microscopic damage and, as they are repeated during the exposure, macroscopic damage will occur [103]. In metallic materials the cavitation erosion rate can typically be divided into three stages. In the first stage, incubation,

dislocation slip planes are formed, and plastic deformation starts to accumulate and causes crack initiation and growth. During the second stage, material removal will accelerate as plastic deformation further accumulates. Material removal is observed in many locations, although some areas appear to remain unchanged. In the third stage, maximum erosion, the original surface is completely removed, as a network of cracks has broken the surface into small pieces, which are gradually removed from the surface. Cavitation thus occurs by a mechanism, shown in Fig. 11, in which a) cracks are formed due to plastic deformation, b) cracks grow as a consequence of continuous load impulses, and c) particles are removed from the surface. The cavitation process requires crack initiation and for this reason it can be considered as a process requiring fatigue cracking. Therefore, materials capable of sustaining fatigue crack growth (high fracture toughness, KIC) and which withstand load impulses without plastic deformation (high yield strength) are the materials that perform best against cavitation erosion. Such materials include stainless steels or nickel and cobalt alloys. Several approaches have been successfully applied to further improve the cavitation erosion resistance of materials. These include surface hardening by shot peening or laser peening processes or other surface treatments in order to harden a surface locally to increase the yield strength and to induce a compressive stress in the surface. This prevents crack opening, hinders crack growth, and has a positive influence on cavitation erosion resistance [104]. It has been discussed in several papers that compressive residual stresses, if present in thermally sprayed coatings, improve their cavitation resistance [72,74,105–107]. However, the residual stress might not have been measured in the studies or the variation in their magnitude was insignificant. Furthermore, combining improved cavitation resistance with a stress state has proven challenging, because changes in the manufacturing parameters that produce different residual stress states produce changes in the other properties of coatings as well. For example, factors like porosity, density, hardness, and other properties of lamella interfaces have been mentioned as affecting cavitation erosion resistance [106,108]. [60,72,74,103–107,109,110]

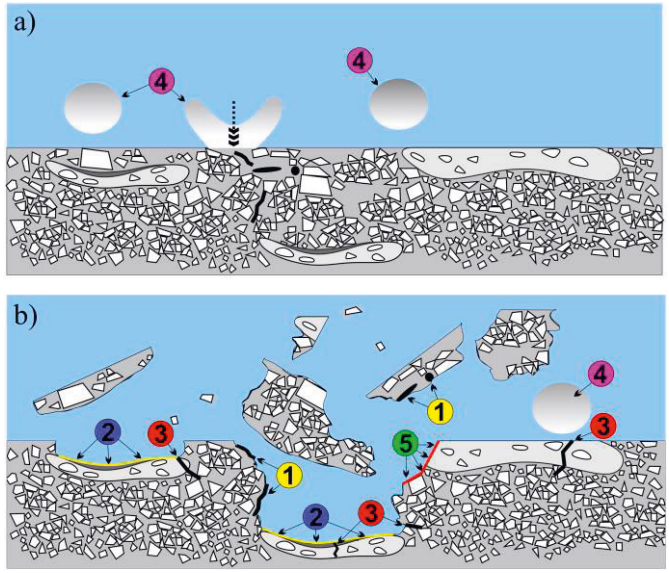

Figure 11. Cavitation erosion mechanism in WC-CoCr coatings according to Matikainen et al.: a) crack initiation stage and b) material removal stage. 1) Existing cracks and pores in the coating, 2) splat surfaces with weak bonding, 3) cracks formed by fatigue wear, 4) cavitation bubbles, and 5) brittle fracture surface. [106]

4.3 Effect of thermally sprayed coating on the fatigue life of a component

Repeated loading can start a fatigue mechanism in the material, leading to the nucleation of a small crack, followed by crack growth, and ultimately complete failure. Cyclic loading, which is below the yield stress (in the elastic region) initiates very local plastic deformation as a result of repeated dislocation slipping and initiation of non-reversable changes in the microstructure. Fatigue failure requires first the initiation of a crack, usually on the surface, thus it is dependent on the surface quality. After initiation, the crack growth rate is dependent on the conditions at the crack tip and is controlled by the load amplitude, frequency, and the material's ability to resist crack growth. As the crack initiation and growth rate are dependent on the stress field in the crack tip, it can be influenced by residual stresses. A compressive stress state on the surface is one of the clear benefits observed to improve the fatigue resistance of the components [111]. Several surface treatment processes that produce compressive residual stress, such as shot peening and laser shot peening, have been utilized to improve the fatigue resistance of shafts, gear

wheels, and other components. It is also known that many surface thermo-chemical treatments such as nitriding and carburizing increase the fatigue life of steel due to the compressive residual stresses they produce [112].

Studies on the effect of applied thermally sprayed coatings on the fatigue life of components show that the coating may have either a positive or negative influence. Several studies show that various HVOF coatings decrease the fatigue life of the component [3,62,113–115]. Only a few studies show that a positive influence on the fatigue life can be achieved by thermal sprayed coatings with compressive residual stresses [73,116], or by increases in the total stiffness of the component thanks to the application of the coating, thus increasing the fatigue life [117]. In the research of Vackel and Sampath [73], shown in Fig. 12, it was shown that a HVOF-sprayed WC-CoCr coating (S + DJB) with high compressive stresses increased the fatigue performance compared to steel (S), while a HVOF-sprayed WC-CoCr coating (S + DJA) with tensile residual stresses decreased it.

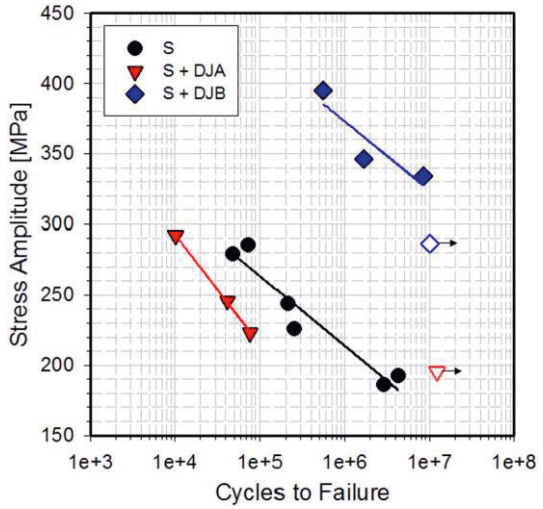

Figure 12. Fatigue life of WC-CoCr coatings sprayed by HVOF compared to steel. Coating can either improve the fatigue performance if the coating is in compression (S+DJB) or worsen the fatigue performance if the coating is in tension ((S+DJA), compared to steel (S). [73]

It is agreed that the fatigue failures of solid materials usually start on the surface of a fatigue specimen or at the locations where the highest tensile stress concentrations have been generated [118–120]. The mechanism of fatigue crack initiation and growth in coated structures have been investigated in relatively few studies but various factors have been shown to influence fatigue life. In the case of coatings, cracks may either occur in the coating or they may be generated in the substrate

under the coating. In several publications, cracks have shown to be initiated directly from the surface of the substrate, most typically from irregularities or grit blasting residues at the coating-substrate interface [115,121–123]. García et al. pointed out that surface roughening produces irregularities for crack initiation, which decreases the fatigue life; on the other hand, the grit blasting process produces compressive stress in the surface, which may increase the fatigue life [116]. However, in some situations, cracks may initiate in the coating. The coating structure, which is full of voids, increases the number of potential locations for crack initiation. Several authors have shown that cracks can initiate in the coating at the locations of weak lamella bonding or pores in the coating [116,117,124]. Zhu et al. also showed crack initiation on the coating surface [125]. Thermally sprayed coatings are relatively brittle and their load carrying capacity is limited. Therefore, perhaps the most important aspect is how the coating influences the crack initiation of the component if the crack has initiated from the coating. Research on the fatigue behavior of bi-layered structures shows that, once initiated, crack propagation is associated with the direction in which the crack approaches the interface. Moreover, it is influenced by the plastic properties of the coating and substrate. If the crack approaches from the less brittle material toward the brittle material, the crack continues to advance through the interface. If the crack approaches the interface from the plastically weak material to the material which can plastically deform, the surface layer can behave as a crack arrestor [126]. Moreover, coating adhesion plays an important role on crack growth in the vicinity of the interface. It has been shown that if the adhesion of the coating is low, the crack can start to advance along the interface and thus delamination of the coating may occur [124]. [3,54,62,73,113,116,117,123,127–129]

5 MATERIALS AND METHODS

There are several parameters in high kinetic thermal spraying that affect the deposit formation and hence the coating properties. The differences in parameters are the greatest between the coating processes such as first generation HVOF, high pressure HP-HVOF, and HVAF. In addition, each coating device may have different hardware setups, which significantly affect the coatings. Finally, the processing parameters are important controllable factors for optimizing the coating microstructure and properties. The main controllable outputs in the high kinetic process are particle temperature, velocity, and melting state. By utilizing in-situ monitoring of the thermal spray process, direct measurements from the spray process can be collected. In this way the relationship between the processing, structure, properties, and performance of the coatings can be determined. By using the on-line particle sensor in flight conditions, T and v, can be monitored, and by using the in-situ curvature monitoring technique direct measurements of the particle impact, quenching, and thermal history can be recorded. Finally, curvature monitoring and the data that it generates allow the determination of the residual stress distribution in the coating by using analytic models, for example.

5.1 Feedstock materials and deposition methods

The focus of this study is mainly on wear resistance materials such as WC-CoCr and Cr_3C_2-NiCr. Commercially available agglomerated sintered powders, with a suitable particle size distribution for each process, were selected as feedstock. The powders used are shown in Table 4. For the cold spray process, the studied materials were atomized metallic powders of copper, titanium and aluminum, which are typically used in this process.

Table 4. Powders used for the study.

Material	Manufacturer	Name	Particle size µm	Spray process
WC-10Co4Cr[a]	Oerlikon Metco	WOKA 3652	15-45	HVOF
WC-10Co4Cr[b]	Durum	Durmat 135.063	15-36	HVOF
WC-10Co4Cr[c]	Durum	Durmat 135.017	5-25	HP-HVOF, HVAF
WC-10Co4Cr[d]	Fujimi	DTS-W827	5-25	HP-HVOF
WC-10Co4Cr[e]	Fujimi	DTS-W828	5-25	HP-HVOF
Cr_3C_2-25NiCr[a]	H.C. Starck	Amperit 584	22-45	HVOF
Cr_3C_2-25NiCr[b]	Oerlikon Metco	WOKA 7304	10-30	HP-HVOF, HVAF
Cr_3C_2-25NiCr[c]	H.C. Starck	Amperit 588	5-30	HVAF
Ti	GfE	-	20-80	Cold Spray
Al	TLS Technik	-	10-50	Cold Spray
Cu	H.C. Starck	Amperit 190.068	10-35	Cold Spray

The spray processes studied were commercial high kinetic HVAF, HVOF, and CS processes. The HVAF process used an AcuKote-07 from Kermetico Inc. (Benicia, CA, USA); the HP-HVOF process used a Carbide Jet Spray (CJS) from Thermico GmbH & Co (Dortmund, Germany); and the HVOF process used a DJ-Hybrid 2600 from Sulzer-Metco (Westbury, NY, USA). The CS system used in this study was a KINETIKS 4000 from Cold Gas Technology GmbH (Ampfing, Germany). These new generation systems were able to produce high particle velocities with various particle temperature histories. The spray parameters are shown in Table 5. For the HVOF and HP-HVOF processes, the parameters A, B, and C were intended to affect the particle temperature by changing the O/F ratio while maintaining the chamber pressure at the level so that the velocities were not significantly affected. It should be noted that the stoichiometric O/F ratios for burning hydrogen (HVOF process) is 0.5, and for kerosene (HP-HVOF process) it is 3.5. In Table 5, the O/F is normalized so that the stoichiometric ratio is 1. In the HVAF process the parameters A, B, and C differed in the total amount of gases fed to the process, with the main aim of affecting the particle velocity.

Table 5. Spray parameters used for the coating deposition.

Parameter	Spray device	H_2 (slpm)	O_2 (slpm)	Air (slpm)	N_2 (slpm)	Normalized O/F ratio	Chamber P (kPa)	SOD* (mm)
HVOF A	DJ-H 2600	660	192	350	14	0.80	538	250
HVOF B	DJ-H 2600	635	216	350	14	0.91	546	250
HVOF C	DJ H 2600	580	233	350	14	1.06	539	250
HVOF D	DJ H 2600	605	246	350	14	1.06	560	250

Parameter	Spray device	Keros. ($l \cdot h^{-1}$)	O_2 (slpm)	H_2 (slpm)	N_2 (slpm)	Normalized O/F ratio	Chamber P (kPa)	SOD* (mm)
HP-HVOF A	CJS 5.2	18	920	80	32	1.33	1330	200
HP-HVOF B	CJS 5.2	16	940	80	32	1.54	1340	200
HP-HVOF C	CJS 5.2	14	960	80	32	1.80	1360	200
HP-HVOF CJS A	CJS 5.2	21	900	80	32	1.11	1400	200
HP-HVOF CJS B	CJS 5.2	18	1000	80	32	1.47	1470	200
HP-HVOF CJS C	CJS 5.2	16	1000	80	32	1.66	1420	200

Parameter	Spray device	C_3H_8 (kPa)	C_3H_8 (slpm)	Air (kPa)	H2 (slpm)	N2 (slpm)	Chamber P (kPa)	SOD* (mm)
HVAF A	AK 07	676	134	824	35	35	600	250
HVAF B	AK 07	600	106	758	35	35	545	250
HVAF C	AK 07	517	94	648	35	35	469	250

Parameter	Spray device	Nozzle	Pressure (kPa)	Temper-ature (°C)	SOD* (mm)
CS Al	Kinetiks 4000	Polymer 22 mm	2500	350	40
CS Ti	Kinetiks 4000	WC-Co 17.5 mm	3000	400	40
CS Cu	Kinetiks 4000	WC-Co 17.5 mm	3500	700	40

** SOD: Stand-off distance*

5.2 Process monitoring and diagnostics

The SprayWatch 2i (Oseir Oy Ltd., Tampere, Finland) diagnostic system was used for the measurement of average particle temperatures and velocities, allowing the presentation of the relative difference of each spray condition. Spray Watch 2i measures the velocities by image analysis of the length of the traces drawn by in-flight particles during the exposure time. The average particle temperature is measured by two-color pyrometry. Coatings were deposited on a 228.6 mm x 25.4 mm x 2.5 mm steel strip, which was mounted on an in-situ coating property sensor (ICP) (ReliaCoat Technologies, East Setauket, USA). The ICP sensor measures the temperature and curvature of the substrate beam during spraying. The curvature

sensor is based on the laser sensing of deflections in a strip during thermal spraying, which is converted to the sample curvature. A simultaneous measurement of temperature is achieved via multiple thermocouples.

5.3 Residual stress evaluation

The ICP curvature was converted to residual stresses using the analytical model as per Tsui and Clyne [2]. The model was developed for progressively deposited coating, in which quenching stresses (or peening stresses) from the deposition stage and post deposition CTE mismatch stresses are superposed to express the stress stage of the coatings. The deposition stage stresses, σ_{dn}, for the new nth layer can be calculated by (5) [2],

$$\sigma_{dn} = \frac{\sigma_q bw \left[\frac{HE'_S+(n-1)\,wE'_d}{HE'_S+nwE'_d}\right]}{bw} - E'_{sd}\Delta\kappa_n\left(\left(n-\frac{1}{2}\right)w-\delta_n\right) \quad (5)$$

where σ_q is the quenching stress, b is the beam width, w is the layer thickness, H is the substrate thickness, E'_d is the effective Young's modulus of the deposit, E'_s is the effective Young's modulus of the substrate, $\Delta\kappa_n$ is the curvature change due to the deposition of layer n, and δ_n is the location of the neutral axis. The calculation of the neutral axis can be found in the original source [2]. In addition, the stresses caused by each new layer, n, affect the layers below, which is taken into account in the Tsui and Clyne model by superposing their effect on the σ_{dn}. For example, the new layer with tensile stresses shifts the underlying layers toward compressive. The stresses caused by the following layers on the underlying layer, j, can be calculated by (6) [2]:

$$\sigma_j = \sum_{i=j+1}^{n}\left(\frac{-E'_d\,\sigma_q bw\left[\frac{HE'_S+(i-1)\,wE'_d}{HE'_S+nwE'_d}\right]}{b\left(HE'_S+(i-1)\,wE'_d\right)} - E'_d\Delta\kappa_n\left(j-\frac{1}{2}\right)w - \delta_l\right) \quad (6)$$

Thus, the deposition stress σ_{dj}in the middle of the ith layer between (1 to n) can be determined based on equations(5) and (6) by (7) [2],

$$\sigma_{di} = \frac{\sigma_q bw\left[\frac{HE'_s+(i-1)\,wE'_d}{HE'_s+nwE'_d}\right]}{bw} - E'_d\Delta\kappa_i\left(\left(i-\frac{1}{2}\right)w-\delta_i\right)+ \sum_{i=j+1}^{n}\left(\frac{-E'_d\sigma_q bw\left[\frac{HE'_s+(j-1)\,wE'_d}{HE'_s+nwE'_d}\right]}{b\left(HE'_s+(\mathrm{j}-1)\,wE'_d\right)} - E'_d\Delta\kappa_j\left(i-\frac{1}{2}\right)w-\ \delta_j\right) \quad (7)$$

which expresses the quenching induced stress in the i[th] layer and adds the effect of all the following layers, j, on that layer. The curvature change, $\Delta\kappa_j$, caused by each layer is (8) [2]:

$$\Delta\kappa_j = \frac{\sigma_q bw\left[\frac{HE'_s+(j-1)\,wE'_d}{HE'_s+nwE'_d}\right]\cdot\left(\left(j-\frac{1}{2}\right)w-\delta_{j-1}\right)}{\left[E'_d b\,(jw)\left(\frac{(nw)^2}{3}-(nw)\,\delta_j+\delta_j{}^2\right)\right]+\left[E'_d bH\left(\frac{(H)^2}{3}+H\delta_j+\delta_j{}^2\right)\right]}. \quad (8)$$

Stresses in the middle of each coating layer can then be calculated even if only the quenching stress, σ_q, is known. Quenching stress can be determined by using the iteration procedure proposed by Tsui and Clyne [1]. In that procedure, the experimentally measured curvature from the deposition stage after x number of spray layers and the sum of calculated curvature changes from equation (8) are set as equal, with the same number of passes. After this procedure, the quenching stress, σ_q, is known and deposition stresses can be calculated for each layer using equation (7).

Post-deposition CTE mismatch stresses, σ_{CTE}, which arise due to the contraction of substrate and coating when cooled from the deposition temperature to room temperature, can be calculated by the formula (9)[2],

$$\sigma_{CTE} = \frac{\left(\frac{2\,\Delta\kappa_C\,\Sigma_S}{h\,H}\right)}{bh} - E'_d\,\Delta\kappa_c\left(\left(n-\frac{1}{2}\right)w-\delta_n\right) \quad (9)$$

where Σ_s is the stiffness of the composite beam, whose calculation can be found in the original source [2], $\Delta\kappa_c$ is the curvature change due to the cooling, n is the number of the layer, and other symbols are as shown earlier. Here, $\Delta\kappa_c$, can be expressed as (10) [2],

$$\Delta\kappa_c = \frac{6E'_dE'_s\,hH(h+H)\,\Delta CTE\,\Delta\mathrm{T}}{E'_d{}^2h^4+4E'_dE'_sh^3H+6E'_dE'_sh^2H^2+4E'_dE'_shH^3+E'_s{}^2H^4} \quad (10)$$

where ΔCTE is the difference in CTE between the coating and the substrate, ΔT is the temperature change during the cooling from deposition temperature to room temperature, and other symbols are as shown earlier. By using these equations, (10) and (11), CTE mismatch stresses can be calculated in the middle of each coating layer by considering that j is the number of layers. The actual in-situ measured substrate temperatures for each layer is now possible to input in equation (11) in order to present the CTE mismatch stresses more accurately and to obtain more realistic data of the residual stresses in the coatings.

The calculation of the layer by layer stresses as per Tsui and Clyne requires the determination of the quenching stress. This can be done by utilizing the ICP curvature measurement and the iteration process they propose [1]. In the original model, the curvature is defined as positive and the residual stress of the layer tensile if the layer of deposit is on the concave side. In this work, the model was also used for negative curvature changes induced by compressive peening stresses. For simplicity, it was assumed that the peening stresses have an influence homogeneously on the previously deposited layer only. However, the peening stress distribution generated from each impinging particle is inhomogeneous and affects the unknown thickness in the layer below the previously deposited layer. In finite element modeling studies, Bansal et al. estimated the stress field thickness in the steel substrate due to impingement of HVOF sprayed particles. They predicted the peening stress field was 30 μm under the diameter of 29 μm AISI 316 particle and 50 μm under the copper particle having the size of 50 μm [43,44]. In the progressive layer by layer calculations of Tsui and Clyne, deposition stresses (originally quenching stresses) are assumed to be formed only on the newly deposited layer. Considering that the thickness of a single layer is typically less than 10 μm, the curvature approach does not necessarily predict the deposition stage peening stresses accurately. However, as the stress field due to peening actions is not exactly known, it is appropriate to assume that peening stresses apply only to the newly added layer. Furthermore, it is assumed that the deposition stresses (peening and quenching stresses) are uniform within the added layers and have each same magnitude. Finally, when the stresses based on the measured curvature changes are superposed over the final coating thickness, calculations of the stresses caused by peening actions can be considered very useful and a relatively accurate representation. The thickness of the peening stress field under the particle is assumed to be only some micrometers, which is less than the thickness of a single layer (10 μm). Further, the thickness of the peening stress field is similar for every layer. Therefore, the calculation of the stresses caused by peening actions using the Tsui and Clyne method can be

considered a good and relatively accurate representation of the residual stresses in coatings.

5.4 Microstructure and mechanical property characterization

The characterization methods included SEM, conventional Vickers hardness measurement with a 300-gram load, carbon and oxygen content analysis using a Leco CS230 carbon analyzer (Leco Corp., St. Joseph, Michigan, USA) and Leco TC600 oxygen analyzer (LECO Corp., St. Joseph, Michigan, USA), and phase structure analysis by X-ray diffraction (Empyrean, PANalytical, Netherlands) using Cu-Kα radiation (1.5406 Å, 40 kV and 45 mA). Phase identification of diffraction peaks was done with HighScorePLUS software (PANalytical, Netherlands). In addition, the elastic modulus and fracture toughness of the coatings were evaluated. The elastic modulus of thermal spray coatings provides a quantitative description of the deposit microstructure. The elastic modulus of coatings was evaluated by instrumented indentation (Zwick ZHU 0.2, Zwick-Roell, Ulm, Germany). For fracture toughness determination, ten indents were taken on polished cross sections at a load of 5 kg. The corner crack lengths of the indents were analyzed by optical microscopy and the fracture toughness was calculated by the equation proposed by Lankford [130] or Evans – Wilshaw [131].

5.5 Wear and fatigue studies

Wear testing was performed using the ASTM G65 abrasive wear test and ASTM G32-16 indirect cavitation erosion tests. In the ASTM G65 rubber wheel abrasion tests, the coating samples were placed in contact with a rubber wheel at a static force of 45 N. Quartz sand with an average size of approximately 250 μm was fed between the rubber wheel and test sample at a rate of 270 g/min. A rubber wheel of 227 mm diameter was used at 200 rpm for a total sliding distance of 4.279 m (6,000 revolutions) for the samples. Prior to testing, the samples were polished to a mirrorlike finish with a 3 μm diamond suspension.

Cavitation erosion tests were performed with an ultrasonic transducer (VCX-750, Sonics & Materials, USA), according to the ASTM G32-16 standard for indirect cavitation erosion. The sample was placed in 25 °C deionized water and a Ti-6Al-4V tip, with a diameter of 13 mm vibrated at a 20 kHz frequency and 50 μm amplitude

at a distance of 0.5 mm from the sample to create cavitation. The coating surfaces were ground flat and polished with a polishing cloth and 3 μm diamond suspension to produce a mirror finish. The volume loss rate ($mm^3 \cdot min^{-1}$) of the samples was determined from the cumulative volume loss curve by using linear fitting.

A force-controlled constant-amplitude axial fatigue test was performed on the coated and non-coated samples according to the ASTM E 466–07 procedure for unalloyed structural steel S355J2G3 bars with a diameter of 20 mm. Corresponding S-N curves of differently treated samples were compared to the coated samples by producing fatigue limit estimates based on the computed staircase tests.

6 RESULTS AND DISCUSSION

This chapter summarizes the main results from Publications I - V and is divided into five sections, describing the relations of the powders used, deposition process, particle conditions, and coating properties. The first section presents the type of powders used for the studies; the second section summarizes the process manipulation strategies and the effect of process manipulation on the particle conditions; the third section introduces the coating structures and main mechanical properties resulting from various spray conditions; the fourth section shows the examples of residual stresses generated from different deposition processes and parameters; finally, the fifth section discusses the most obvious effect of residual stresses on coating performance.

6.1 Powder characteristics

The typical microstructures of the selected WC-10Co4Cr and Cr_3C_2-25NiCr feedstock powders are presented in Fig. 13 and 14. The powder details including the superscripts are explained in Table 4. The microstructures are typical for agglomerated and sintered (a&s) feedstock powders and show the range of powder particle density among the selected powders. With respect to WC-CoCr powders, the WC-10Co4Cr[a] powder used for HVOF (DJ Hybrid) in Publication I (Fig. 13 a) was the most porous and its carbide size was in the micron range. For the HP-HVOF and HVAF spray processes, a smaller carbide size powder was justified due to a smaller tendency for carbide dissolution. Therefore, the submicron nominal carbide size of 0.4 μm was selected and used as the main powder in Publications III and IV. The density of the powder varied depending on the powder manufacturing parameters or pre-treatment. Clearly the densest WC-CoCr powders were WC-10Co4Cr[a] and WC-10Co4Cr[c] (Fig. 13 b), which was also confirmed by the apparent density. The density of WC-10Co4Cr[d] and WC-10Co4Cr[e] powders were adjusted by the powder manufacturer in order to consider the effect of powder density in Publication III. The densest Cr_3C_2-NiCr[b] powder was used in Publication V, which was agglomerated plasma densified powder with spherical morphology and a fully

dense particle cross section, as shown in Fig. 14 b. Agglomerated and sintered Cr_3C_2-NiCr[a] powder (Fig. 14 a) has a more irregular shape and porous cross section. Carbide sizes and shapes were also different. In agglomerated sintered Cr_3C_2-NiCr[a] powder, the carbide size was typically 2-4 μm. The carbide size distribution of the plasma densified powder was wider. The finest carbides in the powder were in the sub-micron range and the largest over 3 μm. During plasma treatment the original carbides partly dissolved in the matrix and precipitated during cooling, which explains the different microstructure of the plasma densified powder.

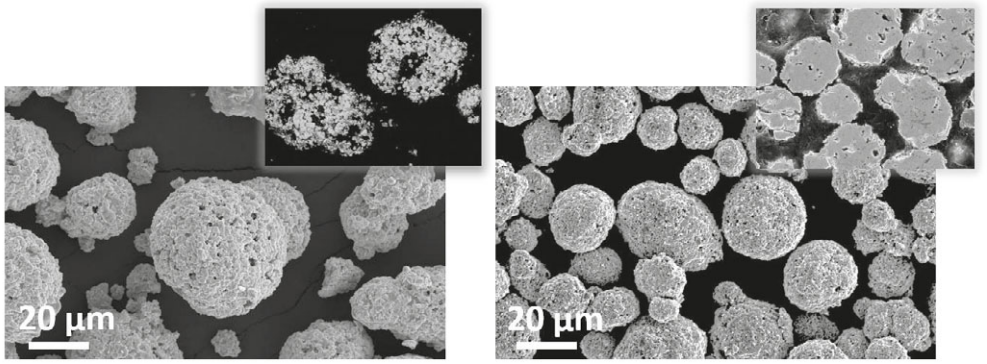

Figure 13. Morphology and cross section of the a) WC-CoCr[a] powder used for HVOF and b) WC-CoCr[b] powder used for the HP-HVOF and HVAF processes.

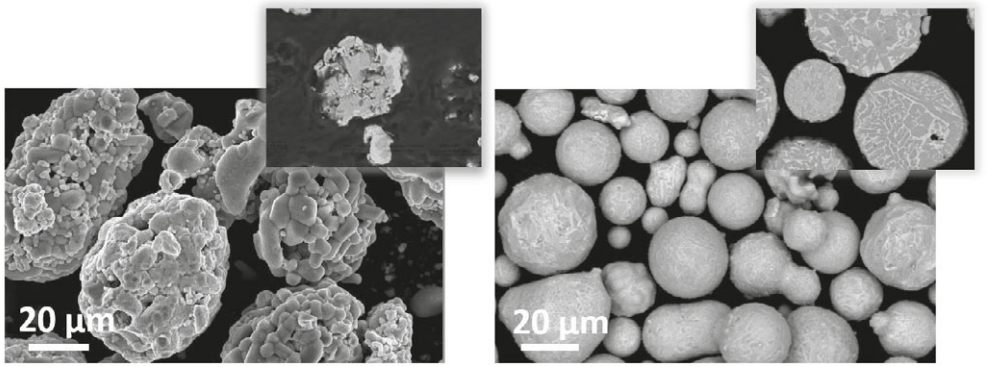

Figure 14. Morphology and single particle cross section of the a) Cr_3C_2-NiCr[a] powder used for HVOF and b) Cr_3C_2-NiCr[b] powder used for the HP-HVOF and HVAF processes.

6.2 Particle in-flight properties and their control

Figure 15 a and b show the first order process maps for WC-CoCr sprayed using various spray torches Publications I, III, and IV and Fig. 15 c shows the first order process map for Cr_3C_2-NiCr sprayed using HVOF. It is evident that the DJ Hybrid HVOF system with a maximum flame temperature of over 2800 °C can produce higher particle temperatures than HP-HVOF (CJS 5.2 configuration) and HVAF. The lower particle heating of the HVAF and HP-HVOF systems makes it possible to spray finer particle size distributions and yet the surface temperatures of the particles do not rise as high as with the HVOF process. The maximum flame temperature of the combustion of a propane-air mixture in HVAF remains under 1900 °C, which is the reason why it has the lowest particle temperatures of the processes. In HP-HVOF, the lower particle heating is a result of feeding the particle radially into a barrel where the flame is cooler, and also due to the fact that very lean O/F ratios can be used because of hydrogen stabilization, resulting in a colder flame. The flame temperatures of the torches can be adjusted to some extent by the O/F ratio and particle velocities by increasing the combustion pressure (CP), as expected. It is worth noting that increasing the CP also increases the temperature of the particle. These behaviors can be explained by considering that, as the gas flow increases the density of the gas flow increases, whereby the drag force increases but also the heat transfer on the powder surface is more effective. Higher chamber pressure also slightly increases the combustion temperature, which increases the temperature of the particles.

The temperature control in HVAF is not possible directly via the O/F ratio, because the system operates with pressure control. The hardware does not measure the air flow to the torch, which can be considered a shortcoming in tuning the flows to certain O/F ratios, because accurate flows are not known. The parameter manipulation of HVAF is limited only to the increase of chamber pressure when using specific gun hardware. The tuning of the O/F ratio is usually based on the visual detection of a stable flame. The margin for the O/F ratio adjustment in HVAF is very limited.

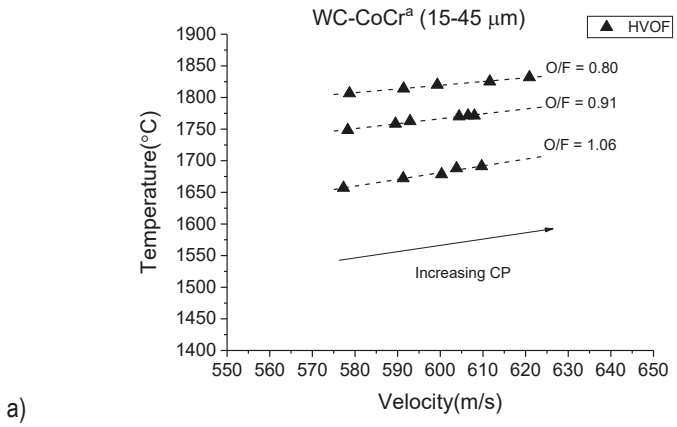

a)

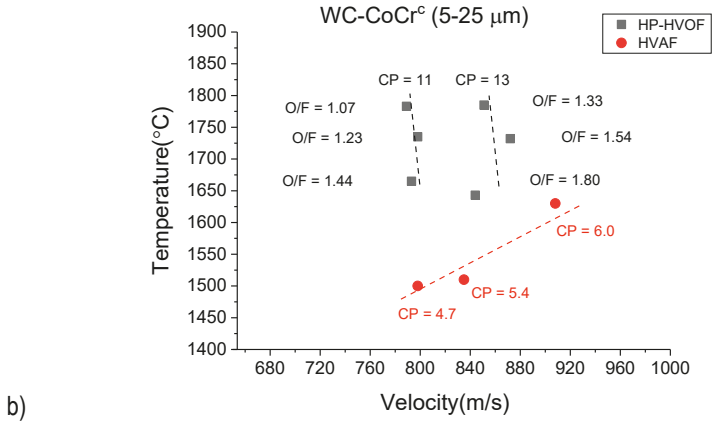

b)

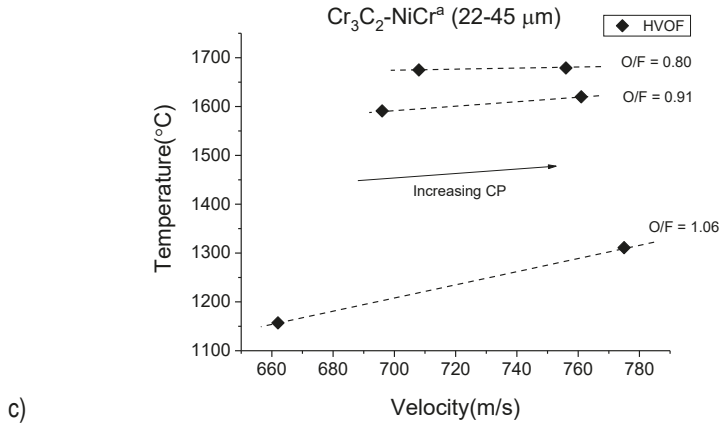

c)

Figure 15. T-v -plots of a) the size of 15-45 WC-CoCr[a] powder sprayed by the DJ Hybrid (H2) HVOF-process, b) the size of 5-25 WC-CoCr[c] powder sprayed by the CJS HVOF- and AK7 HVAF processes, and c) the size of 22-45 Cr_3C_2-NiCr[a] powder sprayed by the DJ Hybrid (H2) HVOF-process. O/F ratios are normalized and chamber pressures (CP) in bars.

6.3 Coating characteristics

Figs. 16 a, b, and c show the cross-section images of WC-CoCr coatings sprayed by HVOF, HP-HVOF, and HVAF. The coatings have a clearly different carbide size. The largest carbide size of the HVOF coating originates from the powder. However, it is noticeable that very fine carbides are missing in the microstructure due to dissolution. In WC-CoCr coatings sprayed by the HP-HVOF and HVAF processes, the fine carbides are still visible in the coatings. The microstructures consist of very fine WC particles homogeneously distributed in the CoCr matrix. A good indicator of the temperature that the particles are exposed to during flight is the amount of W_2C in the coating structure. In Fig. 17, the amount of W_2C is expressed simply by the ratio of the peak heights of W_2C and WC, and is plotted against hardness. It is evident that the increase in hardness in the HVOF process is a result of more effective particle heating and thus the formation of W_2C. Due to hotter parameters the matrix is also hardened, as shown in Publication I. In the HVAF process, the increase in hardness (in Fig. 17 a) does not seem to be related to the significantly increased W_2C formation but is rather a result of higher particle kinetic energy. This can be considered as one clear advantage of a cooler HVAF process as well as the HP-HVAF process. It is also evident in the microstructures of the HP-HVOF and HVAF coatings, shown in Fig. 16, that the higher kinetic energy of the particles along with the finer carbide and powder size distributions result in a finer pore size and a structure having a lower defect population and more homogeneous structure than HVOF. These factors may explain the good hardness and elastic modulus combination of HVAF coatings, as shown in Fig. 17 b.

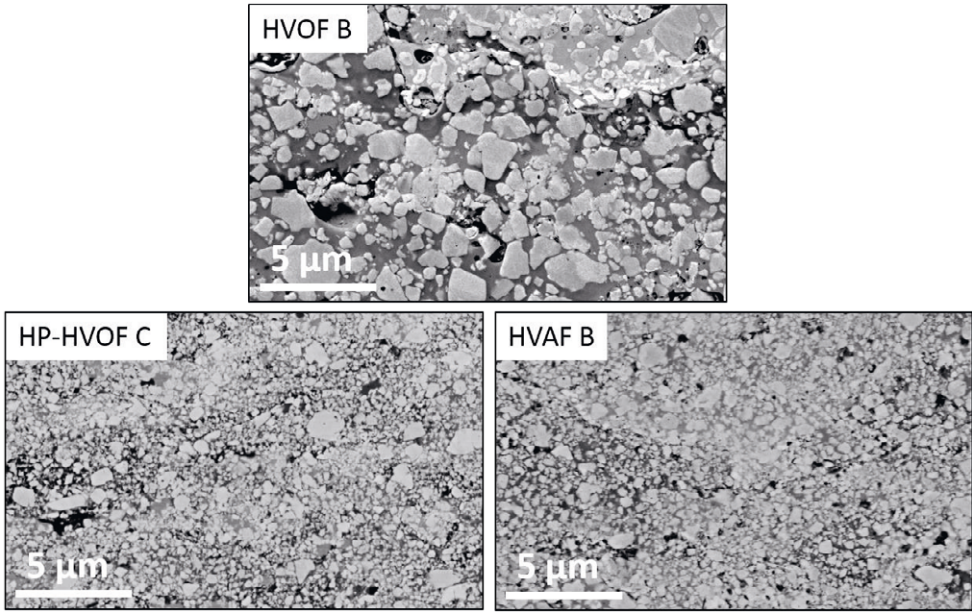

Figure 16. Microstructures of various WC-10Co4Cr-coatings, which were sprayed using the powder shown in Table 4. The powder (WC-10Co4Cr[a]) for HVOF had a coarser particle size distribution and carbide size compared to the powder (WC-10Co4Cr[c]) used for HP-HVOF and HVAF.

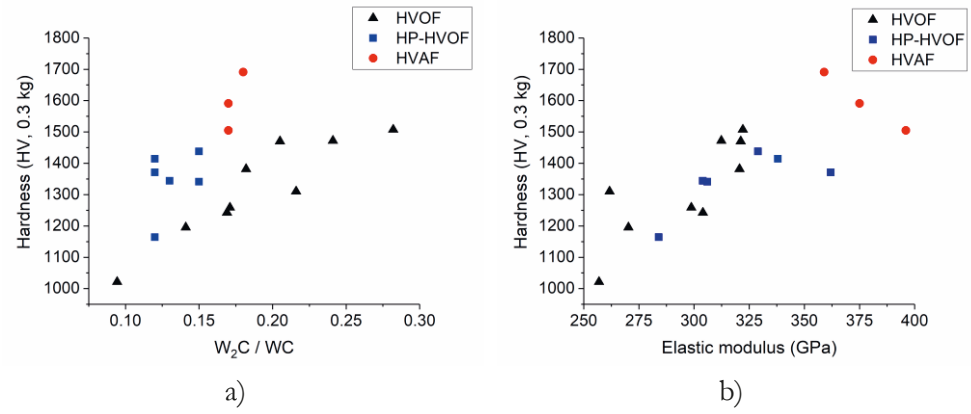

Figure 17. a) Hardness - W_2C/WC relationship and b) hardness-elastic modulus relationship of HVOF-, HP-HVOF-, and HVAF-sprayed WC-CoCr coatings. Publication IV

With respect to Cr_3C_2-NiCr coatings, the visible difference between the microstructures of the HVOF coating (Fig 18 a) and HP-HVOF coating (Fig 18 b) is partly due to the different powder used. In the HP-HVOF coating, the structure

of the powder is clearly visible in the structure. However, it is also clear that the HVOF coating has a lower amount of carbides remaining. Carbide retention may be a reason for the dissolution of carbides and rebounding of the individual carbide particle [92]. Both reasons are more likely for powder that is porous and has a larger carbide size.

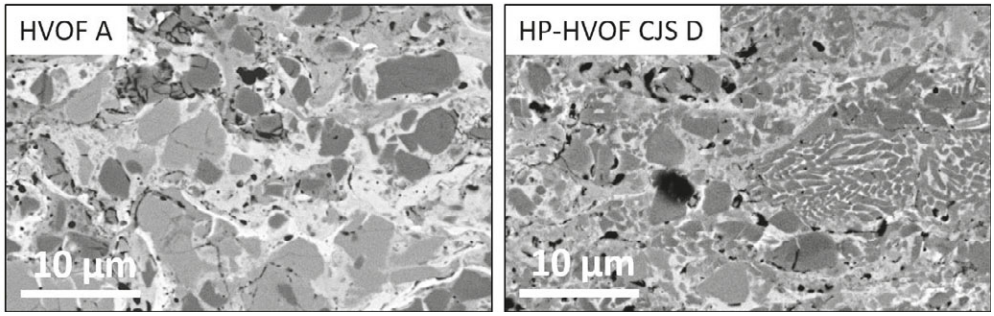

Figure 18. Microstructure of a) HVOF coating sprayed using Cr_3C_2-25NiCr[a] powder and b) HP-HVOF coating sprayed using Cr_3C_2-25NiCr[b] powder.

6.4 Residual stresses in the coatings

Fig. 19 summarizes the in-situ curvature evolution (in the middle column) and corresponding average residual stresses in WC-CoCr coatings sprayed using different parameters. Average residual stresses in the coatings from various residual stress origins were in this case calculated according to the Brenner and Senderoff approximation [48]. In general, it is evident that the particle condition determines the in-situ curvature evolution. However, as the particle temperature is measured on the surface of the particle and processes differ in the particle feeding location, dwell time, and gas flow density, the melting degree of the particles does not directly correspond to the surface temperature. The deposition stresses in the HVOF-sprayed WC-CoCr coatings are tensile, dominated by quenching stresses, whereas HP-HVOF coatings have compressive stresses, dominated by peening stresses. The deposition stresses in HVAF-sprayed WC-CoCr coatings either quench or peen, depending on the level of kinetic energy. It should be noted that the deposition stresses for HVAF shift significantly toward tensile, due to the increase in substrate temperature during the first 3-6 passes. In the Brenner and Senderoff calculations, this effect clearly underestimates the compressive stress state, which is formed due

to peening effects. For better comparison of the processes, this behavior is eliminated in the Tsui and Clyne calculations, as shown in Fig. 20. Only linearly progressing curvature evolution was used for deposition stage stress calculations and the temperature was assumed to be constant throughout the deposition. In Publication IV, stress distributions of the coatings based on the measured substate temperatures are shown. Post deposition cooling stresses due to the CTE differences of the WC-CoCr coatings and steel substrate are compressive and directly proportional to temperature change during cooling. In coatings where the residual stresses were analyzed, as shown in Fig 19, the substrate temperatures were 170 – 260 °C for HVOF, 180 – 210 °C for HP-HVOF, and 275 – 340 °C for HVAF.

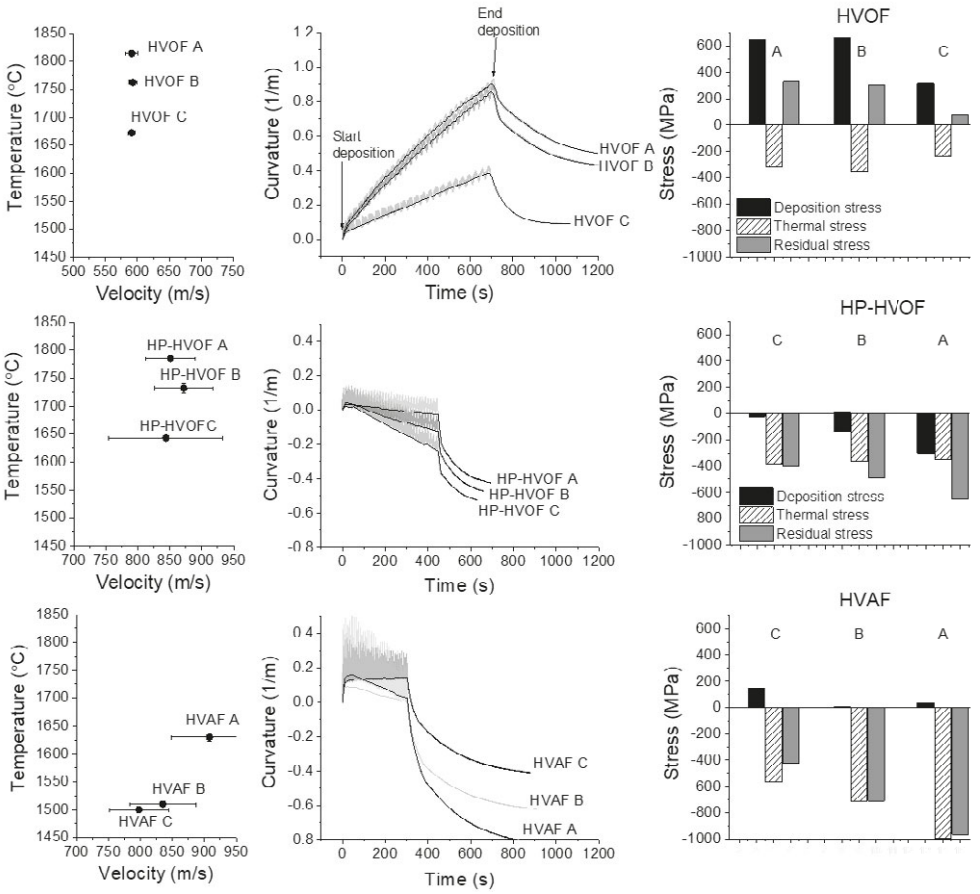

Figure 19. Temperature-velocity data for WC-CoCr and corresponding curvature evolution on ICP sensor. On the right the stresses determined by the Brenner & Senderoff equation from the curvature data.

For better comparison of the processes, Fig. 20 presents the through thickness residual stresses of WC-10Co4Cr coatings at a constant 200 °C according to the Tsui and Clyne analytical model. Here also, the deposition stage stresses (either quenching or peening) were determined from the actual deposition data with the actual substrate temperature given earlier. In contrast, the substrate temperatures were set at 200 °C for the thermal mismatch calculations. Stresses depend significantly on the substrate temperature and to demonstrate this effect, through thickness stresses in HVAF WC-CoCr coatings were also given for a higher substrate temperature, as shown in Fig. 20 c. It should be noted that Publications III and IV show the stress state in these HP-HVOF- and HVAF-sprayed WC-CoCr coatings calculated using the actual deposition temperature. Fig. 21 presents the through thickness residual stresses of Cr_3C_2-NiCr at a substrate temperature of 200 °C. The results show that very high tensile quenching stresses may develop in the WC-CoCr coatings sprayed by the conventional HVOF process, whereas for Cr_3C_2-NiCr coatings, the quenching stresses remain much lower. With the selected parameters it was even possible to generate peening stresses in the HVOF Cr_3C_2-NiCr coating, which was difficult to do with HVOF WC-CoCr. As the particle temperature becomes lower, the peening effects produced by HP-HVOF and HVAF processes increase with both materials used. Peening stresses are evidently the highest in the HP-HVOF coatings. This is probably partly due to a special feature of the CJS process in which very lean O/F ratios can be used thanks to hydrogen stabilization, and partly due to the powder feeding location onto a nozzle. As already shown in Fig. 6 in section 5.2, the O/F ratio influences the flame temperature and thus heat transfer to particles can be lowered by adjusting the O/F ratio further from the ratio that gives the maximum flame temperature. However, stable combustion of kerosene, which is used for CJS, is not possible with very lean O/F ratios. By using a smaller amount of hydrogen, leaner O/F ratios and a colder flame can be used, which is the main reason for the possibility to adjust the cold flame for the CJS process. This is also the reason why relatively fine WC-CoCr powder fractions can be used for the process. On the other hand, in the CJS process, particles are fed onto a nozzle instead of feeding them into a combustion chamber. Therefore, particles do not travel through the combustion chamber, where the temperature of the gases is considerably higher than in the nozzle. To summarize the effect of spraying parameters on residual stresses, the deposition stage residual stresses (quenching and peening) in WC-CoCr and Cr_3C_2-NiCr are strongly related to the spray parameters and their magnitude can vary by several hundreds of megapascals depending on the selected spray parameters alone.

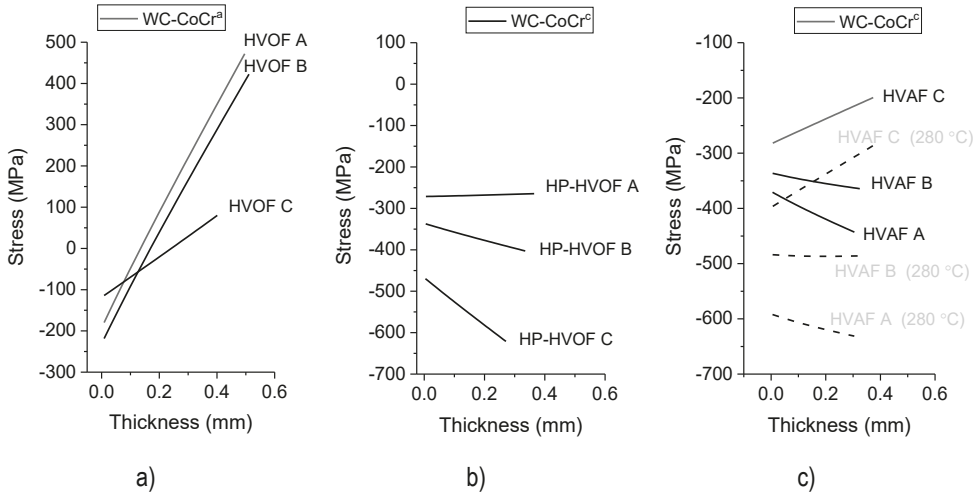

Figure 20. Through thickness residual stresses in various WC-CoCr coatings using the Tsui and Clyne model: a) HVOF with WC-10Co4Cr[a] powder, b) HP-HVOF with WC-10Co4Cr[c] powder, and c) HVAF with WC-10Co4Cr[c] powder.

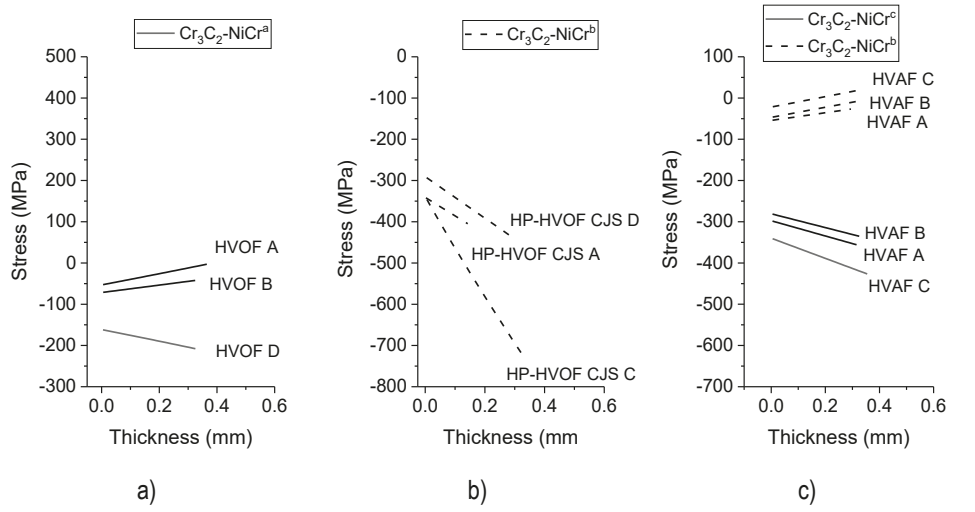

Figure 21. Through thickness residual stresses in various Cr_3C_2-NiCr coatings using the Tsui and Clyne model: a) HVOF with a&s Cr_3C_2-NiCr[a] powder, b) HP-HVOF with a&s plasma densified Cr_3C_2-NiCr[b] powder, and c) HVAF with a&s plasma densified Cr_3C_2-NiCr[b] powder and a&s Cr_3C_2-NiCr[c] powder.

In addition to spray parameters and substrate temperature, the role of the selected powder is crucial. The influence of the particle size distribution and density on the

residual stresses in WC-CoCr coatings are presented in Publication III. Moreover, it is probable that the carbide size and the ability of the matrix to bond the carbide particle may have a strong influence on the peening stresses as well. In Fig. 21 c the HVAF Cr_3C_2-NiCr coating with a powder of dense well bonded carbides (Cr_3C_2-NiCr^b) shows tensile stresses, whereas the more porous a&s powder (Cr_3C_2-NiCr^c) resulted in compressive stresses. This observation is supported by studies concerning the carbide retention of WC-Co/CoCr or Cr_3C_2-NiCr materials, which showed that small size particles cannot bond carbides well, as the size of the carbide approaches the particle size, which increases the bounce-off tendency of individual carbides [91,92]. It became obvious in the work for Publication III that deposition efficiency and peening effect have a strong correlation. Fig. 22 shows almost a linear correlation of deposition efficiency and deposition stress when WC-CoCr^c powder is sprayed via the HP-HVOF and HVAF processes. This powder is relatively dense and has small 0.4 µm carbides. The deposition efficiency – deposition stress relationship of denser Cr_3C_2-NiCr^b powder behaves similarly. However, Cr_3C_2-NiCr^c, which is more porous and has larger carbides, has low deposition efficiency and seems to shift even lower, see Fig 22 b, when the process temperature was increased. With decreasing DE, the peening effects intensifies. This unusual behavior may be explained by the carbide bounce-off effect suggested earlier. In the case of Cr_3C_2-NiCr^c powder, the carbide rebounding must become easier as the ability of the molten matrix to bind the carbides decreases as the temperature of the particles increases.

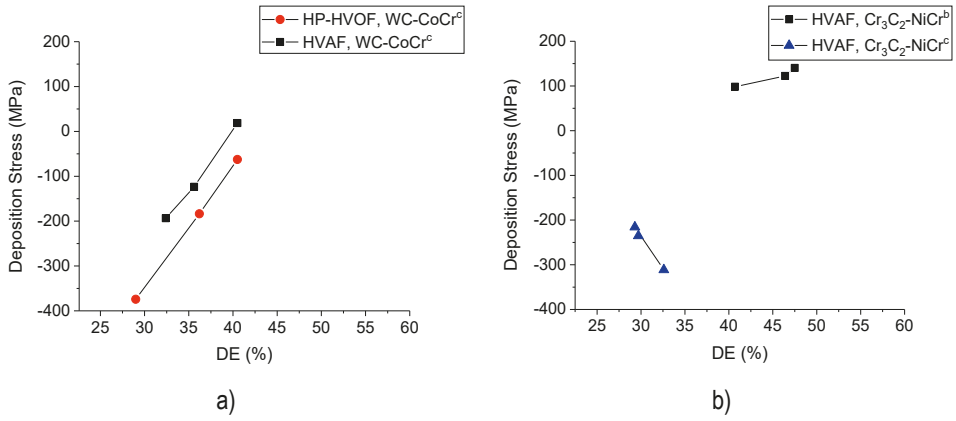

Figure 22. Relationship of deposition stress and deposition efficiency for a) HP-HVOF and HVAF sprayed WC-Co and b) HVAF sprayed higher density Cr_3C_2-NiCr^b and lower density Cr_3C_2-NiCr^c powder.

With respect to residual stress in cold sprayed coatings, it was shown in Publication II that compressive or tensile deposition stresses may develop in the coatings. Due to the solid particle impact, compressive stresses would have been expected. Residual stresses in cold sprayed coatings on top of the steel substrate derived from the data of Publication II are shown in Fig. 23. It was evident that high compressive residual stresses developed only on the copper coating. This result confirms the findings of Luzin et al. [76] who stated that deposition stage stresses play a major role in residual stress development in cold spraying and that thermal effects do not play a notable role in changing the distribution. The higher impact pressure of copper in comparison with aluminum led to significantly higher compressive stresses than in aluminum. It is notable that the deposition stress in aluminum coating is also slightly compressive. However, the high CTE of aluminum transfers the stress state in the coating finally to tensile during cool down. The relatively high tensile stresses that develop during the first two passes are a consequence of the temperature increase during the first passes. This occurred because the substrate had time to cool after preheating before the powder feeding stabilized and deposition could be started. In the case of titanium, it was found that deposition stresses were highly tensile and no significant peening had developed on that material. It was thus shown that the residual stress of cold spray coatings, which are mostly controlled by impact pressure and thus usually develop into compressive, may develop into tensile in conditions with low impact pressure and relatively high thermal energy, which in this case meant a gas temperature of 700 °C.

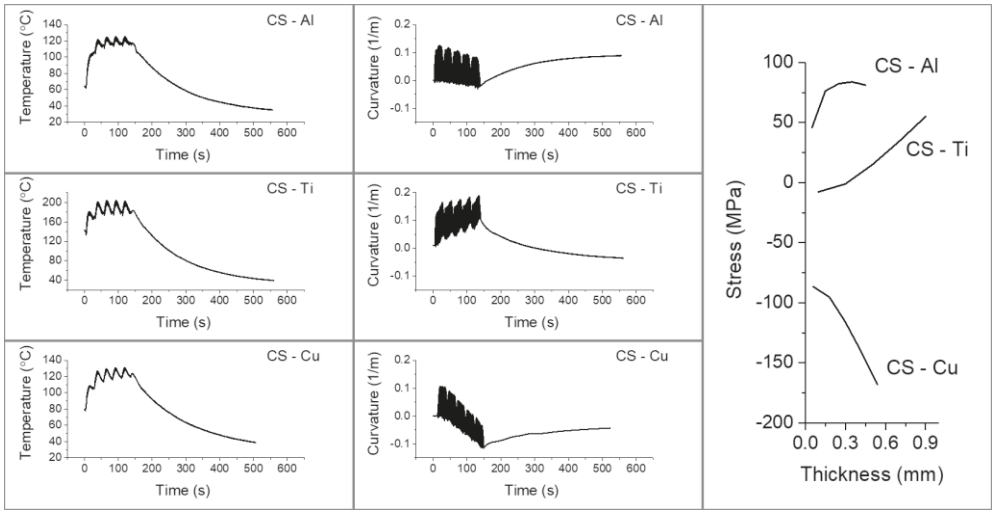

Figure 23. Substrate temperature, curvature evolution, and through thickness residual stresses as per Tsui and Clyne for Al, Ti, and Cu coatings on steel substrate.

6.5 Effect of residual stress on mechanical response, cavitation erosion, and fatigue performance

In this section it is considered how residual stresses in the coating might affect performance, and the potential benefits they can bring. As a general comment, it should be noted that mechanical properties such as the hardness, fracture toughness, and elastic modulus of the coatings are widely published based on indentation techniques. It is known that coatings can contain very high local stress concentrations, but it is not well known how the stresses affect the measured values. In Publication IV it was shown, for example, that the cracking behavior of coatings in indentation fracture toughness measurements may be significantly influenced by residual stresses. Further, it is probable that due to residual stresses different results can be obtained for the same coating, depending on the indentation location and direction. Not enough attention has been paid to this phenomenon in earlier publications.

One noticeable advantage of compressive stress can be found in the fatigue resistance of the coated component Publication V. Fig 24 shows the results from the ASTM E 466–07 fatigue test for steel coated with Cr3C2-NiCr with high compressive stresses, compared to steel with various other surface treatments including turning, polishing, and grit blasting. The improved fatigue resistance of the steel in this case is a consequence of compressive residual stress in the surface of substrate near the interface between the substrate and coating and in the coating, which hinders crack initiation from the substrate coating interface, or from the coating and growth toward the substrate. The significant improvement in fatigue life requires relatively high compressive residual stresses in the Cr3C2-NiCr coating produced with a HP-HVOF kerosene torch. A beneficial effect of compressive stresses has been shown by other studies as well [73,116]. It was also shown in several studies [3,62,113–115] that the coating may also have a negative influence on fatigue resistance, which emphasizes the importance of residual stress control in the coating in order to improve fatigue life.

In Publication IV it was shown that compressive residual stresses may have a beneficial influence on wear resistance. Compressive stresses are beneficial against wear mechanisms in which the wear rate is controlled by fatigue crack growth as is the case in cavitation erosion. Figure 25 shows the very high cavitation resistance of the HVAF- and HP-HVOF-sprayed WC-CoCr coatings, which had high compressive stresses, in comparison with the HVOF coating with tensile residual stresses. The improved wear resistance of the coatings sprayed via HVAF was shown to be related to their high compressive residual stress as well as a homogeneous

coating structure. However, high compressive residual wear stresses did not significantly affect abrasion wear resistance, where the wear mechanism is different.

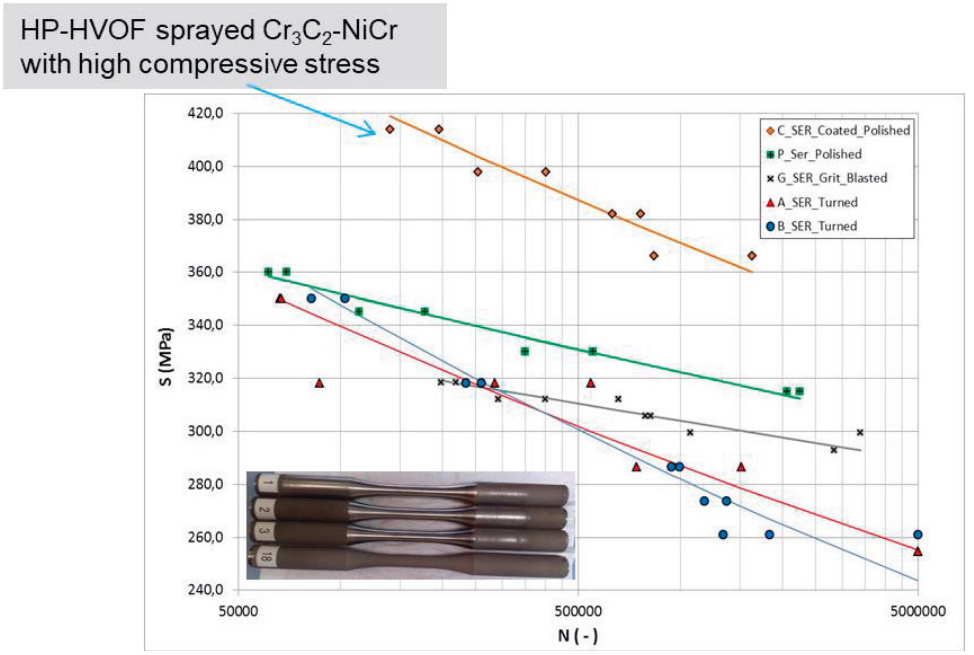

Figure 24. Fatigue life increase in a steel bar due to Cr_3C_2-NiCr coating with compressive stresses (Publication III).

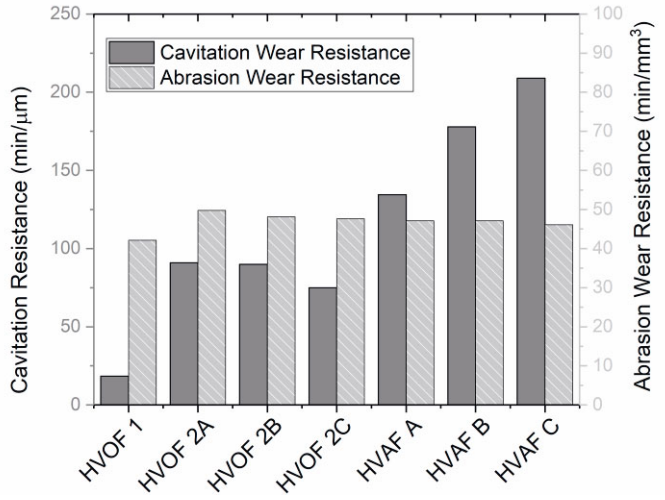

Figure 25. Comparison of cavitation erosion wear and abrasion wear of HVOF, HP-HVOF, and HVAF coatings (Publication IV).

7 CONCLUSIONS

In terms of coating property and performance optimization, it is essential to understand the effect of the particle state, impact conditions, and particle quenching or peening effect, on the formation of the coating microstructure including phases, voids, porosity, and composition. This work took a systematic approach to link the spray particle conditions on coating formation and especially on residual stresses. Various high kinetic energy thermal spray processes such as HVOF, high pressure HVOF, HVAF, and CS were evaluated. First, process mapping methodology was used for evaluating the effect of process adjustments on the particle state for each process. Coatings having a different particle state were deposited on an in-situ curvature device to monitor the particle impact and shrinking induced curvature. The curvature data was further processed into through thickness residual stress presentations according to the Tsui and Clyne analytic model.

7.1 Scientific contribution

The research questions set in chapter 1 are discussed below.

i. **What are the most feasible approaches for assessing stresses via curvature monitoring?**

It was shown that the analytical residual stress model by Tsui and Clyne combined with the in-situ data collected by an ICP curvature and temperature-sensing device allowed through thickness residual stress evaluation of the coatings. In-situ curvature data is essential in order to use a layer by layer analytical model as they are dependent on the determination of the deposition stage stresses (quenching or peening) resulting from each individual pass. In comparison with the Stoney or Brenner and Senderoff equations, which are also useful, the clear benefit of using analytical models with in-situ collected data is that a) stresses can be presented through thickness, whereas the above-mentioned methods give average stresses in the coating and b) temperature variations during the spray process can be taken into account.

ii. How do different spraying processes such as HVOF, HP-HVOF, HVAF, and CS, and the particle state they can provide affect the mechanical properties and stress states of the coating, and how can they be controlled, influenced, and optimized?

It was evident that processes, such as HVAF and HP-HVOF, that possess higher kinetic energy and lower flame temperature, achieved hardmetal coatings with very good mechanical properties. In particular, this can be considered as one clear advantage of WC-CoCr coatings sprayed using the HVAF process, as almost 1700 Vickers hardness and 400 GPa elastic modulus can be achieved without significant W_2C formation. In a conventional HVOF process, over 1500 HV can be achieved as well but this is a result of more effective particle heating and thus the formation of W_2C and loss of ductility.

A systematic procedure of linking the particle state and residual stresses enabled the adjustment of the spray parameters of Kermetico AK-07 (HVAF), Thermico CJS (HP-HVOF), and DJ Hybrid HVOF high kinetic thermal spray processes to significantly influence the stresses in the coatings. The results showed that the difference in the final stress state was mainly due to the stresses generated during the deposition stage (peening or quenching). These stresses could be effectively altered by adjusting the particle state. Moreover, the parameters of high kinetic HVAF and HP-HVOF processes can be adjusted such that deposition induced stresses are highly compressive due to the peening effects. In the case of cold spray, the focus was mainly on the deposition of different metallic materials such as Al, Ti, and Cu on various substrate materials in order to evaluate their residual stresses. It was shown that relatively high tensile deposition stresses may develop in cold sprayed Ti coatings.

Residual stresses are an integral part of thermally sprayed coatings and their generation cannot be avoided. However, as shown, it is possible to influence the magnitude of residual stresses significantly. The generation of stresses is a complex process affected by several factors, which are most importantly: a) the substrate temperature and CTE mismatches, b) spray equipment and selected process parameters, and c) powder properties.

iii. How do residual stresses influence the mechanical response and wear performance of the coating?

High compressive stresses played a significant role in improving the fatigue performance of Cr_3C_2-NiCr coated steel. Thermally sprayed WC-10Co4Cr coatings sprayed using the high pressure HVOF and HVAF processes were shown to provide significant performance improvements in cavitation erosion resistance. The cavitation erosion resistance of the HVAF-sprayed coatings was seven to times higher and for high pressure HVOF four to five times higher compared to conventional gas-fueled HVOF processes. The superior cavitation erosion resistance of the HVAF and high pressure HVOF coatings was partly a result of the dense and homogeneous non-brittle microstructure. The significant factor behind the superior cavitation erosion resistance was probably the high compressive residual stress state in the coatings, which made fatigue crack formation more difficult, hindered fatigue crack growth along the lamellae interfaces, and improved the cavitation erosion resistance.

iv. In what way do the properties of the powder affect the residual stresses?

In addition to spray parameters and substrate temperature, the role of the selected powder is crucial. We showed the influence of powder properties, such as size distribution, density, and carbide size, on the residual stresses in WC-CoCr coatings. Further, it is probable that the carbide size and the ability of the matrix to bond the carbide particle also have a strong influence on the peening stresses.

7.2 Suggestions for future research

It was shown that the residual stress state of coatings varied significantly and influenced wear and fatigue performance. Residual stresses in the coating may have a significant effect on the measured properties as well; this effect is largely unknown because the residual stress state of the coating under measurement is in many cases unknown. This would certainly merit more systematic studies.

Although in this study the effect of residual stress on cavitation resistance was clear, it must be noted that other factors such as mechanically improved coating may also have a role on improved performance. For future studies, the role of lamellar

interface integrity would need further research in order to separate the effect of the possibly improved lamellae adhesion and residual stresses, both of which are affected by adjusting the spray parameters. The challenge would be then to implement such a test method that could measure the lamellae interface adhesion directly.

In this work, it was shown that the effects of residual stresses mainly due to the deposition state may be varied significantly by simply changing the powder particle size distribution or particle density of the WC-CoCr powder. We found a strong relation between the peening effect and deposition efficiency. The mechanism behind the peening effect and its magnitude is not completely understood and a clearly advantageous target would be the ability to generate high compressive stresses without reducing the deposition efficiency. There are several powder related factors which require further and deeper research in order to be able to achieve this target. This could include the effect of powder chemical composition, particle size, carbide size, particle mass, and further increase in kinetic energy. Further, the possibility to use separate peening particles during spraying among the powder, with the purpose of not sticking to the substrate, would be an interesting approach for increasing the compressive stress.

REFERENCES

[1] Y.C. Tsui, T.W. Clyne, An analytical model for predicting residual stresses in progressively deposited coatings: Part 3: Further development and applications, Thin Solid Films. 306 (1997) 52–61. https://doi.org/10.1016/S0040-6090(97)00208-3.

[2] Y.C. Tsui, T.W. Clyne, An analytical model for predicting residual stresses in progressively deposited coatings: Part 1: Planar geometry, Thin Solid Films. 306 (1997) 23–33. https://doi.org/10.1016/S0040-6090(97)00199-5.

[3] A. Agüero, F. Camón, J. García De Blas, J.C. Del Hoyo, R. Muelas, A. Santaballa, S. Ulargui, P. Vallés, HVOF-deposited WCCoCr as replacement for hard Cr in landing gear actuators, J. Therm. Spray Technol. 20 (2011) 1292–1309. https://doi.org/10.1007/s11666-011-9686-1.

[4] A. Vackel, S. Sampath, Fatigue behavior of thermal sprayed WC-CoCr- steel systems: Role of process and deposition parameters, Surf. Coatings Technol. 315 (2017) 408–416. https://doi.org/10.1016/j.surfcoat.2017.02.062.

[5] M. Gui, R. Eybel, S. Radhakrishnan, F. Monerie-Moulin, R. Raininger, P. Taylor, Residual Stress in HVOF Thermally Sprayed WC-10Co-4Cr Coating in Landing Gear Application, J. Therm. Spray Technol. 28 (2019) 1295–1307. https://doi.org/10.1007/s11666-019-00894-w.

[6] P. Vuoristo, Comprehensive Materials Processig, Elsevier Ltd, 2014.

[7] L. Pawlowski, The Science and Engineering of Thermal Spray Coatings: Second Edition, John Wiley and Sons, 2008. https://doi.org/10.1002/9780470754085.

[8] J.R. Davis, Handbook of thermal spray technology. A, ASM International, 2004.

[9] R. McPherson, B.. Schafer, Interlamellar contact within plasma-spreyed coatings, Thin Solid Films. 97 (1982) 201–204.

[10] M. Oksa, S. Tuurna, T. Varis, Increased Lifetime for Biomass and Waste to Energy Power Plant Boilers with HVOF Coatings : High Temperature Corrosion Testing Under Chlorine-Containing Molten Salt, 22 (2013) 783–796. https://doi.org/10.1007/s11666-013-9928-5.

[11] D. Fantozzi, V. Matikainen, M. Uusitalo, H. Koivuluoto, P. Vuoristo, Surface & Coatings Technology Chlorine-induced high temperature corrosion of Inconel 625 sprayed coatings deposited with different thermal spray techniques, Surf. Coat. Technol. 318 (2017) 233–243. https://doi.org/10.1016/j.surfcoat.2016.12.086.

[12] M.A. Uusitalo, P.M.J. Vuoristo, High temperature corrosion of coatings and boiler steels below chlorine-containing salt deposits, 46 (2004) 1311–1331. https://doi.org/10.1016/j.corsci.2003.09.026.

[13] A.S.M. Ang, N. Sanpo, M.L. Sesso, S.Y. Kim, C.C. Berndt, Thermal spray maps: Material genomics of processing technologies, J. Therm. Spray Technol. 22 (2013) 1170–1183. https://doi.org/10.1007/s11666-013-9970-3.

[14] M. Oksa, E. Turunen, T. Suhonen, T. Varis, S.P. Hannula, Optimization and characterization of high velocity oxy-fuel sprayed coatings: Techniques, materials, and applications, Coatings. 1 (2011) 17–52. https://doi.org/10.3390/coatings1010017.

[15] V. Matikainen, H. Koivuluoto, P. Vuoristo, J. Schubert, Houdková, Effect of Nozzle Geometry on the Microstructure and Properties of HVAF-Sprayed WC-10Co4Cr and Cr3C2-25NiCr Coatings, J. Therm. Spray Technol. 27 (2018) 680–694. https://doi.org/10.1007/s11666-018-0717-z.
[16] R. Kreye, H Gärtner, F Kirsten, A Schwetzke, High Velocity Oxy-Fuel Flame Spraying: State of the art, prospects and alternatives, in: Conf. Proc. 5th Kolloquium Hochgeschwindigkeits-Flamspmspritzen, 2000: pp. 5–18.
[17] M. Li, D. Shi, P.D. Christofides, Diamond Jet hybrid HVOF thermal spray: Gas-phase and particle behavior modeling and feedback control design, Ind. Eng. Chem. Res. (2004). https://doi.org/10.1021/ie030559i.
[18] J. Villafuerte, Recent trends in cold spray technology: Looking at the future, Surf. Eng. 26 (2010) 393–394. https://doi.org/10.1179/026708410X12687356948715.
[19] S. Dosta, M. Couto, J.M. Guilemany, Cold spray deposition of a WC-25Co cermet onto Al7075-T6 and carbon steel substrates, Acta Mater. 61 (2013) 643–652. https://doi.org/10.1016/j.actamat.2012.10.011.
[20] S. Dosta, G. Bolelli, A. Candeli, L. Lusvarghi, I.G. Cano, J.M. Guilemany, Plastic deformation phenomena during cold spray impact of WC-Co particles onto metal substrates, Acta Mater. 124 (2017) 173–181. https://doi.org/10.1016/j.actamat.2016.11.010.
[21] M. Couto, S. Dosta, J. Fernández, J.M. Guilemany, Comparison of the Mechanical and Electrochemical Properties of WC-25Co Coatings Obtained by High Velocity Oxy-Fuel and Cold Gas Spraying, J. Therm. Spray Technol. 23 (2014) 1251–1258. https://doi.org/10.1007/s11666-014-0123-0.
[22] M. Couto, S. Dosta, J.M. Guilemany, Comparison of the mechanical and electrochemical properties of WC-17 and 12Co coatings onto Al7075-T6 obtained by high velocity oxy-fuel and cold gas spraying, Surf. Coatings Technol. 268 (2015) 180–189. https://doi.org/10.1016/j.surfcoat.2014.04.034.
[23] P. Fauchais, G. Montavon, G. Bertrand, From powders to thermally sprayed coatings, J. Therm. Spray Technol. 19 (2010) 56–80. https://doi.org/10.1007/s11666-009-9435-x.
[24] Karthikeyan J, Development of oxidation resistant coatings on GRCop-84 substrates by cold spray process, Nasa/Cr. 214706 (2007) 1–16.
[25] G. Richter, H. J. May, Fluid Mechanic and Thermal aspects of High Velocity Spraying, in: Conf. Proc. 5th Kolloquium Hochgeschwindigkeits-Flamspmspritzen, 2000: pp. 19–28.
[26] W. Rusch, Comparison of Operating Characteristics for Gas and Liquid Fuel HVOF Torches, Combustion. (2007) 572–576.
[27] M. Li, P. Christofides, Control of Particulate Processes, in: 2010. https://doi.org/10.1201/b10382-18.
[28] M. Li, P.D. Christofides, Modeling and control of high-velocity oxygen-fuel (HVOF) thermal spray: A tutorial review, J. Therm. Spray Technol. 18 (2009) 753–768. https://doi.org/10.1007/s11666-009-9309-2.
[29] M. Li, D. Shi, P.D. Christofides, Model-based estimation and control of particle velocity and melting in HVOF thermal spray, Chem. Eng. Sci. 59 (2004) 5647–5656. https://doi.org/10.1016/j.ces.2004.06.049.
[30] M. Li, P.D. Christofides, Multi-scale modeling and analysis of an industrial HVOF thermal spray process, Chem. Eng. Sci. (2005). https://doi.org/10.1016/j.ces.2005.02.043.

[31] M. Li, P.D. Christofides, Feedback Control of HVOF Thermal Spray Process Accounting for Powder Size Distribution, J. Therm. Spray Technol. (2004). https://doi.org/10.1361/10599630418086.
[32] M. Friis, C. Persson, Control of thermal spray processes by means of process maps and process windows, J. Therm. Spray Technol. 12 (2003) 44–52. https://doi.org/10.1361/105996303770348492.
[33] S. Sampath, X. Jiang, A. Kulkarni, J. Matejicek, D.L. Gilmore, R.A. Neiser, Development of process maps for plasma spray: Case study for molybdenum, Mater. Sci. Eng. A. (2003). https://doi.org/10.1016/S0921-5093(02)00642-1.
[34] A. Valarezo, S. Sampath, An integrated assessment of process-microstructure-property relationships for thermal-sprayed NiCr coatings, J. Therm. Spray Technol. 20 (2011) 1244–1258. https://doi.org/10.1007/s11666-011-9665-6.
[35] A. Vaidya, T. Streibl, L. Li, S. Sampath, O. Kovarik, R. Greenlaw, An integrated study of thermal spray process-structure-property correlations: A case study for plasma sprayed molybdenum coatings, Mater. Sci. Eng. A. (2005). https://doi.org/10.1016/j.msea.2005.04.056.
[36] D.L. Gilmore, P.A. Neiser, Y. Wan, S. Sampath, Process Maps for Plasma Spray Part I: Plasma-Particle Interactions, in: Proc. Int. Therm. Spray Conf., 2000.
[37] X. Jiang, J. Matejicek, A. Kulkarni, H. Herman, S. Sampath, D.L. Gilmore, R.A. Neiser, Process Maps for Plasma Spray Part II: Deposition and Properties, in: Proc. Int. Therm. Spray Conf., 2000.
[38] S. Kuroda, T.W. Clyne, The quenching stress in thermally sprayed coatings, Thin Solid Films. 200 (1991) 49–66. https://doi.org/10.1016/0040-6090(91)90029-W.
[39] S. Kuroda, T. Dendo, S. Kitahara, Quenching stress in plasma sprayed coatings and its correlation with the deposit microstructure, J. Therm. Spray Technol. 4 (1995) 75–84. https://doi.org/10.1007/BF02648531.
[40] S. Kuroda, Y. Tashiro, H. Yumoto, S. Taira, H. Fukanuma, S. Tobe, Peening action and residual stresses in high-velocity oxygen fuel thermal spraying of 316L stainless steel, J. Therm. Spray Technol. 10 (2001) 367–374. https://doi.org/10.1361/105996301770349457.
[41] A.A. Abubakar, A.F.M. Arif, K.S. Al-Athel, S.S. Akhtar, J. Mostaghimi, Modeling Residual Stress Development in Thermal Spray Coatings: Current Status and Way Forward, J. Therm. Spray Technol. 26 (2017) 1115–1145. https://doi.org/10.1007/s11666-017-0590-1.
[42] S. Sampath, X.Y. Jiang, J. Matejicek, L. Prchlik, A. Kulkarni, A. Vaidya, Role of thermal spray processing method on the microstructure, residual stress and properties of coatings: An integrated study of Ni-5 wt. % Al bond coats, Mater. Sci. Eng. A. 364 (2004) 216–231. https://doi.org/10.1016/j.msea.2003.08.023.
[43] P. Bansal, P.H. Shipway, S.B. Leen, Residual stresses in high-velocity oxy-fuel thermally sprayed coatings - Modelling the effect of particle velocity and temperature during the spraying process, Acta Mater. 55 (2007) 5089–5101. https://doi.org/10.1016/j.actamat.2007.05.031.
[44] P. Bansal, P.H. Shipway, S.B. Leen, Effect of particle impact on residual stress development in HVOF sprayed coatings, in: Proc. Int. Therm. Spray Conf., 2006: pp. 570–575. https://doi.org/10.1361/105996306X146703.
[45] A.M. Kamara, K. Davey, Simplified models for residual stress prediction in thermally sprayed coatings, Proc. Inst. Mech. Eng. Part C J. Mech. Eng. Sci. 222 (2008) 2053–2068. https://doi.org/10.1243/09544062JMES979.

[46] A.S.M. Ang, C.C. Berndt, A review of testing methods for thermal spray coatings, Int. Mater. Rev. 59 (2014) 179–223. https://doi.org/10.1179/1743280414Y.0000000029.
[47] G.G. Stoney, The Tension of Metallic Films Deposited by Electrolysis, Proc. R. Soc. A Math. Phys. Eng. Sci. 82 (1909) 172–175. https://doi.org/10.1098/rspa.1909.0021.
[48] A. Brenner, S. Senderoff, Calculation of stress in electrodeposits from the curvature of a plated strip, J. Res. Natl. Bur. Stand. (1934). 42 (1949) 105. https://doi.org/10.6028/jres.042.009.
[49] M.J. Azizpour, S. Nourouzi, Evaluation of surface residual stresses in HVOF sprayed WC-12Co coatings by XRD and ED-hole drilling, J. Mech. Sci. Technol. 27 (2013) 2709–2713. https://doi.org/10.1007/s12206-013-0715-5.
[50] M. Jalali Azizpour, Evaluation of through thickness residual stresses in thermal sprayed WC–Co coatings, J. Brazilian Soc. Mech. Sci. Eng. 39 (2017) 613–620. https://doi.org/10.1007/s40430-016-0523-9.
[51] A.J. Perry, J.A. Sue, P.J. Martin, Practical measurement of the residual stress in coatings, Surf. Coatings Technol. 81 (1996) 17–28. https://doi.org/10.1016/0257-8972(95)02531-6.
[52] T.C. Totemeier, J.K. Wright, Residual stress determination in thermally sprayed coatings - A comparison of curvature models and X-ray techniques, Surf. Coatings Technol. 200 (2006) 3955–3962. https://doi.org/10.1016/j.surfcoat.2005.06.003.
[53] T.C. Totemeier, R.N. Wright, W.D. Swank, Residual stresses in high-velocity oxy-fuel metallic coatings, Metall. Mater. Trans. A Phys. Metall. Mater. Sci. 35 A (2004) 1807–1814. https://doi.org/10.1007/s11661-004-0089-5.
[54] M. Wenzelburger, D. López, R. Gadow, Methods and application of residual stress analysis on thermally sprayed coatings and layer composites, Surf. Coatings Technol. (2006). https://doi.org/10.1016/j.surfcoat.2006.04.040.
[55] J. Stokes, L. Looney, Residual stress in HVOF thermally sprayed thick deposits, Surf. Coatings Technol. 177–178 (2004) 18–23. https://doi.org/10.1016/j.surfcoat.2003.06.003.
[56] M. Buchmann, R. Gadow, J. Tabellion, Experimental and numerical residual stress analysis of layer coated composites, Mater. Sci. Eng. A. 288 (2000) 154–159. https://doi.org/10.1016/S0921-5093(00)00862-5.
[57] T. Valente, C. Bartuli, M. Sebastiani, A. Loreto, Implementation and development of the incremental hole drilling method for the measurement of residual stress in thermal spray coatings, J. Therm. Spray Technol. 14 (2005) 462–470. https://doi.org/10.1361/105996305X76432.
[58] Y.Y. Santana, P.O. Renault, M. Sebastiani, J.G. La Barbera, J. Lesage, E. Bemporad, E. Le Bourhis, E.S. Puchi-Cabrera, M.H. Staia, Characterization and residual stresses of WC-Co thermally sprayed coatings, Surf. Coatings Technol. (2008). https://doi.org/10.1016/j.surfcoat.2008.04.042.
[59] J. Matejicek, S. Sampath, D. Gilmore, R. Neiser, In situ measurement of residual stresses and elastic moduli in thermal sprayed coatings part 2: Processing effects on properties of Mo coatings, Acta Mater. 51 (2003) 873–885. https://doi.org/10.1016/S1359-6454(02)00477-9.
[60] G. Bolelli, L.M. Berger, T. Börner, H. Koivuluoto, L. Lusvarghi, C. Lyphout, N. Markocsan, V. Matikainen, P. Nylén, P. Sassatelli, R. Trache, P. Vuoristo, Tribology of HVOF- and HVAF-sprayed WC-10Co4Cr hardmetal coatings: A comparative assessment, Surf. Coatings Technol. 265 (2015) 125–144. https://doi.org/10.1016/j.surfcoat.2015.01.048.

[61] G.M. Smith, E.J. Gildersleeve, X.T. Luo, V. Luzin, S. Sampath, On the surface and system performance of thermally sprayed carbide coatings produced under controlled residual stresses, Surf. Coatings Technol. 387 (2020) 125536. https://doi.org/10.1016/j.surfcoat.2020.125536.
[62] R.T.R. McGrann, D.J. Greving, J.R. Shadley, E.F. Rybicki, T.L. Kruecke, B.E. Bodger, The effect of coating residual stress on the fatigue life of thermal spray-coated steel and aluminum, Surf. Coatings Technol. 108–109 (1998) 59–64. https://doi.org/10.1016/S0257-8972(98)00665-3.
[63] O.P. Oladijo, A.M. Venter, L.A. Cornish, Correlation between residual stress and abrasive wear of WC-17Co coatings, Int. J. Refract. Met. Hard Mater. 44 (2014) 68–76. https://doi.org/10.1016/j.ijrmhm.2014.01.009.
[64] A.M. Venter, O.P. Oladijo, V. Luzin, L.A. Cornish, N. Sacks, Performance characterization of metallic substrates coated by HVOF WC-Co, Thin Solid Films. 549 (2013) 330–339. https://doi.org/10.1016/j.tsf.2013.08.075.
[65] Y.Y. Santana, J.G. La Barbera-Sosa, M.H. Staia, J. Lesage, E.S. Puchi-Cabrera, D. Chicot, E. Bemporad, Measurement of residual stress in thermal spray coatings by the incremental hole drilling method, Surf. Coatings Technol. (2006). https://doi.org/10.1016/j.surfcoat.2006.04.056.
[66] W. Luo, U. Selvadurai, W. Tillmann, Effect of Residual Stress on the Wear Resistance of Thermal Spray Coatings, J. Therm. Spray Technol. 25 (2016) 321–330. https://doi.org/10.1007/s11666-015-0309-0.
[67] J. Pina, A. Dias, J.L. Lebrun, Study by X-ray diffraction and mechanical analysis of the residual stress generation during thermal spraying, Mater. Sci. Eng. A. 347 (2003) 21–31. https://doi.org/10.1016/S0921-5093(02)00580-4.
[68] C. Larsson, M. Odén, X-ray diffraction determination of residual stresses in functionally graded WC-Co composites, Int. J. Refract. Met. Hard Mater. 22 (2004) 177–184. https://doi.org/10.1016/j.ijrmhm.2004.06.002.
[69] T.W. Clyne, S.C. Gill, Residual stresses in thermal spray coatings and their effect on interfacial adhesion: A review of recent work, J. Therm. Spray Technol. 5 (1996) 401–418. https://doi.org/10.1007/BF02645271.
[70] J. Stokes, L. Looney, Predicting quenching and cooling stresses within HVOF deposits, J. Therm. Spray Technol. 17 (2008) 908–914. https://doi.org/10.1007/s11666-008-9274-1.
[71] J. Pina, A. Dias, J.L. Lebrun, Mechanical stiffness of thermally sprayed coatings and elastic constants for stress evaluation by X-ray diffraction, Mater. Sci. Eng. A. 267 (1999) 130–144. https://doi.org/10.1016/s0921-5093(99)00050-7.
[72] M.S. Lamana, A.G.M. Pukasiewicz, S. Sampath, Influence of cobalt content and HVOF deposition process on the cavitation erosion resistance of WC-Co coatings, Wear. 398–399 (2018) 209–219. https://doi.org/10.1016/j.wear.2017.12.009.
[73] A. Vackel, S. Sampath, Fatigue behavior of thermal sprayed WC-CoCr- steel systems: Role of process and deposition parameters, Surf. Coatings Technol. (2017). https://doi.org/10.1016/j.surfcoat.2017.02.062.
[74] R.K. Kumar, M. Kamaraj, S. Seetharamu, T. Pramod, P. Sampathkumaran, Effect of Spray Particle Velocity on Cavitation Erosion Resistance Characteristics of HVOF and HVAF Processed 86WC-10Co4Cr Hydro Turbine Coatings, J. Therm. Spray Technol. 25 (2016) 1217–1230. https://doi.org/10.1007/s11666-016-0427-3.
[75] G. Bolelli, L.M. Berger, T. Börner, H. Koivuluoto, L. Lusvarghi, C. Lyphout, N. Markocsan, V. Matikainen, P. Nylén, P. Sassatelli, R. Trache, P. Vuoristo, Tribology

of HVOF- and HVAF-sprayed WC-10Co4Cr hardmetal coatings: A comparative assessment, Surf. Coatings Technol. (2015). https://doi.org/10.1016/j.surfcoat.2015.01.048.
[76] V. Luzin, K. Spencer, M.X. Zhang, Residual stress and thermo-mechanical properties of cold spray metal coatings, Acta Mater. (2011). https://doi.org/10.1016/j.actamat.2010.10.058.
[77] K. Spencer, V. Luzin, N. Matthews, M.X. Zhang, Residual stresses in cold spray Al coatings: The effect of alloying and of process parameters, Surf. Coatings Technol. 206 (2012) 4249–4255. https://doi.org/10.1016/j.surfcoat.2012.04.034.
[78] R. Ghelichi, S. Bagherifard, D. Macdonald, I. Fernandez-Pariente, B. Jodoin, M. Guagliano, Experimental and numerical study of residual stress evolution in cold spray coating, Appl. Surf. Sci. 288 (2014) 26–33. https://doi.org/10.1016/j.apsusc.2013.09.074.
[79] K. Holmberg, A. Matthews, Coatings tribology properties. techniques. and applications in surface engineering, ELSEVIER SCIENCE B.V., 2004.
[80] A. V. Olver, H.A. Spikes, A.F. Bower, K.L. Johnson, The residual stress distribution in a plastically deformed model asperity, Wear. 107 (1986) 151–174. https://doi.org/10.1016/0043-1648(86)90025-6.
[81] P.J. Blau, Fifty years of research on the wear of metals, Tribol. Int. 30 (1997) 321–331. https://doi.org/10.1016/S0301-679X(96)00062-X.
[82] R.G. Bayer, Engineering design for wear, Second, 2004.
[83] G.W. Stachowiak, A.W. Batchelor, Engineering Tribology, 2014.
[84] J. Zackrisson, H.-O. Andren, E□ ect of carbon content on the microstructure and mechanical properties of (Ti, W, Ta, Mo)(C, N)-(Co, Ni) cermets, Int. J. Refract. Met. Hard Mater. 17 (1999) 265–273.
[85] L.M. Berger, Hardmetals as thermal spray coatings, Powder Metall. 50 (2007) 205–214. https://doi.org/10.1179/174329007X246078.
[86] C. Verdon, A. Karimi, J.L. Martin, A study of high velocity oxy-fuel thermally sprayed tungsten carbide based coatings. Part 1: Microstructures, Mater. Sci. Eng. A. 246 (1998) 11–24.
[87] P. Chivavibul, M. Watanabe, S. Kuroda, Effect of Microstructure of HVOF-Sprayed WC-Co Coatings on Their Mechanical Properties, Therm. Spray 2007 Glob. Coat. Solut. Proc. 2007 Int. Therm. Spray Conf. (2007) 297.
[88] J.M. Guilemany, J. de Paco, J. Nutting, J.. Miguel, Characterization of the W2C phase formed during the high velcity ..., Metall. Mater. Trans. Phys. Metall. Mater. Sci. A. 30A (1999) 1913–1931.
[89] C. Verdon, A. Karimi, J.L. Martin, Microstructural and analytical study of thermally sprayed WC-Co coatings in connection with their wear resistance, Mater. Sci. Eng. A. 234–236 (1997) 731–734. https://doi.org/10.1016/s0921-5093(97)00377-8.
[90] J. Yuan, Q. Zhan, J. Huang, S. Ding, H. Li, Decarburization mechanisms of WC-Co during thermal spraying: Insights from controlled carbon loss and microstructure characterization, Mater. Chem. Phys. 142 (2013) 165–171. https://doi.org/10.1016/j.matchemphys.2013.06.052.
[91] C.J. Li, G.C. Ji, Y.Y. Wang, K. Sonoya, Dominant effect of carbide rebounding on the carbon loss during high velocity oxy-fuel spraying of Cr3C2-NiCr, Thin Solid Films. 419 (2002) 137–143. https://doi.org/10.1016/S0040-6090(02)00708-3.
[92] V. Matikainen, G. Bolelli, H. Koivuluoto, M. Honkanen, M. Vippola, L. Lusvarghi, P. Vuoristo, A Study of Cr3C2-Based HVOF- and HVAF-Sprayed Coatings:

Microstructure and Carbide Retention, J. Therm. Spray Technol. 26 (2017) 1239–1256. https://doi.org/10.1007/s11666-017-0578-x.
[93] S. Zimmermann, H. Kreye, Chromium carbide coatings produced with various HVOF spray systems, in: Proc. 9th Natl. Therm. Spray Confrence, Cincinnati, 1996: p. 147.
[94] G.C. Ji, C.J. Li, Y.Y. Wang, W.Y. Li, Microstructural characterization and abrasive wear performance of HVOF sprayed Cr3C2-NiCr coating, Surf. Coatings Technol. 200 (2006) 6749–6757. https://doi.org/10.1016/j.surfcoat.2005.10.005.
[95] R.B. Waterhouse, Residual Stresses and Fretting, Crack Initiation and Propagation., Adv Sur Treat, Technol - Appl - Eff. 4 (1987) 511–525. https://doi.org/10.1016/b978-0-08-034062-3.50032-x.
[96] B.B. Bartha, J. Zawadzki, S. Chandrasekar, T.N. Farris, Wear of hard-turned AISI 52100 steel, Metall. Mater. Trans. A Phys. Metall. Mater. Sci. 36 (2005) 1417–1425. https://doi.org/10.1007/s11661-005-0234-9.
[97] I.I. Garbar, Correlation between abrasive wear resistance and changes in structure and residual stresses of steels, Tribol. Lett. 5 (1998) 223–229. https://doi.org/10.1023/A:1019189624160.
[98] R.A. Waikar, Y.B. Guo, Residual stress evolution and mechanical state of hard machined components in sliding contact, Tribol. Trans. 50 (2007) 531–539. https://doi.org/10.1080/10402000701643788.
[99] O.P. Oladijo, N. Sacks, L.A. Cornish, A.M. Venter, Effect of substrate on the 3 body abrasion wear of HVOF WC-17 wt.% Co coatings, Int. J. Refract. Met. Hard Mater. 35 (2012) 288–294. https://doi.org/10.1016/j.ijrmhm.2012.06.011.
[100] A.K. Maiti, N. Mukhopadhyay, R. Raman, Improving the wear behavior of WC-CoCr-based HVOF coating by surface grinding, J. Mater. Eng. Perform. 18 (2009) 1060–1066. https://doi.org/10.1007/s11665-009-9354-5.
[101] H. Liao, B. Normand, C. Coddet, Influence of coating microstructure on the abrasive wear resistance of WC/Co cermet coatings, Surf. Coatings Technol. 124 (2000) 235–242. https://doi.org/10.1016/S0257-8972(99)00653-2.
[102] J.K.N. Murthy, B. Venkataraman, Abrasive wear behaviour of WC-CoCr and Cr3C2 -20(NiCr) deposited by HVOF and detonation spray processes, Surf. Coatings Technol. 200 (2006) 2642–2652. https://doi.org/10.1016/j.surfcoat.2004.10.136.
[103] M. Fivel, Franck J-P, Cavitation erosion, in: G.E. Totten (Ed.), Frict. Lubr. Wear Technol., ASM International, 2017: pp. 290–301. https://doi.org/10.31399/asm.hb.v18.a0006384.
[104] S. Hattori, E. Nakao, R. Yamaoka, T. Okada, Cavitation erosion mechanisms and its quantitative evaluation based on erosion particles, Nihon Kikai Gakkai Ronbunshu, A Hen/Transactions Japan Soc. Mech. Eng. Part A. 65 (1999) 393–399. https://doi.org/10.1299/kikaia.65.393.
[105] H.K. R. Schwetzke, Cavitation erosion of HVOF coatings, in: C.C .Berndt (Ed.), Therm. Spray Pract. Solut. Eng. Probl., ASM International, 1996: pp. 153–158.
[106] V. Matikainen, S. Rubio Peregrina, N. Ojala, H. Koivuluoto, J. Schubert, Houdková, P. Vuoristo, Erosion wear performance of WC-10Co4Cr and Cr3C2-25NiCr coatings sprayed with high-velocity thermal spray processes, Surf. Coatings Technol. 370 (2019) 196–212. https://doi.org/10.1016/j.surfcoat.2019.04.067.
[107] H. Kumar, C. Chittosiya, V.N. Shukla, HVOF Sprayed WC Based Cermet Coating for Mitigation of Cavitation, Erosion & Abrasion in Hydro Turbine Blade, in: Mater. Today Proc., 2018. https://doi.org/10.1016/j.matpr.2017.12.253.

[108] K. Sugiyama, S. Nakahama, S. Hattori, K. Nakano, Slurry wear and cavitation erosion of thermal-sprayed cermets, Wear. 258 (2005) 768–775. https://doi.org/10.1016/j.wear.2004.09.006.
[109] Q. Wang, Z. Tang, L. Cha, Cavitation and Sand Slurry Erosion Resistances of WC-10Co-4Cr Coatings, J. Mater. Eng. Perform. (2015). https://doi.org/10.1007/s11665-015-1496-z.
[110] L.L. Silveira, G.B. Sucharski, A.G.M. Pukasiewicz, R.S.C. Paredes, Influence of Particle Size Distribution on the Morphology and Cavitation Resistance of High-Velocity Oxygen Fuel Coatings, J. Therm. Spray Technol. 27 (2018) 695–709. https://doi.org/10.1007/s11666-018-0708-0.
[111] J. Zhang, X.D. He, Y. Sha, S.Y. Du, The compressive stress effect on fatigue crack growth under tension-compression loading, Int. J. Fatigue. 32 (2010) 361–367. https://doi.org/10.1016/j.ijfatigue.2009.07.008.
[112] H.C. Child, S.A. Plumb, G. Reeves, The effect of thermo chemical treatments on the mechanical properties of tool steel, Mater. Des. (1983). https://doi.org/10.1016/0261-3069(83)90222-4.
[113] R.C. Souza, H.J.C. Voorwald, M.O.H. Cioffi, Fatigue strength of HVOF sprayed Cr3C2-25NiCr and WC-10Ni on AISI 4340 steel, Surf. Coatings Technol. 203 (2008) 191–198. https://doi.org/10.1016/j.surfcoat.2008.07.038.
[114] J.G. La Barbera-Sosa, Y.Y. Santana, C. Villalobos-Gutiérrez, D. Chicot, J. Lesage, X. Decoopman, A. Iost, M.H. Staia, E.S. Puchi-Cabrera, Fatigue behavior of a structural steel coated with a WC-10Co-4Cr/Colmonoy 88 deposit by HVOF thermal spraying, Surf. Coatings Technol. 220 (2013) 248–256. https://doi.org/10.1016/j.surfcoat.2012.05.098.
[115] H.J.C. Voorwald, L.F.S. Vieira, M.O.H. Cioffi, Evaluation of WC-10Ni thermal spraying coating by HVOF on the fatigue and corrosion AISI 4340 steel, Procedia Eng. 2 (2010) 331–340. https://doi.org/10.1016/j.proeng.2010.03.037.
[116] J.R. García, J.E. Fernández, J.M. Cuetos, F.G. Costales, Fatigue effect of WC coatings thermal sprayed by HVOF and laser treated, on medium carbon steel, Eng. Fail. Anal. 18 (2011) 1750–1760. https://doi.org/10.1016/j.engfailanal.2011.03.026.
[117] A. Ibrahim, C.C. Berndt, Fatigue and deformation of HVOF sprayed WC-Co coatings and hard chrome plating, Mater. Sci. Eng. A. 456 (2007) 114–119. https://doi.org/10.1016/j.msea.2006.12.030.
[118] N.E. Frost, K.J. Marsh, L.. Pook, Metal fatigue, Dover Publications, 1974.
[119] J. Schivje, Fatigue of structures and materials, 2nd ed., Springer, 2009.
[120] R.. Herzberg, R.. Vinci, J.. Herxberg, Deformation and Fracture Mechanics of Engineering Materials, 5th ed., Wiley, 2013.
[121] H.J.C. Voorwald, R.C. Souza, W.L. Pigatin, M.O.H. Cioffi, Evaluation of WC-17Co and WC-10Co-4Cr thermal spray coatings by HVOF on the fatigue and corrosion strength of AISI 4340 steel, Surf. Coatings Technol. 190 (2005) 155–164. https://doi.org/10.1016/j.surfcoat.2004.08.181.
[122] K. Padilla, A. Velásquez, J.A. Berríos, E.S. Puchi Cabrera, Fatigue behavior of a 4140 steel coated with a NiMoAl deposit applied by HVOF thermal spray, Surf. Coatings Technol. (2002). https://doi.org/10.1016/S0257-8972(01)01447-5.
[123] E.S. Puchi Cabrera, J.A. Berríos-Ortiz, J. Da-Silva, J. Nunes, Fatigue behavior of a 4140 steel coated with a Colmonoy 88 alloy applied by HVOF, Surf. Coatings Technol. 172 (2003) 128–138. https://doi.org/10.1016/S0257-8972(03)00342-6.

[124] S. Watanabe, J. Amano, T. Tajiri, N. Sakoda, Fatigue cracks in HVOF thermally sprayed WC-Co coatings, J. Therm. Spray Technol. 7 (1998) 93–96. https://doi.org/10.1361/105996398770351098.
[125] D. Zhu, R.A. Miller, Investigation of thermal high cycle and low cycle fatigue mechanisms of thick thermal barrier coatings, Mater. Sci. Eng. A. 245 (1998) 212–223. https://doi.org/10.1016/S0921-5093(97)00852-6.
[126] S. Suresh, Y. Sugimura, L. Grondin, Fatigue crack growth at arbitrary angles to bimaterial interfaces, Int. J. Fatigue. 19 (1997) 2007–2012.
[127] E.S. Puchi-Cabrera, M.H. Staia, M.J. Ortiz-Mancilla, J.G. La Barbera-Sosa, E.A.O. Pérez, C. Villalobos-Gutiérrez, S. Bellayer, M. Traisnel, D. Chicot, J. Lesage, Fatigue behavior of a SAE 1045 steel coated with Colmonoy 88 alloy deposited by HVOF thermal spray, Surf. Coatings Technol. 205 (2010) 1119–1126. https://doi.org/10.1016/j.surfcoat.2010.01.011.
[128] M.A.M. Halmi, M.A. Harimon, L.M. Tobi, M.F. Mahmod, Fatigue Performance of Thermal Spray Coatings on Carbon Steel: A Review, Int. J. Mech. Eng. Technol. 10 (2019) 1285–1300. http://www.iaeme.com/IJMET/index.asp1285http://www.iaeme.com/ijmet/issues.asp?JType=IJMET&VType=10&IType=3http://www.iaeme.com/IJMET/index.asp1286http://www.iaeme.com/IJMET/issues.asp?JType=IJMET&VType=10&IType=3.
[129] Y.Y. Santana, J.G. La Barbera-Sosa, M.H. Staia, J. Lesage, E.S. Puchi-Cabrera, D. Chicot, E. Bemporad, Measurement of residual stress in thermal spray coatings by the incremental hole drilling method, Surf. Coatings Technol. 201 (2006) 2092–2098. https://doi.org/10.1016/j.surfcoat.2006.04.056.
[130] James Lanklord, Indentation microfracture in the Palmqvist crack regime: implications for fracture toughness evaluation by the indentation method, J. Mater. Sci. Lett. 1 (1982) 493–495.
[131] A.G. Evans, T.R. Wilshaw, Quasi-static solid particle damage in brittle solids-I. Observations analysis and implications, Acta Metall. 24 (1976) 939–956. https://doi.org/10.1016/0001-6160(76)90042-0.

PUBLICATIONS

PUBLICATION I

Formation mechanisms, structure, and properties of HVOF-sprayed WC-CoCr coatings: An approach toward process maps

T. Varis, T. Suhonen, A. Ghabchi, A. Valarezo, S. Sampath, X. Liu, and S.-P. Hannula

Journal of Thermal Spray Technology, vol 23, No.6, pp. 1009-1018, August 2014
DOI: 10.1007/s11666-014-0110-5

Formation mechanisms, structure and properties of HVOF sprayed WC-CoCr coatings: an approach toward process maps

T. Varis, T. Suhonen, A. Ghabchi*
VTT Technical research centre of Finland, P.O..Box 1000, VTT, Espoo, 02044, Finland
**Currently The Boeing Company, Thermal Spray Advance Research Team, Seattle, USA*

A. Valarezo**, S. Sampath
Center of Thermal Spray Research at Stony Brook University, New York, USA
***Currently Mechanical Engineering Department at Universidad San Francisco de Quito, Ecuador*

X. Liu, S-P. Hannula
Materials Science, Aalto University School of Chemical Technology, Espoo, Finland

Abstract

Our study focuses on understanding the damage tolerance and performance reliability of WC-CoCr coatings. In this paper the formation of HVOF sprayed tungsten carbide based cermet coatings is studied through an integrated strategy: First order process maps are created by using online-diagnostics to assess particle states in relation to process conditions. Coating properties such as hardness, wear resistance, elastic modulus, residual stress and fracture toughness are discussed with a goal to establish a linkage between properties and particle characteristics via second order process maps. A strong influence of particle state on the mechanical properties, wear resistance and residual stress stage of the coating was observed. Within the used processing window (particle temperature ranged from 1687 to 1831 °C and particle velocity from 577 to 621 m/s), the coating hardness varied from 1021 to 1507 HV and modulus from 257 to 322 GPa. The variation in coating mechanical state is suggested to relate to the microstructural changes arising from carbide dissolution, which affects the properties of the matrix and, on the other hand, cohesive properties of the lamella. The complete tracking of the coating particle state and its linking to mechanical properties and residual stresses enables coating design with desired properties.

Keywords: Process Map, WC-CoCr, HVOF, Fracture Toughness, Residual Stress

1. Introduction

Thermal sprayed WC-CoCr –cermet coatings are well known and widely used for different wear and corrosion protection purposes, because of their good performance in abrasion, erosion, cavitation or slurry type of dynamic contact conditions. Wear resistance of materials usually depends on their fracture toughness and hardness in a complex manner, because for most materials the increase in hardness results in decrease in toughness. Furthermore, in

thermal spraying, the coating performance is not only related to the inherent properties of material but also to the process induced degradation of material properties resulting from the thermal exposure. The most suitable and used technology among thermal spray processes for deposition of carbide based materials has been HVOF-spraying due to the favorable relationship between kinetic and thermal energy in the process, represented by the particle velocity and the flame temperature. Recently, HVAF and even Cold spraying have challenged HVOF deposited WC-CoCr coatings. However, the variation of coating properties within each thermal spray process is not very well understood neither to what level of accuracy process parameters in HVOF spraying is needed to control to obtain reliable coating performance [1-4]

All high velocity processes involve a number of operational parameters, which affect the temperature history and kinetic energy of the particles. How these parameters determine a flame condition and consequently the interaction with the particles and finally coating properties will be addressed in this study. Representation of process materials interactions through the use of *process maps* applied at different stages of any thermal spray process provides a science base approach to design, assess and optimize high performance coatings [5]. Such maps allow spraying parameters to be successively related to in-flight particle state, to the linkage between particle state and microstructure, to the microstructure-property relationships and then finally to the performance of the coating. Such a strategy has been made possible in recent years through availability of process sensors and materials characterization tools [6, 7].

It is well known that when spraying the WC-Co there are compositional changes arising from particle/flame interactions during the spraying, which can affect the properties and damage tolerance of the coating. The mechanism of compositional changes in WC-Co-coatings is well described. It has been observed that significant dissolution of WC into the Co binder phase takes place when the Co binder phase is molten during spraying [8]. Molten Co dissolves the WC grains and the carbon and tungsten content of the matrix increases and relative size of carbides decreases. Carbon loss occurs by diffusion of dissolved carbon through the liquid followed by reaction with the oxygen from the surroundings. During cooling, Co-rich liquid becomes supersaturated resulting in the formation of W_2C and amorphous or nanocrystalline W rich phases. During cooling, precipitation of *eta*-carbide [$(Co_6W_6)C$] phases may occur in the Co-rich material [8]. Despite the decarburization, the properties of WC-Co and WC-CoCr materials are not necessarily degraded during spraying, and coatings in general are known to represent the most wear resistant material applied by using thermal spray processes. However, special features derived from the use of CoCr-matrix, are not so well understood. Furthermore, detailed information on the effect of these changes on the properties of carbides and matrix and on coating performance is not often reported [8, 9].

Process maps allow a science base strategy to study the effect of operational variables on particle state in ensuing flame conditions. For WC-Co-based material it is well known that during flight spray particles melt to different extents depending on their size, density and dwell times. The aim in this study is to find correspondence between particle state, coating properties and performance. Coatings produced by selected operational parameters from the first order process map were evaluated by measuring their hardness, elastic modulus, fracture toughness, residual stresses and wear resistance. For more detailed analysis of the coating instrumented nano-indentation was carried out at nanometer resolution via *in-situ* SPM (Scanning Probe Microscopy) imaging. Finally, the coating properties are correlated to wear resistance and analyzed to establish the linkage between properties and particle state via second order process maps. The process mapping approach adopted in this paper is shown to offer a methodology for better control of the coating deposition process and to provide tools for microstructural design and property optimization of the coating.

2. Experimental Methods

2.1 Feedstock Characteristics

Agglomerated and sintered WC-10%Co-4%Cr powder (Sulzer Metco WOKA GmbH, Germany) having particle size 15 to 45 μm was used to spray coatings. Fig. 1a shows the spherical morphology of the powder and Fig. 1b shows the cross section of the powder particles.

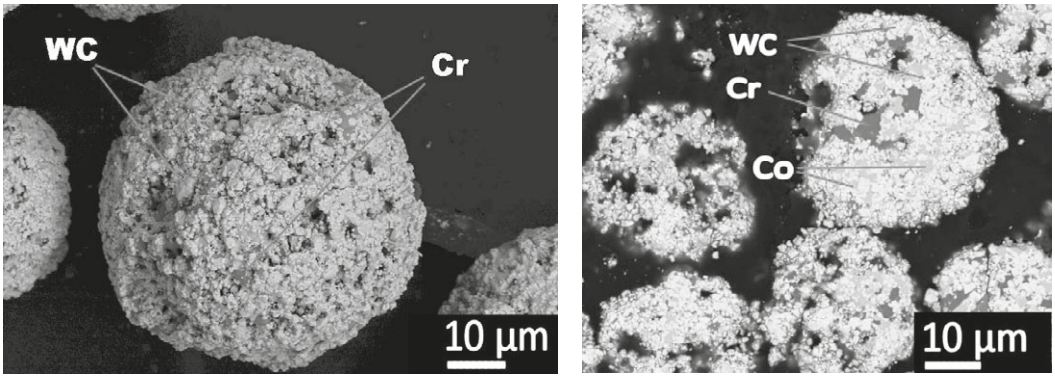

a) b)

Fig. 1. a) Typical spherical morphology of the WC-10%Co-4%Cr particles. b) Cross section of the powder particles.

2.2 HVOF process control, diagnostics and coating deposition

Water cooled HVOF DJ-Hybrid 2600 (Sulzer-Metco, Westbury, NY, USA) with hydrogen as a fuel gas was used in this study. Average values of temperature and velocity of the spray stream of several different conditions were measured. The operating space of DJ-system was

explored by tuning two independent operational parameters: Oxygen (O_2) volume flow and fuel (H_2) volume flow. Air and nitrogen (carrier gas) volume flows were kept constant. Two main variables were taken into account for the design of experiments: fuel to oxygen ratio (F/O-ratio) and total volume flow (or back pressure). F/O ratios (γ) were calculated by using equation (1):

$$\gamma = \frac{Hydrogen\text{flow}}{\text{Oxygen flow} + 0.21 \times \text{Air flow}} \quad (1)$$

To manipulate process temperature, different Fuel/Oxygen (F/O) -ratios 1.9, 2.2 and 2.5 were used. At each F/O-ratio, the chamber pressure was increased gradually by increasing the total gas flow at each constant F/O- ratio level. The value of backpressure was measured in the nitrogen line (carrier gas), and was registered as it is directly related to the pressure in the combustion chamber. Used parameter set for particle online measurements is shown in Table 1. Average values of temperature and velocity of the spray stream of several different conditions were measured. For particle diagnostics, Spray Watch 2i (Oseir Oy, Tampere, Finland) was used. Spray Watch uses a digital CCD camera with special spectrally resolving optics. The ultra-fast electronic shutter camera and dedicated real-time image processing software enables on-line measurement of the velocity. Velocities are measured by image analysing the length of the traces drawn by in-flight particles during the exposure time. The average particle temperature is measured by two-colour pyrometry.

The coatings from various conditions indicated with A to I from Table 1 and Fig. 2, were deposited on beam samples and evaluated with an *in-situ* coating property sensor (ICP) [6] (ReliaCoat Technologies, East Setauket, USA). ICP sensor measures the temperature and curvature of the substrate beam during spraying. Low carbon steel beams of 228.6 mm length, 25.4 mm width and 2.5 mm thickness, grit blasted on both sides, were used as a substrates. In all experiments 18 to 29 passes were sprayed to produce coatings of 0.3 to 0.5 mm thickness.

Single splats were collected onto polished stainless steel substrates at room temperature. A shuttering system consisting of a window moved by a pneumatic arm in front of the particle stream was used to collect a snapshot of in-flight particles. A splat map at a feed rate of 5 g/min was qualitatively characterized by SEM.

2.3 Coating characterization

The phase structure of the powder and coatings were characterized by X-ray diffraction (Philips PW3710 applying Mo K-alpha radiation and Philips PW3830 applying Cu K-alpha radiation). Carbon and oxygen contents were analysed by using Leco CS230 carbon analyser and Leco TC600 oxygen analyser. Analysers involve combustion of the 50 – 100 g of the crushed coating and measurement of combustion gases by infrared absorption.

Coatings were cut, mounted, ground and polished and cross sections were examined by SEM (JEOL JSM-6400, Japan). The conventional Vickers hardness was measured with 300 grams load (HV 0.3) for all of the coatings assuring that the applied loads did not lead to

formation of the cracks. Elastic modulus for thermal spray coatings provides a quantitative description of the deposit microstructure. Elastic modulus of coatings was evaluated by instrumented indentation (Zwick ZHU 0.2). Elastic modulus or Young´s modulus values were calculated from the load-displacement data taken from the indentations at the coating surface following the procedure proposed by Oliver and Pharr [10]. The elastic modulus, E can be calculated with the help of the following Equations (2) and (3):

$$S = \frac{\partial P}{\partial h} = \frac{2}{\sqrt{\pi}} E_r \sqrt{A} \tag{2}$$

$$\frac{1}{E_r} = \frac{\left(1-\nu^2\right)}{E} + \frac{\left(1-\nu_i{}^2\right)}{E_i}\ , \tag{3}$$

where S is the contact stiffness, E_r is the reduced modulus, E_i and ν_i are the indenters elastic modulus and Poisson´s ratio respectively (for diamond indenter $\nu_i = 0.07$ and $E_i = 1140$ GPa). Elastic modulus for the sample is E and its Poisson´s ratio is ν [10].

Indentation fracture toughness K_{IC} was measured from the cross-section or the surface of thermal sprayed coating. From the surface, one usually gets four corner cracks with the same length and the boundary conditions described in JIS R 1607-1990 can be used. Because of higher loads needed to initiate corner cracks compared to hardness measurements, the maximum plastic depth of the indentation cannot be more than one tenth of coating thickness to avoid any substrate effects. The cracks prefer to grow in the direction parallel to the substrate and vertical cracks are rarely produced in HVOF WC-CoCr coatings. Because of this preferred crack growth direction, the equations and boundary conditions developed for homogenous bulk ceramics cannot apply. If the cracks grow only in parallel direction, the average crack length (l) is calculated by dividing the total crack length (=sum of the cracks) by two, not by four as when measured from the surface. One requirement is that the cracks should initiate near the diagonal corners. If other major cracks than the corner cracks are developed, the measurement is not valid. In present work, because of preferred Palmqvist crack geometry developed in WC-CoCr coatings, the Fracture toughness values were calculated with the Evans – Wilshaw –equation (4 and 5) [11]:

$$K_{IC} = 0.079\left(\frac{P}{a^{3/2}}\right)\log\left(\frac{4.5a}{c}\right) \tag{4}$$

$$K_{IC} = MPam^{1/2} = \frac{MN}{m^{3/2}}, \tag{5}$$

where K_{IC} = fracture toughness ($MPa*m^{1/2}$), a is indentation half-diagonal (µm), c is crack length measured from the centre of indentation (µm) and P is applied load (mN) [11]. The equation is valid in the range of $0.6 \leq c/a \leq 4.5$. Furthermore, it does not use materials hardness or Young´s modulus values, like most K_{IC} –equations do. This eliminates the uncertainty from the hardness (H) and Young´s modulus (E) measurements. The loads used,

in this case, sufficient to initiate the cracks to the corner of the Vickers tip were 196.2 N for the top surface and 98.1 for the cross-section surface.

2.4 Residual Stress

In thermal spraying, there are three main origins for residual stresses [12]: a) quenching of the lamellas on the substrate, which generates tensile stresses, b) peening of the spray particles to the subsequent coating layer, resulting in compressive stresses and c) thermal mismatch, when substrate and coating having different CTE's are cooled down to e.g. room temperature after the deposition. The latter stresses are tensile or compressive depending on the CTE's of the materials. Final residual stress state is a sum of these stress components. By using curvature technique the stresses can be monitored in-situ. For this study, the in-situ coating property (ICP) –sensor was used to monitor the curvature and temperature while spraying of coatings at different spraying conditions. The curvature sensor is based on laser sensing of deflections in a strip during thermal spraying, which is converted to sample curvature. A simultaneous measurement of temperature is achieved via multiple thermocouples. Curvature sign convention is described as follows. If the beam is bending with the coating in the concave side, the curvature is of positive sign and the coating is in tension, whereas if the beam is bending with the coating in the convex side, the curvature is of negative sign and the coating is in compression. Evolution of residual stresses can be discussed by considering that during spraying quenching stress [12] promotes positive curvature (tension), peening results in the negative curvature (compression) and the difference in thermal contraction (CTE of WC-10%Co4Cr coating, taken as reference, is $5.3*10^{-6}$ m/m K and CTE of steel is $12*10^{-6}$ m/m K) will input compressive stresses in the coatings during cooling. Evolving stress formed by each coating layer can be calculated by Stoney´s equation (6):[13]

$$\sigma_{ev} = \frac{E_s' t_s^2}{6} \frac{d\kappa}{dt_c}, \tag{6}$$

where σ_{ev} is evolving stress of the layer with thickness dt_c that causes a curvature of $d\kappa$, E_s' is the in-plane elastic modulus (=E_s/(1-v_s), where E_s is Young´s modulus and v_s Poisson´s ratio of the substrate) and t_s is the thickness of the substrate [14, 15]. Deposition stress can be determined from the curvature change in the substrate-coating system during coating deposition by Brenner and Senderoff equation (7) [15].

$$\sigma_d = \frac{(E_s' t_s (t_s + \beta^{\S} dt_c)}{6 dR dt_c}; \beta = \frac{E_c'}{E_s'} \text{ .....} \tag{7}$$

where σ_d is deposition stress, E_c' is the in-plane modulus of deposited coating, dR is the change in radius caused by deposition stress in a deposited layer thickness dt_c and the rest as in equation (2) above.

Thermal stress can also be calculated with Brenner and Senderoff´s equation [15] for thick coatings. The curvature change due to different CTE's from the end of spraying to the cooling down of substrate-coating system to the room temperature is analysed. The following material specific values were used to calculate the stresses with equations (2) and (3): Young´s modulus [GPa], Poisson´s ratio and coefficient of thermal expansion [µm/m°C] of 300, 0.22 and 5.3 for WC-CoCr and 200, 0.3 and 12 for steel. The actual coating thicknesses determined from the cross sectional images of each deposited coating were used for calculations.

2.5 Wear Testing

Rubber wheel abrasion tests were performed according to ASTM G65 procedure D. Prior to testing samples were grinded to a surface finish of R_a 0.3. Samples were put in contact against a rubber wheel at a static force of 45 N. A rubber wheel of 227 mm diameter was used at 200 rpm for a total sliding distance of 4.279 m (6.000 revolutions). Quartz sand used was of rounded particles with an average size between 212 and 300 µm. Sand mass flow rate was 270 g/min. Two samples per coating were tested.

3. Results and Discussion

3.1 First Order Process Map

First order process maps were determined using the parameters shown in Table 1. The results from the temperature and velocity measurements are shown in Fig. 2. It should be noticed that F/O-ratio is the main factor determining the temperature levels of the particles. Salient differences in particle temperatures were observed when going from a hydrogen rich flame to an oxygen rich flame. Oxygen rich chemistry conditions results in low temperature of particles, and when tuning towards fuel rich conditions the temperature increases reaching the maximum at F/O ratio of 2.5, as can be detected in Fig. 2. The increase in particle temperature is approximately 150 °C when changing the F/O-ratio from 1.9 to 2.5.

The velocity at each selected F/O-ratio can be increased by increasing the flow of oxygen and hydrogen. The velocity increase can be explained by a higher combustion pressure resulting from the increase of total volume flow of the gases and therefore higher flow density of the gases, which provides higher drag force to the spray particles. The increase of total flow (or back pressure) was also slightly affecting the particle temperature, which can be detected from the increasing trend of particle temperature at higher velocities. This responds to the amount of power inserted in the flame. It could, however, be noticed that particle velocities are not directly proportional to the backpressure level. With F/O-ratio 2.5, for example, the velocity was higher with similar backpressure than at F/O ratio 1.9. This finding

indicates that gas composition and residues of the combustion gases has also significant effect on the acceleration of the particles.

Table 1. Spray parameters used for the determination of the first order process map.

Condition	Gas flows						N_2 Back Pressure (bar)
	H_2 (slpm)	O_2 (slpm)	Air (slpm)	N_2 (slpm)	F/O-ratio	Total (slpm)	
1 (A)	565	225	350	14	1.9	1154	5.28
2 (D)	580	233	350	14	1.9	1177	5.39
3	590	238	350	14	1.9	1192	5.46
4 (G)	605	246	350	14	1.9	1215	5.53
5	615	250	350	14	1.9	1229	5.60
6 (B)	610	205	350	14	2.2	1179	5.34
7	626	212	350	14	2.2	1202	5.40
8 (E)	635	216	350	14	2.2	1215	5.46
9	644	220	350	14	2.2	1228	5.50
10	650	223	350	14	2.2	1237	5.54
11 (H)	665	230	350	14	2.2	1259	5.62
12 (C)	645	185	350	14	2.5	1194	5.33
13 (F)	660	192	350	14	2.5	1216	5.38
14	670	196	350	14	2.5	1230	5.43
15	690	204	350	14	2.5	1258	5.53
16 (I)	710	212	350	14	2.5	1286	5.61

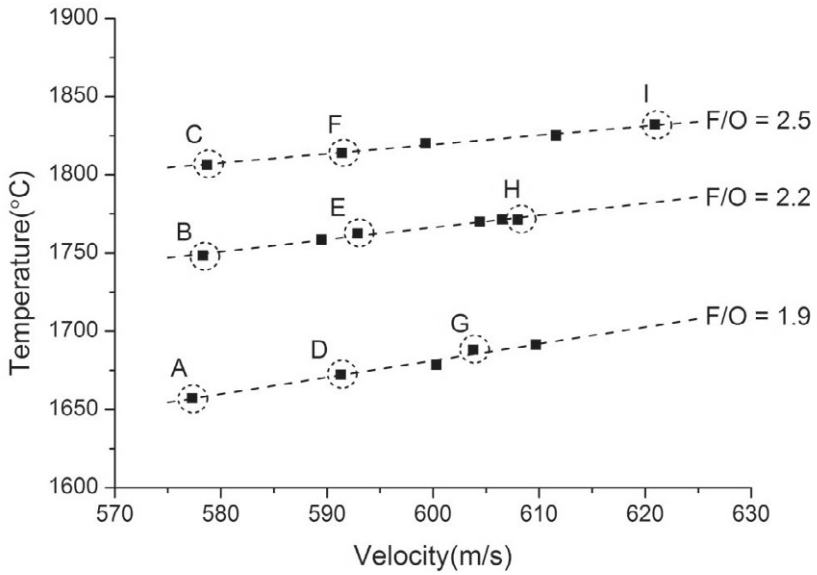

Fig. 2. Results for the determination of first order process map. The conditions selected for spraying the test coatings are indicated with dotted circles.

As a summary from parameter manipulation, these results ensure that the velocity of the sprayed particles can be controlled by adjusting the chamber pressure and particle temperature can be adjusted by adjusting the F/O-ratio. This gives a possibility to travel in the T-v space horizontally and vertically.

3.2 Evolution of residual stresses

The differences in residual stress built up in different conditions, which are selected from the corners of process window (Fig. 2) are shown in Fig. 3 (A, C, G and I). In each condition each pass contributes to the curvature by inserting tensile stresses. In DJ Hybrid spraying of WC-CoCr, the evolving stress, which is simply the slope of the curvature during spraying, is in all cases tensile as presented in Table 2 and Fig.3. This effect can only be explained by dominant quenching stress. Note, that evolving stress can be also compressive if peening effects dominates the residual stress formation. After completing the coating in the present case when the coating CTE ($5{,}3*10^{-6}$ m/m K) is lower than that of the substrate ($12*10^{-6}$ m/m K), cooling will reduce the stress state towards the compressive, but resulting in stress state after cool down to room temperature, which remains tensile in all cases. Noteworthy is the significant difference in final stress state between high particle temperature coatings (I and C) and low particle temperature coatings (A and G). When the final stress is calculated by using Stoney's equation, the residual tensile stress values for A and G (lower temperature) were 92 MPa and 109 MPa respectively and for I and C (higher temperature) 291 MPa and 359 MPa, respectively.

Table 2: Measured properties for WC-10%Co-4%Cr –coatings.

Sample code	F/O-ratio	Back pressure, bar	Carbon loss, %	Oxygen content, w-%	W_2C/WC	Hardness, HV 0,3	Abrasive Wear, mg/30 min	Evolving Stress, MPa	Indentation Modulus, GPa	Fracture Toughness, Cross Section, $MPa*m^{1/2}$	Fracture Toughness, Top Surface, $MPa*m^{1/2}$
A	1.9	5.28	7.0	0.450	0.09	1021 ± 172	17.5 ± 0.0	118	257 ± 25	4.4 ± 1.2	-
B	2.2	5.34	6.9	0.323	0.17	1259 ± 86	14.2 ± 0.5	296	299 ± 13	5.1 ± 0.1	5.5 ± 0.6
C	2.5	5.33	9.5	0.154	0.22	1310 ± 145	9.6 ± 1.0	460	262 ± 9	4.6 ± 0.7	5.7 ± 0.4
D	1.9	5.39	6.7	0.400	0.14	1195 ± 66	13.2 ± 1.2	199	270 ±15	-	-
E	2.2	5.46	9.1	0.260	0.18	1382 ± 152	9.2 ± 0.5	516	321 ± 26	6.1 ± 0.6	6.7 ± 0.6
F	2.5	5.38	11.0	0.218	0.24	1472 ± 164	8.3 ± 0.1	553	312 ± 29	5.7 ± 1.1	5.4 ± 0.7
G	1.9	5.53	5.5	0.375	0.17	1242 ± 146	13.0 ± 1.4	411	304 ± 13	5.5 ±1.3	7.4 ± 0.3
H	2.2	5.62	8.2	0.199	0.21	1470 ± 212	9.8 ± 1.0	636	321 ± 24	6.2 ± 0.6	7.4 ± 0.4
I	2.5	5.61	13.8	0.174	0.28	1507 ± 117	8.9 ± 0.4	559	322 ± 12	5.4 ± 0.5	4.1± 1.0

- **Could not be measured due to unfavourable cracking behaviour**

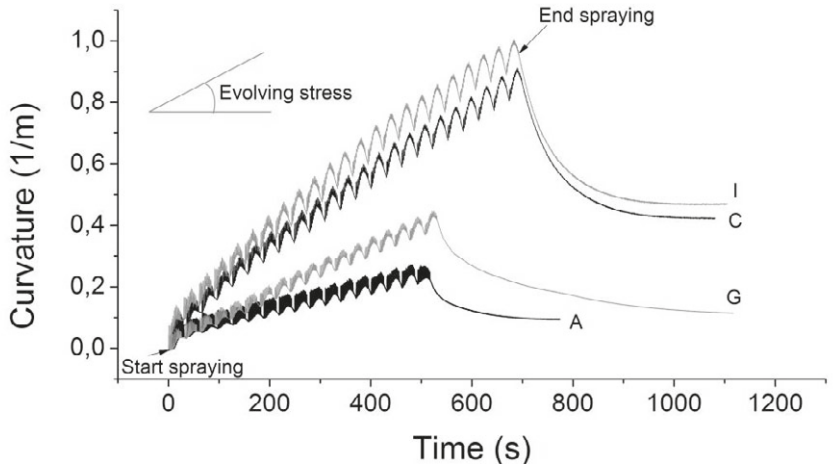

Fig. 3. Difference in curvature evolution during spraying and cooling for four different particle temperature – velocity combinations (A, G, C, and I). Positive curvature change denotes the generation of tensile stress and negative the generation of compressive stress.

Higher evolving stress during the deposition at higher temperatures (steeper slope of the curvatures curves I and C) compared to lower (curves A and G) may be a result from better lamella cohesion. From its definition the quenching stress is generated to a solid material from the constrained shrinking of individual lamellas from solid material to a substrate temperature. Stresses can increase up to the point, at which relaxation mechanisms like yielding, interfacial sliding or micro cracking takes place [12]. Therefore, increased lamella cohesion may explain the increased capacity of coating to bear evolving stress. Further details and analysis of the stress evolution will be needed as well as thffect of stress state of coating on properties like modulus etc. It is evident that process parameters have considerable influence on residual stress generation of WC-CoCr deposits.

3.3 Microstructural examination and compositional changes

Micrographs of the coatings sprayed at conditions A, E, I and G (as presented in Fig. 2 and Table 2) are shown in Fig. 4. It is well known that during flight spray particles melt to different extent depending on their size and dwell times. These effects concentrate on the outer core of the particles. On small size particles, the whole particle can be affected from melting and decarburization. Thus, regions of tungsten rich phases formed can be observed in these particles as brighter regions in SEM backscatter imaging.

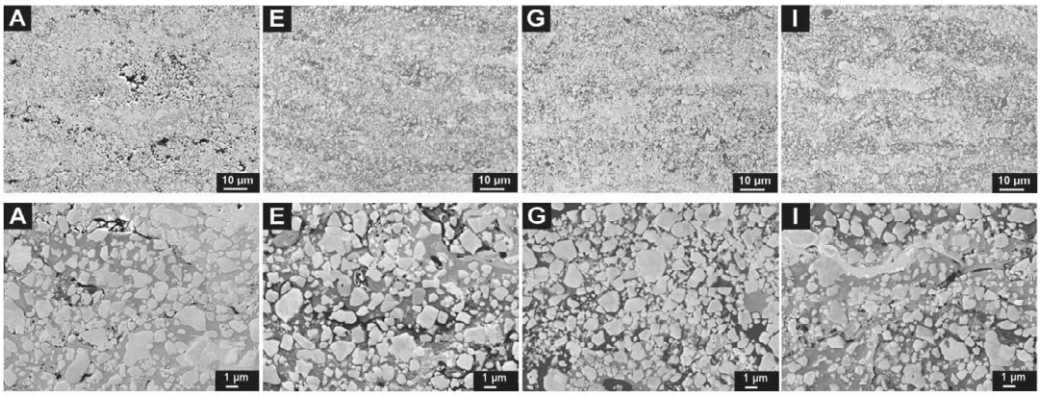

Fig. 4. SEM microstructures of WC-CoCr coatings obtained at different temperature – velocity combinations (A, E, I, and G).

Appreciable differences in porosity are observed in the cross-sectional microstructures of the various deposits in Fig. 4. In coating A, in deposition of which the particle temperature and velocity has been lowest, large amount of macro porosity is visible in the coating. In coating G, where particle temperature is low and velocity is increased the porosity is reduced, but still some micro porosity related to the original internal porosity of the spray particles is evident. In coating I, which represents the highest particle temperature and highest velocity the density is excellent, but noteworthy is the massive carbide dissolution witnessed by the loss of small carbides, rounding of bigger carbides, white W_2C areas around the carbides and even metallic W stripes in the coating. In coating E, the coating structure is dense without significant carbide dissolution effects. Results point out the importance of the melting state of the particles in obtaining high density of the coatings. In general, particle state conditions at a relative low temperature (and low velocity) show higher porosity. Therefore, it can be concluded that for the DJ Hybrid HVOF process the inherent melting stage of the spray particle during flight is an important factor for determining the coating porosity. On the other hand, the effect of compositional changes on the coating properties and performance in the coatings deposited at higher temperatures needs to be carefully evaluated.

It is well known from the Ellingham-Richardson diagram that WC becomes less stable than W_2C above 1242 ˚C (1515 K) [16] as considered the decomposition kinetics depending on the temperature. In Fig. 5 the carbon loss, oxygen content and W_2C/WC-ratio (given as a ratio of XRD peak intensities) in the coatings are shown as a function of particle temperature at each nitrogen backpressure level. Backpressure I is in the level of 5.2 to 5.27 (conditions A, B and C), backpressure II is between 5.4 and 5.41 (conditions D, E, and F) and backpressure III is from 5.6 to 5.68 (Conditions G, H, I). The ratio of W_2C and WC peaks clearly depends on particle temperature. Carbon loss and the ratio of W_2C phase and WC phase can be noticed as measures of the heat load on the particles. In literature there is not, however, general agreement of the acceptable level of W_2C in the coating. It is presented that some extent of W_2C formation on the WC and matrix interface is advantageous for good bonding between the matrix and carbide [17], but on the other hand, dissolution of carbide to the

matrix will decrease the ductility of matrix and in some cases W rich lamella may form onto the coating as seen in coating I (Fig.4). These lamellae will definitely decrease the damage tolerance of coatings [18]. Also, evolving stress can be seen as an indicator for heat load on the particle. Higher the temperature, the higher is the tensile evolving stress as presented in Fig. 3. However, it can be seen, that if the particle temperature increase is excessive (in this case above 1830 °C), the coating capacity to bear tensile stress becomes limited and evolving stress cannot increase further higher. Lowered capacity for tensile stress at high particle temperatures might be linked to microstructural changes in the coating. This may activate the different relaxation mechanisms, for example micro cracking, in the coating.

It was clear that when spraying with DJ Hybrid, the matrix was fully molten with all parameters, which was confirmed by single splat studies (Fig. 6). Although the peening stresses may occur in the material underneath the impinging particles having partly molten structure, this result shows that the magnitude of tensile stresses was controlled mainly by the particle temperature and the effect of particle velocity and the peening are insignificant.

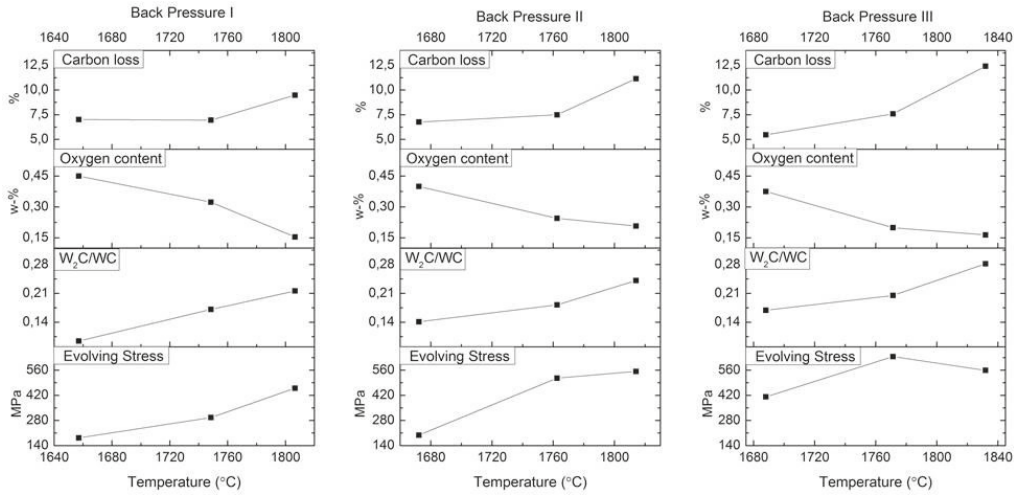

Fig. 5. Carbon loss, oxygen content, W_2C/WC-ratio and evolving stress as a function of particle temperature at each back-pressure level.

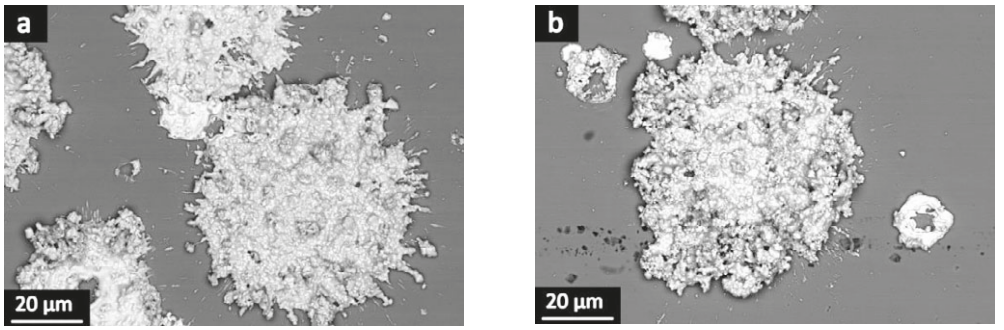

a) b)

Fig. 6. Single splat sprayed by using a) spray condition F and b) spray condition G.

Oxygen content in the coating was found to decrease and carbon loss to increase with increasing temperature. This is expected, since the higher is the temperature the more carbon is dissolved to the molten droplets and the more effective reducing agent carbon is based on the Ellingham diagram [16]. Furthermore, in the current hydrogen-oxygen combustion the flame temperature decreases at oxygen rich gas mixtures, while the oxygen partial pressure increases. It is evident that at higher temperatures and lower oxygen partial pressures in the gas phase carbon acts as a more effective reductant than at lower temperatures, where oxidation of matrix metal may occur to a larger extent. It can therefore be concluded that carbon-oxygen reaction in WC-CoCr spraying plays a decisive role in the oxidation of metallic material in the coating during the spraying. Similar behaviour has also been found by Sampath and Wayne, when they observed that oxide content in the Mo-Mo_2C system is reduced due to preferential carbon oxidation [19]. Needless to say, the dissolution of WC carbide into the molten matrix is a key factor for carbon to act as an effective reducing agent. Its dissolution is highly temperature controlled and restricted at lower temperatures where WC is more stable than W_2C. It should be pointed out that according to the results high partial pressure of oxygen at relatively low temperature does not increase the carbon loss and hence increase the formation of more brittle W_2C. Therefore, the lower temperature oxygen rich flame can be used without the risk of marked loss of properties. However, in this case the risk of chromium oxidation is more pronounced, which may affect the corrosion resistance of the matrix. The preferred chromium oxidation instead of Co has been found in several studies, which show that oxidation of the Co matrix is usually very low (<0,2 %) compared to CoCr matrix [20, 21]. Therefore, it is likely that oxidation of chromium is responsible for the increased oxide content at lower temperatures also in the present study.

3.4 Linkage between the process and properties

The properties of the coatings are presented in Table 2. The linkage between the process conditions and coating performance are visualized in the second order process maps in Figures 7 a to f. The maps were generated by interpolating the contours from originally nine spray conditions. In the process window studied particle temperature varied from 1687 to 1831 °C and particle velocity from 577 to 621 m/s. It should be noted that the top values for temperature and velocity are at maximum, which can be achieved with the particular spray system. The inlet gas pressures cannot be further increased, which limits the gas flow velocities and thus the particle velocity. Also, it was found that maximum particle temperature is achieved at approximately 2.5 F/O-ratio. Within the current process window the hardness varied from 1021 to 1507 HV and modulus varied from 257 to 322. It can be seen (Fig. 7a and 7b) that elastic modulus and hardness increases towards the top-right corner where particle velocity and particle temperature is at maximum. The results thus strongly suggest that both increased particle temperature and particle velocity have a beneficial effect on the mechanical properties of the coatings. In thermal sprayed coatings the mechanical properties of a coating are complexly dependent on the intrinsic micro-structure of the lamellas, cohesion between individual lamellas (microporosity) and the macroporosity and it

is usually difficult to evaluate, which factor is dominating the reduced mechanical performance compared to bulk materials having same phase composition. Nevertheless, it can be assessed that reduced visible porosity and increased lamella cohesion are among the key factors behind improved hardness and elastic modulus.

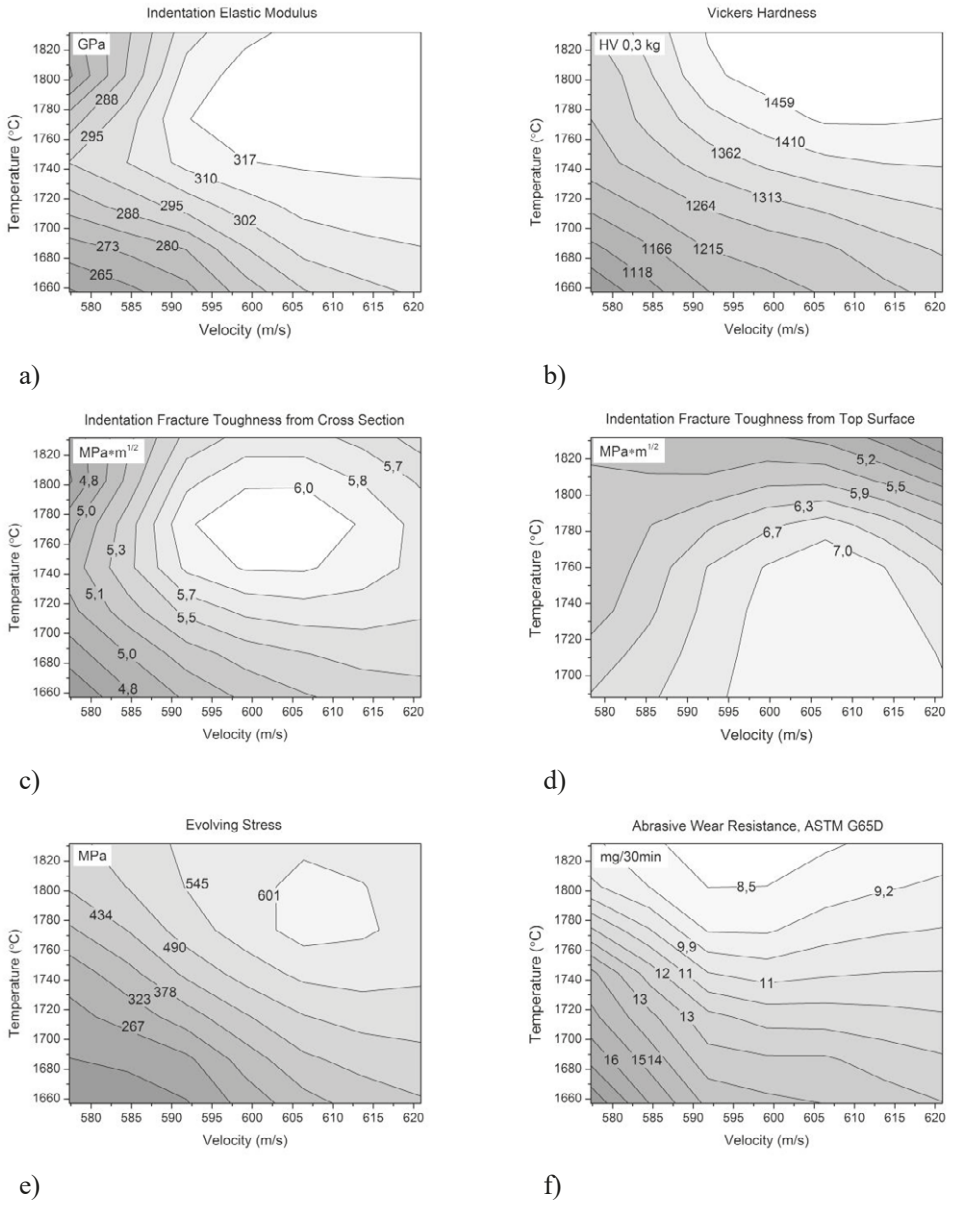

Fig. 7. Second order Process Maps of various properties for WC-CoCr deposited by DJ Hybrid.

Even though the magnitudes of fracture toughness's from the cross section and the top surface are not directly comparable due to the difference in used loads, an interesting perspective for lamella cohesion and inherent lamella property could be found by comparing the cross section and the top surface fracture toughness's maps, which show significantly different behaviour in each case. The fracture toughness measured from cross-section increases up to certain point when going to hotter and faster conditions until at the hottest spray conditions the toughness decreases again. It was found that the cracks initiating from the edge of the Vickers indenter tip follows the path of lamella boundaries as shown in Fig. 8. It is evident that the increased particle temperature improves the lamella bonding and makes more difficult for crack to grow until the toughness of the lamella boundary region has decreased excessively due to carbide dissolution effects described earlier. Fracture toughness, which is measured from the cross section of the coating, is therefore connected to the properties of the lamella interfaces. The fracture toughness measured from top surface behaves differently reaching a maximum value at coldest and fastest parameters where also tensile residual stress is at minimum. Actually, top surface fracture toughness decreases when more heat is introduced to the particle and similarly tensile residual stress increases. It was already presented that when particle temperature was increased the dissolution of the carbide was higher. A conclusion, which can be made, based on these findings is that the cross section fracture toughness is related to the fracture and cohesion properties of the lamella boundaries and the top surface fracture toughness is related to the intrinsic properties of the matrix material in the lamella and residual stresses. As the top surface K_{IC} value is related to the inherent state of the lamella, the cross-section K_{IC} is related to the composition of lamella boundaries, lamella cohesion and interlamellar porosity. Similar findings from the anisotropy in indentation fracture of WC-Co coatings has been made earlier by Usmani et.al [23]. They proposed that crack growth in the top surface will require fracture within a splat which would in turn require substantially larger fracture energy while in the cross section interfacial discontinuity provides an easy path for crack propagation along the splat interfaces.

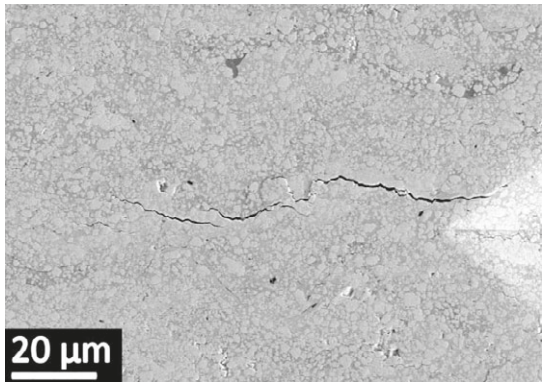

Fig.8. Crack path starting from the edge of indentation tip is following the lamella boundary (edited from [22]).

When comparing the maps for cross section fracture toughness and evolving stress, a clear tendency can also be noticed. If the evolving stress is tensile, its origin is particle quenching during deposition. From Fig. 7e it can be noticed that similar to cross section indentation fracture toughness the evolving stress reaches the maximum at a specific temperature velocity range after which it does not increase further. Though, maximum tensile evolving stress is dependent on both particle temperature and lamella cohesion and the highest evolving stress is generated when lamella interfacial cohesion is maximized. Also, it is clear that cross section fracture toughness is not significantly improving, when particle velocity is increasing. This indicates that the increase in the particle velocity in this case was not enough for significant improvement of lamella cohesion. As seen from Fig. 2, the particle surface temperature at constant F/O-ratio increases, when the process is forced to a higher velocity by increasing the back pressure. This leads to excessive decarburization, carbide dissolution and W_2C formation especially at the particle surface area. It is likely that a rim of brittle phases is formed on the surface of solidified spray particle. This type of effects are not beneficial for fracture toughness and therefore increased velocity of WC-CoCr particles at high temperature (when spraying with DJ Hybrid) does not significantly improve the fracture toughness of coating and hinder the increase of evolving stress. However, at lower temperatures the increase in velocity leads to the maximum top surface fracture toughness. Thus it is more beneficial to increase velocity at lower flame temperatures, which may give interesting possibilities for processes like HVAF, which has lower particle temperature, but high velocity.

Regarding the abrasive wear there was relatively small difference in wear performance between conditions. However, the coatings C, F and I produced by the hottest spray conditions seemed to represent the highest abrasive wear resistance, which is most probably related to the high density of the coatings. The surface porosity plays an important role for the abrasion resistance as the initiation of the scratches become easier at the pore edges, which has been shown elsewhere /24/. Also the hardening of the matrix phase can play an advantageous role, as it was evident that the wear resistance improves as more heat is introduced to the particles. The fact that the hottest condition, G, does not represent the highest wear resistance might be linked to the lowered fracture toughness of the coating. The fracture toughness might be even more important, for example, if load-carrying capability or erosion resistance is needed. Then the importance of surface K_{IC}, as design parameter of the coating might be more pronounced.

4. Conclusions

The present study examined the effect of spraying parameters on the formation, microstructure and properties of WC-CoCr -coatings by HVOF through the framework of process maps. The presented process map constitutes an excellent tool towards addressing the effects of spraying parameters on cermet coatings, on which particle temperature and velocity plays a decisive role in coating performance.

It was demonstrated that spray conditions have a significant effect on coating elastic modulus, hardness, residual stress stage and fracture toughness. Within the used processing

window, in which the particle temperature ranged from 1687 to 1831 °C and particle velocity from 577 to 621 m/s, the coating hardness varied from 1021 to 1507 HV and the modulus from 257 to 322 GPa. It was also found, that a moderate heat load in DJ Hybrid spraying of WC-CoCr has a beneficial effect for all the mentioned coating properties. This behaviour was proved to be linked to both a) the improved lamella cohesion and b) hardening of matrix. The amount of heat is critical and excessive heat input was found to reduce the fracture toughness of the WC-CoCr coating specially if measured from the top surface by indentation. Results showed also an effect of process conditions on matrix properties. A complete tracking of the coating particle state (temperature and velocity) linking to mechanical properties and residual stresses enables coating design with desired properties.

Acknowledgement

In Finland this research was supported by the Finnish Funding Agency for Technology and Innovation, VTT, Aalto University, Metso Paper Oy, Metso Automation Oy, Fortum Power and Heat Oy, Condens Oy and Oseir Oy via FUNSURF-project (1175/31/05) and in US by the GOALI program of the National Science Foundation under award number CMMI-1030942.

References

[1] Ding Z, Zhang Y, Zhao H (2007) Resistance of HVOF Nanostructured WC12Co Coatings to Cavitation Erosion International in Thermal Spray Conference 2007: Global Coating Solutions B.R. Marple, M.M. Hyland, Y.C. Lau, C.J. Li, R.S. Lima, and G. Montavon (Ed.) Materials Park, Ohio, USA

[2] Jia K, Fischer TE (1996) Abrasion Resistance of Nanostructured and Conventional Cemented Carbides. Wear 200: 206 – 214

[3] Ghabchi A, Varis T, Turunen E, Suhonen T, Liu X, Hannula S-P (2010) Behavior of HVOF WC-10Co4Cr Coatings with Different Carbide Size in Fine and Coarse Particle Abrasion. J Therm Spray Techn 19(1-2): 368 – 377

[4] Stewart DA, Shipway PH, McCartney DG (1999) Abrasive Wear Behaviour of Conventional and Nanocomposite HVOF Sprayed WC-Co coatings, Wear 225-229: 789 – 798.

[5] Sampath S, Jiang X, Kulkarni A, Matejicek J, Gilmore DL, Neiser RA (2003) Development of process maps for plasma spray: case study for molybdenum. Mater Sci Eng A 348: 54 – 66.

[6] Matejicek J, Sampath S (2003) In situ measurement of residual stresses and elastic moduli in thermal sprayed coatings: Part 1: apparatus and analysis. Acta Mater 51 (3) Issue 3: 863 – 872

[7] Vaidya A, Streibl T, Li L, Sampath S, Kovarik O, Greenlaw R (2005) An integrated study of thermal spray process–structure–property correlations: A case study for plasma sprayed molybdenum coatings. Mater Sci Eng A 403(1-2): 191 – 204

[8] Verdon C, Karimi A, Martin J-L (1998) A study of high velocity oxy-fuel thermally sprayed tungsten carbide based coatings. Part 1: Microstructures. Mater Sci Eng A 246: 11 – 24

[9] Kear BH, Skandan G, Sadangi RK (2001) Factors controlling decarburization in HVOF sprayed nano-WC/Co hardcoatings. Scripta Mater 44: 1703 – 1707

[10] Oliver WC, Pharr GM (1992) An improved technique for determining hardness and elastic modulus using load and displacement sensing indentation experiments. J Mater Res 7(6): 1564 – 1583

[11] Evans AG, Wilshaw TR (1976) Quasi-static solid particle damage in brittle solid. I. Observations analysis and implications Acta Metall 24: 939 – 956

[12] Kuroda S, Clyne TW (1991) The quenching stress in thermally sprayed coatings. Thin Solid Films 200: 49 – 66

[13] Stoney GG (1909) Proc Roy Soc Lond A82:172

[14] Ohring M (1992) The materials science of the thin films. San Diego (CA), Academic Press

[15] Brenner A, Senderoff S (1949) Journal Res Natl Bur Stand 42: 105

[16] Gaskell DR (2008) Introduction to the Thermodynamics of Materials. Taylor & Francis, New York, NY, USA, 5th edition

[17] Qiao Y, Fischer TE, Dent A (2003) The effects of fuel chemistry and feedstock powder structure on the mechanical and tribological properties of HVOF thermal-sprayed WC–Co coatings with very fine structures. Surf Coat Tech 172: 24 – 41
[18] Valarezo A, Bolelli G, Choi WB, Sampath S, Cannillo V, Lusvarghi L, Rosa R (2010) Damage tolerant functionally graded WC–Co/Stainless Steel HVOF coatings. Surf Coat Tech 205: 2197 – 2208
[19] Sampath S, Wayne SF (1994) Microstructure and properties of plasma –sprayed Mo-Mo_2C composites. J Therm Spray Techn 3 (3): 282 – 288
[20] Zimmerman S, Keller H, Schwier G (2003) New carbide based materials in HVOF spraying in ITSC 2003: Advancing the science and applying the technology Marple BR, Moreau C (ed.) Materials Park, Ohio, USA: 227 – 232
[21] Schwetzke R, Kreye H, (1999) Microstructure and Properties of Tungsten Carbide Coatings Sprayed with Various High- Velocity Oxygen Fuel Spray Systems J Therm Spray Techn 8 (3): 433 – 439
[22] Suhonen T, Varis T, Turunen E, Liu X, Ge Y, Söderberg O, Hannula S-P (2008) Modelling the Effect of Microstructure on Mechanical Properties of HVOF Sprayed WC-CoCr Coatings. World Materials Research Institute Forum, Proceedings of the Workshop for Young Materials Scientists (1st International Workshop), Tsukuba, Japan National Institute for Materials Science (NIMS) No: 16:1 – 14
[23] Usmani S, Sampath S, Houck D, Lee D (1997) Effect of Carbide Grain Size on the Sliding and Abrasive Wear Behavior of Thermally Sprayed WC-Co Coatings. Tribol T 40 (3): 470 – 478
[24] Ghabchi A, Varis T, Turunen E, Suhonen T, Liu X, Hannula S-P (2010) Behavior of HVOF WC-10Co4Cr Coatings with Different Carbide Size in Fine and Coarse Particle Abrasion. J Therm Spray Techn 19 (1-2): 368 – 377

PUBLICATION II

Residual stress development in cold sprayed Al, Cu and Ti coatings

T. Suhonen, T. Varis, S. Dosta, M. Torrell, J.M. Guilemany

Acta Materialia, vol 61, pp. 6329-6337, Aug 2013
DOI: 10.1016/j.actamat.2013.06.033

Available online at www.sciencedirect.com
SciVerse ScienceDirect
Acta Materialia 61 (2013) 6329–6337
Acta MATERIALIA
www.elsevier.com/locate/actamat

Residual stress development in cold sprayed Al, Cu and Ti coatings

T. Suhonen [a,*], T. Varis [a], S. Dosta [b], M. Torrell [b], J.M. Guilemany [b]

[a] VTT Technical Research Centre of Finland, Advanced Materials, Metallimiehenkuja 8, 02044 Espoo, Finland
[b] Barcelona University, CPT, Martí I Franqués 1, 08028 Barcelona, Spain

Received 26 March 2013; received in revised form 14 June 2013; accepted 16 June 2013
Available online 8 August 2013

Abstract

Residual stresses play an important role in the formation and performance of thermal spray coatings. A curvature-based approach where the substrate–coating system deflection and temperature are monitored throughout the coating deposition process was used to determine residual stress formation during cold spray deposition of Al, Cu and Ti coatings. The effect of substrate material (carbon steel, stainless steel and aluminium) and substrate pre-treatment (normal grit blasting, grit blasting with the cold spray system and grinding for carbon steel substrate) were studied for all coating materials with optimized deposition parameters. Mainly compressive stresses were expected because of the nature of cold spraying, but also neutral as well as tensile stresses were formed for studied coatings. The magnitudes of the residual stresses were mainly dependent on the substrate/coating material combination, but the surface preparation was also found to have an effect on the final stress stage of the coating.

Keywords: Cold spraying; Residual stresses; Aluminium; Copper; Titanium

1. Introduction

In cold spraying, the feedstock material in powder form is injected into a heated gas jet behind the nozzle, from where it is propelled onto the substrate with compressed and heated gas, generally nitrogen or helium. Solid-state particles are accelerated in a high-pressure supersonic gas jet, causing the particles to plastically deform during the impact with the substrate or with the previously deposited coating itself. Above a certain particle velocity, which is characteristic of the respective coating material as well as e.g. the powder oxide scale thickness, particle size distribution and morphology, the particles can form a dense, solid, well-adhered coating upon impact. Because of lower operating temperatures compared with more conventional thermal spray methods, cold spraying is highly suitable for depositing oxygen and temperature sensitive materials such as aluminium, copper and titanium. Also, thick coatings can be produced without adhesion failure from several materials. The high kinetic energy/low temperature formation of the coating leads to a wrought-like microstructure with near theoretical density values [1–4]. The distinguishing feature of the cold spray process compared with conventional thermal spray processes is that the detrimental effects of high temperature oxidation, evaporation, melting, recrystallization, phase transformations, residual stresses, decohesion and other concerns associated with thermal spray methods can be minimized or even eliminated [5].

In conventional thermal spraying, like plasma spraying, most of the residual stresses originate from the quenching of the molten particles. The temperature drop in the solidification of molten particles upon impact with the substrate leads to tensile stresses (also known as quenching stress) because the contraction is restricted by the adherence to the substrate [6,7]. The temperature of the substrate is also typically increased during deposition of the coating. When the substrate–coating system is cooled down to e.g. room temperature after the deposition, a thermal mismatch stress (also known as thermal stress) is generated. The nature of

* Corresponding author. Tel.: +358 40 501 2163; fax: +358 20 722 7069.
E-mail address: tomi.suhonen@vtt.fi (T. Suhonen).

1359-6454/$36.00
http://dx.doi.org/10.1016/j.actamat.2013.06.033

the thermal stress (tensile, neutral or compressive) is determined by the difference in the coefficients of thermal expansion (ΔCTE) of the coating and the substrate [7,8]. In high-velocity thermal spray systems, like high-velocity oxy–fuel (HVOF) or high-velocity air–fuel, and cold spraying, a compressive component (also known as peening stress) can be introduced during the deposition. This is caused by the high-velocity impact of the particles causing plastic deformation of the substrate and/or previously deposited coating material [9]. Typically, all of these components will be present in thermal sprayed coatings, but the magnitude of the quenching, thermal and peening stress is dependent on, for example, the temperature difference before and after the impact of the particle with the substrate, the temperature difference of the substrate–coating system during and after the spraying, and the ability of the substrate and coating to plastically deform and work harden upon impact of the particle. The combined effect of quenching and peening is known as evolving stress, and represents a stress developed when a layer of material is deposited in the substrate–coating system. Compressive evolving stress indicates that the peening effect is more dominant, and the tensile mode indicates that the quenching effect is more dominant [10,11].

In the cold spray process, the feedstock powder, usually with metal as a main component, is injected into a gas stream and accelerated to a speed of ~500–1000 m s^{-1}. When the particles impact on a metallic substrate, the plastic deformation of the particles under pressure generates new interfaces with conformal contact, enabling metallic bonding, which forms the coating. Although a localized increase in temperature occurs at the interface due to the impact, the overall temperature of the substrate does not increase considerably. The bond strength and cohesion of the coating are determined in part by the residual stresses arising from the peening process [12]. Residual stresses are very important factors influencing the make-up of the coating–substrate system, as well as its performance. In cold spray coatings, a compressive residual stress in the coating can be expected as a result of the plastic deformation, in a similar fashion to some HVOF coatings [13].

In situ residual stress measurements have been reported in the literature for plasma- and HVOF-sprayed coatings [10,11,13]. The same curvature-based method has also been used to extract the in-plane elastic modulus or the CTE of the coatings deposited. Elastic modulus of the coatings can be calculated from the coating–substrate system curvature change due to the thermal mismatch [10,11]. Sprayed beams can be subjected to low temperature thermal cycling after deposition. In these experiments, the deposited coating–substrate system is uniformly heated (e.g. to 150 °C) and cooled down to room temperature by free convection. The cooling portion can be taken for analysis. According to Tsui and Clyne's [14] curvature change model, during cooling, the elastic modulus can be calculated from Eq. (1):

$$\Delta k = \frac{1}{\Delta R} = \frac{6E'_c E'_s t_c t_s (t_c + t_s)\Delta T \Delta\alpha}{E_c^2 t_c^4 + 4E_c E_s t_c^3 t_s + 6E_c E_s t_c^2 t_s^2 + 4E_c E_s t_c t_s^3 + E_s^2 t_s^4} \quad (1)$$

where Δk is the curvature change due to the decrease in temperature (ΔT) and $\Delta\alpha$ is the ΔCTE between the deposit and the substrate. t_c is the coating thickness, t_S is the substrate thickness, and E'_c and E'_S are the moduli of the coating and the substrate, respectively. Continuous monitoring of the curvature and the temperature during the heating–cooling experiment allows the estimation of the deposit modulus by the curve-fitting method. By spraying coatings with the same parameters on substrates having different CTEs, the CTE of the coating can be determined by iterating the unknown E_c and α_c, Young's modulus and CTE of the coating, respectively. However, the different substrate materials might have a minor effect on the coating structure and, because E_c is known to be more sensitive than α_c to the substrate material, an alternative method to determine the E_c could be used.

Several methods have been used for residual stress measurement and estimation of cold sprayed coatings. Methods including theoretical models and experimental methods like the modified layer removal technique, X-ray and neutron diffraction [15–19] have been used for residual stress characterization of cold spray coatings, but no information about the in situ measurements have been reported in the literature. In this study, for the first time, an in situ technique has been used to measure the in situ residual stress of several cold spray materials.

2. Experimental procedure

2.1. Materials

Three different powders, three different substrate materials and three different substrate pre-treatments were used in this study.

The Al, Cu and Ti powders are commercially available and especially designed for thermal spraying. The Al powder was provided by TLS Technik GmbH, the Cu powder was from H.C. Starck (Amperit 190.068) and the Ti powder was from Gfe GmbH. Gas atomized aluminium powder had a purity of 99.7% (according to manufacturer). The particle size distribution was $-50 + 10$ μm with an average particle size (d_{50}) of 32 μm. The copper powder was also gas atomized with 99.89% purity (according to manufacturer), a particle size distribution of $-35 + 10$ μm and average particle size of 22 μm. In the case of titanium, a crushed powder with purity of 99.7% (according to manufacturer) was used to deposit the coatings. The particle size distribution was $-80 + 20$ μm with an average particle size of 38 μm.

Coatings were deposited on carbon steel (S355), stainless steel (AISI316) and aluminium (6061-T6) substrates with dimensions of 228.6 mm × 25.4 mm × 2.5 mm. Three

different surface pre-treatments were performed in order to improve the coating adhesion: grinding with P240 SiC paper, grit blasting with 24-grade corundum and grit blasting with 220-grade corundum using a cold spray system (with coating deposition parameters).

The cold spray system used in this study was a KINETICS 4000 (Cold Gas Technology GmbH), with nitrogen as an operating gas. Different types of nozzles were used for the different feedstock materials. A polymeric nozzle (type 33) was used to deposit the aluminium coatings, whereas a cermet nozzle (type 24) was used to produce the copper and titanium coatings. The main spray parameters used for each powder are presented in Table 1.

2.2. Microstructural characterization

For the microstructural characterization of cross-sections of all of the deposited coatings, the surfaces of pre-treated substrates and the morphologies of used powders, a JEOL JSM-5310 scanning electron microscope was used. The surface roughness of the substrates pre-treated with grinding or grit blasting were measured with MITUTOYO Surftest-301 equipment.

2.3. Residual stress measurements

An in situ coating property sensor (ICP-sensor, Reliacoat Technologies, US) is an in situ curvature device, in which the curvature of a plate sample is monitored online by three lasers during the deposition process. In this way, the various stages of stress build-up can be monitored and the various stress contributions can be evaluated separately. The curvature sensor is based on laser sensing of deflections in a strip during thermal spray deposition, which is then converted to the sample curvature. A simultaneous measurement of temperature is achieved via multiple thermocouples.

Evolving stress formed by each coating layer can be calculated by Stoney's equation:

$$\sigma_{ev} = \frac{E'_s t_s^2}{6}\frac{d\kappa}{dt_c} \tag{2}$$

where σ_{ev} is the evolving stress of the layer with thickness dt_c, which causes a curvature of $d\kappa$, E'_s is the in-plane elastic modulus ($= E_s/(1-v_s)$, where E_s is Young's modulus and v_s is Poisson's ratio of the substrate) and t_s is the thickness of the substrate [20,21].

Deposition stress can be determined from the curvature change in the substrate–coating system during coating deposition by Brenner and Senderoff's equation [22]:

$$\sigma_d = \frac{E'_s t_s (t_s + \beta^{\frac{5}{4}} dt_c)}{6dRdt_c}; \quad \beta = \frac{E'_c}{E_s} \tag{3}$$

where σ_d is the deposition stress, E'_c is the in-plane modulus of deposited coating, dR is change in radius caused by deposition stress in a deposited layer thickness dt_c and the rest are as in Eq. (2) above.

Thermal stress can also be calculated with Brenner and Senderoff's equation [22] for thick coatings. The portion from the end of spraying to the cooling down of the substrate–coating system to room temperature is analysed. The residual stress value reported is the sum of the deposition stress and thermal stress.

The following material-specific values were used to calculate the stresses with Eqs. (2) and (3): Young's modulus (GPa), Poisson's ratio and CTE (μm m °C^{-1}) of 70, 0.33 and 23 for aluminium, 110, 0.35 and 16.4 for copper, 103, 0.34 and 8.6 for titanium, 205, 0.3 and 12 for carbon steel and 193, 0.284 and 16 for stainless steel. The actual coating thicknesses determined from the cross-sectional images of each deposited coating were used for the calculations.

3. Results

3.1. Microstructures

3.1.1. Feedstock powders

The aluminium and copper powders (Fig. 1a and b, respectively) used to deposit the coatings showed a spherical morphology, typical of gas atomized powders. In the case of titanium, a crushed powder (Fig. 1c) with irregular morphology was used to produce the coatings.

3.1.2. Substrates and coatings

The coatings were produced on three different substrates, carbon steel, stainless steel and Al alloy, which were superficially activated before the coating deposition. The effect of grinding with P240 SiC paper (Fig. 2a), typical grit blasting with 24-grade corundum (Fig. 2b) and grit blasting with 220-grade corundum directly with the cold spray system (Fig. 2c) were evaluated for carbon steel substrate. Grinding with P240 SiC paper resulted in groove-like but smooth surface with negligible amount of abrasive residue. A residue of corundum can be observed on the substrate surface when grit blasted with 24-grade corundum. Even more corundum residue was observed when grit blasting was performed by the cold spray system, caused by higher temperature and velocity of corundum particles. In all substrate materials, alumina particles adhered after the grit blasting processes.

Table 1
The main coating-material-specific cold spray parameters for deposited coatings.

Powder	Pressure (bar)	Temperature (°C)	Nozzle	Average coating thickness (μm)
Al	25	350	Polymer (22 mm)	500
Cu	30	400	WC-Co (17.5 mm)	600
Ti	35	700	WC-Co (17.5 mm)	1000

Five deposition layers, with 1 mm step size, 500 mm s^{-1} traversing velocity and 40 mm distance from the substrate were used for all coatings.

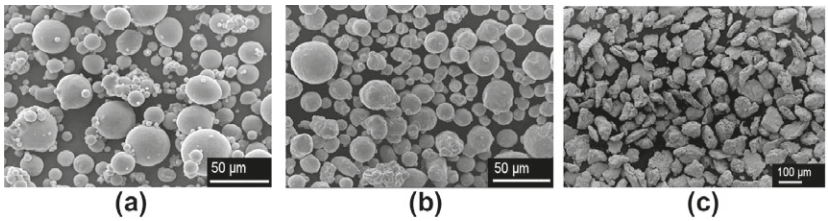

Fig. 1. Secondary electron images of (a) aluminium, (b) copper and (c) titanium powders used to deposit the coatings.

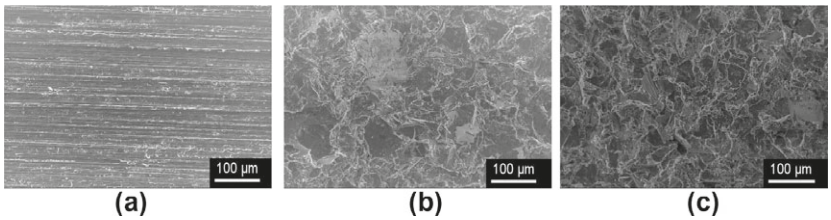

Fig. 2. Scanning electron microscopy images of different surface pre-treatments produced on carbon steel substrate: (a) substrate grinding, (b) grit blasting with 24-grade corundum and (c) grit blasting with 220-grade corundum with a cold spray system.

Besides the differences in residues, the pre-treatments produced different surface roughness values for the studied carbon steel substrates. The surface roughness values (R_a) for the different surface treatments are 0.5 ± 0.1, 5.6 ± 0.3 and 4.7 ± 0.4 for the substrate grinding, grit blasting 24-grade Al_2O_3 and grit blasting 220-grade Al_2O_3 with the cold spray system, respectively.

The spraying parameters used to produce the coatings (shown in Table 1) were adequate to obtain dense coatings for each respective feedstock material. One pre-heating pass was done prior to the coating deposition in all experiments. The coating material-specific deposition parameters were kept the same for all the substrates and surface treatments. Cross-sections of copper coatings deposited onto different substrate materials are presented in Fig. 3.

Slight differences in deposition efficiency were observed when changing the substrate material but maintaining the same spraying parameters. The obtained surface roughness and the amount of abrasive residue were also seen to be affected by the substrate material in the grit blasting with the cold spray system.

Fig. 4 shows cross-sections of Al, Cu and Ti coatings with the same substrate material and surface preparation (carbon steel, grit blasted with the cold spray system). All the coatings, except the topmost surface, appear to be dense and well bonded to the substrate.

Fig. 5 shows a comparison of titanium coating cross-sections deposited on carbon steel substrate with different substrate surface preparations. Variation in the substrate surface roughness and abrasive residue can be also observed.

3.2. Residual stresses

In situ residual stress measurements were performed on 15 samples. The variables between samples were: the powder used, the substrate material and the substrate pre-treatment. The coatings deposited, the substrates used and the pre-treatments are shown with sample numbering in Table 2.

Typical ICP-sensor curvature and temperature curves with explanations of the stress component are presented

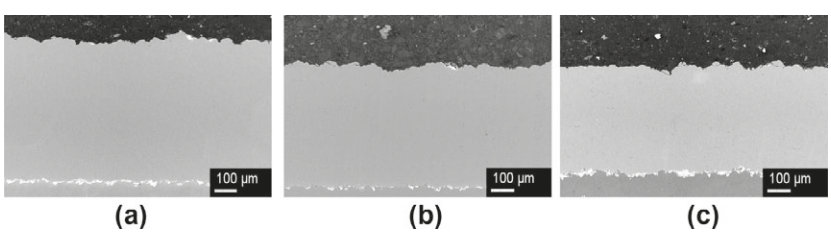

Fig. 3. Cross-sections of Cu coatings produced with the same surface preparation (grit blasting with a cold spray gun) on different substrate materials: (a) carbon steel, (b) stainless steel and (c) aluminium alloy.

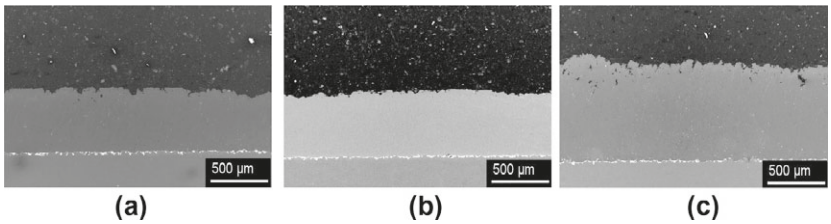

Fig. 4. Cross-sectional images of coatings deposited on carbon steel substrate (grit blasting with a cold spray system): (a) aluminium, (b) copper and (c) titanium.

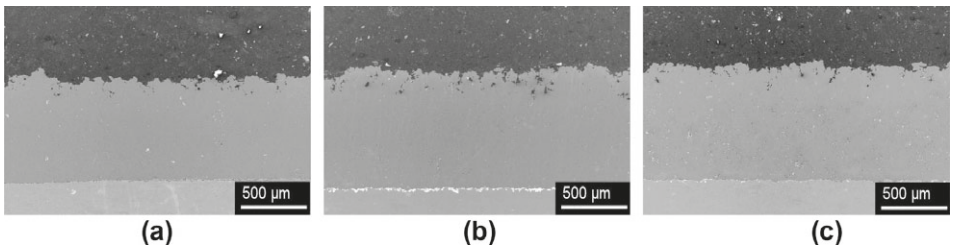

Fig. 5. Ti coating cross-sections deposited on carbon steel substrate with different substrate surface preparations. (a) Ground, (b) grit blasted with a cold spray gun and (c) normal grit blasting.

in Fig. 6. The evolving and deposition stresses were monitored from the start to the end of the actual coating deposition, the thermal stresses from the end of the deposition to the cooling down of the coating–substrate system to room temperature, and the final residual stress state is given as the sum of the stresses generated. Fig. 6 presents the recorded data from sample 6 (Ti coating, carbon steel substrate with cold spray system grit blasting).

Eq. (2) was used for thin films, and Eq. (3) for thick films, to calculate the formed stresses from the sensor data. Results for all samples are presented in Table 3 for aluminium coatings, in Table 4 for titanium coatings and in Table 5 for copper coatings. The results are graphically presented according to Eq. (3) because of the relatively high coating to substrate thickness ratio in all samples in Figs. 7–9.

The results in Table 3 are also graphically presented in Fig. 7a for Al coatings according to Eq. (3). The deposition and thermal stresses are presented separately for various pre-treatments and substrates. It can be seen that, for aluminium, which has a relatively high CTE, thermal stresses dominate the final residual stresses when sprayed on carbon steel or stainless steel. After the coatings had been completed, the resulting residual stress state in the aluminium coatings was tensile in all cases. When aluminium was sprayed onto aluminium, the final stress state was close to zero.

Interestingly, the results shows variations in the deposition stresses when sprayed onto carbon steel substrates that had been pre-treated with different procedures. It can also be seen that stresses formed during the deposition can be either compressive (peening dominant) or tensile (quenching dominant). The low density and high CTE of aluminium are factors which affect the peening–quenching ratio during deposition. The variation in the thermal stress component in sample 2 (compared to samples 1 and 3) was caused by slight delamination of the coating during cooling. The effect of deposition stresses can be more clearly seen from Fig. 7b, where the curvature history in aluminium deposition for each pre-treatment for carbon steel is presented. Clear tensile stress development can be seen for the coating deposited on top of a typically grit blasted substrate during the first deposition layer (sample 3). The stresses formed during the deposition and cooling down of five coating passes can be clearly seen in Fig. 7b.

The deposition, thermal and residual stress results for deposited titanium coatings are presented in Table 4. The results are also graphically presented in Fig. 8a for Ti coatings according to Eq. (3).

Table 2
Deposited coatings, substrates and pre-treatments, with respective sample numbers.

Coating material	CS substrate (GBC)	CS substrate (Gr)	CS substrate (NGB)	SS substrate (GBC)	Al substrate (GBC)
Al	1	2	3	4	5
Ti	6	7	8	9	10
Cu	11	12	13	14	15

CS, carbon steel; SS, stainless steel; GBC, grit blasting with the cold spray system; Gr, grinding; NGB, normal grit blasting.

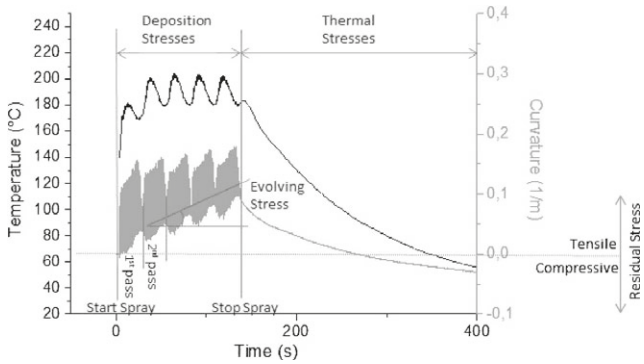

Fig. 6. Temperature and curvature graphs of sample 6, illustrating the concepts of evolving, deposition, thermal and final residual stresses.

Table 3
Deposition, thermal and residual stresses for deposited aluminium coatings.

Al	CS substrate (GBC)	CS substrate (Gr)	CS substrate (NGB)	SS substrate (GBC)	Al substrate (GBC)
Deposition stress (MPa)	−10.9/−11.6	−3.8/−4.1	25.8/27.1	10.7/11.2	0.3/0.4
Thermal stress (MPa)	59.4/63.0	41.9/44.8	55.3/58.1	38.4/40.2	0.8/1.0
Residual stress (MPa)	48.5/51.5	38.1/40.7	81.2/85.2	49.1/51.4	1.1/1.4

Results from Eq. (2) for thin films are shown first, then results from Eq. (3) for thick films. A positive value represents tensile stress and a negative value, compressive stress. GBC, grit blasting with the cold spray system; Gr, grinding; NGB, normal grit blasting.

Table 4
Deposition, thermal and residual stresses for deposited titanium coatings.

Ti	CS substrate (GBC)	CS substrate (Gr)	CS substrate (NGB)	SS substrate (GBC)	Al substrate (GBC)
Deposition stress (MPa)	30.1/35.6	47.4/54.5	71.5/83.5	38.5/45.9	72.4/86.0
Thermal stress (MPa)	−44.1/−52.0	−46.4/−53.4	−47.6/−55.6	−99.3/−118.3	−213.6/−253.7
Residual stress (MPa)	−13.9/−16.4	1.0/1.1	23.9/27.9	−60.8/−72.4	−141.2/−167.7

Results from Eq. (2) for thin films are shown first, then results from Eq. (3) for thick films. A positive value represents tensile stress and a negative value, compressive stress. GBC, grit blasting with the cold spray system; Gr, grinding; NGB, normal grit blasting.

Table 5
Deposition, thermal and residual stresses for deposited copper coatings.

Cu	CS substrate (GBC)	CS substrate (Gr)	CS substrate (NGB)	SS substrate (GBC)	Al substrate (GBC)
Deposition stress (MPa)	−35.5/−51.6	−38.1/−42.0	−15.7/−17.6	−58.8/−66.4	−47.5/−66.1
Thermal stress (MPa)	21.8/31.6	36.5/40.2	35.8/40.1	0.9/1.1	−29.7/−41.3
Residual stress (MPa)	−13.7/−19.9	−1.6/−1.8	20.1/22.5	−57.9/−65.3	−77.3/−107.5

Results from Eq. (2) for thin films are shown first, then results from Eq. (3) for thick films. A positive value represents tensile stress and a negative value, compressive stress. GBC, grit blasting with the cold spray system; Gr, grinding; NGB, normal grit blasting.

In the case of cold spraying of titanium, which has a lower CTE than any of the substrates, the thermal stresses are compressive and dependent only on the substrate used. Also, it can be seen that, as expected, the higher the CTE difference, the higher the compressive thermal stresses are. Similarly to aluminium, the pre-treatment affects the resulting deposition stresses, but in the case of titanium the deposition stresses are all tensile.

When looking at the curvature history of spraying of titanium on carbon steel in Fig. 8b, it can be seen from positive evolving stress generation that significant quenching stresses are generated during the deposition.

The deposition, thermal and residual stress results for deposited copper coatings are presented in Table 5. The results are also graphically presented in Fig. 9a for Cu coatings according to Eq. (3).

When spraying copper, which has a CTE (16.5) between those of carbon steel and aluminium and very close to that of stainless steel, the thermal stresses correspond very well to the CTE differences between the coating material and substrate, as shown in Fig. 9a.

By looking at the deposition stresses, it can be observed that relatively high peening stresses are generated during spraying, which can be confirmed from the negative

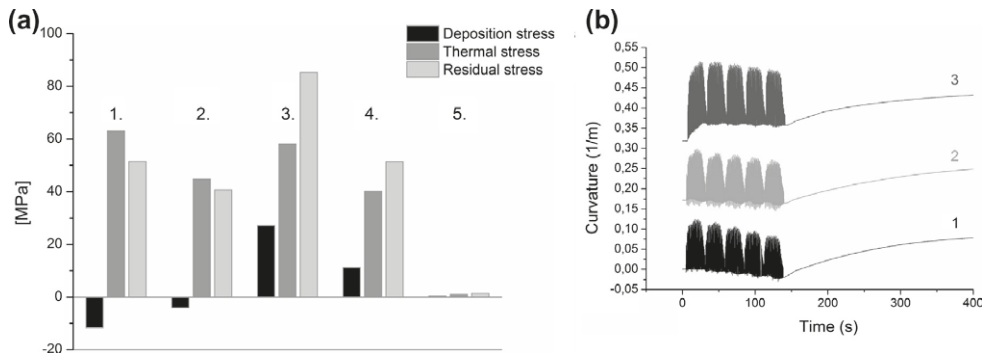

Fig. 7. (a) Stresses for aluminium coatings: 1, CS substrate, grit blasting with a cold spray system; 2, CS substrate, grinding; 3, CS substrate, normal grit blasting; 4, SS substrate, grit blasting with a cold spray system; and 5, Al substrate, grit blasting with a cold spray system. (b) Stress formation during and after aluminium coating deposition on carbon steel substrate with different pre-treatments (sample numbers presented in Table 2).

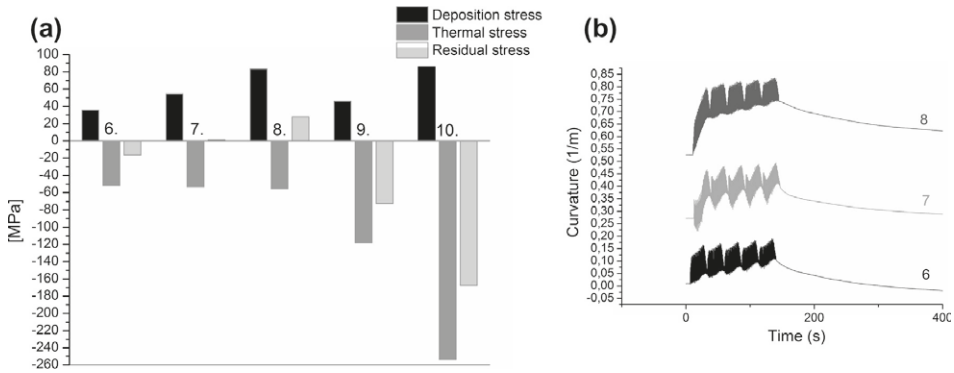

Fig. 8. (a) Stresses for titanium coatings: 6, CS substrate, grit blasting with a cold spray system; 7, CS substrate, grinding; 8, CS substrate, normal grit blasting; 9, SS substrate, grit blasting with a cold spray system; and 10, Al substrate, grit blasting with a cold spray system. (b) Stress formation during and after titanium deposition on carbon steel substrate with different pre-treatments (sample numbers presented in Table 2).

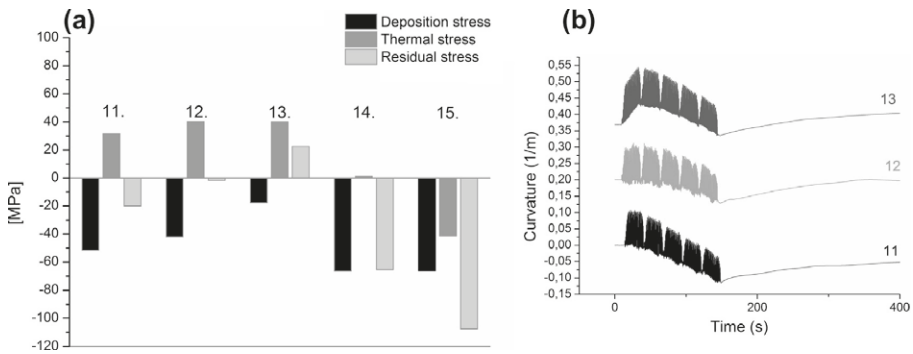

Fig. 9. (a) Stresses for copper coatings: 11, CS substrate, grit blasting with a cold spray system; 12, CS substrate, grinding; 13, CS substrate, normal grit blasting; 14, SS substrate, grit blasting with a cold spray system; and 15, Al substrate, grit blasting with a cold spray system. (b) Stress formation during and after copper coating deposition on carbon steel substrate with different pre-treatments (sample numbers presented in Table 2).

curvature generation during deposition in Fig. 9b. The high density and medium CTE affect the peening–quenching ratio during Cu deposition. In the case of copper, like both aluminium and titanium, substrate pre-treatment plays an important and similar role on the deposition stress evolution.

The graphs of residual stress development of Al, Cu and Ti coatings deposited on top of a stainless steel substrate are presented in Fig. 10. The development of deposition stresses during the first pass of copper is observed to be quite neutral (the peening and quenching stresses are the same), but compressive stress development is observed for the following four passes. The thermal stresses are observed to be neutral because of the similar CTEs of copper (16.4 μm m°C^{-1}) and stainless steel (16 μm m°C^{-1}). The deposition stresses for the aluminium coating are observed to be quite neutral, but slight tensile stresses are generated during cooling of the coating–substrate system caused by $CTE_{Al} > CTE_{SS}$. The high gas temperature used to deposit titanium (twice that for aluminium coatings) is observed to result in tensile deposition stresses, but the final residual stress state is observed to be compressive because of the highly compressive thermal stresses that develop during the cooling, caused by $CTE_{Ti} < CTE_{SS}$.

4. Discussion

Three different substrate materials were used to study the effects of substrate CTE, and mechanical and deformation behaviour. When considering the role and magnitude of different residual stress origins (thermal stress, peening or quenching stress) in various substrate material systems, it should first be noted that thermal stresses, which are generated after the deposition, are directly proportional to the ΔCTE between materials. In the case of aluminium deposition, the thermal stresses are most tensile for the carbon steel substrate because of the largest ΔCTE, less tensile for the stainless steel substrate because of a slightly smaller ΔCTE and basically zero for the aluminium substrate because of no ΔCTE. For copper, the thermal stresses follow the same tendency as with Al coatings: most tensile for the carbon steel substrate because $CTE_{CS} < CTE_{Cu}$, basically zero for the stainless steel substrate because the ΔCTE is close to zero and compressive for the aluminium substrate because $CTE_{Al} > CTE_{Cu}$. For titanium, the thermal stresses increase in compression as a function of the increased ΔCTE.

Secondly, the generation of evolving stresses seemed to be dependent on (i) the density of the particles and their deformation behaviour upon impact, (ii) the CTEs of the sprayed material and the substrate, and (iii) the temperature and velocity of the particles. For titanium coatings, the medium-low density (4.5 g cm^{-3}), low CTE (8.6 μm m°C^{-1}) but high deposition temperature resulted in tensile deposition stresses for all substrate materials. It was hence observed that quenching stresses can develop even in relatively low temperature kinetic cold spraying. It was also found that the greater the ΔCTE, the larger the tensile stress observed during deposition (samples 6, 9 and 10). For copper coatings, the high density (8.9 g cm^{-3}) and medium-high CTE (16.4 μm m°C^{-1}) are responsible for the highly compressive deposition stresses for all substrate materials (samples 11, 14 and 15), which indicates that the peening stresses dominate the stress generation. For aluminium coatings, the low density (2.7 g cm^{-3}) and high CTE (23 μm m°C^{-1}) are responsible for the low deposition stresses for the carbon steel, stainless steel and Al substrates with the same pre-treatment (samples 1, 4 and 5), and the resulting evolving stresses are relatively neutral.

Three different substrate pre-treatments were studied for the carbon steel substrate. It was found that the effect of the first layer on residual stresses is the most important. The residual stress on the first coating layer in many cases differs from subsequent layers; for example, tensile stresses were generated during the first deposition layer even though the other four deposition layers generated compressive stresses. The effect of surface preparation was clearly observed, and the tendency was the same for all of the coating materials studied. Deposition stresses went from "more compressive" to "more tensile" in the order of: 220-grade corundum with the cold spray system, grinding with P240 SiC paper and typical grit blasting with 24-grade corundum (as observed from Figs. 7a, 8a and 9a). The most likely reason for this is the adhesion of the first deposition layer (as observed in Figs. 7b, 8b and 9b). The greater the adhesion of the first layer, the greater the quenching effect and the higher the tensile residual stress. The improved adhesion is in correlation with the measured surface roughness and the observed residue of the abrasive medium. It was observed that the grinding with P240 SiC paper resulted in the lowest surface roughness, but basically no residue of the abrasive medium was left on the surface. Grit blasting with typical 24-grade corundum resulted in the highest surface roughness, with a small amount of abrasive medium on the surface. Grit blasting with 220-grade corundum using the cold spray system also gave good surface roughness, but a large amount of the abrasive medium was left on the surface, which hindered the adhesion and tensile residual stress generation on the first coating layer. Some stress relief might also have occurred with the grit blasted samples, but this was not observed during the single preheating pass prior to deposition. Thermal stresses were

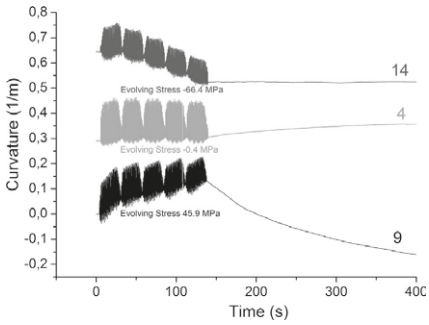

Fig. 10. Deposition and thermal stress development during and after Cu (sample 14), Al (sample 4) and Ti (sample 9) coating depositions on stainless steel substrate. Evolving stresses are shown below curves.

approximately equal within each coating material when deposited on the carbon steel, as expected, unless there was a coating adhesion problem observed during cooling (as for sample 2). It should also be noted that the grit blasting with 220-grade corundum with the cold spray system was only performed for the side of the plate to be coated, unlike in typical grit blasting with 24-grade corundum (where both sides are grit blasted in order to avoid bending of the substrate before coating deposition). This resulted in slight pre-compressive bending of the substrates. The curvatures used for the stress calculations were taken as differences from the initial curvatures.

The final residual stresses were calculated as a sum of the stresses during (deposition stress) and after (thermal stress) the deposition. Tensile residual stresses can be observed for all Al coatings, with the exception of neutral stresses when deposited on top of an aluminium substrate. For Ti coatings deposited on carbon steel substrates with different pre-treatments, residual stresses from tensile to compressive can be observed. Large compressive stresses can be observed for Ti coatings deposited on larger CTE substrates like stainless steel and aluminium. Cu coatings deposited on top of carbon steel samples resulted in residual stresses ranging from tensile to compressive, depending on the pre-treatment. Large compressive stresses can be observed for Cu coatings deposited on larger CTE substrates like stainless steel and aluminium, caused by compressive deposition and neutral or compressive thermal stresses.

Eq. (3) for thick films was used in graphical presentations due to the high coating to substrate thickness ratio (over 1:5 in all cases), even though the differences between the results obtained with Eqs. (2) and (3) were observed to be relatively small.

5. Conclusions

Residual stresses in cold sprayed coatings manufactured from aluminium, copper and titanium powders were measured by using an in situ curvature technique. The residual stresses were determined for coatings deposited on carbon steel (S355), stainless steel (AISI316) and aluminium (6061-T6) substrates. The effect of various pre-treatments, such as normal grit blasting, grit blasting with a cold spray device and grinding, on the residual stress was studied.

The magnitude of residual stresses of cold sprayed coatings may vary significantly, depending on the substrate/coating material system and the substrate pre-treatment. The following conclusions can be drawn from the studies:

- The effect of the first layer's adhesion, which is dependent on the method used to pre-treat the substrate, strongly influenced the ability to generate tensile stress during the deposition of the first layer.
- The generation of evolving stresses in cold sprayed coatings can be either compressive or tensile, dependent on (i) the density of particles and their deformation behaviour upon impact, and (ii) the CTEs of the sprayed material and the substrate.
- The thermal residual stresses, which are generated after the deposition, are directly proportional to the ΔCTE between the materials.
- Mainly compressive stresses were expected because of the nature of cold spraying, but neutral as well as tensile stresses were also formed with the coatings studied.

References

[1] Ghelichi R, Guagliano M. Frattura ed Integrità Strutturale 2009;8:30.
[2] Assadi H, Gärtner F, Stoltenhoff T, Kreye H. Acta Mater 2003;51:4379.
[3] Klinkov SV, Korasev VF, Rein M. Aerosp Sci Technol 2005;9:582.
[4] Schmidt T, Assadi H, Gärtner F, Richter H, Stoltenhoff T, Kreye H, et al. J Therm Spray Technol 2009;18:794.
[5] Voyer J, Stoltenhoff T, Kreye H. Proc Int Ther Spray Conf 2003:71.
[6] Kuroda S, Dendo T, Kitahara S. J Therm Spray Technol 1995;4(1):75.
[7] Clyne TW, Gill SC. J Therm Spray Technol 1996;5:401.
[8] Matejicek J, Sampath S. Acta Mater 2001;49:1993.
[9] Kuroda S, Tashiro Y, Yumoto H, Taira S, Fukanuma H. Int Therm Spray Conf 1998;1:569.
[10] Matejicek J, Sampath S. Acta Mater 2003;51(3):863.
[11] Sampath S, Srinivasan S, Valarezo A, Vaidya A, Streibl T. J Therm Spray Technol 2009;18(2):243.
[12] Spencer K, Luzin V, Matthews N, Zhang MX. Surf Coat Technol 2012;206:4249.
[13] Valarezo A, Sampath S. J Therm Spray Technol 2011;20(6):1244.
[14] Tsui YC, Clyne TW. Thin Solid Films 1997;306(1):23.
[15] Choi WB, Li L, Luzin V, Neiser R, Gnäupel-Herold T, Prask HJ, et al. Acta Mater 2007;55:857.
[16] Luzin V, Spencer K, Zhang MX. Acta Mater 2011;59:1259.
[17] Sampath S, Jiang XY, Matejicek J, Prchlik L, Kulkarni A, Vaidya A. Mater Sci Eng 2004;A364:216.
[18] Ahmed R, Faisal NH, Paradowska AM, Fitzpatrick ME, Khor KA. J Mech Behav Biomed Mater 2011;4:2043.
[19] Lima CRC, Nin J, Guilemany JM. Surf Coat Technol 2006;200:5963.
[20] Stoney GG. Proc Roy Soc Lond 1909;A82:172.
[21] Ohring M. The materials science of thin films. San Diego (CA): Academic Press; 1992.
[22] Brenner A, Senderoff S. J Res Natl Bur Stand 1949;42:105.

PUBLICATION III

Influence of powder properties on residual stresses formed in high-pressure liquid fuel HVOF sprayed WC-CoCr coatings

T. Varis, T. Suhonen, M. Jokipii, P. Vuoristo

Surface & Coatings Technology, vol 388, March 2020
DOI: 10.1016/j.surfcoat.2020.125604

Surface & Coatings Technology 388 (2020) 125604

Contents lists available at ScienceDirect

Surface & Coatings Technology

journal homepage: www.elsevier.com/locate/surfcoat

Influence of powder properties on residual stresses formed in high-pressure liquid fuel HVOF sprayed WC-CoCr coatings

Tommi Varis[a,*], Tomi Suhonen[b], Mika Jokipii[b], Petri Vuoristo[a]

[a] Tampere University, Faculty of Engineering and Natural Sciences, Materials Science and Environmental Engineering, Surface Engineering Research Group & Thermal Spray Center Finland (TSCF), P.O.Box 589, FI-33014, Finland
[b] VTT Technical Research Centre of Finland Ltd, P.O. Box 1000, FI-02044 Espoo, Finland

ARTICLE INFO

Keywords:
High pressure HVOF
Thermal spraying
Residual stress
WC-CoCr
Apparent density
Agglomerated powder

ABSTRACT

This paper presents a systematic study of the effect of various WC-CoCr powders on the residual stresses of the high pressure HVOF sprayed coating. As the residual stresses are recognized to play a significant role in the mechanical and fatigue resistance of the coating, it is understandable that their management is important for damage tolerant coating design. Several studies have recently shown that processes, which produce high particle kinetic energy and lower particle temperature, such as Warm spray, HVAF and high-pressure HVOF processes, generate higher peening stresses and therefore final residual stresses is more compressive compared to lower kinetic energy HVOF systems. In addition to the spraying process, powder properties are known to be one of the most important variables in thermal spraying. Nevertheless, only few studies can be found on the effect of powder properties on residual stresses. The aim of this study was to understand the effect of different powder properties on the formation of residual stress. In situ monitoring was utilized to record curvature and temperature during spraying and to calculate coating residual stresses. This approach is a useful tool for understanding of residual stresses during the thermal spraying process enabling their manipulation. It was found that the powders, with only minor differences in density and particle size, produced a significant difference of about 350 MPa in the stress states of the coatings. The combined effect of spray powder properties and spray parameters on residual stress was almost 560 MPa.

1. Introduction

Residual stresses can in worst-case cause delamination or macroscopic cracking of a thermal sprayed coating [8, 14, 34, 35]. Moreover, the high magnitude of residual stresses may have an effect on the coating performance such as adhesion strength, wear resistance, and fatigue life of the coatings during its use [1, 11, 23, 28, 32]. Recently, results of WC-CoCr -coatings sprayed by high kinetic thermal spray processes, such as Warm spray (WS), high velocity air fuel (HVAF and high-pressure high velocity oxygen fuel (HP-HVOF)) -process, show that residual stresses generated from these processes are more in compressive stress compared to conventional HVOF process. Very good cavitation wear resistance of WC-CoCr HVAF-coatings has been linked partly to these highly compressive residual stresses [5, 6, 15, 20, 27].

Particle size distribution, density and homogeneity of the powder are known to have a critical influence on the coating quality, and therefore powder is considered as one of the most important variables in thermal spraying [4, 10, 36]. For this reason, the powder manufacturing process is of great importance. Agglomerated and sintered (a&s) powders, which has become more common, have some porosity in the powder structure while fused and crushed (f&c) powders are fully dense. Moreover, the density among a&s powders from different sources may vary. This is because the equipment and parameters used in spray drying have a major influence on the properties of the powder. Moreover, slurry chemistry in powder agglomeration and sintering temperature have a great influence on the powder density, morphology and strength. In addition, powder chemical composition and carbide size may influence on the powder morphology and density as well. The apparent densities of WC-CoCr powders may vary e.g. from 4.0 to 5.8 $g \cdot cm^{-3}$ [3, 10, 36].

The density of the powder was shown to have a great influence on the carbon loss in HVOF spraying of WC-Co materials, which is related to a melting behaviour of porous particles [3, 4, 7, 36]. The original porosity of the initial powder particles was also shown to have an influence on the density of coating as the filling of spray droplet is insufficient and porosity in the powder remains in the coating structure

* Corresponding author.
E-mail addresses: tommi.varis@tuni.fi (T. Varis), tomi.suhonen@vtt.fi (T. Suhonen), mika.jokipii@vtt.fi (M. Jokipii), petri.vuoristo@tuni.fi (P. Vuoristo).

https://doi.org/10.1016/j.surfcoat.2020.125604
Received 15 January 2020; Received in revised form 6 March 2020; Accepted 8 March 2020
Available online 10 March 2020

[21]. However, due to a lower heat load of the new generation high kinetic processes, decarburization of porous particle can mostly be avoided [5, 6]. In addition, the higher kinetic energy of the particles can be thought to facilitate particle condensations. Low heating gives also a possibility to use smaller powder size distribution [6], which minimises the problems arising from insufficient filling [3, 6, 21].

The origins of residual stresses in thermal spraying (quenching, thermal mismatch stress, and peening stress) are well known [2, 8, 16-19]. However, the effect of the powder characteristic on the residual stresses are not often discussed. This study addresses the effect of apparent density of WC-10Co4Cr powder on the residual stresses in high pressure HVOF spraying.

2. Experimental

Three a&s WC-10Co4Cr powders, two (D1, D2) from Fujimi (Fujimi Incorporated, Kiyosu, Japan) and one (D3) from Durum (Durum Verschleiss-Schutz GmbH, Krefeld, Germany), were selected for the studies. The powders had different apparent densities and the particle size distributions were relatively similar. The powders had nominal size of 0.4 μm WC-particles in CoCr matrix and their nominal size distribution was 5–25 μm. Particle strength for the powders D1 and D2 was measured by the procedure shown in [7]. More detailed data on the powders are given in Table 1.

Coatings were deposited by using a robot on 228.6 × 25.4 × 2.5 mm low carbon steel (S355) flat bars by Carbide Jet Spray (CJS) high pressure liquid fuel HVOF -process (Thermico GmbH & Co, Dortmund, Germany) equipped with K5.2 nozzle configuration. This new configuration was specially developed for the spraying of fine powders (< 25 μm). In the Thermico CJS liquid kerosene HVOF-process, the combustion chamber has been designed such that the combined combustion of kerosene and hydrogen (with oxygen) is optimized. In the K 5.2 configuration, hydrogen and kerosene combustion takes place in different areas of the chamber and allows stable burning of the flame with lean kerosene ratios as it is assisted by hydrogen. This results to a colder flame temperature and make spraying of fine powders without particle overheating possible. In this study, the flame temperature was varied by changing the fuel/oxygen (F/O)-ratio and gas velocity by changing chamber pressure. Spray parameters with the information of the F/O-ratios and combustion chamber pressures are shown in Table 2. Selected kerosene flow rates were 14, 16 and 18 $l{\cdot}h^{-1}$, and the oxygen flow was varied to produce three different F/O-ratios at two different chamber pressure levels, which were approximately 13.4 bars for parameters P1, P2, and P3 and 11.3 bars for parameters P4, P5 and P6. As the stoichiometric F/O_{mass}-ratio of kerosene ($C_{12}H_{26}$) combustion is 0.29, all parameters (P1-P6) were all clearly oxygen-rich. It is commonly known the flame temperature decreases as it is moved away from the stoichiometric ratio. It should be mentioned that complete burning of added hydrogen (80 l) consumes 160 $l{\cdot}min^{-1}$ of oxygen. This amount is subtracted from the oxygen flow rate and taken into account in the calculation of the F/O-ratios in Table 2. With respect to gas velocities it was expected that they were relatively constant at each chamber pressure levels. Average particle velocities and temperatures were measured at the spraying distance (200 mm) by Spray Watch 2i particle monitoring device from Oseir ltd, Tampere, Finland, which measures the velocities by inbuilt image analysing the length of the traces drawn by in-flight particles during the known exposure time of digital CCD camera. The average particle temperature is measured by two-colour pyrometry.

Table 1
The information of the powders from powder manufacturers.

	D1	D2	D3
Apparent density [$g{\cdot}cm^{-3}$]	4.43	5.02	5.38
Size distribution [μm], D10-D90%	−26 + 12	−26 + 11	−29 + 15
Average size [μm], D50%	17.2	16.6	21.0
Carbon content [w-%]	5.94	5.87	5.38
Particle Strength [MPa]	300	490	–

Table 2
Spray parameters used for the deposition of the coatings with HP-HVOF spray gun.[a]

	P1	P2	P3	P4	P5	P6
Kerosene [$l{\cdot}h^{-1}$]	14	16	18	14	16	18
Hydrogen [slpm]	80	80	80	80	80	80
Oxygen [slpm]	960	940	920	800	785	770
Nitrogen [slpm]	32	32	32	32	32	32
Fuel/oxygen-ratio[a]	0.17	0.19	0.22	0.20	0.24	0.29
Combustion Chamber Pressure [bar]	13.6	13.4	13.3	11.3	11.2	11.3

[a] Assumed in the calculations that hydrogen burns 160 l/min of oxygen, Fuel/Oxygen-ratio for neutral flame: 0.29.

Prior to deposition, the substrates were grit blasted on both sides using 500–700 μm corundum particles. Gun traverse speed of 1 m/s and step of 4 mm were used. During the deposition, the substrates were mounted on an in-situ coating property (ICP) sensor [25] (ReliaCoat Technologies, East Setauket, USA). The fixture on the ICP sensor allows the free bending of the sample and enables the monitoring of deflection of the bar by using three laser sensors. The temperature from the backside of the substrate was recorded by using two contacting thermocouples.

Deposition efficiency (DE) was measured by weight gain principle in which the deposited mass per fed mass is calculated by using the Eq. (1):

$$DE = \frac{m_{s2} - m_{s1}}{R_f \cdot t},\ t = \frac{l}{U} \cdot \frac{w}{W_z} \cdot n_p, \tag{1}$$

where m_{s2} = mass of the substrate and coating, m_{s1} = mass of the substrate, R_f = powder federate, t = effective time when gun is spraying on the substrate, l = length of the substrate, w = width of the substrate, U = gun traverse speed, W_z = step, and n_p = number of passes.

With the used method for DE calculation, there is an error since some of the material is over sprayed from the sides of the samples during the "effective time". The estimated effect from the overspray on the DE is approximately −20%. However, coatings were made with same robot program and thus DE values are comparable with each other.

The powders and the polished cross section samples of coatings were characterized with a field-emission scanning electron microscope (FESEM, Zeiss ULTRA plus, Carl Zeiss AG, Oberkochen, Germany). The mechanical properties of the coatings were determined by indentation-based techniques. An instrumented indentation device (Zwick ZHU 0.2, Zwick-Roell, Ulm, Germany) was used for evaluating the coating hardness. For Vickers hardness 9 indentations were taken on polished cross section with 300 g load (HV0.3). The fracture toughnesses of the coatings were determined from the corner cracks of the seven Vickers indented with the load of 5 kg by using Evans and Wilshaw Eq. (3) [9]:

$$K_{IC} = 0.079\left(\frac{P}{a^{3/2}}\right)\log\left(\frac{4.5a}{c}\right) \tag{3}$$

where: P is load of Vickers indenter (mN), a = half-diagonal of the Vickers mark (μm), c = length of the cracks obtained in the tip of the Vickers marks (μm).

Through thickness residual stress of the coatings were determined by using Tsui and Clyne analytical model [29] with following procedure. First, the deposition stress either quenching or peening, was determined by iterating the deposition stress by procedure proposed by Tsui and Clyne [30]. In the procedure, deposition stress (quenching or peening stress) was adjusted to a value, which produces equal curvature with the analytical model and ICP sensor. Then through thickness

stresses resulted from the quenching or peening were calculated for progressive deposited coating by using Tsui and Clyne analytical model [29]. The actual temperature data before each coating pass from the ICP sensor was used for calculation of thermal mismatch stresses for each layer. Finally, deposition stress and thermal mismatch stress for each layer were superposed. Equation for example for the residual stress in the midpoint of nth layer was Eq. (2) [29]:

$$\sigma_d = \frac{F_n}{bw} - E_d(\kappa_n - \kappa_{n-1})\left(\left(n - \frac{1}{2}\right)w - \delta_n\right) + \frac{F_{(CTE)}}{bh} - E_d(\kappa_j - \kappa_n)\left(\left(j - \frac{1}{2}\right)w - \delta_n\right) \quad (2)$$

where n = layer in question, 1 < j < n, F_n = normal force due to quenching stress, $F_{(CTE)}$ = force due to CTE difference, b = beam width, w = single layer thickness, h = coating thickness, E_d = Young's modulus of the deposit, $\kappa_n - \kappa_{n-1}$ = curvature change due to the deposition of layer n, δ_n = location of neutral axis.

3. Results and discussion

3.1. Powders

The differences in the powder characteristics are shown in powder morphology figures (Fig. 1) and Table 1, which shows apparent density, carbon content, and particle strength. Particle morphologies show a structure typical of agglomerated and sintered WC-10Co4Cr powder. Higher density of the powder D3 comparing to D1 and D2 is evident from the morphology figures. The differences between the powders D1 and D2 are mainly due to the sintering temperature. Higher sintering temperature of powder D2 resulted in higher apparent density and, and higher particle strength of powder compared to powder D1. It may also have contributed to the slight decrease in carbon content in powder D2.

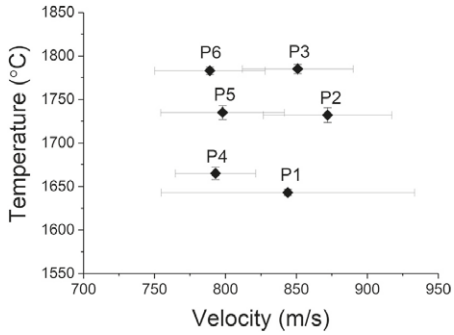

Fig. 2. Temperature and velocity of the powder D3 measured by Spray Watch device.

The surface morphology figures also show that powders D1 and D2 has more fine particles (< 5 μm), which can also be seen in the particle size distributions.

3.2. Spray diagnostics

Particle velocities were measured for the powder D3 to determine the relative differences in spraying parameters. The temperature-velocity plot in Fig. 2 shows, as expected, that particle temperatures depend on the F/O-ratio. Closer the F/O-ratio to the stoichiometric ratio, 0.29, higher the particle temperature at constant chamber pressure. With the same kerosene flow rates, the particle temperatures at parameters P1-P3 were approximately same level as those at parameters P4-P6 although the F/O-ratios (Table 2) of parameters P1-P3 were significantly lower than those of corresponding P4-P5 parameter. One would expect that a change in the F/O-ratio would lead to lower particle

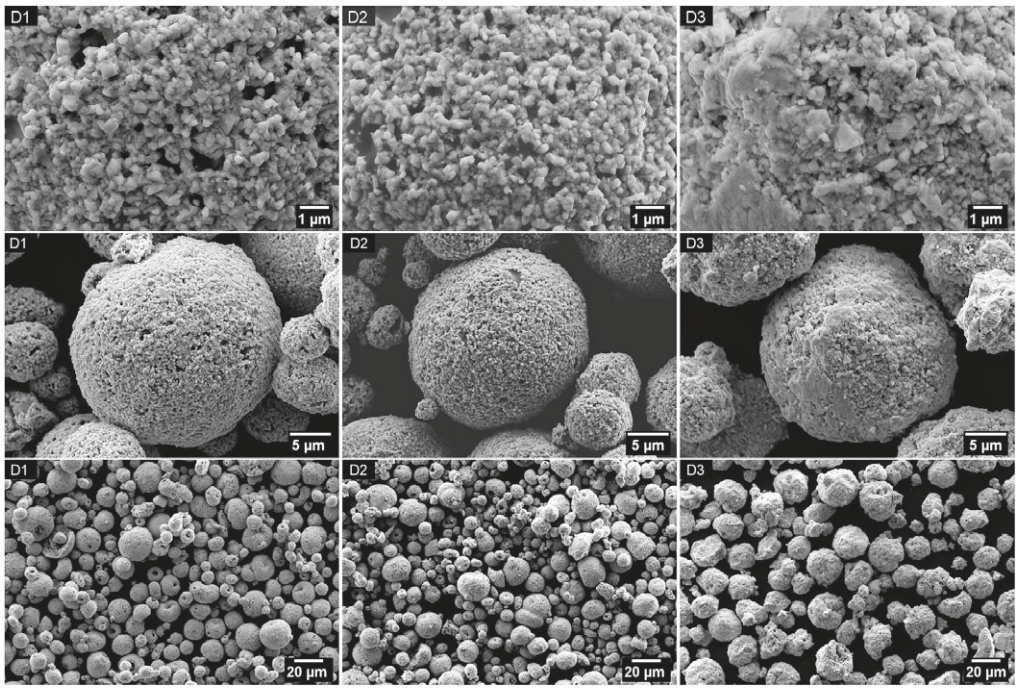

Fig. 1. Surface morphologies of the powders D1 (apparent density = 4.43 g/cm^3), D2 (apparent density = 5.02 g/cm^3), and D3 (apparent density = 5.38 g/cm^3).

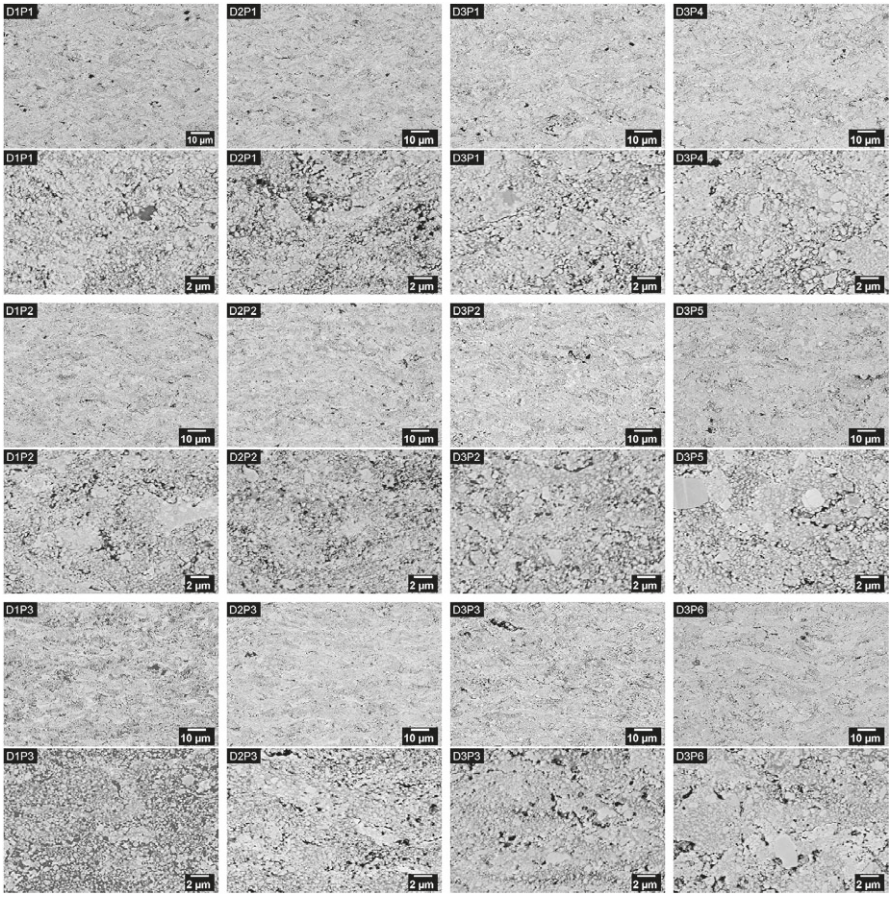

Fig. 3. Back scatter SEM images of the coating microstructures with two magnifications, where D refers to a power density in Table 1 and P refers to a spray parameter in Table 2. Lower magnification (upper) shows a difference in splat flattening degree and higher magnification (below) a micro porosity structure of the coatings.

temperatures when using P1-P3 parameters. However, since the particle temperatures are at the same level, it can be assumed that the higher combustion chamber pressure with parameters P1-P3, will result in a higher gas flow density and thereby more efficient heat transfer to the particle. This may explain why a lower F/O-ratio resulted in the same particle surface temperature levels. With respect to particle velocity, difference between parameter sets P1, P2, P3 and P4, P5, P6 showed that the particle velocity increased with increased chamber pressure and the particle velocities at different temperatures were possible to adjust satisfactory to a desired level by adjusting the chamber pressure with oxygen.

3.3. Microstructures, phase structure, and mechanical properties of the coatings

Evaluation of the coatings from microstructural bases showed only some minor differences in coating structures. In general, coatings shown in Fig. 3 are all relatively dense but have some, the size typically < 1 µm, micro-porosity. Such porosity maybe a result of incomplete filling. Part of this porosity may also be due to incomplete melting of the largest powder particles, which has caused pull-out porosity to occur during sample preparation. High amount of micropores is most noticeable in coating D1 P3 but also overheated areas in this coating are visible. This coating is sprayed using the hottest flame temperature of the powder with a low apparent density, whereby larger porous powder particles can adhere to the substrate and cause porosity. On the other hand, Chivavibul et al. [6] explained that the porosity of the coating with a powder having a low particle strength could be due to disintegration of the powder particles in flight and thus they have smaller size and less peening effect. In this study, no similar signs of degradation could be observed in the microstructure, but in any case, the porous particles have less mass and less peening effect, which may explain the high micro-porousness. In other respects, the largest noticeable difference in the microstructures was the greater portion of well flattened lamellae as the flame temperature increased. Furthermore, it can also be observed that the smallest carbides dissolved in the matrix in coatings, which were sprayed by parameters P5 and P6.

Coating hardness, fracture toughness, W_2C/WC-ratio, and DE are shown in Table 3. A good indication of the temperature particles was exposed to is the amount of W_2C in the structure. In here the proportion of W_2C was presented simply by ratio of W_2C ($2\theta = 39.8^{\circ}$) and WC (35.7°) peaks. When looking at the w-ray diffraction (XRD) results, in Fig. 4, it was evident that the higher the temperature the higher the amount of W_2C at $2\theta = 39.8^{\circ}$. W_2C is formed in the structure as a result of carbon loss from the particles during the flight. The carbon is oxidized directly from the carbide surface and from the molten matrix in

Table 3
Hardness, fracture toughness, W_2C/WC-ratio, and deposition efficiency of the coatings.

Coating	Hardness [HV 0.3]	Fracture toughness [MPa·m$^{1/2}$]	W_2C/WC	DE [%]
D1 P1	1287 ± 88	4.61 ± 0.37	0.10	39.6
D1 P2	1377 ± 125	4.37 ± 0.88	0.13	43.6
D1 P3	1405 ± 83	3.41 ± 0.72	0.17	44.4
D2 P1	1342 ± 83	4.34 ± 0.27	0.10	37.2
D2 P2	1415 ± 54	4.46 ± 0.66	0.12	38.7
D2 P3	1426 ± 24	4.48 ± 0.47	0.17	40.6
D3 P1	1414 ± 30	3.50 ± 0.43	0.12	29.1
D3 P2	1371 ± 98	4.35 ± 0.41	0.12	33.9
D3 P3	1341 ± 135	4.36 ± 0.22	0.15	39.4
D3 P4	1164 ± 146	4.41 ± 0.53	0.12	41.6
D3 P5	1344 ± 109	4.62 ± 0.15	0.13	46.3
D3 P6	1438 ± 112	4.27 ± 0.43	0.15	46.7

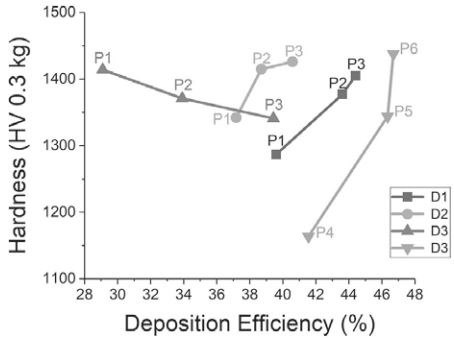

Fig. 5. Vickers hardness and deposition efficiency for powders D1, D2 and D3 sprayed with different parameters P1-P6.

which some minor amount of the carbide is dissolved. As a result, during the rapid cooling some of the tungsten and carbon in the matrix form W_2C on the surface of original WC grains [12, 33]. In addition, mixed carbides of W, Co and Cr may crystallize in the matrix or contribute to the formation of an amorphous phases in the matrix during rapid cooling [12, 33]. Although the amount of W_2C is a direct index of decarburization and thus the heat input, it is not detrimental for the properties in small quantities. In Table 3, the W_2C/WC-ratios are much lower than the ratios that have been presented for gas fuelled low pressure HVOF process [12].

A clear trend in most cases in Table 3 and Fig. 5 is that when the particle temperature is higher, the hardness is higher. Hardness increase could be related to the spray temperature due to a hardening of matrix when it is alloying with tungsten and carbon [31, 33]. In Table 3, in most cases, the increase of flame temperature did not have significant negative influence on the fracture toughness of the coatings. However, the coating sprayed by powder of low apparent density and hot flame (D1 P3) had low fracture toughness assumably due to too high flame temperature, which resulted to a poor microstructure. A good indication of higher flame temperature is slightly increased amount of W_2C in the coating. The formation of relatively low amount of W_2C, like in this case, is not believed itself to sufficiently lower the fracture toughness, because it is formed as thin rims around original WC particles [33]. Solubility of the carbide in the matrix is more likely to have a greater effect on fracture toughness. The properties of CoCr-matrix in HVOF sprayed WC-CoCr coating are known to be degraded due to the partial (minor) dissolution of WC grains to the matrix, which may leads to the formation of amorphous phases in the W and C rich matrix during a rapid cooling [33]. Indeed, in the XRD of D1P3 coating a notable increase of the background intensity can be detected between 2θ angles 35° and 45°, which may explain the loss of the fracture toughness of the matrix. On the other hand, the microstructure of this coating showed a lot of micro-pores in the structure, which may be caused by large porous particles, which stack onto the substrate and had insufficient filling. In addition, the coating D3P1 sprayed using the highest apparent density powder sprayed by cold parameters had low fracture toughness as well which most likely was due to high

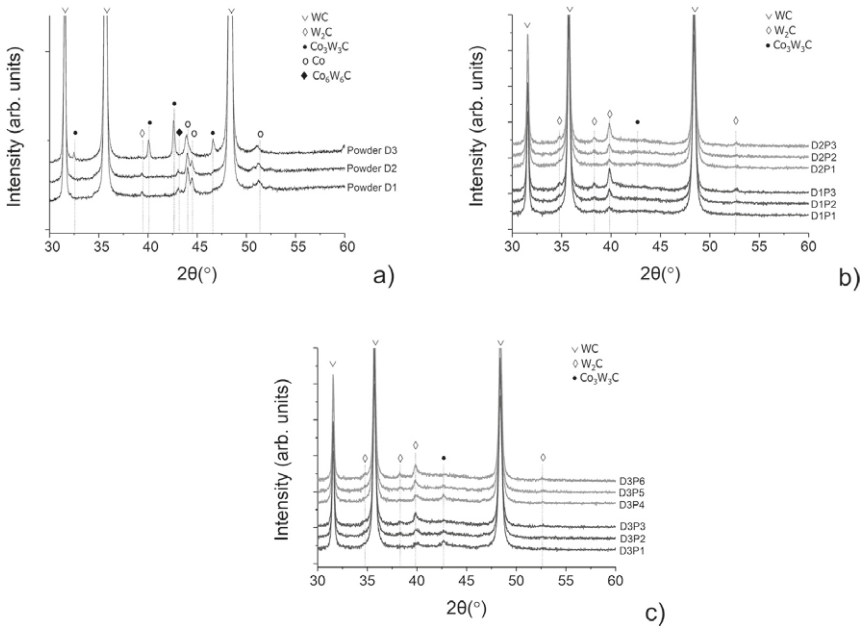

Fig. 4. XRD-diffraction curves for the WC-CoCr a) powders D1, D2 and D3 of different density and b) and c) resulted coatings sprayed using parameters P1-P6.

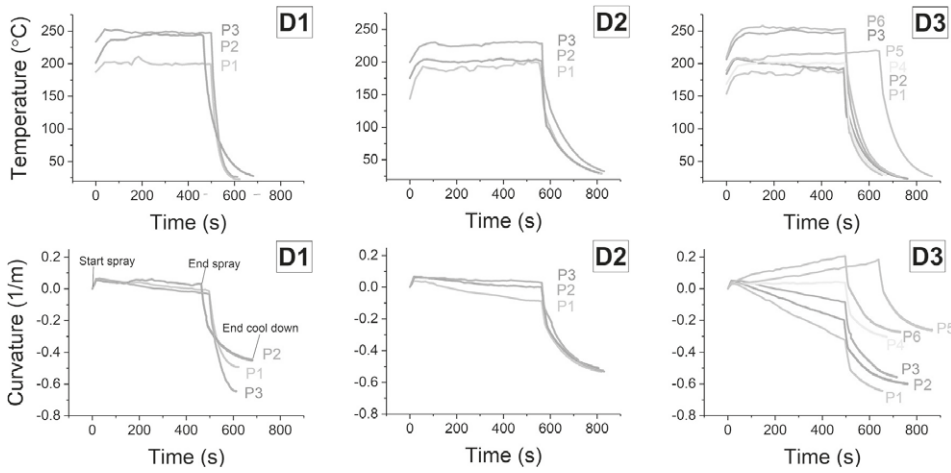

Fig. 6. Temperature and Curvature graphs of the deposited samples measured in-situ by ICP-sensor, where temperature variations during spraying clearly affected curvature. D refers to a powder density D1 < D2 < D3 and P refers to a spraying parameter (in Table 2 and Fig. 2).

compressive residual stresses, which are known to effect on the crack growth around Vickers indentation [13, 24].

As shown in Fig. 5, generally the DE decrease as the apparent density of the powder increases, which is well in line with the study of Chivavibul et al. [6]. Furthermore, in Fig. 5, the hardness – DE relation of powder D3 sprayed with parameters P1, P2 and P3 was different from what was obtained by powders D1and D2. The hardness of the coatings sprayed using densest D3 powder increased as the flame temperature and DE decreased. The hardening of the coating in this case may take place by different mechanism and evokes the thought that strong peening effect, may be responsible for hardening, which idea is supported by literature [6].

3.4. Curvature and residual stresses

Substrate temperature and curvature evolution during the sprayings are shown in Fig. 6, where positive curvature change indicates tensile stresses and negative curvature change compressive stresses. Typically, during the first 1–5 passes curvature changes to a positive direction due to increasing temperature evolution of the substrate, which had higher coefficient of thermal expansion (CTE) than that of the coating. After this, the substrate temperature is relatively constant and the curvature changes linearly in either a positive or a negative direction, depending on whether quenching stresses or peening stresses dominate, respectively. After completing the coating, during the cool down the curvature change in this case is negative, because the (CTE) of the substrate ($11 \times 10^{-6}\,K^{-1}$) is higher than that of the coating ($5.2 \times 10^{-6}\,K^{-1}$). Stresses (+ for quenching and − for peening) at the surface of the coatings resulted from different residual stress origins (deposition, thermal mismatch, and final) by Tsui and Clyne procedure, thermal mismatch stresses, and final residual stress are shown in Table 4 and Fig. 7. Overall, substrate temperatures varied depending on spray parameters and cooling adjustments from 185 to 255 °C and it is notable that due to this temperature differences (and coating thicknesses), the thermal stresses in the coatings varied only from −191.8 to −253.3 MPa. Fluctuations seen in temperature with parameter P1 are presumably due to unstable combustion due to the low F/O-ratio and the curvature change for the coating D1 P2 after 120 s was due to cooling problem, which increased the temperature approximately by 15 °C.

Through thickness residual stress profiles of the coatings by Tsui and Clyne procedure are shown in Fig. 8. Real substrate temperatures were used in the calculations and it can therefore be noted that lower substrate temperatures during the first 5 passes lowered the thermal mismatch stresses of the first spray layers. More specifically, during the spraying of first passes the increase of the substrate temperature caused a tensile stress for previously deposited layers. This tensile stress transfers to a compressive during cool down, but remains lower than for the layers, which were deposited onto hotter substrate.

Table 4
Deposition stress, CTE mismatch stress, and final stress on the surface of the coatings by Tsui and Clyne model (+ tensile and − compressive).

	Deposition stress [MPa]	Thermal mismatch stress [MPa]	Final stress [MPa]
D1 P1	−56.0	−211.3	−267.3
D1 P2	−36.4	−242.2	−278.5
D1 P3	−60.1	−244.4	−304.5
D2 P1	−91.1	−197.7	−288.8
D2 P2	−72.1	−191.8	−263.8
D2 P3	−25.8	−220.3	−246.1
D3 P1	−363.1	−253.5	−616.6
D3 P2	−313.4	−241.5	−554.9
D3 P3	−151.8	−247.4	−399.4
D3 P4	+15.7	−171.8	−156.1
D3 P5	+130.6	−187.9	−57.3
D3 P6	+134.1	−219.0	−84.9

By looking at the final residual stress levels on the surface of the coating in Fig. 8 and Table 4, it was evident that all the coatings were at the compressive residual stress. When WC-CoCr is deposited on top of steel, the thermal stresses due to CTE differences provide a compressive stress state when cooled from deposition temperature onto a room temperature. As stated earlier, the thermal mismatch stresses due to differences in CTE of the coatings varied from −191.8 to −253.3 MPa. In many lower kinetic energy and hotter flame temperature HVOF processes, the stresses generated during coating deposition are strongly dominated by tensile quenching stresses, whereby the final residual stress state is typically close to neutral or may be even tensile [31]. The spray parameters of high pressure HVOF process can be selected such that, due to the high particle velocity and low DE, the impact energy of the particles generates compressive peening stresses in the coating. In this study, the peening stresses were dominant with all parameters except with parameters P4-P6 for powder D3. It was clear that the CJS process has a wide enough process window to significantly influence

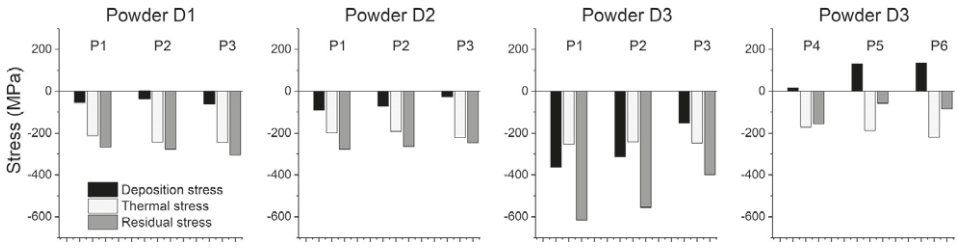

Fig. 7. Effect of powder and spraying parameters on the deposition stresses, thermal stresses and final residual stresses at the surface of the coatings determined by Tsui and Clyne analytical model.

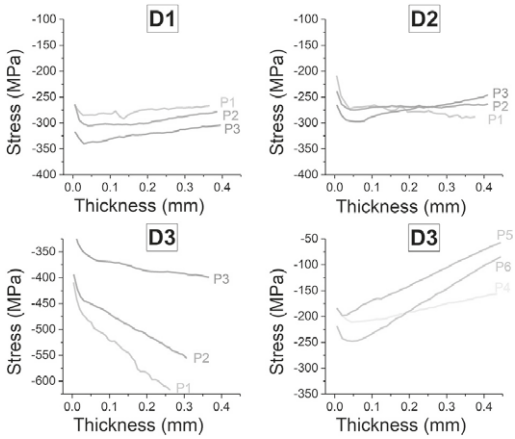

Fig. 8. Through thickness residual stress profiles of the coatings by Tsui and Clyne analytical model. Substrate is on the left side.

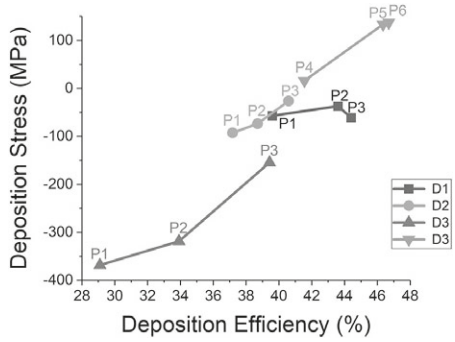

Fig. 9. Relation of deposition stress of coatings and deposition efficiency of powder D1, D2 and D3 sprayed with parameters P1-P6.

the coating stresses on powder D3 by parameter selection. It was clear that the CJS process had a sufficiently wide process window to significantly influence the deposition stresses of the coatings by parameter selection for powder D3. With high gas flow parameters (P1, P2, and P3), the D3 powder provided high compressive deposition stresses and by reducing the total gas flow and increasing the F/O-ratio with parameters (P4, P5 and P6), tensile deposition stresses were developed on the coatings. A change in the parameters increased the heat transfer to the particles, which can be deduced from increased DE. Improved particle heating was due to an the increase in the flame temperature at a higher F/O-ratio and a longer dwell time of the particles at a lower velocity.

It was evident that particle properties played an important role in the magnitude of peening stresses. Different powders produced significantly different peening stresses with same parameters as shown in Figs. 7, 8 and Table 4. The deposition stress of the densest powder, D3, was clearly the highest and even with the same deposition efficiency, the peening effect with D3 powder was higher (D3P3 in Fig. 9) comparing to powders D2 (D2P2 in Fig. 8) and D1. Furthermore, spraying parameters clearly influence the deposition stress in the coating when using the densest powder (D3). For the powders D3 and D2 the noticeable was that high peening stresses were not developed. In addition, it was found that deposition stresses correlate well with DE in Fig. 9, which shows an increase in compressive stresses as DE decreases. The results confirmed the obvious assumption that higher proportion of particles bounce off from the substrate, the higher the peening effect. Instead, if the hot particles stick on the substrate, the quenching effect compensates the peening effect, which was why correlation between DE and compressive stress was seen. Thus, whether the particle adheres to the substrate or not is of great importance for the stress state. Therefore, high compressive peening stresses could be produced only by using powder D3 with highest density and peening effect for that powder was higher the lower the spray temperature and lower the DE. For powder D2 the compressive peening stress increased slightly when flame temperature was lowered from parameter P3 to P2 to P1. For powder D1 the peening stresses during the deposition remained relatively similar although the process temperature was changed and DE improved. It was obvious that with the same spraying parameters, porous particles reach higher temperature, or the melting rate is higher, which increases the effect of quenching stresses compared to peening. This is most probably the reason why lower apparent density powders do not produce high compressive stresses. However, even the high DE parameters for D1 and D2 powders did not yield high tensile deposition stress. It remains unclear why tensile stresses could not develop into more porous powders, but the cause can be searched for example from the role of different relaxation mechanisms, which influence on the coating and relaxes some of the stress components. For example, it is conceivable that quenching stresses do not develop during the particle cooling, because the tensile stresses are relaxed by microcracking or lamella sliding. It might be possible that the peening effect due to the high particle velocity is significant and moves the stress state towards the compression even if the DE is high.

This study demonstrates that powder properties had a strong influence on the residual stress and more specifically ability to generate compressive peening stresses. However, the formation of residual stresses is complex in nature and is influenced by many factors, that was earlier highlighted. Since the particle size distributions of the powders differed slightly, it is also necessary to consider the relative effect of the particle size of the powders on the residual stresses. As known the particle kinetic energy (impact energy) can be calculated by $E_{kin} = 1/2mv^2$, where v is particle velocity, and m is particle mass. Mass is obtained by multiplying density (ρ) and volume (V), where volume of the

presumably circular powder particles is expressed by $V = 4/3\pi r^3$. Thereby, the particle impact energy is directly proportional to the density, to the square of the particle velocity, and to the cube of the particle diameter. Impact energy calculations show that the size of 29 μm fully dense WC-CoCr particle has approximately 100 times more impact energy than the size of 5 μm particle, but only 30% more than size of 26 μm. Therefore, large particles play a major role in development of peening stresses. It is notable that small particles may have an important role for peening effect as well in the cases when they do not attach on the substrate. In studies concerning the carbide retention of WC-Co/CoCr or Cr_3C_2-NiCr materials, it is shown that small size particles cannot bond carbides well, as the size of the carbide approaches the particle size, which increases the bounce of tendency of individual carbides [22, 26]. What comes to the effect of velocity on the impact energy, the difference in kinetic energy between the parameters P1-P3 and P4-P6 (for size of D50 particle) is only 20%. As the impact energy is directly proportional to the density the particle with 50% porosity has a 50% lower impact energy. When assessing the effects of various factors on the formation of peening stresses of this study it can be stated that the particle size distribution has the most significant effect on the generation of peening stresses. Highest particle population is around average particle size (D50 value in Table 1) and hence it is appropriate to look at the impact energy of average size particle. By comparing the impact energy of average size, assumingly fully dense, particle of D1 and D3 powders, D3 powder has approximately 5 times more impact energy. This difference is further increased by the lower density of the D1 powder. This may explain the high peening effect achieved for D3 powders compared to D1 and D2 powders. The effective peening action requires the particles to bounce off the substrate. For this reason, the particle density has a great influence also on the residual stress state as it effects significantly on the whether the particle will stick onto a substrate or not.

This study emphasizes that powder properties such as size distribution and density play an important role in coating quality and the formation of residual stresses coating in high kinetic energy process. Powders of the same nominal composition and only slightly different apparent densities may result in a very different residual stress state. Therefore, it is important to identify powder properties and their effect when selecting WC-CoCr powder for a thermal spray process and when designing the coating performance for the application. The resulting stress state particularly peening effect is significantly dependent on the powder size, powder density, and selected spraying parameters. High compression stresses can be useful in applications, which requires fatigue resistance or cavitation erosion resistance [20, 27, 32]. Peening effect is strongly related to deposition efficiency and to achieve high compressive residual stress it is advisable to choose compact powder, cold parameters. However, in this case DE will be lower. By using a dense powder, high-quality coatings can be obtained which, depending on the coating parameters, are in compressive or tensile stress. In the case of a more porous powder DE is typically higher (with comparable parameters), but the stress state is not so easily controllable by the parameters. Furthermore, care must be taken with respect to the parameters so that the coating properties are not impaired by excessive heating of the particles. Finally, it should be noted that residual stresses are strongly process dependent and similar effects might be impossible to achieve by the process having lower particle velocity and higher temperature and/or more limited temperature-kinetic energy process window.

4. Conclusions

The effect of various WC-10Co4Cr powder on the residual stresses of the coatings sprayed by liquid fuelled high kinetic HVOF processes was studied. The powders differed mainly in their apparent density and particle size distribution. They had same nominal particle size distribution, but measured particle size distribution differed. The coatings were sprayed by using six different spray conditions onto a substrate, which was mounted on the integrated coating property (ICP) -sensor. As the ICP enables accurate in-situ monitoring the curvature and temperature of the sample, it was possible to calculate residual stresses arising from the deposition (peening or quenching stress) and thermal mismatch by using Tsui and Clyne analytical model.

Following conclusions were made from the study:

- Powder properties (apparent density and particle size distribution) have a significant influence on stress states of the high pressure HVOF-sprayed WC-CoCr-coatings. The difference in residual stress arising mainly from powder was approximately 300 MPa.
- Powder density clearly affected on the deposition efficiency (DE) which had a strong correlation with peening stresses. The peening (compressive) stress was higher if the particle bounced off from the substrate instead of sticking onto it. Therefore, denser powder having slightly larger particle size deposited with low DE parameters produced a coating which had clearly highest compressive stresses.
- Deposition stress of the densest powder, D3, was able to be affected strongly by spray parameters. The final residual stresses on the surface of the coating varied approximately 530 MPa depending on spray parameters used for D3 powder.
- The most noticeable effect of powder density was that the melting of porous powder was easier leading to higher DE and therefore compressive stresses could not be developing as much with same parameters, that produced high peening stresses for D3 powders.

CRediT authorship contribution statement

Tommi Varis:Investigation, Conceptualization, Methodology, Visualization, Writing - review & editing.**Tomi Suhonen**:Investigation, Conceptualization, Writing - original draft.**Mika Jokipii**:Investigation.**Petri Vuoristo**:Supervision.

Declaration of competing interest

The authors declare that they have no known competing financial interests or personal relationships that could have appeared to influence the work reported in this paper.

Acknowledgements

The work was supported by DIMECC Ltd, its HYBRIDS programme and Tekes (Finnish Funding Agency for Technology and Innovation). The authors would like to thank Fujimi Corporation, Japan, and DURUM Verschleißschutz GmbH, Germany, for providing powders with necessary information for the study. Authors would like to also thank Jarmo Laakso for performing the SEM microscopy and XRD analysis of the coatings and powders. MSc Varis gratefully acknowledges the personal grant from the K. F. and Maria Dunderberg Testament Foundation (Finland).

References

[1] P. Araujo, D. Chicot, M. Staia, J. Lesage, Residual stresses and adhesion of thermal spray coatings, Surf. Eng. 21 (1) (2005) 35–40.
[2] P. Bansal, P.H. Shipway, S.B. Leen, Effect of particle impact on residual stress development in HVOF sprayed coatings, Proceedings of the International Thermal Spray Conference (2006) 570–575.
[3] L.M. Berger, Application of Hardmetals as thermal spray coatings, Int. J. Refract. Met. Hard Mater. 49 (2015) 350–364.
[4] L.M. Berger, P. Ettmayer, P. Vuoristo, T. Mäntylä, W. Kunert, Microstructure and properties of WC-10%Co-4% Cr spray powders and coatings: part 1. Powder characterization, J. Therm. Spray Technol. 10 (2) (2001) 311–325.
[5] P. Chivavibul, M. Watanabe, S. Kuroda, J. Kawakita, M. Komatsu, K. Sato, J. Kitamura, Development of WC-Co coatings deposited by warm spray process, J. Therm. Spray Technol. 17 (5–6) (2008) 750–756.
[6] P. Chivavibul, M. Watanabe, S. Kuroda, J. Kawakita, M. Komatsu, K. Sato,

J. Kitamura, Effect of powder characteristics on properties of warm-sprayed WC-Co coatings, J. Therm. Spray Technol. 19 (1–2) (2010) 81–88.
[7] P. Chivavibul, M. Watanabe, S. Kuroda, J. Kawakita, M. Komatsu, K. Sato, J. Kitamura, Effects of particle strength of feedstock powders on properties of warm-sprayed WC-Co coatings, J. Therm. Spray Technol. 20 (5) (2011) 1098–1109.
[8] T.W. Clyne, S.C. Gill, Residual stresses in thermal spray coatings and their effect on interfacial adhesion: a review of recent work, J. Therm. Spray Technol., ASM International 5 (1996) 401–418.
[9] A.G. Evans, T.R. Wilshaw, Quasi-static solid particle damage in brittle solids-I. Observations analysis and implications, Acta Metall. 24 (10) (1976) 939–956.
[10] P. Fauchais, G. Montavon, G. Bertrand, From powders to thermally sprayed coatings, J. Therm. Spray Technol. 19 (1–2) (2010) 56–80.
[11] J.R. García, J.E. Fernández, J.M. Cuetos, F.G. Costales, Fatigue effect of WC coatings thermal sprayed by HVOF and laser treated, on medium carbon steel, Eng. Fail. Anal. 18 (2011) 1750–1760.
[12] J.M. Guilemany, J. de Paco, J. Nutting, J.. Miguel, Characterization of the W2C phase formed during the high velocity …, Metall. Mater. Trans. Phys. Metall. Mater. Sci. A 30A (1999) 1913–1931.
[13] N. Huber, J. Heerens, On the effect of a general residual stress state on indentation and hardness testing, Acta Mater. 56 (20) (2008) 6205–6213.
[14] K. Kaneko, K. Higaki, Delamination strength of WC-Co thermal sprayed coating under combined stresses by torsion-tension pin-test method, Proc. Indian Natl. Sci. Acad. 79 (4) (2013) 505–511.
[15] R.K. Kumar, M. Kamaraj, S. Seetharamu, T. Pramod, P. Sampathkumaran, Effect of spray particle velocity on cavitation erosion resistance characteristics of HVOF and HVAF processed 86WC-10Co4Cr hydro turbine coatings, J. Therm. Spray Technol., Springer US 25 (6) (2016) 1217–1230.
[16] S. Kuroda, T.W. Clyne, The quenching stress in thermally sprayed coatings, Thin Solid Films 200 (1) (1991) 49–66.
[17] S. Kuroda, T. Fukushima, S. Kitahara, Significance of quenching stress in the cohesion and adhesion of thermally sprayed coatings, J. Therm. Spray Technol., Springer-Verlag 1 (4) (1992) 325–332.
[18] S. Kuroda, T. Dendo, S. Kitahara, Quenching stress in plasma sprayed coatings and its correlation with the deposit microstructure, J. Therm. Spray Technol. 4 (1) (1995) 75–84.
[19] S. Kuroda, Y. Tashiro, H. Yumoto, S. Taira, H. Fukanuma, S. Tobe, Peening action and residual stresses in high-velocity oxygen fuel thermal spraying of 316L stainless steel, J. Therm. Spray Technol. 10 (2) (2001) 367–374.
[20] M.S. Lamana, A.G.M. Pukasiewicz, S. Sampath, Influence of cobalt content and HVOF deposition process on the cavitation erosion resistance of WC-Co coatings, Wear, Elsevier B.V. 398–399 (December 2017) (2018) 209–219, https://doi.org/10.1016/j.wear.2017.12.009.
[21] C.J. Li, G.J. Yang, Relationships between feedstock structure, particle parameter, coating deposition, microstructure and properties for thermally sprayed conventional and nanostructured WC-Co, Int. J. Refract. Met. Hard Mater. 39 (2013) 2–17.
[22] C.J. Li, G.C. Ji, Y.Y. Wang, K. Sonoya, Dominant effect of carbide rebounding on the carbon loss during high velocity oxy-fuel spraying of Cr3C2-NiCr, Thin Solid Films 419 (1–2) (2002) 137–143.
[23] W. Luo, U. Selvadurai, W. Tillmann, Effect of residual stress on the wear resistance of thermal spray coatings, J. Therm. Spray Technol., Springer US 25 (1–2) (2016) 321–330.
[24] W.G. Mao, J. Wan, C.Y. Dai, J. Ding, Y. Zhang, Y.C. Zhou, C. Lu, Evaluation of microhardness, fracture toughness and residual stress in a thermal barrier coating system: a modified Vickers indentation technique, Surf. Coatings Technol. 206 (21) (2012) 4455–4461.
[25] J. Matejicek, S. Sampath, D. Gilmore, R. Neiser, In situ measurement of residual stresses and elastic moduli in thermal sprayed coatings part 2: processing effects on properties of Mo coatings, Acta Mater. 51 (3) (2003) 873–885.
[26] V. Matikainen, G. Bolelli, H. Koivuluoto, M. Honkanen, M. Vippola, L. Lusvarghi, P. Vuoristo, A study of Cr3C2-based HVOF- and HVAF-sprayed coatings: microstructure and carbide retention, J. Therm. Spray Technol. 26 (6) (2017) 1239–1256.
[27] V. Matikainen, S. Rubio Peregrina, N. Ojala, H. Koivuluoto, J. Schubert, Houdková, P. Vuoristo, Erosion wear performance of WC-10Co4Cr and Cr3C2-25NiCr coatings sprayed with high-velocity thermal spray processes, Surf. Coatings Technol., Elsevier 370 (August 2018) (2019) 196–212.
[28] R.C. Souza, H.J.C. Voorwald, M.O.H. Cioffi, Fatigue strength of HVOF sprayed Cr3C2-25NiCr and WC-10Ni on AISI 4340 steel, Surf. Coatings Technol., Elsevier 203 (3–4) (2008) 191–198.
[29] Y.C. Tsui, T.W. Clyne, An analytical model for predicting residual stresses in progressively deposited coatings: part 1: planar geometry, Thin Solid Films, Elsevier 306 (1) (1997) 23–33.
[30] Y.C. Tsui, T.W. Clyne, An analytical model for predicting residual stresses in progressively deposited coatings: part 3: further development and applications, Thin Solid Films 306 (1) (1997) 52–61.
[31] T. Varis, T. Suhonen, A. Ghabchi, A. Valarezo, S. Sampath, X. Liu, S.P. Hannula, Formation mechanisms, structure, and properties of HVOF-sprayed WC-CoCr coatings: an approach toward process maps, J. Therm. Spray Technol. 23 (6) (2014) 1009–1018.
[32] T. Varis, T. Suhonen, O. Calonius, J. Čuban, M. Pietola, Optimization of HVOF Cr3C2-NiCr coating for increased fatigue performance, Surf. Coatings Technol., Elsevier B.V. 305 (2016) 123–131.
[33] C. Verdon, A. Karimi, J.L. Martin, Microstructural and analytical study of thermally sprayed WC-Co coatings in connection with their wear resistance, Mater. Sci. Eng. A 234–236 (1997) 731–734.
[34] S. Watanabe, J. Amano, T. Tajiri, N. Sakoda, Fatigue cracks in HVOF thermally sprayed WC-Co coatings, J. Therm. Spray Technol. 7 (1) (1998) 93–96.
[35] X.C. Zhang, B.S. Xu, H.D. Wang, Y.X. Wu, Effect of graded interlayer on the mode I edge delamination by residual stresses in multilayer coating-based systems, Appl. Surf. Sci. 254 (7) (2008) 1881–1889.
[36] S. Zimmerman, H. Keller, Just one prediction for the success of the coating, 8th Kolloquium HVOF Spraying 2009, Erding, 2009, pp. 167–173.

PUBLICATION IV

Evaluation of residual stresses and their influence on cavitation erosion resistance of high kinetic HVOF and HVAF-sprayed WC-CoCr coatings

T. Varis, T. Suhonen, J. Laakso, M. Jokipii, p. Vuoristo

Journal of Thermal Spray Technology, May 2020
DOI: 10.1007/s11666-020-01037-2

J Therm Spray Tech (2020) 29:1365–1381
https://doi.org/10.1007/s11666-020-01037-2

PEER REVIEWED

Evaluation of Residual Stresses and Their Influence on Cavitation Erosion Resistance of High Kinetic HVOF and HVAF-Sprayed WC-CoCr Coatings

Tommi Varis[1] · Tomi Suhonen[2] · Jarmo Laakso[1] · Mika Jokipii[3] · Petri Vuoristo[1]

Submitted: 25 November 2019 / in revised form: 6 March 2020 / Published online: 14 May 2020

Abstract Thermal spray processes have been developing toward lower particle temperature and higher velocity. Latest generation high-velocity oxygen-fuel (HVOF) and high-velocity air-fuel (HVAF) can produce very dense coating structures due to the higher kinetic energy typical for these thermal spray processes. Thermally sprayed coatings usually contain residual stresses, which are formed by a superposition of thermal mismatch, quenching and, in case of high kinetic energy technologies, peening stresses. These stresses may have a significant role on the mechanical response and fatigue behavior of the coating. Understanding these effects is mandatory for damage tolerant coating design and wear performance. For instance, wear-resistant WC-CoCr coatings having high compressive stresses show improved cavitation erosion performance. In this study, comparison of residual stresses in coatings sprayed by various thermal spray systems HVOF (Thermico CJS and Oerlikon Metco DJ Hybrid) and HVAF (Kermetico AcuKote) was made. Residual stresses were determined through thickness by utilizing Tsui and Clyne analytical model. The real temperature and deposition stress data were collected in the coating process by in situ technique. That data were used for the model to represent realistic residual stress state of the coating. The cavitation erosion and abrasion wear resistance of the coatings were tested, and relationships between residual stresses and wear resistance were discussed.

Keywords cavitation-resistant coatings · fracture toughness · HVAF · HVOF · in situ monitoring · residual stresses · WC-CoCr

Introduction

The unique droplet-by-droplet manufacturing process of thermally sprayed coatings may generate relatively high residual stresses, which are necessary to understood and controlled well to avoid residual stresses causing failures during the coating manufacturing process or in use (Ref 1-3). Some of the latest high kinetic thermal spray processes, such as high-pressure high-velocity oxygen-fuel (HVOF) or high-velocity air-fuel (HVAF), typically produce lower flame temperatures and higher particle velocities compared to traditional HVOF spray devices (Ref 4). The temperature-velocity conditions of the spray particles certainly have a major influence on the coating residual stresses, whose effect on the wear performance is of interest. There have been numerous studies on the effect of residual stresses on interfacial adhesion, wear resistance, and fatigue performance of HVOF and HVAF coatings. Luo et.al. showed that the wear resistance decreased in adhesive wear test (pin-on-disk, POD) when coating tensile stresses grew with increased coating thickness (Ref 5). Studies on fatigue resistance of coatings have shown that the effect of HVOF-

This article is part of a special topical focus in the *Journal of Thermal Spray Technology* on Advanced Residual Stress Analysis in Thermal Spray and Cold Spray Processes. This issue was organized by Dr. Vladimir Luzin, Australian Centre for Neutron Scatte

✉ Tommi Varis
tommi.varis@tuni.fi

[1] Materials Science and Environmental Engineering, Tampere University Ringgold Standard Institution, Korkeakoulunkatu 6, P.O. Box 589, Tampere 33014, Finland

[2] Material Modeling and Ecodesign, VTT Technical Research Centre of Finland, Espoo, Finland

[3] Nuclear Reactor Materials, VTT Technical Research Centre of Finland, Espoo, Finland

sprayed carbide coatings may have either positive or negative influence on fatigue life of steel. (Ref 6-9) Positive influence on the fatigue life has been observed with coatings that have been in high compressive residual stresses caused by spray particle shot peening, which is shown to play an important role in preventing the crack initiation within the coating or at the interface between the coating and the substrate (Ref 8). Good cavitation erosion resistance of HVAF coatings has been reported in several other studies, in which this was proposed to be mainly related to the high kinetic energy of the particles (Ref 10-12). Studies on cavitation erosion resistance of WC-CoCr has shown that erosion of HVAF coatings takes place by the mechanism of fatigue crack growth, preferably along the weak lamella boundaries. Continuous impacts resulted in crack propagation, crack growth and material removal in larger blocks. It has been discussed that compressive residual stresses hinder the crack growth and positively influence cavitation erosion resistance of the thermally sprayed coatings (Ref 13-15). However, the residual stresses of coatings have been determined with adequate precision only in few studies yet, thus being able to link the residual stresses to wear performance. This may be attributed to the general limitations on experimental measurements of residual stresses in thermally spray coatings, since the origins of residual stresses are known to be relatively complex.

The origins of residual stresses regarding the coating process are well known (a) quenching stresses, (b) peening stresses, and (c) thermal mismatch stresses. Quenching stresses are tensile (−) and generate from the rapid shrinkage and contraction of the splats during the formation stage of the coating from these splats. Peening stresses are compressive (+) and are known to be originated from the high-velocity impacts of the particles resulting in plastic deformation of the substrate and/or previously deposited coating material. As the quenching stresses and peening stresses generate during the deposition stage, they are referred hereafter to as deposition stresses separated by negative or positive sign, respectively. Thermal mismatch stresses generate in the post-deposition cooling stage due to material mismatch between the coating and the substrate which have different coefficients of thermal expansion (CTE) (Ref 3, 16-21).

Several methods can be used for residual stress measurement and/or estimation. Typically, layer removal techniques, hole thrilling method, bending techniques, x-ray diffraction and neutron diffraction are used as experimental methods in the case of thermally sprayed coatings as well as computational models. All of these methods are useful but have some limitations (Ref 22). By conventional laboratory x-rays only a low depth from the sample surface can be measured. Therefore, determination of through thickness residual stress profiles requires progressive mechanical or chemical layer removal, which makes the measurement of depth profiles time consuming. Furthermore, only crystalline phases, with known elastic parameters can be measured, although coatings often include also amorphous phases. Neutron diffraction method requires relatively thick coatings and is an expensive method. Hole drilling method is one of the most commonly used due to its simplicity, portability and ability to track residual stress variation with depth. Accuracy of the hole drilling method as well as layer removal method is dependent on which calibration coefficients are used; these calibration coefficients of the inhomogeneous coatings do not often exist. The accuracy of hole drilling method for thermally sprayed coatings has been further improved by utilizing finite element analysis to determine the required calibration coefficients (Ref 22-27)

In situ curvature method, by which the coating substrate curvature is measured during spraying, is the only method, which can track the origin of the all residual stresses; quenching or peening, and thermal mismatch (Ref 22). The main limitation of the curvature method is, that the curvature data is not simple to transform into coating stresses. Stoney (Ref 28) or Brenner and Senderoff (Ref 29) equations have been used in many cases for the residual stress estimation although these methods have some assumptions and the accuracy is therefore arguable. Tsui and Clyne (Ref 30) have developed their analytical model to determine residual stresses through thickness for progressively deposited coatings. The model combines quenching or peening and thermal mismatch stresses. However, it requires the deposition stresses and temperature data from the deposition process as input parameters (Ref 22, 24, 31-34).

In the present study, the residual stress state of WC-CoCr coatings produced by various high kinetic thermal spray processes was compared by using the Tsui and Clyne model. In combination with in situ curvature technique, which can be used to determine the deposition stresses and measure the temperatures, a realistic estimation of through thickness stresses can be achieved. The main subject of this study is to address the effect of stress state on the cavitation erosion resistance of HVAF- and high-pressure HVOF-sprayed WC-CoCr coatings, which has been found to be particularly good. Additively, abrasion wear resistances of the coatings were studied less extensively in order to compare the effect of differently coatings under exposing another type of wear mechanism. In addition, the abrasion resistance of coatings was investigated less extensively to compare the durability of differently processed WC-CoCr coatings under another type of wear mechanism.

Experimental

Spraying of the Coatings

WC-10Co4Cr powder from Durum Verschleiss-Schutz GmbH, Krefeld, Germany was used for the sprayings with AcuKote-07 (AK7) HVAF device (Kermetico Inc., Benicia, CA, USA), and Thermico Carbide Jet Spray (CJS) high-pressure HVOF device (Thermico GmbH & Co, Dortmund, Germany) The feedstock used was an agglomerated and sintered powder with a nominal size distribution of 5-25 μm, which had a nominal size of 0.4 micron WC-particles in the CoCr matrix. For spraying with Diamond Jet Hybrid 2700 (DJH 2700) spray device (Oerlikon-Metco, Westbury, NY, USA) the similar type of WC-10Co4Cr powder from Durum was used. This powder had nominal particle size distribution 15-36 μm, and the nominal carbide size was 0.4 μm too.

Spray parameters for the Diamond Jet Hybrid 2700 (later HVOF 1) process were selected based on the recommendation of the equipment manufacturer. For the Thermico Carbide Jet Spray (later HVOF 2), three parameters (HVOF 2A, 2B, and 2C) with different kerosene levels, 14, 16, and 18 $m^3\ h^{-1}$ were selected. Kerosene flow is known to affect the flame temperature strongly. Kerosene level alteration was compensated with oxygen adjustment targeting to maintain combustion chamber pressure and this way keep the particle velocity relatively constant. For the AcuKote HVAF (later HVAF) process, the operating window for the adjustment of fuel-oxygen - ratio was relatively limited. Therefore, particle conditions were to be affected by increasing the pressures of the gases fed to the HVAF gun and hence keeping the ratio in the accessible range. This increases the chamber pressure, which is expected to give the particles higher velocity (shorter dwell time) and higher temperatures. Three parameters were selected for HVAF (HVAF A, B, and C), which had increasing chamber pressures. The spray parameters are presented in Table 1. Particle temperature and velocity (Table 1) were measured with Spray Watch 2i (Oseir Oy, Tampere, Finland) in case of both HVOF processes and Spray Watch 4i (Oseir Oy, Tampere, Finland) in case of HVAF, which confirmed that parameter adjustments affect the particles as earlier presented.

The coatings were deposited on S355 low carbon steel flat bars of 228.6 mm in length, 25.4 mm in width, and 2.5 mm thick, which were grit blasted on both sides by using the size of 500-700 μm corundum particles. Gun traverse speed of 1 m s^{-1} and step width of 4 mm was used. Deposition was evaluated in situ using in-situ coating property (ICP) sensor (Ref 2) by ReliaCoat Technologies, East Setauket, NY, USA. The ICP sensor measures the temperature and curvature of the substrate beam during spraying. Details of the technology are given below.

Characterization of Microstructure and Mechanical Properties

The polished cross-sectional samples of the coatings and worn surfaces in the erosion test were characterized with a Zeiss ULTRA plus field-emission scanning electron microscope (Carl Zeiss AG, Oberkochen, Germany) using accelerating voltage of 15 kV. The porosities of the coatings were measured from the backscatter images using ImageJ software. The lateral depth of the surface craters after the wear tests was analyzed from the $0.81 \times 0.81\ mm^2$ area with an optical profilometer (InfiniteFocus G5, Alicona Imaging GmbH, Austria). The phase compositions of the coatings were determined by x-ray diffractometry (XRD: Empyrean, PANalytical, Netherlands) using Cu-Kα radiation (1.5406 Å, 40 kV and 45 mA). Phase identification was done with HighScorePLUS software (PANalytical, Netherlands). Coating hardness and elastic modulus were measured using an instrumented indenter (Zwick ZHU 0.2, Zwick-Roell, Ulm, Germany) with a Vickers tip. Hardness and indentation modulus were measured on the polished cross sections at a load of 300 g. Ten indentations were performed on each coating. Elastic modulus was calculated from the load-displacement data taken from the indentations at the coating cross section following the procedure proposed by Oliver and Pharr (Ref 35). For fracture toughness determination, ten indents were taken on polished cross sections at a load of 5 kg. Corner crack lengths of the indents were analyzed by optical microscopy, and the fracture toughness's were calculated by the equation proposed by Lankford (1) (Ref 36):

$$K_{IC} = 0,0363(E/HV)^{\frac{2}{5}} \cdot \left(P/a^{1.5}\right) \cdot (a/c)^{1.56}, \qquad \text{(Eq 1)}$$

where E is indentation modulus with 0.3 kg, HV is Vickers hardness with 0.3 kg, P is indentation load, a is half-length of the indentation diagonal and, c is average crack length measured from the center of the imprint of the indent. Equation 1 is valid for both crack modes: radial cracks (known as Plamqvist cracks) formed radially from the corners of the imprint and median cracks formed with higher loads under the pyramid tip.

Wear Tests

Cavitation erosion tests were performed with an ultrasonic transducer (VCX-750, Sonics & Materials, USA) according to the ASTM G32-16 standard for indirect cavitation erosion. The vibration tip was an alloy of Ti-6Al-4 V and

Table 1 Spray parameters used for the deposition of the coatings, corresponding particle temperature and velocity, and resulting coating thicknesses

	HVOF 1	HVOF 2 A	HVOF 2 B	HVOF 2 C	HVAF A	HVAF B	HVAF C
Propane pressure, kPa	…	…	…	…	517	600	676
Propane flow, L min^{-1}	…	…	…	…	94	106	134
Air pressure, kPa	…	…	…	…	648	758	827
Kerosene flow, m^3 h^{-1}	…	14	16	18	…	…	…
Oxygen flow, L min^{-1}	215	960	940	920	…	…	…
Air flow, L min^{-1}	350				…	…	…
Hydrogen flow, L min^{-1}	635	80	80	80	35	35	35
Nitrogen flow, L min^{-1}	15	16 + 16	16 + 16	16 + 16	35	35	35
Chamber pressure, kPa	538	1358	1338	1331	469	545	600
Stand off distance, mm	230	200	200	200	250	250	250
Particle temperature, °C	1867	1643	1732	1785	1500	1510	1630
Particle velocity, m s^{-1}	621	844	872	851	798	835	908
Powder feed rate, g min^{-1}	40	69	68	67	95	94	97
Thickness, µm	350	275	340	370	380	330	310
Number of passes	26	34	34	34	30	30	30

tip diameter was 13 mm. In the test, the frequency was 20 kHz, amplitude 50 µm. Samples were attached at 0.5 mm distance of the transducer and water temperature was kept at 25 °C. The coating surfaces were ground flat and polished with a polishing cloth and 3 µm diamond suspension to produce a mirror finish. Samples were cleansed in an ultrasonic bath with ethanol, dried, and weighed after 0, 2, 4, and 6 h. Volume loss rate (mm^3 - min^{-1}) was determined from the cumulative volume loss curve by using linear fitting. The material densities used for calculating the volume losses from the weight losses was 14.6 g cm^{-1}. The volume losses were further divided by the tip area of 123 mm^2 and multiplied by a 1000 to get the maximum rate of erosion (µm h^{-1}).

Rubber wheel abrasion tests were performed according to ASTM G65 procedure *D*. Prior to testing samples were ground to a surface finish of Ra 0.3. Samples were placed in contact against a rubber wheel at a static force of 45 N. A rubber wheel of 227 mm diameter was used at 200 rpm for a total sliding distance of 4.279 m (6.000 revolutions). The quartz sand used consisted of rounded particles with an average size between 212 and 300 µm. Sand mass flow rate was 270 g min^{-1}. One sample per coating was tested.

Determination of Residual Stresses

An ICP-sensor monitors the curvature and temperature of a flat bar sample during the deposition process. Three lasers in the center and 45 mm from the both ends of the beam detect the curvature. A simultaneous measurement of temperature was recorded via multiple thermocouples. Laser data was converted to the sample curvature, which can be used to determine the stresses evolved during deposition and cooling. Average deposition stresses and thermal mismatch stresses inside the coating was calculated by Brenner and Senderoff's equation (Ref 29) for thick coatings (2):

$$\sigma_c = \frac{E_s' t_s \left(t_s + \beta^{1.25} dt_c\right)}{6 dR dt_c}; \beta = \frac{E_c'}{E_s'} \quad \text{(Eq 2)}$$

where σ_c is the average stress in the coating, E_c' is the in-plane modulus of the coating, E_s' is in-plane modulus of the substrate, t_s is thickness substrate and dR is change in radius caused by deposition of layer thickness dt_c. Deposition stresses were calculated from the initial curvature (0) to the curvature, which exists immediately after deposition, while the thermal stresses were calculated from the end of spraying to the cooling down of the substrate-coating system to final curvature at 30 °C. The final average stress in the coating is the sum of the deposition stresses and thermal mismatch stresses. The material-specific values for WC-CoCr and steel, which were used to calculate the stresses with Eq 2-5 are presented in Table 2.

Residual stress distribution in the coating was determined by Tsui-Clyne analytic model. Compared to the Brenner and Senderoff's equation, it results in through thickness residual stress data. In addition, the effect of varying substrate temperatures on the residual stresses can be considered. In the following it will be only explained how the model was used in the scope of this study, while the complete description of the model can be found in its original source (Ref 30). The model considers the

Table 2 Material-specific values for WC-CoCr and steel used for calculations

	Steel substrate	WC-CoCr coating
Young's modulus, GPa	200	In Table 4
Coefficient of thermal expansion, 10^{-6} C^{-1}	11	5.2[a]
Poisson's ratio	0.3	0.22

[a]Ref 40

deposition stresses generated by each individual coating layer, as well as the stresses caused by the different thermal expansion coefficients of the coating and substrate. The model determines the stress in the middle of the coating layer and can be calculated between the first and last coating layers ($1 < j < n$). For example deposition stress in the middle of the n[th] layer (last deposited layer) can be calculated by using formula (3) (Ref 30):

$$\sigma_{\mathrm{dn}} = \frac{F_n}{bw} - E_{\mathrm{d}}(\kappa_n - \kappa_{n-1})\left(\left(n - \frac{1}{2}\right)w - \delta_n\right), \qquad \text{(Eq 3)}$$

where F_n = normal force, b = beam width, w = layer thickness, E_{d} = Young's modulus of the deposit, $\kappa_n - \kappa_{n-1}$ = curvature change due to the deposition of layer n, δ_n = location of neutral axis. Each deposited layer causes deposition stresses, either being of peening or quenching nature, which either increases or decreases the stresses of underlying layers, respectively. The stress of these layers are added to the underlying layer by superposing the effect of each following layer by (4) (Ref 30):

$$\sigma_i = \sum_{i=j+1}^{n}\left(\frac{-E_{\mathrm{d}}F_i}{b(HE_{\mathrm{s}} + (i-1)wE_{\mathrm{d}})} - E_{\mathrm{d}}(\kappa_i - \kappa_{i-1})\left(j - \frac{1}{2}\right)w - \delta_{\mathrm{l}}\right), \qquad \text{(Eq 4)}$$

where $1 < j < n$, E_{s} = Young's modulus of the substrate and H = thickness substrate. The normal force (F_n) for each layer in Eq 3 and normal force (F_i, found by replacing n with i) in Eq 4 for following layers is calculated by using Eq 5 (Ref 30):

$$F_n = \sigma_{\mathrm{d}} bw\left[\frac{HE_{\mathrm{s}} + (n-1)wE_{\mathrm{d}}}{HE_{\mathrm{s}} + nwE_{\mathrm{d}}}\right], \qquad \text{(Eq 5)}$$

where term σ_{d} is the deposition stress, which is needed to be determined in order to further calculate the stresses in each layer. In this case, an iteration process described by Tsui and Clyne (Ref 37) was used, in which the deposition stresses were adjusted as such, that the measured curvatures from the ICP sensor and the curvatures from the Tsui and Clyne model were equal. Only that part of the curvature curve was used, where the temperature was constant, and curvature caused by each pass was changing relatively linearly. In practice, this meant curvature change between the passes 5 and 25.

Stresses due to CTE mismatch can be determined if the decline in temperature, the specimen dimensions, the Young's modulus and the CTEs of the materials are known from Eq 6 (Ref 30):

$$\sigma_{\mathrm{CTE}} = \frac{F_{(\mathrm{CTE})}}{bh} - E_{\mathrm{d}}(\kappa_j - \kappa_n)\left(\left(j - \frac{1}{2}\right)w - \delta_n\right) \qquad \text{(Eq 6)}$$

where $F_{(\mathrm{CTE})}$ is a balancing force due to CTE mismatches, and other symbols as earlier. The calculation of the thermal mismatch stresses can be found more detailed in the original source (Ref 30).

Finally, the stress in the middle of each coating layer was calculated by superposing the stresses from (a) the layer in question, (b) stresses caused by layers deposited after layer in question, and (c) thermal mismatch stresses during the cool down. In these calculations, the only modification on the original procedure was that the actual temperature before each pass was used instead of a constant temperature. The temperature was recorded by ICP from the back of the flat steel bar. This allows capturing the effect of altering temperature on the residual stress profile. Often at the beginning of the spray process the temperature increases until it stabilizes on a certain level for the rest of the deposition.

As a summary, in this case the residual stresses distribution inside the coatings was determined by using Tsui and Clyne analytical model with following procedure: (a) The deposition stresses either quenching or peening were determined by iterating the deposition stress by using the real curvature data from the ICP, (b) through thickness stresses were calculated for progressive deposited coatings (Eq 3, 4, and 5), (c) the temperature data before each coating layer was used for the calculation of the thermal mismatch stresses (Eq 5) and (d) stresses from (b) and (c) were superposed.

Results

Coating Microstructures and Phase Compositions

The microstructures of the coatings with the measured porosity in the upper right corner of the image are shown in Fig. 1. Coatings HVOF 2 and HVAF are very dense and only some minor micro-porosity in the coatings can be

detected. Although the porosity of all coatings is relatively low, there is a clear difference in pore size and location between HVAF/HVOF 2 and HVOF 1 coatings. In HVAF and HVOF 2 coatings, the pores are small and evenly distributed in the coating structure. HVOF 1 coating clearly has larger size pores and some microcracking, which are concentrated on interlamellar region. HVAF coatings are the densest and have a lower porosity as the particle velocity increases. Regarding to HVOF 2 process, it can be stated that the coldest spraying parameter (*A*) does not sufficiently compact the initial porosity of the powder which has remained in the coating structure.

Further observations on coating structures can be made based on the XRD analysis and contrast differences. There are two mechanisms for WC-CoCr coatings, which change the coating microstructure. These can be detected either from the microstructure or from the XRD: (a) carbon loss reactions and (b) dissolution of carbide into a liquid matrix. In general, heavier elements appear brighter in SEM backscattering images. Thus, dissolution of W can be estimated to some extent from contrast differences. Carbon loss results in a formation of W_2C on the surface of original WC, which is detectable by XRD. In all the coatings, some of the WC is dissolute into the matrix, which appears lighter after intake of tungsten. In HVAF process, due to lower flame temperature and longer residence time compared to HVOF 2 process particles the particles have heated more evenly and coatings shows relatively homogenous microstructure and no major differences between parameters A, B, and C was found. The HVOF 2 coatings are more inhomogeneous compared to the HVAF coatings. Carbide dissolution into the matrix seems to be more concentrated on the surface of the particles, which causes the visible concentration difference between the inner and outer regions of the lamellae. In the HVOF 1, coating significant amount of carbide dissolution was evident in the microstructure and small carbides are missing inside the microstructure. The W_2C peak in Fig. 2 (location of $2\theta = 40°$) for HVOF 1 coating the highest among all coatings. Other coatings contained an increasing amount of W_2C with the increasing measured particle temperature resulting from decarburization process, but to such an extent that it has no significant effect on the coating properties. Other observations from the XRD are that the HVOF 2A coating has either a visible Co_3W_3C- or Co/Cr-peak (location of $2\theta = 42.7°$), which most probably originates from the powder, and shows that the heating of the particles during the deposition of HVOF 2A coating has been the lowest among all coatings. For all of the coatings except for HVOF 2A, there was also a notable increase in the background intensity between 2θ angles 35° and 45°, from the formation of amorphous and nanocrystalline phases due to carbide dissolution can be inferred (Ref 38).

Curvature and Temperature Measurements and Calculated Residual Stresses

Table 3 presents the deposition stress, thermal mismatch stresses and final residual stresses at the surface of the coating evaluated by Tsui and Clyne model and average residual stresses by Brenner and Senderoff equation. The temperature and curvature curves from the ICP device are presented in Fig. 3 and corresponding residual stresses at the coating surface according to Tsui and Clyne-model in Fig. 4. Through thickness residual stresses of the coatings by Tsui and Clyne analytical model are given in Fig. 5.

The coating HVOF 1 shows the increasing convex (positive) curvature during spraying, which means that negative deposition stresses (tensile quenching stresses) are dominating during the spraying process. During the cool down, the beam convexity decrease and the coating shifts toward a lower tensile stress state. After the cool down, the beam is still convex and final residual stress in HVOF 1 coating is tensile, compare Figs. 3 and 4. The average residual stress in the coating by Brenner and Senderoff equation was + 166 MPa. Tsui and Clyne through thickness residual stress profile shows increasing tensile stress toward the coating surface as the thickness increases. The residual stress on the surface was + 299 MPa for HVOF 1 process.

In contrast to HVOF 1, HVOF 2 and HVAF processes produced negative or very slight positive curvature during the deposition stage, which shows that compressive deposition stresses were mainly dominant. Post-deposition thermal mismatch stresses for HVOF 2 developed similarly as for HVOF 1 and are almost constant across variations. For HVAF, thermal mismatch stresses were higher due to the higher deposition temperature and decreased with rising particle velocity. The final average residual stresses determined by Brenner and Senderoff equation varied from − 404 to − 652 MPa for HVOF 2 and from − 422 to − 965 MPa for HVAF. The residual stress on the surface of HVOF 2 and HVAF coatings according to Tsui and Clyne model were highly compressive varying from − 281 to − 586 MPa and − 289 to − 628 MPa, respectively.

As it is shown in Table 1, the particle temperatures in the HVOF 2 process were higher, when the kerosene level was increased, while the particle velocities were comparable. Having higher kerosene flows causes higher flame temperature, which heats up the substrates more and thus results in higher thermal mismatch stress during cool down. From the HVOF 2 curvature changes in Fig. 3, lower particle temperatures increase the peening effect during the deposition as a negative curvature change is developing in the HVOF 2B and 2A coatings. For the HVOF 2 coatings it was evident that a lower flame temperature correlates with higher developed compressive deposition stresses, which is

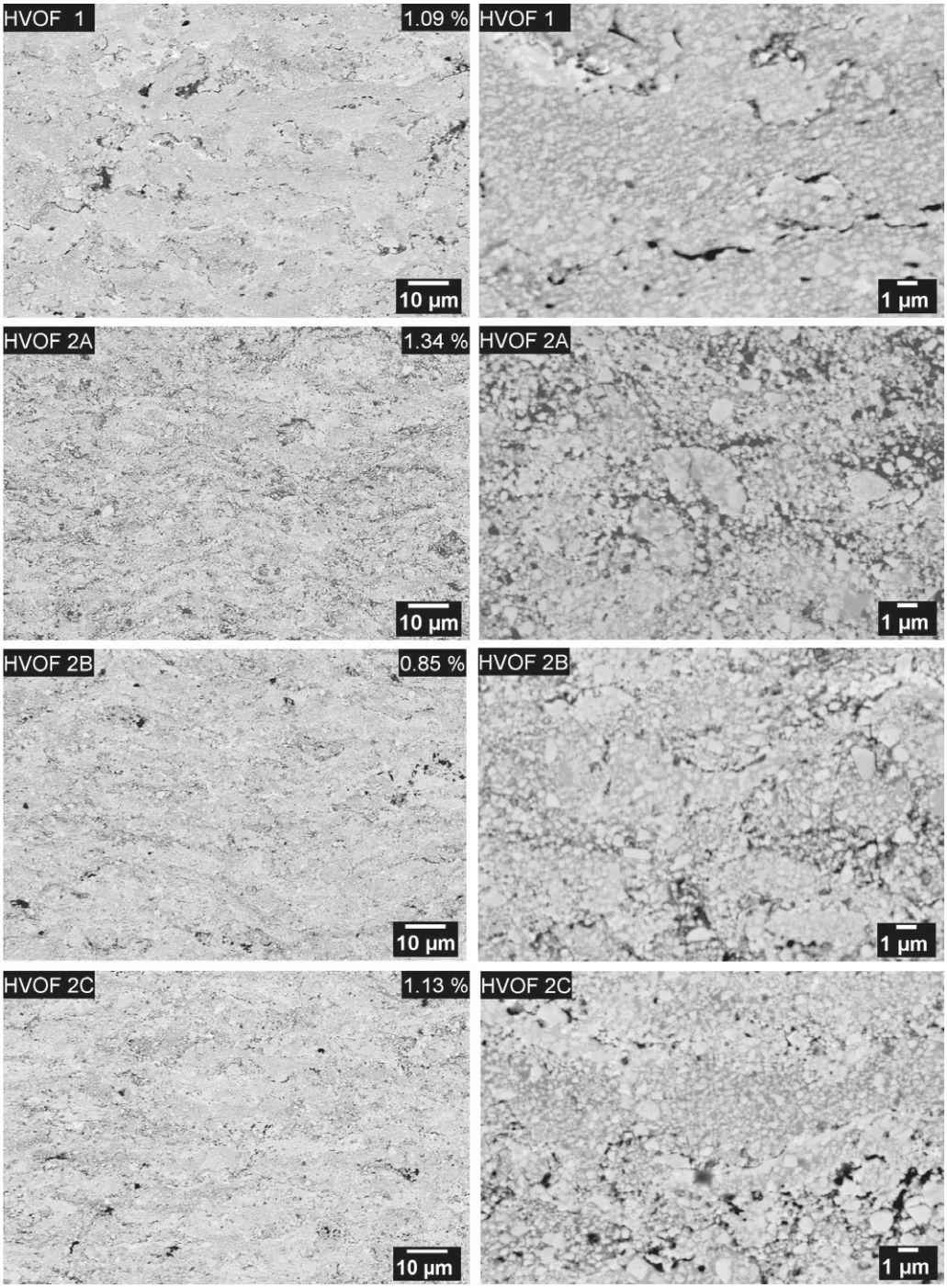

Fig. 1 Microstructures of the coatings by scanning electron microscope with backscatter detector. Porosity, if measured, in the upper right corner of the image

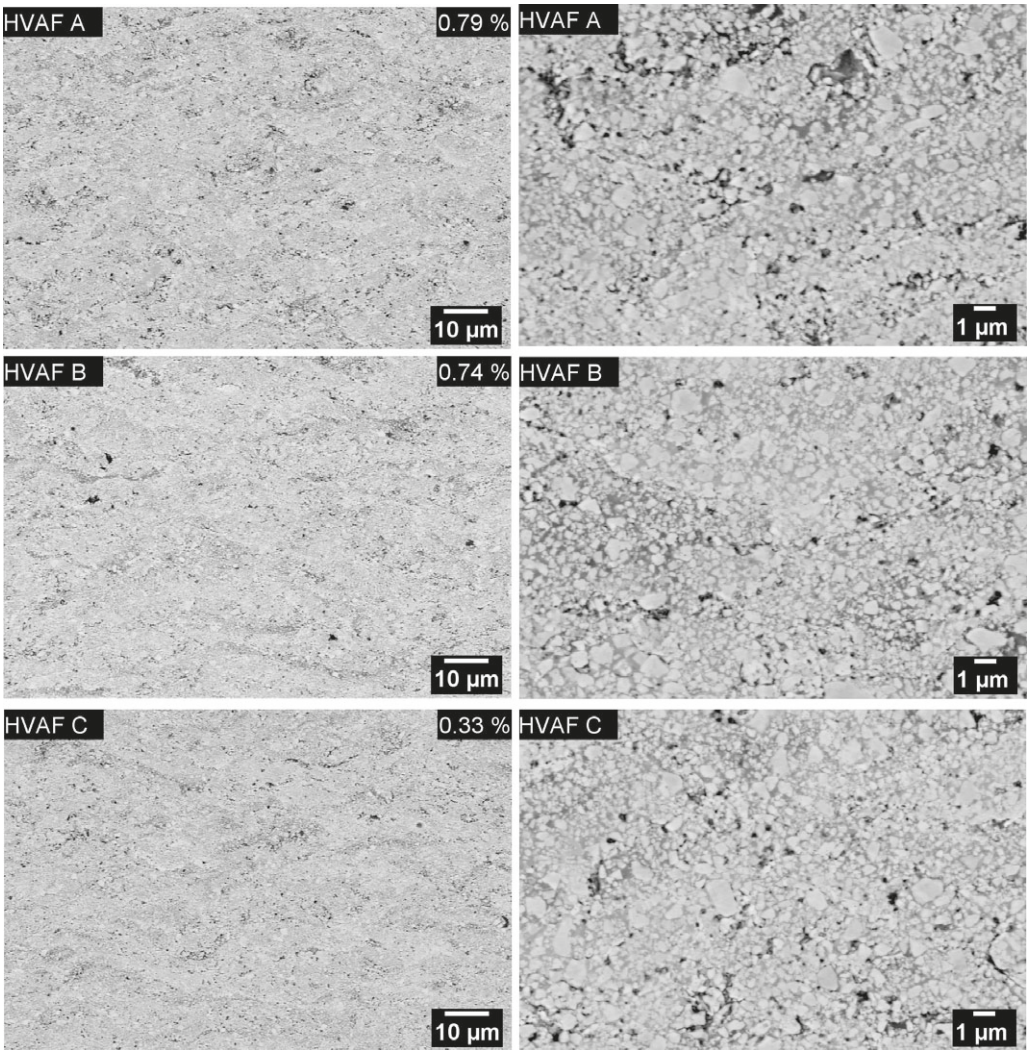

Fig. 1 continued

summarized in Fig. 4. It was noticed that the HVOF 2A coating had the highest amount of positive deposition stresses (peening stresses) among all coatings.

In the HVAF deposition (Fig. 3), rapid curvature changes to a positive direction during the first 4-5 passes were seen, which can obviously be attributed to a simultaneous temperature increase. The effect of the temperature during early passes on the residual stresses can be seen in through thickness residual stress profile in Fig. 5. It shows lower compressive stresses for the first passes than for subsequent passes. For HVAF, the particle temperature and velocity both increased from parameters A to B to C. From the curvature curves in Fig. 3 and Brenner and Senderoff presentation in Table 3 for HVAF, lowest particle T and v parameter (HVAF A) produces tensile deposition stresses while the highest T and v parameter (HVAF C) results in compressive deposition stress.

Mechanical Properties and Wear

Mechanical properties and wear resistances of the coatings are shown in Table 4. Hardness and elastic modulus are clearly the highest for the HVAF coatings and relatively similar for the both HVOF coatings. Fracture toughness

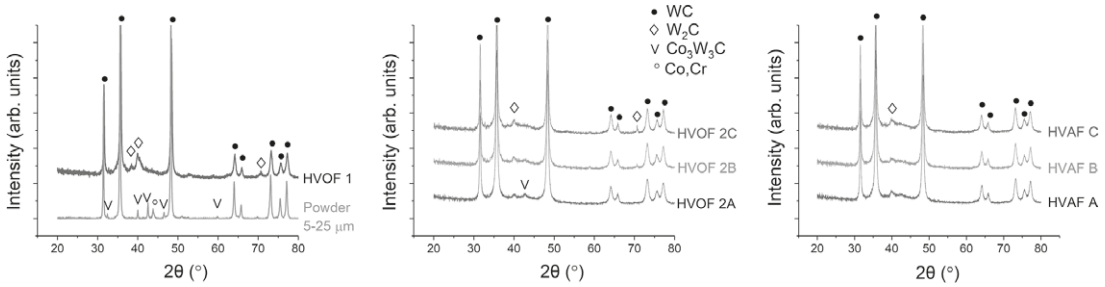

Fig. 2 XRD patterns of the coatings

Table 3 Average residual stresses of the coatings by Brenner and Senderoff (B&S) approximation, and surface residual stresses by Tsui and Clyne (T&C) model (+ tensile and − compressive)

Coating	Deposition stress, MPa		Thermal mismatch stress, MPa		Final residual stress, MPa	
	T&C (on surface)	B&S (average)	T&C (on surface)	B&S (average)	T&C (on surface)	B&S (average)
HVOF 1	+ 553	+ 498	− 254	− 332	+ 299	+ 166
HVOF 2 A	− 369	− 302	− 217	− 349	− 586	− 652
HVOF 2 B	− 181	− 129	− 225	− 364	− 406	− 493
HVOF 2 C	− 61	− 24	− 219	− 381	− 281	− 404
HVAF A	+ 18	+ 147	− 307	− 568	− 289	− 422
HVAF B	− 121	+ 1.1	− 373	− 711	− 494	− 710
HVAF C	− 192	30.5	− 436	− 995	− 628	− 965

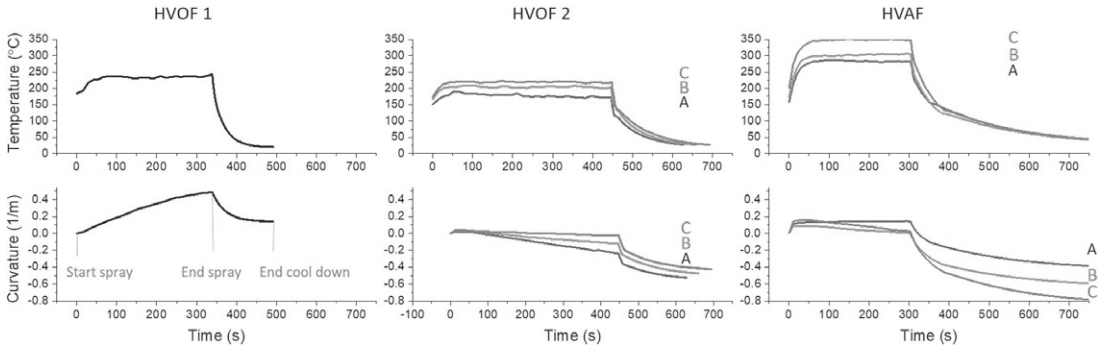

Fig. 3 Temperature and curvature of the deposited samples measured in situ by ICP-sensor

results with 5 kg loads show significant differences between coatings. The best coatings, HVAF 2B, HVOF 2C and HVAF A, had very good fracture toughness's while HVAF B and C had surprisingly low fracture toughness's. HVAF B and C coatings had crack lengths typical of "half-penny"-type cracking while other coatings had crack lengths typical of Palmqvist type cracking. The abrasion wear resistances of the coatings, in Fig. 6(b), did not vary significantly, while significant differences in the cavitation erosion resistance was evident in Fig. 6(a). Compared to the HVOF 1 coatings, of HVOF 2 coatings had 4-5 times and HVAF coatings even 7-11 times better cavitation erosion resistances.

SEM studies revealed a clear difference in remained non-eroded surface areas of the eroded surfaces of coatings depending on the spray method used as shown in Fig. 7. Coatings sprayed by HVAF process had large amount of non-eroded surface after the 6 h of erosion and HVOF 2 coatings had some. HVOF 1 coatings surface was almost completely eroded. It was clear that at the areas where the surface of the coating had the appearance of an original polished surface there were no signs of matrix or carbide removal. In the worn, area fractured surfaces and already

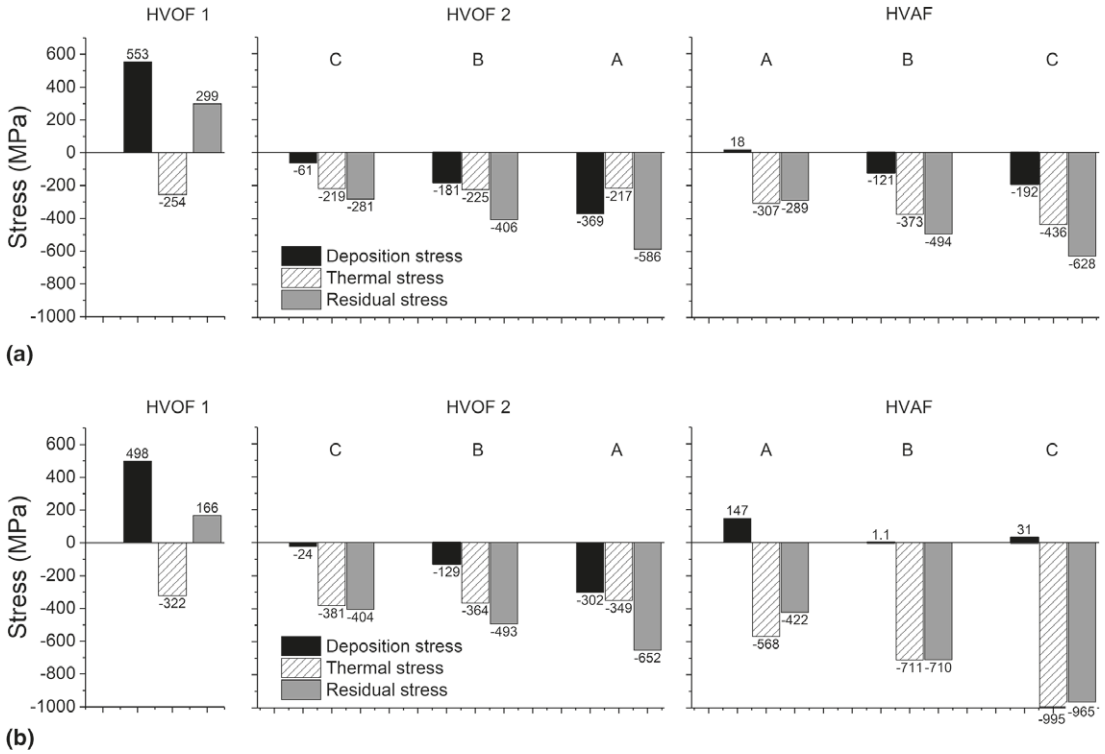

Fig. 4 Deposition stresses, thermal stresses and final residual stresses at the surface of the coatings by (a) Tsui and Clyne and (b) Brenner and Senderoff

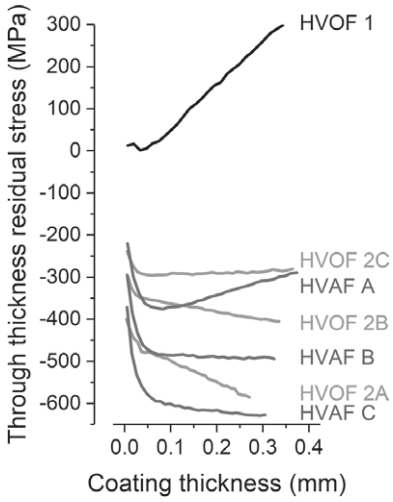

Fig. 5 Through thickness residual stress profiles of the coatings by Tsui-Clyne analytical model. Substrate is on the left side

initiated cracks were observed. Examination of the wear surfaces showed that cavitation erosion of the coatings takes place by fatigue crack growth preferably along the weak lamellae boundaries and removal of fractured areas, similarly as shown by Matikainen et al. (Ref 13) and Lamana et al. (Ref 15). The maximum depth of the wear scar shown in topography images (Fig. 7) was 60-70 μm for HVOF 1 coating, 20-30 μm for HVOF 2A coatings, and 10-15 μm for HVAF C coating. Thus, the crack growth rate was clearly the highest with HVOF 1 coating, next highest with HVOF 2 coating and slowest with HVAF coating.

Discussion

Residual Stresses

In the present study, the curvature data from the deposition process was used for determination of deposition stress and real temperature data from in situ curvature device for determination of thermal mismatch stress. This data was used for residual stress calculation with the Tsui and Clyne

Table 4 Mechanical properties and wear resistances of the coatings

	Vickers hardness (0.3 kg)	Elastic modulus, GPa	Fracture toughness (crack type*), MPa $m^{1/2}$	Cavitation erosion resistance, min μm^{-1}	Abrasion resistance, min mm^{-3}
HVOF 1	1455 ± 198	303 ± 29	4.6 ± 1.3 (*P* or *M*)	18.4	42.1
HVOF 2 A	1400 ± 195	306 ± 32	5.4 ± 0.5 (*P*)	91.0	49.8
HVOF 2 B	1395 ± 125	318 ± 26	6.5 ± 1.0 (*P*)	90.0	48.1
HVOF 2 C	1355 ± 192	301 ± 8	6.1 ± 0.6 (*P*)	75.0	47.6
HVAF A	1505 ± 119	396 ± 25	7.2 ± 1.3 (*P*)	134.5	47.1
HVAF B	1591 ± 56	375 ± 62	5.5 ± 0.9 (*M*)	177.8	47.1
HVAF C	1691 ± 97	359 ± 21	2.4 ± 0.4 (*M*)	209.0	46.1

*P for radial Palmqvist cracks when $c/a < 2.5$ and M for median crack, when $c/a > 2.5$

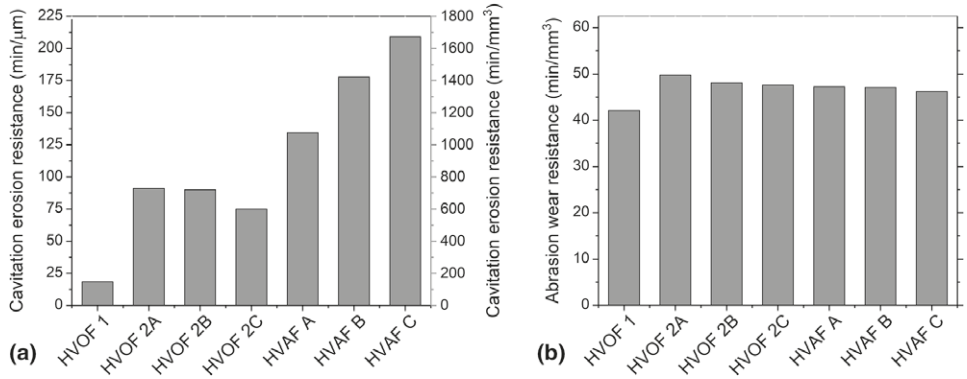

Fig. 6 (a) ASTM G 32 cavitation wear resistance and (b) ASTM G65D abrasion resistance of the coatings

procedure layer by layer. It was found, that residual stresses calculated by using Brenner and Senderoff approximation and Tsui Clyne model showed mostly similar tendencies. However, it was evident that the Brenner and Senderoff's equation overestimated especially the thermal mismatch stresses quite much. This result corresponds to the error analyses of Zhang et al. (Ref 39) regarding the use of Brenner and Senderoff equation for relatively hard coating with high thickness ratio of coating and substrate. They stated, that in the worst-case residual stress values can be overestimated approximately 30% using this method. However, in this case most of the errors for Brenner and Senderoff calculations came from the temperature increase during the first 3-5 passes. Temperature increase in the beginning causes the positive curvature change and hence shifts the deposition stresses, which are determined from curvatures between "start spray" and "end spray" (Fig. 3), toward the tensile stresses and thus exaggerates the thermal mismatch stresses by increasing the "end spray" curvature. If the temperature could have been kept constant during the deposition the difference between Brenner and Senderoff and Tsui and Clyne calculations would probably have been less.

Analytical model as per Tsui and Clyne had two advantages compared to Brenner and Senderoff calculation: (a) it represents through thickness residual stresses for progressively deposited coatings and (b) stresses arising from different origins can be evaluated. However, this requires that the deposition stresses and temperature change during the spraying process can be defined realistically by using real data from the deposition, which can be done by using an ICP sensor. It was clear that the temperature data during the spraying is significant for the resulting final stress state. Thus, in this case, the substrate

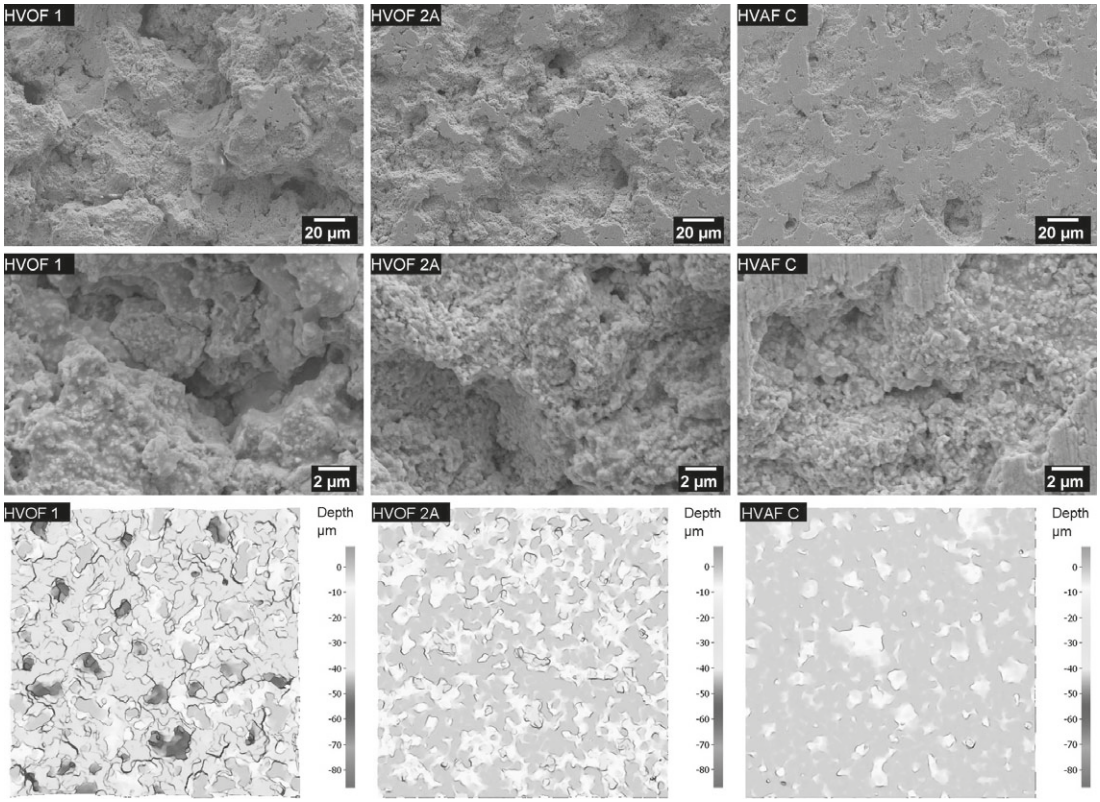

Fig. 7 SEM and optical profilometer images of cavitation erosion surfaces of the HVOF 1-, HVOF 2A- and HVOF 2C-coatings

temperature data from the beginning of each pass was used. Considering the temperatures, it was evident that the HVAF process heats up the substrates more effectively than the two HVOF systems used in this work. Therefore, the high substrate temperature, which in this case created compressive thermal stresses due to CTE differences of coating and substrate materials, was the main reason for extremely high compressive residual stresses in the HVAF coatings. In the experiments, the temperatures of the substrates were under 230 °C for HVOF systems as they were between 280 and 340 °C when the HVAF system was used. High temperature of the HVAF substrates was certainly affecting the residual stresses, and it should be noted that these high temperatures are usually not possible in industrial coatings in cases where the workpieces are large, or the dimensions of the workpieces are critical. In this regard, the substrate temperatures in this study might not correspond exactly to those demanded in industry. However, the residual stress profiles presented here are realistic for the current sample geometry.

From the residual stress profiles in Fig. 5 and deposition stresses from Table 3, it can be seen that using the DJH 2700 HVOF (HVOF 1) process creates tensile stresses, which increase toward the surface of the coatings as the number of passes increase. In the CJS HVOF (HVOF 2) and Kermetico AK7 HVAF-processes, the peening stresses were dominant and the final residual stress states were compressive. The compressive deposition stresses (peening stresses) increased along with a lowered thickness/pass, which shows that the stresses here were related to the heat transfer onto the particles. However, the amount of heat transfer could not be deduced from the surface temperatures of the particles. Actually, it was found that in the HVOF 2 process the peening stresses (compressive deposition stresses) were of higher amount compared to HVAF process although the particle surface temperature in the HVOF 2 process was higher. The explanation for this can most likely be the particle dwell time, which is different in these spray guns due to the particle feeding location. In the CJS (HVOF 2) -process, the particles were fed radially into the nozzle, while in Kermetico AK7 HVAF and DJH

(HVOF 1) processes, the powder was injected axially into the combustion chamber. This resulted in a shorter dwell time for particles in the HVOF 2 process compared to the HVAF process. Albeit the higher flame temperature (and particle surface temperature) the dwell time kept the particle melting rate lower, which meant lower deposition efficiency and a higher peening effect. Furthermore, it was found that for HVAF process the lowest particle surface T parameter produces the highest tensile deposition stress, which can also be explained by the dwell time effect. Decrease of the total gas flows in HVAF increases the dwell time of the particles and therefore melting rate increases. This can also be witnessed by highest thickness/pass with HVAF A parameter.

Mechanical Properties

Hardness and elastic modulus were on a good level for all of the coatings, but the highest elastic modulus and hardness were clearly achieved with HVAF coatings. Hardness and elastic modulus of thermally sprayed coatings typically increase, when the coating is denser. However, the hardness of a WC-CoCr coating may increase as well if the particle temperature has been sufficiently high to create hard and brittle secondary phases in the matrix (e.g., eta phase) and on the surface of carbides (W_2C) by carbon loss and carbide dissolution (Ref 38, 40). By looking at the microstructure and considering that the HVOF 1 coating was the only coating, which had significant amount of W_2C in the XRD analysis, it can be proposed that its high hardness is a result of the high spray temperature. For the HVOF 2 and HVAF coatings, the microstructures were extremely dense and no major W_2C was found. From the microstructure, a high amount of retained small carbides was detectable too, which may partly explain the good mechanical properties of HVAF coatings. Obviously, the significant advantage of the HVAF and HVOF 2 coatings is the achievement of very good mechanical properties by relying on their high density and structural homogeneity without a risk of formation of brittle phases.

The good mechanical properties and wear resistance of thermally sprayed coatings are to be improved by the well-bonded lamellae. Lamellae boundaries often weaken thermally sprayed coatings, which resembles grain boundaries in solid material. In particular, the high elastic modulus and high hardness (without significant W_2C formation) of HVAF-coatings indicate good lamella cohesion. In this study, the lamellae cohesion was further evaluated by indentation fracture toughness measurements, in which the cracks were formed from the edge of Vickers tip. It was earlier found that Palmqvist type of cracks initiating from the edge of the Vickers indenter tip usually follow the path of lamellae boundaries. Hence, fracture toughness, which is measured from the cross section of the coating, is linked to the lamellae cohesion (Ref 40). In the current study, there was no indication of improved cross section fracture toughness for coatings, which had excellent other mechanical properties. In contrast, fracture toughness of coatings HVAF B and C was clearly reduced. For these coatings, the thermal mismatch stresses were − 373 to 436 MPa, respectively. In order to understand the observed reduction of fracture toughness's linked to high compressive stress the occurrence of cracking under indentation needs to be discussed. Indenting the material with relatively small loads the plastic deformation at the edge of the Vickers tip creates usually Palmqvist type cracks. These cracks initiates at the edge of the indenter and develop in the surface of the material driven by tensile stresses when the lateral faces of the Vickers tip push the material in different directions (Ref 41). Palmqvist cracks are addressed to be present if ratio of average crack length to indenter half diagonal (c/a) is < 2.5 (Ref 42). Median cracks are formed with higher loads. First, a plastic zone is formed under the indenter and if the load is increased enough the median cracks parallel to the loading direction are formed under the plastic zone (Ref 41, 43). During the unloading plastic zone do not relax and stress field remains and is responsible of development of the "half-penny" - cracks onto a surface (Ref 41). These cracks are visible at the same locations on the sample surface as Palmqvist cracks and are addressed to be present if $c/a > 2.5$ (Ref 42). Considering the high compressive stresses in the HVAF and HVOF 2 coatings it is obvious that in our case they have an influence on the crack initiation and growth. When hardness measurement is made on the cross section of the coating, it is likely that compression at the crack tip hinders the crack growth at the Palmqvist crack region. On the other hand, compressive stresses parallel to indentation direction increases the depth of plastic region and thus median cracks develop deeper into the material resulting to longer "half- penny"-cracks as they develop onto the surface (Ref 44-46). It is conceivable that, due to the stress state in the coating," half-penny"-cracks become more favorable. Since the effect of the stress state on the formation of indentation cracks was not the scope of this study, it is sufficient to state that due to the strong effect of the residual stresses in the coatings on the indentation fracture toughness measurements, the fracture toughness values cannot be considered comparable figures without taking into account of these residual stresses.

It was further noted that high compressive stresses did not reduce the fracture toughness of the HVOF 2A coating, which had high compressive residual stress (− 580 MPa) on the coating surface as well. On this basis it may be suggested that HVOF 2A had either better lamella cohesion compared to HVAF B and C or then the way the tensile

stress is created (peening or CTE mismatch) has an effect. It may be possible that the residual stresses generated from the peening are not that detrimental in terms of crack propagation due to their local nature. In contrast, thermal mismatch stresses uniformly affect the entire structure and provide steady stress field under the indentation tip for the formation of longer half-penny cracks.

Wear

Cavitation erosion resistance results varied considerably between different coatings. In addition, the cavitation erosion resistance of the HVAF coatings was superior compared to the both HVOF coatings. These results are consistent with the findings of other recent studies carried out on WC-10Co4Cr coatings (Ref 13, 15, 47). Matikainen et al. that the cavitation erosion performance of the coatings can be improved by increasing kinetic energy and decreasing particle temperature from HVOF to HP/HVOF to HVAF, which they linked to higher density and lower degree of decarburization. Similar results have been found in other studies as well (Ref 47). Based on the results in this study, seems evident that the high compressive residual stress state of these coatings plays a very important role in improved cavitation erosion resistance. This suggestion is supported by a higher cavitation erosion resistance of the HVOF 2 an HVAF coatings, which showed compressive residual stresses compared to the HVOF 1 coating, which were characterized by tensile residual stresses. Moreover, the cavitation erosion resistance increased for the HVOF 2 and HVAF processes, when compressive residual stress increased too. Cavitation erosion can be considered as a cyclic fatigue load caused by continuous collapsing of cavitation bubbles on the surface. Therefore, the erosion rate is controlled by fatigue crack growth mechanism preferably along the weak lamellae boundaries and a rate of removal of fractured areas. Probably the high compressive stresses resulted from the spraying process of the WC-CoCr coatings impede the fatigue crack formation and growth along the lamellae interfaces and therefore improve the cavitation erosion resistance, which is supported by the literature (Ref 15). Furthermore, it may be more advantageous if the compressive stresses are originated from thermal stresses rather than peening stress, since the stress in previous case is more homogeneous and acts at the macro-level. This may explain the improved performance of the HVAF coating over the HVOF 2 coatings.

The influence of other factors on the good cavitation erosion performance may be important as well. Considering the cavitation erosion resistance of solid material, in addition to hardness, the strain-hardening ability of material plays an important role in resisting the crack growth caused by pressure of the collapsing cavitation bubbles. The CoCr matrix in solid WC-CoCr has a relatively high strain-hardening exponent and thus resists cavitation well. However, the thermally sprayed WC-CoCr coatings always reveal some amount of the dissolution of the WC into the matrix, which increases the tendency of formation of mixed $(Co,W)_xC$ -carbides or amorphous phases during the rapid cooling. Hence, the matrix is not an optimally composed metal alloy, but instead hardened and more brittle. Based on the microstructure and XRD it seems evident that less solution occurs in the HVAF and HVOF 2 coatings compared to the HVOF 1 coatings and that spraying conditions do not affect the properties as much as compared to HVOF 1. It is known that too much carbide dissolution into the matrix can decrease the fracture toughness of the matrix (Ref 40), which may result to the poor cavitation erosion performance of HVOF 1. Actually, Matikainen et al. (Ref 13) showed that especially brittle phases in HVOF-sprayed coatings are susceptible to brittle fractures. In addition, the lamellae cohesion is commonly believed to affect the wear performance of the thermally sprayed coatings. Superior performance of the HVAF and HVOF 2 coatings might be therefore partly related to optimal particle heating. This results in good lamellae cohesion and lack of brittle areas inside the coatings and thus hinders brittle fracture in the lamellae interfaces. Lamana et al. (Ref 15) showed that fatigue cracking caused by cavitation mainly began at the interface between the lamellae and found a strong correlation between fracture toughness measured at the cross section of the specimens and cavitation erosion resistance of the coatings. In this study, such a correlation could not be demonstrated since residual stress state was found to significantly influence the fracture toughness measured from the coating cross section. Perhaps, a better correlation might have been obtained if the fracture toughness had been measured from the surface of the coating, since the cracks produced would then have been initiated correspondingly to those generated by cavitation. However, this was not possible, because very high loads and thus thick coatings would have been needed that such an experiment could have been done.

With respect to abrasive wear resistance, it was relatively unaffected by the used spray process, and residual stresses and the spray parameters. Only the abrasion wear resistance of HVOF 1 coating was slightly lower compared to HVOF 2 and HVAF coatings. In order to consider, the removed material volumes in various wear tests in Fig. 6(a) and (b), it should be noted that in abrasion tests the wear area is about twice as large as in cavitation erosion test. Proportional to the same area material removal rate for most worn sample (HVOF 1) in abrasion test is roughly two times more than in cavitation test. The most cavitation-resistant coating the material removal rate is approximately 20 times higher in abrasion test. The large

difference in wear rates between tests can be explained by a different wear mechanism. Considering the abrasion wear the proposed mechanism is mainly micro-cutting, i.e., sand particle needs to penetrate on the material and remove the material from the surface in the form of a chip (Ref 48). Therefore, in the abrasion test unlike the cavitation erosion test, the wear rate is not controlled by fatigue crack growth and it is not surprising that residual stresses do not have effect on abrasion wear rate. Rather, the abrasion wear rate is controlled by such factors as hardness of the softest phase in material, carbide size related to the abrasive size, mean free path of carbides related to the abrasive size. For thermally sprayed WC-CoCr, the wear may further be affected by the factors related to spray process such as porosity, lamellae adhesion, toughness reduction/hardening of matrix due to the dissolution of carbides onto a matrix, which may explain the minor differences between HVAF and HVOF 2 coatings. The surface porosity may be in this case an important factor, which may explain the lower wear resistance of HVOF 1 coating, which had larger size porosity in the microstructure. The abrasive particles can more easily cut the chip from the material from the edge of the pore as presented by Ghabchi et al. (Ref 49). However, it may be concluded that the abrasion resistance was good for all of the coatings and the coating characteristics did not affect significantly on abrasion wear resistance.

Conclusions

In the study, the residual stress state of the high kinetic thermal spray processes such as high-pressure HVOF and HVAF were compared to conventional thermal spray processes. Residual stress state of WC-CoCr coatings was determined by Tsui and Clyne laye-by-layer analytical model. The in-situ coating property device was utilized to determine the realistic quenching stress and temperature data as input to the analytical model. By this way, a realistic through thickness calculation of residual stresses was achieved. Cavitation erosion, abrasion wear and mechanical property tests were conducted, and the effect of the residual stress state on the wear resistance and mechanical performance was discussed.

Following conclusions were made from the study:

- The analytical residual stress model by Tsui and Clyne combined with the data from ICP curvature and temperature-sensing device allows for the determination the through thickness residual stress state of the coating. However, to achieve a result the specific flat bar samples needs to be used. Compared to the values achieved by Brenner and Senderoff equation, which is commonly used for average residual stress approximation, the final residual compressive stresses were significantly lower.
- The spray parameters of the Kermetiko AK7 and Thermico CJS high kinetic thermal spray processes can be adjusted to produce compressive deposition stresses. For DJ Hybrid, the deposition stress was tensile. As a result, relatively high compressive final stress states inside the WC-CoCr coatings can be achieved by the high kinetic processes and altered significantly by spraying parameters. In this study, the final compressive stress state at the surface of coating, determined by Tsui and Clyne analytical model, altered from − 289 to − 628 MPa for the AK7 HVAF process and form − 281 to − 586 MPa in the case of Thermico CJS (HVOF 2) process.
- Thermally sprayed WC-10Co4Cr coatings sprayed by high-pressure HVOF and HVAF processes can provide significant performance improvements in cavitation erosion resistance. The cavitation erosion resistance of the HVAF-sprayed coatings was 7-11 times higher and for high-pressure HVOF still 4-5 times higher compared to conventional gas-fuelled HVOF processes.
- Superior cavitation erosion resistance of the HVAF and high-pressure HVOF coatings was partly a result from the dense and homogenous non-brittle microstructure. Moreover, it seems that the most important factor behind the superior cavitation erosion resistance might probably be the high compressive residual stress state in the coatings. The high compressive stresses make the fatigue crack formation more difficult and hinder the fatigue crack growth along the lamellae interfaces and in this way improves the cavitation erosion resistance.

References

1. S. Sampath, X.Y. Jiang, J. Matejicek, L. Prchlik, A. Kulkarni, and A. Vaidya, Role of Thermal Spray Processing Method on the Microstructure, Residual Stress and Properties of Coatings: An Integrated Study of Ni-5 wt. % Al Bond Coats, *Mater. Sci. Eng. A*, 2004, **364**(1-2), p 216-231

2. J. Matejicek, S. Sampath, D. Gilmore, and R. Neiser, In Situ Measurement of Residual Stresses and Elastic Moduli in Thermal Sprayed Coatings Part 2: Processing Effects on Properties of Mo Coatings, *Acta Mater.*, 2003, **51**(3), p 873-885
3. T.W. Clyne and S.C. Gill, Residual stresses in Thermal Spray Coatings and Their Effect on Interfacial Adhesion: A Review of Recent Work, *J. Therm. Spray Technol.*, 1996, **5**, p 401-418
4. V. Matikainen, H. Koivuluoto, P. Vuoristo, J. Schubert, and Š. Houdková, Effect of Nozzle Geometry on the Microstructure and Properties of HVAF-Sprayed WC-10Co4Cr and Cr3C2-25NiCr Coatings, *J. Therm. Spray Technol.*, 2018, **27**(4), p 680-694
5. W. Luo, U. Selvadurai, and W. Tillmann, Effect of Residual Stress on the Wear Resistance of Thermal Spray Coatings, *J. Therm. Spray Technol.*, 2016, **25**(1-2), p 321-330
6. R.C. Souza, H.J.C. Voorwald, and M.O.H. Cioffi, Fatigue Strength of HVOF Sprayed Cr3C2-25NiCr and WC-10Ni on AISI, 4340 Steel, *Surf. Coatings Technol.*, 2008, **203**(3-4), p 191-198
7. R.T.R. McGrann, D.J. Greving, J.R. Shadley, E.F. Rybicki, T.L. Kruecke, and B.E. Bodger, The Effect of Coating Residual Stress on the Fatigue Life of Thermal Spray-Coated Steel and Aluminum, *Surf. Coat. Technol.*, 1998, **108-109**(1-3), p 59-64
8. T. Varis, T. Suhonen, O. Calonius, J. Čuban, and M. Pietola, Optimization of HVOF Cr3C2-NiCr Coating for Increased Fatigue Performance, *Surf. Coat. Technol.*, 2016, **305**, p 123-131
9. A. Agüero, F. Camón, J. García De Blas, J.C. Del Hoyo, R. Muelas, A. Santaballa, S. Ulargui, and P. Vallés, HVOF-Deposited WCCoCr as Replacement for Hard Cr in Landing Gear Actuators, *J. Therm. Spray Technol.*, 2011, **20**(6), p 1292-1309
10. R.K. Kumar, M. Kamaraj, S. Seetharamu, T. Pramod, and P. Sampathkumaran, Effect of Spray Particle Velocity on Cavitation Erosion Resistance Characteristics of HVOF and HVAF Processed 86WC-10Co4Cr Hydro Turbine Coatings, *J. Therm. Spray Technol.*, 2016, **25**(6), p 1217-1230
11. G. Bolelli, L.M. Berger, T. Börner, H. Koivuluoto, L. Lusvarghi, C. Lyphout, N. Markocsan, V. Matikainen, P. Nylén, P. Sassatelli, R. Trache, and P. Vuoristo, Tribology of HVOF- and HVAF-Sprayed WC-10Co4Cr Hardmetal Coatings: A Comparative Assessment, *Surf. Coatings Technol.*, 2015, **265**, p 125-144
12. V. Matikainen, G. Bolelli, H. Koivuluoto, P. Sassatelli, L. Lusvarghi, and P. Vuoristo, Sliding Wear Behaviour of HVOF and HVAF Sprayed Cr3C2-Based Coatings, *Wear*, 2017, **388-389**(April), p 57-71. https://doi.org/10.1016/j.wear.2017.04.001
13. V. Matikainen, S. Rubio Peregrina, N. Ojala, H. Koivuluoto, J. Schubert, S. Houdková, and P. Vuoristo, Erosion Wear Performance of WC-10Co4Cr and Cr3C2-25NiCr Coatings Sprayed with High-Velocity Thermal Spray Processes, *Surf. Coat. Technol.*, 2018, **2019**(370), p 196-212
14. H.K.R. Schwetzke, Cavitation Erosion of HVOF Coatings, *Thermal Spray: Practical Solutions for Engineering Problems*, C.C. Berndt, Ed., ASM International, Cleveland, 1996, p 153-158
15. M.S. Lamana, A.G.M. Pukasiewicz, and S. Sampath, Influence of Cobalt Content and HVOF Deposition Process on the Cavitation Erosion Resistance of WC-Co Coatings, *Wear*, 2017, **2018**(398-399), p 209-219. https://doi.org/10.1016/j.wear.2017.12.009
16. S. Takeuchi, M. Ito, and K. Takeda, Modelling of Residual Stress in Plasma-Sprayed Coatings: Effect of Substrate Temperature, *Surf. Coat. Technol.*, 1990, **43-44**(PART 1), p 426-435
17. S. Kuroda, T. Fukushima, and S. Kitahara, Significance of Quenching Stress in the Cohesion and Adhesion of Thermally Sprayed Coatings, *J. Therm. Spray Technol.*, 1992, **1**(4), p 325-332
18. P. Bansal, P.H. Shipway, and S.B. Leen, "Effect of Particle Impact on Residual Stress Development in HVOF Sprayed Coatings," *Proceedings of the International Thermal Spray Conference*, 2006, p 570-575.
19. S. Kuroda and T.W. Clyne, The Quenching Stress in Thermally Sprayed Coatings, *Thin Solid Films*, 1991, **200**(1), p 49-66
20. S. Kuroda, T. Dendo, and S. Kitahara, Quenching Stress in Plasma Sprayed Coatings and Its Correlation with the Deposit Microstructure, *J. Therm. Spray Technol.*, 1995, **4**(1), p 75-84
21. S. Kuroda, Y. Tashiro, H. Yumoto, S. Taira, H. Fukanuma, and S. Tobe, Peening Action and Residual Stresses in High-Velocity Oxygen Fuel Thermal Spraying of 316L Stainless Steel, *J. Therm. Spray Technol.*, 2001, **10**(2), p 367-374
22. A.A. Abubakar, A.F.M. Arif, K.S. Al-Athel, S.S. Akhtar, and J. Mostaghimi, Modeling Residual Stress Development in Thermal Spray Coatings: Current Status and Way Forward, *J. Therm. Spray Technol.*, 2017, **26**(6), p 1115-1145
23. T. Valente, C. Bartuli, M. Sebastiani, and A. Loreto, Implementation and Development of the Incremental Hole Drilling Method for the Measurement of Residual Stress in Thermal Spray Coatings, *J. Therm. Spray Technol.*, 2005, **14**(4), p 462-470
24. Y.Y. Santana, J.G. La Barbera-Sosa, M.H. Staia, J. Lesage, E.S. Puchi-Cabrera, D. Chicot, and E. Bemporad, Measurement of Residual Stress in Thermal Spray Coatings by the Incremental Hole Drilling Method, *Surf. Coat. Technol.*, 2006, **201**(5), p 2092-2098
25. M. Buchmann, R. Gadow, and J. Tabellion, Experimental and Numerical Residual Stress Analysis of Layer Coated Composites, *Mater. Sci. Eng. A*, 2000, **288**(2), p 154-159
26. M.S.J. Hashmi, Ed., *Comprehensive Materials Processig*, Elsevier Ltd, Amsterdam, 2014
27. A.S.M. Ang and C.C. Berndt, A Review of Testing Methods for Thermal Spray Coatings, *Int. Mater. Rev.*, 2014, **59**(4), p 179-223
28. G.G. Stoney, The Tension of Metallic Films Deposited by Electrolysis, *Proc. R. Soc. A Math. Phys. Eng. Sci.*, 1909, **82**(553), p 172-175
29. A. Brenner and S. Senderoff, Calculation of Stress in Electrodeposits from the Curvature of a Plated Strip, *J. Res. Natl. Bur. Stand.*, 1949, **42**(2), p 105
30. Y.C. Tsui and T.W. Clyne, An Analytical Model for Predicting Residual Stresses in Progressively Deposited Coatings: Part 1—Planar Geometry, *Thin Solid Films*, 1997, **306**(1), p 23-33
31. D.J. Greving, E.F. Rybicki, and J.R. Shadley, Through-Thickness Residual Stress Evaluations for Several Industrial Thermal Spray Coatings Using a Modified Layer-Removal Method, *J. Therm. Spray Technol.*, 1994, **3**(4), p 379-388
32. T.C. Totemeier and J.K. Wright, Residual Stress Determination in Thermally Sprayed Coatings - A Comparison of Curvature Models and X-Ray Techniques, *Surf. Coat. Technol.*, 2006, **200**(12-13), p 3955-3962
33. J. Pina, A. Dias, and J.L. Lebrun, Study by X-Ray Diffraction and Mechanical Analysis of the Residual Stress Generation during Thermal Spraying, *Mater. Sci. Eng. A*, 2003, **347**(1-2), p 21-31
34. C. Lyphout, P. Nylén, A. Manescu, and T. Pirling, Residual Stresses Distribution through Thick HVOF Sprayed Inconel 718 Coatings, *J. Therm. Spray Technol.*, 2008, **17**(5-6), p 915-923
35. G.M. Pharr, An Improved Technique for Determining Hardness and Elastic Modulus Using Load and Displacement Sensing Indentation Experiments, *J. Mater. Res.*, 1992, **7**(6), p 1564-1583
36. James Lanklord, Indentation Microfracture in the Palmqvist Crack Regime: Implications for Fracture Toughness Evaluation by the Indentation Method, *J. Mater. Sci. Lett.*, 1982, **1**, p 493-495
37. Y.C. Tsui and T.W. Clyne, An Analytical Model for Predicting Residual Stresses in Progressively Deposited Coatings: Part 3—Further Development and Applications, *Thin Solid Films*, 1997, **306**(1), p 52-61
38. C. Verdon, A. Karimi, and J.L. Martin, A Study of High Velocity Oxy-Fuel Thermally Sprayed Tungsten Carbide Based Coatings.

Part 1: Microstructures, *Mater. Sci. Eng. A*, 1998, **246**(1-2), p 11-24
39. X.C. Zhang, B.S. Xu, H.D. Wang, and Y.X. Wu, Error Analyses on Some Typically Approximate Solutions of Residual Stress within a Thin Film on a Substrate, *J. Appl. Phys.*, 2005, **98**(5), p 053516
40. T. Varis, T. Suhonen, A. Ghabchi, A. Valarezo, S. Sampath, X. Liu, and S.P. Hannula, Formation Mechanisms, Structure, and Properties of HVOF-Sprayed WC-CoCr Coatings: An Approach toward Process Maps, *J. Therm. Spray Technol.*, 2014, **23**(6), p 1009-1018
41. R.F. Cook, Fracture Sequences during Elastic-Plastic Indentation of Brittle Materials, *J. Mater. Res.*, 2019, **34**(10), p 1633-1644
42. C.B. Ponton and R.D. Rawlings, Vickers Indentation Fracture Toughness Test Part 1 Review of Literature and Formulation of Standardised Indentation Toughness Equations, *Mater. Sci. Technol. (United Kingdom)*, 1989, **5**(9), p 865-872
43. T. Fett, A.B. Kounga Njiwa, and J. Rödel, Crack Opening Displacements of Vickers Indentation Cracks, *Eng. Fract. Mech.*, 2005, **72**(5), p 647-659
44. W.G. Mao, J. Wan, C.Y. Dai, J. Ding, Y. Zhang, Y.C. Zhou, and C. Lu, Evaluation of Microhardness, Fracture Toughness and Residual Stress in a Thermal Barrier Coating System: A Modified Vickers Indentation Technique, *Surf. Coat. Technol.*, 2012, **206**(21), p 4455-4461
45. C.L. Eriksson, P.L. Larsson, and D.J. Rowcliffe, Strain-Hardening and Residual Stress Effects in Plastic Zones around Indentations, *Mater. Sci. Eng.*, 2003, **340**(1-2), p 193-203
46. N. Huber and J. Heerens, On the Effect of a General Residual Stress State on Indentation and Hardness Testing, *Acta Mater.*, 2008, **56**(20), p 6205-6213
47. Q. Wang, Z. Tang, and L. Cha, Cavitation and Sand Slurry Erosion Resistances of WC-10Co-4Cr Coatings, *J. Mater. Eng. Perform.*, 2015, **24**(6), p 2435-2443
48. K.H.Z. Gahr, Wear by Hard Particles, *Tribol. Int.*, 1998, **31**(10), p 587-596
49. A. Ghabchi, T. Varis, E. Turunen, T. Suhonen, X. Liu, and S.P. Hannula, Behavior of HVOF WC-10Co4Cr Coatings with Different Carbide Size in Fine and Coarse Particle Abrasion, *J. Therm. Spray Technol.*, 2010, **19**(1-2), p 368-377

PUBLICATION V

Optimization of HVOF Cr_3C_2-NiCr coating for increased fatigue performance

T. Varis, T. Suhonen, O. Calonius, J. Čuban, M. Pietola

Surface & Coatings Technology, vol 305, pp.123-131, August 2016
DOI:10.1016/j.sutfcoat.2016.08.012

Surface & Coatings Technology 305 (2016) 123–131

Contents lists available at ScienceDirect

Surface & Coatings Technology

journal homepage: www.elsevier.com/locate/surfcoat

Optimization of HVOF Cr_3C_2—NiCr coating for increased fatigue performance

T. Varis [a,*], T. Suhonen [b], O. Calonius [c], J. Čuban [d], M. Pietola [c]

[a] Tampere University of Technology, Department of Materials Science, P.O. Box 589, FI-33101, Tampere, Finland
[b] VTT Technical Research Centre of Finland Ltd, P.O. Box 1000, FI-02044, VTT, Espoo, Finland
[c] Aalto University, Department of Engineering Design and Production, P.O. Box 11000, FI-00076, Aalto, Espoo, Finland
[d] Technical University of Liberec, Studentská 1402/2, 46117 Liberec 1, Czech Republic

ARTICLE INFO

Article history:
Received 16 May 2016
Revised 4 August 2016
Accepted in revised form 5 August 2016
Available online 6 August 2016

Keywords:
Fatigue performance
Wear resistance
HVOF thermal spray
Residual stress
S-N curve
Cr_3C_2—NiCr coating

ABSTRACT

Thermally sprayed coatings are strong candidates to be used for replacement of hard chromium – process which is regarded as an environmental risk – in many sliding surfaces for engineering applications such as hydraulic cylinders and aircraft landing gears. Recent advance in thermal spraying technology, based on the increase of the spray particle velocity, has led to improved coating quality. This study focuses on the fatigue performance of structural steel coated with Cr_3C_2—NiCr coating. Coating has been produced by using high kinetic HVOF thermal spray process. First, the coating was optimized for fatigue purposes by studying the residual stress generation. The optimized coating was selected for deposition of axial fatigue tests specimens, whose fatigue performance was compared to the uncoated steel specimens having different surface treatments (turning, polishing, and shot blasting) relevant for the target applications. The results showed that by using a high kinetic energy coating, the fatigue performance of Cr_3C_2—NiCr coated structural steel was clearly improved compared to uncoated steel of similar surface quality. Increased fatigue resistance of the coated material was attributed to the substantial compressive residual stresses that hindered crack initiation and that was caused by the high velocity spray particles during the coating process.

1. Introduction

Hard coatings, produced by laser cladding or thermal spraying, are potential solutions for many engineering applications [1,2]. In recent years, thermally sprayed Cr_3C_2—NiCr or WC-CoCr coatings have been used widely for hard chrome replacement in several applications, e.g., pistons and valves in hydraulic cylinders and aircraft landing gear components [2,3]. It has been shown that compared to hard chromium coating, thermally sprayed coatings can improve wear resistance, corrosion resistance and in some cases also the fatigue life of the component [4,5]. Improved fatigue performance relative to hard chromium is the consequence of compressive residual stresses generated both during grit blasting of the substrate material prior to spraying, as well as compressive residual stresses generated during the actual coating deposition phase [6–9]. However, compared to uncoated samples, a reduction of fatigue performance of the coated samples has usually been reported [5,6,8,10–12]. In component design, this ambivalent effect caused by coating needs to be carefully considered.

The mechanism of fatigue crack initiation and growth in coated structures has been viewed in relatively few studies but various factors have been shown to influence on fatigue life. Moreover numerous factors issues that influence fatigue crack initiation and growth has been brought out. It is agreed that fatigue failures usually start at the surface of a fatigue specimen or at the locations where highest tensile stress concentrations have been generated [13], [14]. In case of coated components the crack can initiate from substrate [8] or from the coating at the locations of weak lamella bonding, pores in the coating [7,15] or from the cracks on the coating surface [16]. In several publications cracks have shown to be initiated from the irregularities or grit blasting residues at the coating-substrate interface [9–11,17]. The research of fatigue behaviour of bi-layered structures shows that once initiated, crack propagation is associated to the direction in which the crack approaches the interface and moreover influenced by the plastic properties of coating and substrate. If the crack approaches from the less brittle material to the brittle material the crack continues to advance through the interface. If the crack approaches the interface from the plastically weak material to the material which can plastically deform, the surface layer can behave as a crack arrestor [18]. It has been shown that coating adhesion plays an important role on the crack propagation. If the adhesion of the coating is low the crack can start to advance along the interface and thus the delamination of the coating may occur [7].

An essential effect on the fatigue resistance of the coated structure is caused by the surface roughness and residual stress arising from the

* Corresponding author.
E-mail address: tommi.varis@tut.fi (T. Varis).

http://dx.doi.org/10.1016/j.surfcoat.2016.08.012
0257-8972/

preparation of the coating. Surface roughness by grit blasting along with grit residues on the blasted surface creates irregularities for crack initiation which decreases the fatigue life, but on the other hand the grit blasting process produces compressive stress in the surface, which may increase the fatigue life [15]. Perhaps, in practice, the only effective way to increase the fatigue life of the component by HVOF spraying is to increase the compressive residual stresses at the component surface. It has been shown that when relatively heavy WC-Co particles are deposited by using DJ Hybrid HVOF process the fatigue strength of the component was increased [8], but other authors have suggested that in case of lighter Cr3C2—NiCr deposited by JP 5000 particle deposition the residual stress was not enough to delay the fatigue fracture of the component [6].

Thermally sprayed coating is formed by accelerated molten or semi molten particles, which impacts onto a substrate. Recently, thermal spray processes, such as newest generation high pressure HVOF, HVAF, and Cold Spraying, have been developing towards lower spray particle temperature and higher particle velocity. High particle velocities, which can exceed 1000 m s^{-1}, assist to produce very dense coating structures. Also importantly, due to higher kinetic energy and lower particle temperatures residual stresses in the coating are going towards compressive. The overall residual stress state after spraying has three sources: a) quenching stress b) thermal mismatch stress and c) peening stress. In conventional thermal spraying like plasma spraying most of the residual stresses originate from the quenching of the solidified particles, which have impacted the substrate and stuck to it. [19,20] During the deposition of the coating, temperature of the substrate and coating is typically increased to 50–200 °C. After completing the coating, the substrate-coating system is cooled down to, e.g., room temperature, which generates a thermal mismatch stress. The nature of the thermal stress (tensile, neutral or compressive) is determined by the difference in the coefficient of thermal expansion (CTE) of the coating and the substrate [20,21]. In high-velocity thermal spray systems, like HVOF, HVAF and cold spray, a compressive component (also known as peening stress) can be introduced during the deposition. This is caused by the high velocity impact of the particles causing plastic deformation of the substrate and/or previously deposited coating material [22,23]. Typically all of these components are developing in a thermal sprayed coating, but the magnitude of the final stress state is dependent on temperature difference of the individual particles before and after the impact of the particle to the substrate, CTE differences of the substrate and coating, as well as the ability of substrate and coating to plastically deform and work harden upon impact of the particle. These issues may have a significant role on the fatigue behaviour of the coating and understanding these effects are crucial for damage tolerant coating design. Nowadays, the possibility to determine residual stresses by in situ techniques [23,24], offers interesting tool to evaluate the origins of residual stresses on each coating-substrate system and makes it possible to tailor the stresses to a great extent.

In this study, a liquid fuelled HVOF system (Carbide Jet Spray system from Thermico GmbH, Germany) was used to produce coating having significant compressive residual stress. The goal was to increase fatigue performance of the component by introducing maximised compressive residual stress state onto the coating and substrate. The experimental part of the paper is divided into two parts: first, coating was carefully optimized for its intended purpose – wear resistance and fatigue performance, then the coated specimens were fatigue tested and their performance was compared with the fatigue performance of uncoated substrate material having undergone different surface treatments (turning, grit blasting and polishing) relevant for the production of components for the target applications.

2. Experimental procedure

2.1. Spraying processes, materials, and coating preparation

In the study two HVOF systems Carbide Jet Spray (CJS, from Thermico Germany), and DJ Hybrid (DJH, from Oerlikon Metco, Westbury, USA) was used. Before producing actual fatigue test specimens coating optimization tests was made. The coatings were sprayed on flat carbon steel (S355) substrates mounted on In-situ Coating Property sensor (ICP-sensor, Reliacoat Technologies, US) for residual stress measurements (technique described in Section 2.2.2) and 50 mm × 40 mm × 8 mm for wear test. ICP sensor allows monitoring of the sample curvature and temperature from the back side of the sample. Prior to deposition, all coated substrate materials were grit blasted with size of 500–700 μm alumina particles.

For the fatigue testing, Cr_3C_2—NiCr coatings were deposited on top of axial fatigue test specimens made of unalloyed structural steel S355J2G3 (more detailed description in Section 2.2.3). During the spraying of actual fatigue specimens, temperature was monitored by infrared temperature device and specimen temperature was maintained under 180 °C by using air cooling and controlling the spray interval. This temperature is supposed to be low enough in order to avoid residual stress relaxation of the grit blasted surface.

Agglomerated, sintered and plasma densified Cr_3C_2—25(80Ni20Cr) powder from Sulzer Metco WOKA GmbH, Germany was used as feedstock material. Particle size distribution of 10 to 30 μm was used, which is suitable for CJS. Agglomerated and sintered Cr_3C_2—25(80Ni20Cr) powder from H.C. Starck, with particle size from 22.5 to 45 μm, was used for DJH. Fig. 1a shows the surface morphology of the agglomerated, sintered and plasma densified powder and Fig. 1b shows the surface morphology of more typical agglomerated and sintered powder.

Thermico Carbide Jet Spray (CJS) uses kerosene as a fuel gas and it is characterized as a temperature controlled process since it uses hydrogen in addition to kerosene for more precise control of the flame temperature. Hydrogen addition enables to use very lean kerosene mixtures without a risk of unstable burning. Therefore the temperature window in the CJS process is wider compared to spray guns using only kerosene. Before spraying the actual fatigue test specimens, six parameters for CJS were selected to evaluate the optimal spray condition for Cr_3C_2—NiCr powder. Only in four of those parameters temperature was high enough to actually deposit the coating. Therefore, actual samples for optimization purposes were produced by using four different parameters with CJS and, as a reference, one sample set sprayed by using Diamond Jet Hybrid with hydrogen as fuel gas (DJH).

The spray parameters used are shown in Table 1. In liquid kerosene HVOF process (Thermico CJS) two significant parameters were varied. Kerosene levels of 16, 18 and 21 l h^{-1} and oxygen levels of 900 and 1000 l min^{-1} was used. As an indicator of the thermal and kinetic energy of the flame, cooling power and chamber pressure can be monitored during spraying. Cooling power is defined here as power loss to the cooling water and it can be determined from difference of cooling water inlet and outlet temperatures with known water flow by using the equation $dQ = C\,(T_{out} - T_{in})$, where C (J K^{-1} mol^{-1}) is a heat capacity. Chamber pressure was measured directly from the combustion chamber. The Cooling power-combustion pressure values used for the experiments is presented in Fig. 2, which shows that by increasing

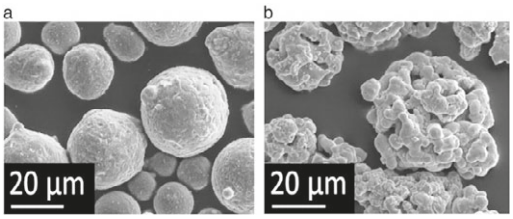

Fig. 1. Surface morphologies of the a) typical plasma densified and b) agglomerated and sintered Cr_3C_2—NiCr–powder.

Table 1
Spray parameters used for thermal spraying.

Coating code	Spray system	Kerosene (l h^{-1})	Hydrogen (l min^{-1})	Oxygen (l min^{-1})	Air (l min^{-1})	Nitrogen (l min^{-1})
CJS A	Thermico CJS	18	80	1000	–	32
CJS B	Thermico CJS	18	80	900	–	32
CJS C	Thermico CJS	21	80	1000	–	32
CJS D	Thermico CJS	21	80	900	–	32
CJS E	Thermico CJS	16	80	1000	–	32
CJS F	Thermico CJS	16	80	900	–	32
DJH	Oerlikon Metco DJ Hybrid		660	192	344	14

kerosene flow the cooling power increased and similarly combustion pressure increased. Oxygen flow adjustment from 900 l min^{-1} to 1000 l min^{-1} increases only chamber pressure and has an insignificant effect on temperature. It should be noted, that at spray conditions CJS E and CJS F conditions were too cold to be able to deposit the coating.

2.2. Coating characterization methods

2.2.1. Abrasive wear test, mechanical testing and microstructures

Sand abrasion tests were performed according to ASTM G65 (procedure D) with samples ground to a surface finish of R_a 0.3 μm. A static contact force of 45 N against the rubber wheel was used. The rubber wheel was 227 mm in diameter and during the testing time of 30 min at 200 rpm the total sliding distance was 4279 m (6000 revolutions).

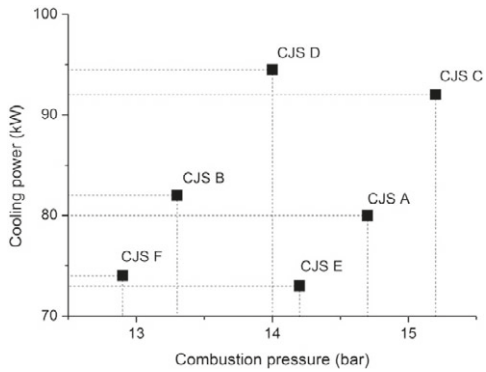

Fig. 2. Cooling power and combustion pressures measured for the spray parameters.

Quartz sand used was of rounded particles with an average size between 212 and 300 μm. Sand mass flow rate was 270 g min^{-1}. Two samples per coating were tested. Mass loss of samples was measured by using at different time intervals (10, 20, and 30 min) to ensure the linear wear performance during dry rubber wheel abrasion testing. The mass of the coatings was measured by using high accuracy precision balance. Before each intermediate measurement the samples were refined from abrasive particles by using pressurized air blasting. The initial mass and the mass after abrasion test was determined for the air blasted and ethanol washed sample which was then dried and let stabilize in the desiccator overnight.

2.2.2. Residual stress measurements

In-situ Coating Property (ICP-sensor, Reliacoat Technologies, US) sensor is an in-situ curvature device, which monitors the curvature of a plate sample by three lasers during the deposition process. It enables the evaluation of the various stress contributions separately. The curvature sensor is based on laser sensing of deflections in a strip during thermal spray deposition. Deflections can be converted to sample curvature. A simultaneous measurement of temperature is achieved via contacting thermocouples on the back side of the sample.

Evolving stress formed by each coating layer can be calculated by Stoney's Eq. (1):

$$\sigma_{ev} = \frac{E_s' t_s^2}{6} \frac{d\kappa}{dt_c} \tag{1}$$

where σ_{ev} is evolving stress of the layer with thickness dt_c that causes a curvature of $d\kappa$, E_s' is the in-plane elastic modulus ($= E_s / (1 - \nu_s)$), where E_s is Young's modulus and ν_s Poisson's ratio of the substrate and t_s is the thickness of the substrate [25,26].

Deposition stress (quenching or peening) can be determined from the curvature change in the substrate-coating system during coating deposition by Brenner and Senderoff Eq. (2) [27].

$$\sigma_d = \frac{E_s' t_s \left(t_s + \beta^5 dt_c\right)}{6dRdt_c}; \beta = \frac{E_c'}{E_s'} \tag{2}$$

where σ_d is deposition stress, E_c' is the in-plane modulus of deposited coating, dR is change in radius caused by deposition stress in a deposited layer thickness dt_c and E_s' and t_s as in Eq. (1) above.

Brenner and Senderoff's equation [27] for thick coatings can also be used for the calculation of thermal stresses. The portion from the end of spraying to the cooling down of substrate-coating system to the room temperature is analysed. The final residual stress value reported is a sum of deposition stress and thermal stress.

The following material specific values were used for calculations for Eqs. (1) and (2). Young's modulus, Poisson's ratio and the coefficient of

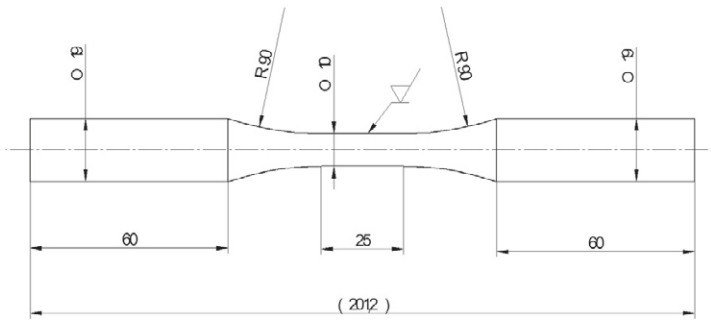

Fig. 3. Dimensions of axial fatigue test specimens machined from S355J2G3 structural steel. For each test series, the midsection was machined to the corresponding target R_a value.

Table 2
Cutting conditions in machining of specimens.

Specimens	Machining	Feed rate (mm rev^{-1})	Depth of cut (mm)	Cutting speed (m min^{-1})	Corner radius (mm)
Series A (R_a 1.6–1.7 μm)	Roughing	0.18	0.6	120	0.8
	Finishing	0.062	0.24	114	0.4
Series B (R_a 2.7–2.8 μm)	Roughing	0.18	0.6	120	0.8
	Finishing	0.078	0.24	114	0.4

Table 3
Source material machining steps of specimen series.

Specimens	Roughness	Source material	Machining
Series A	R_a 1.6–1.7 μm	S355J2G3 round bar	Turned (Table 2)
Series B	R_a 2.7–2.8 μm	S355J2G3 round bar	Turned (Table 2)
Series C	R_a 0.15–0.20 μm	Specimens from Series B production	Turned, grit blasted, coated, diamond belt ground and emery paper polished on lathe
Series G	R_a 4.3 μm	Specimens from Series B production	Turned, grit blasted
Series P	R_a 0.16 μm	Specimens from Series A production	Turned, emery paper polished on lathe

thermal expansion for Cr_3C_2—NiCr were 230 GPa, 0.3 and 8.3 μm m^{-1} °C^{-1}, and for carbon steel 205 GPa, 0.3 and 12 μm m^{-1} °C^{-1}. The actual coating thicknesses determined from the cross sectional images of each deposited coating were used for calculations. Examples of calculated stress values are shown in Table 6, Section 3.2.

For fatigue specimens, residual stress measurements of a number of specimens were done with an X-ray diffraction (XRD) based stress analyser, XStress3000 (manufactured by Stresstech Oy, Vaajakoski, Finland). A CrKα radiation source was used and a theta angle of 156° for the base metal and 148° for the Cr_3C_2 coating. For the base metal the exposure times ranged from five to 15 s, while for the coated specimens the exposure time was 180 s. For residual stress measurements pertaining to the fatigue test specimens, see Table 7, Section 3.2.

2.2.3. Axial fatigue test

The axial fatigue tests were performed on an MTS 810 (100 kN) materials test rig and encompassed five test series with differently treated specimens. Corresponding S-N curves were produced and fatigue limit estimates based on stair case tests were computed.

The different test series were selected in order to study how the fatigue performance of the base material (substrate) was influenced by the effect of different machining and surface treatment phases and by HVOF coating. Please refer to a later section in this chapter (after Table 4) for a discussion of the selection of the different surface treatments.

The base material was unalloyed structural steel S355J2G3, received as round bar (diameter 20 mm h9) from which specimens according to ASTM E 466–07 [28], cf. Fig. 3, were produced. All specimens were produced from the same batch of steel.

According to the manufacturer's certificate, the chemical composition of the steel was: 0.16% C, 0.22% Si, 1.17% Mn, 0.010% P, 0.023% S, 0.023% Al. The proof strength (Rp0.2) was 560 MPa, the tensile strength (Rm) was 610 MPa, and elongation (A5) was 14%. For HVOF coating, the material chosen was chromium carbide Cr_3C_2—25(80Ni20Cr), as explained in Section 2.1.

The cutting conditions used during turning (lathe: Okuma LB-15) are specified in Table 2 and an overview is given in Table 3 of the source material and the machining steps used for producing the different specimen series.

The thickness of the coating of the 15 diamond belt ground and polished fatigue specimens of Series C was 173 μm ± 18 μm (ave ± sd). The thickness was determined from the difference in specimen gauge diameter before coating and after coating and surface treatments (Fig. 4).

The grit blasting of Series G was done using brown aluminium oxide grit with blocky and sharp edged shape (Duralum Blast E 24/30). The size was 24–30 mesh. The grit blasting system used 8.2 bar pressure and the manual blasting was done from a distance of 5 to 8 cm with an angle of about 60°. The samples were brushed with acetone before blasting to get rid of unwanted compositions such as grease. After the blasting, brushing was done to remove the grit from the surface.

Surface finishing in Series C was done by diamond belt grinding (manually, circumferentially) on the lathe, followed by polishing with 3 M micro-finishing film 472 L (40 μm) and Wendt fine finishing film (30 μm), both using silicon carbide abrasives. In Series P, the surface finishing was also done on the lathe manually and circumferentially, using emery papers with progressively smaller grit size (P240, P320, and P400 for the last phases).

When inspecting the produced fatigue specimens, some scatter was detected in the surface roughness values due to variations during machining and polishing, cf. Table 4. Surface roughness was measured with a stylus profilometer (Taylor-Hobson Surtronic 3+) and analysed with the Talysurf software. In Table 4, it is also shown that within each series the specimens were grouped such that those with a slightly lower R_a value were used for the S-N curve (the slope) whereas the specimens with a slightly higher R_a value were used for the fatigue limit. Accordingly, the former specimen surface quality groups were tagged A1, B1, etc., and the latter groups A2, B2, etc. While the differences in mean R_a values are not large, the fatigue limit estimates may be somewhat

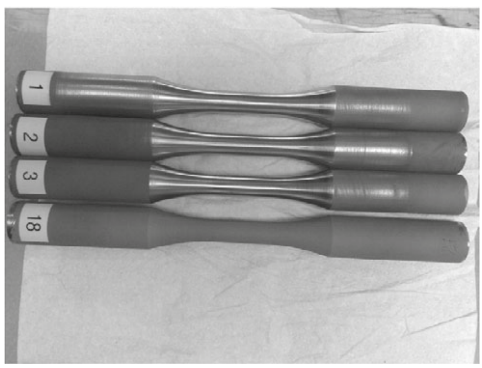

Fig. 4. Photo of coated specimens (from Series C). The specimens received coating all along the length of the specimen (no. 18 in the photo). Subsequently the midsections were polished to a surface quality representative of sealing surfaces of hydraulic cylinder rods (no. 1–3).

Table 4
Surface roughness characteristics of fatigue specimens of the different test series.

Series	Surface quality	Part of test	R_a (μm) (ave ± sd)	R_z (μm) (ave ± sd)	R_{sk} (−) (ave ± sd)	No of specimens
A	A1	S-N slope	1.63 ± 0.03	8.78 ± 0.36	0.06 ± 0.23	9
	A2	Fatigue limit	1.70 ± 0.04	8.97 ± 0.27	0.05 ± 0.13	7
B	B1	S-N slope	2.72 ± 0.09	14.07 ± 0.59	0.61 ± 0.07	11
	B2	Fatigue limit	2.82 ± 0.08	14.73 ± 0.80	0.51 ± 0.14	7
C	C1	S-N slope	0.15 ± 0.04	1.55 ± 0.43	−3.80 ± 2.37	8
	C2	Fatigue limit	0.20 ± 0.03	2.07 ± 0.35	−4,03 ± 2.49	7
G	G1	S-N slope	4.32 ± 0.33	22.20 ± 1.53	n/a	10
	[a]	Fatigue limit	[a]	[a]	[a]	0
P	P1	S-N slope	0.16 ± 0.00	1.21 ± 0.04	−0.95 ± 0.18	8
	P2	Fatigue limit	0.16 ± 0.00	0.30 ± 0.33	−0.98 ± 0.31	7

R_a: arithmetic average deviation from center line of surface profile.
R_z: average maximum height of surface profile.
R_{sk}: skewness of surface profile.
n/a: data not available.
[a] No fatigue limit (staircase) tests were done for the grit blasted specimens.

lower than what would have been the case, had all specimens featured the better R_a value level.

Series C represents a surface that could replace hard chrome plated sealing surfaces in fluid power components. Series B was made as an alternative to Series A to see if machining to a higher R_a value (with possible increased throughput in production) had any significant effect on the fatigue performance of the base material already in the beginning of the chain of production. Turned surfaces with a surface quality corresponding to either Series A or B would be used in the starting phase in producing sealing surfaces. Series G was tested to see how grit blasting contributed to fatigue performance compared to the corresponding starting point, Series B. Would better performance be achieved through compressive stresses or would the roughened surface instead reduce fatigue resistance. Series P (polished/sanded base material) was tested for comparison with the coated and polished C series (that has approximately the same mean R_a value); possible differences should be attributable to the coating process (including grit blasting to make the coating adhere better to the substrate). Hard chrome plating of specimens was not done in this study, but Series P represents specimens with a surface quality suitable for chrome plating. Chrome plating adds only a thin coating, so the substrate needs to be prepared very close to the final sealing surface quality.

The fatigue tests were performed mainly according to the procedure specified in reference [29] (p. 108), even if slightly more specimens were used in the present study and a different testing order was followed. First, the S-N slope was determined (8–11 specimens) and then the staircase method was used to estimate the fatigue limit (7 specimens). No fatigue limit test was done for the grit blasted specimens as they only represented an intermediate production state in producing coated specimens.

Constant amplitude, fully reversed (stress ratio $R = -1$) fatigue tests were performed. The tests were run continuously until fracture or until the runout limit of five million cycles was reached. Loading frequency was 8 Hz in all tests but the G Series, which was run at 20 Hz. The 8 Hz frequency was selected so as to avoid heating of the specimens, which would occur at high load levels if higher frequencies were used. The grit blasted specimens (G Series) were tested first and at the load levels needed for those tests no adverse heating of the specimens were detected. The need for lower loading frequency was detected in pre-tests of the coated specimens, which had to be loaded with clearly higher forces. After that, all tests (A, B, C, and P Series) were run at 8 Hz. In the tests, the applied stress (and load) ranges were: for uncoated specimens: 248 MPa–360 MPa (19.5 kN–28 kN), and for coated specimens 350 MPa–414 MPa (27.5 kN–32.5 kN). All tests were conducted at room temperature and in air (in the open atmosphere in the laboratory).

3. Results

3.1. Coating microstructure and properties

The microstructures of the coatings, which were prepared by using adequate spray conditions (CJS A–D, shown in Fig. 2), are presented in Fig. 5. Mechanical properties and wear resistance of the coatings are presented in Table 5. Results show that coating hardness and wear resistance did not vary significantly when sprayed with CJS but higher kerosene level (higher cooling power) increases the Elastic modulus of the coating.

The coating D, which gave the best combination of mechanical performance, deposition rate and compressive stress was selected for fatigue testing.

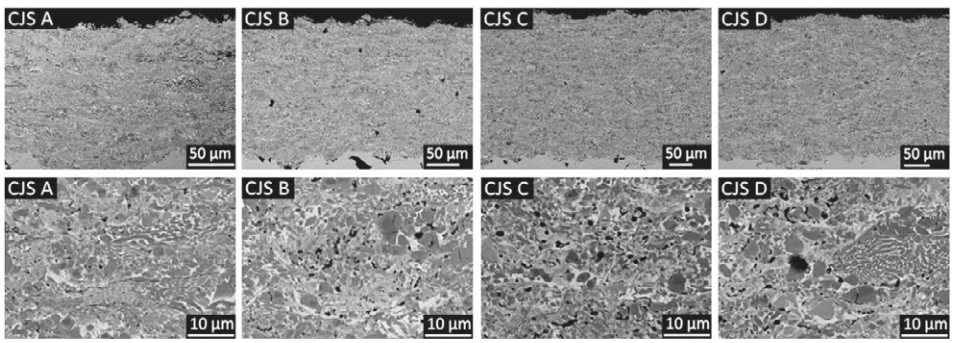

Fig. 5. SEM microstructures of the coatings CJS A–D. Deposition layer is shown at two magnifications.

Table 5
Results from the coating optimization.

Coating code	Spray system	Thickness/pass [μm]	Substrate temperature [°C]	DE[a] [%]	Hardness [HV 0,3 kg]	Elastic modulus [GPa]	Abrasive wear [mg 30 min^{-1}]
CJS A	Thermico CJS HVOF	4.8	215	27.1	1096 ± 117	227 ± 16	41.7 ± 0.45
CJS B	Thermico CJS HVOF	6.3	220	33.9	1127 ± 103	224 ± 11	35.8 ± 0.56
CJS C	Thermico CJS HVOF	7.8	240	44.7	1180 ± 50	240 ± 6	36.8 ± 0.66
CJS D	Thermico CJS HVOF	9.7	260	55.4	1177 ± 108	235 ± 12	34.5 ± 0.47
DJH	Sulzer Metco DJ Hybrid	10.9	265	55.2	1143 ± 64	203 ± 6	34.6 ± 0.40

ρ = density, U = gun traverse speed, W_z = step, R_f = powder feed rate.
[a] Deposition efficiency was calculation by using equation $DE = \frac{h_{eq}\rho UW_z}{R_f}$, where h_{eq} = thickness/pass.

3.2. Residual stress measurement results

The comparison of in-situ curvature measurements for CJS D and DJH are shown in Fig. 6, and calculated residual stress (Table 6) shows significant difference in residual stress evolutions for two coatings. During spraying (between "start spray" and "end spray") in-situ curvature of DJH is developing towards positive, which means that tensile deposition stresses (quenching stress) are generating and in CJS D the curvature is negative resulting from compressive peening stresses. During the cool down (between "end spray" and "end cool") the negative curvature change in both coatings indicates that coefficient of thermal expansion of substrate is higher than that of coating and during cool down thermal stresses pushes coatings towards compression. As a result, the final residual stress is compressive in both coatings. It is clear that spray device has a significant effect on the residual stress evolution in the coating and it was evident that evolution of high compressive residual stresses was only possible for CJS. The temperature of the optimization samples sprayed onto thin ICP plate substrate (in Table 5) was between 215 and 265 °C, which may cause some the relaxation of the grit blasted substrate. However, the purpose in optimization samples was to evaluate and demonstrate the residual stress of the coating and these samples were not fatigue tested. It should be noted that thermal mismatch stresses (in Table 6) are therefore overestimated.

For fatigue specimens, the results of residual stress measurements (XRD) are shown in Table 7. We did not have the possibility to measure residual stresses of all tested specimens. Nevertheless, in order to assess the initial surface stress level of the specimens, one to two specimens from the test Series B, C, G, and P were measured. The measurements were taken in the middle of the specimen, on both sides, i.e., 180° apart. A choice between samples form Series A and Series B had to be made, and Series B was considered more important as Series C was made from specimens taken from the Series B production. In addition, tensile residual stresses of the order of 200 MPa were measured in a previous study for turned fatigue specimens with an R_a value of 3.2 μm [30], so it would be instructive to see if similar stresses would be present in Series B having an average R_a value of 2.8 μm. In the same study, specimens with a R_a value of 1.6 μm had compressive residual stresses in three out of four measured samples.

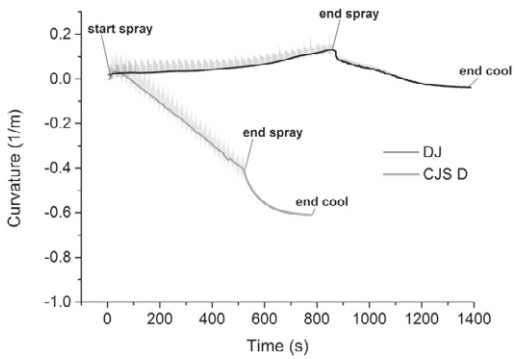

Fig. 6. Comparison of the curvature evolution of the coatings, which were sprayed by using CJS and DJH torches.

3.3. Fatigue results

The results of the fatigue tests are shown in the S-N curves in Fig. 7.

The fatigue limits were estimated by running staircase tests for the A, B, C, and P series, Table 8. The estimation was done according to the procedure presented in [29]. Table 8 also shows the stress increment, the lowest stress level, the number of stress levels and the number of specimens used in the stair case test.

The results show that the lowest fatigue limit was for turned series B, which had the highest surface roughness (R_a 2.8 μm in fatigue limit tests, Table 4). Series A, which was turned to lower surface roughness (R_a 1.7 μm in fatigue limit tests), had higher fatigue resistance, the increase in the fatigue limit being 12%. It is perhaps easier to detect the difference in fatigue performance between Series A and B in terms of fatigue limit values than by looking at the S-N curves of Fig. 7.

The fatigue limit of the polished specimens (Series P) was 4–16% higher than the fatigue limit of the specimens with turned surfaces. By comparing the fatigue limits of Series P and C (having similar surface roughness), it can be seen that the beneficial influence of the coating procedure was 18%. When compared to fatigue limit values of untreated (only turned) specimens of Series A and B, the overall treatment of Series C (coating procedure and polishing) increased the fatigue limit by 23% to 38%.

Typical fracture surface of coated (C) and uncoated (P) specimens are shown in Figs. 8a and b. In the figures, the regions separated with dotted line are marked as 1) slow crack growth 2) fast crack growth and 3) final overload fracture. Comparison of fracture surfaces shows that the fatigue crack propagation in the C and P samples are different. In the uncoated sample the fatigue crack has been initiated from the top and propagated towards the bottom of the surface. In the coated sample multiple cracks have been initiated at the circumference of the surface and they have grown towards the center. Moreover, no cracks or delamination along the coating-substrate interface could be detected (Fig. 8b), which indicates that adherence of the coating, is good.

4. Discussion

4.1. Spray parameter optimization

Six different parameter combinations, suitable for CJS process, were selected for coating optimization with the target of producing

Table 6
Calculated residual stresses for the coatings.

Coating code	Deposition stress [MPa]	Thermal stress [MPa]	Residual stress [MPa]
CJS D	−470.7	−227.9	−698.5
DJH	96.0	−114.9	−18.9

Table 7
Residual stress of sample fatigue specimens measured by XRD at mid-specimen.

			Axial direction		Circumferential direction	
Series	Material	Surface state	Average (MPa)	Number of measurements (−)	Average (MPa)	Number of measurements (−)
B	Base metal	Turned, R_a 2.8 μm	334.9	4	371.4	4
C	Coated	Polished, R_a 0.15 μm[a]	−652.3	4	−660.4	4
G	Base metal	Grit blasted	−141.7	4	−110.3	3
P	Base metal	Polished, R_a 0.15 μm	−300.1	2	−266.0	2

[a] A value of the elastic modulus of 235 GPa was used in the calculations.

compressive residual stress. Based on the results, one of the parameter sets (CJS D) was selected for use in actual fatigue specimen deposition. With all the selected coating parameter sets it was possible to produce coatings, which all have relatively similar microstructure, mechanical properties and wear resistance. However, deposition efficiency (DE) varies significantly, being reasonably high only for the coating CJS D. The DE result of CJS D is comparable to the reference coating DJH. It was found that despite similar DE the processes produces completely different residual stresses, which is most probably related to the particle impact velocity and particle temperature. As a conclusion, the selected coating CJS D gave the best combination of mechanical performance and deposition efficiency. Most importantly, despite the highest DE the residual stress in the coating was highly compressive, which made the coating suitable for fatigue testing purposes.

4.2. Fatigue performance

Increased surface roughness decreases the fatigue performance because of the notch-like surface structure involved which can promote cyclic slip and fatigue crack nucleation [13, pp. 48–49], [31]. Consequently, crack initiation life will be much shorter than for surfaces with fine surface finish [14]. Certain surface production methods, such as non-gentle grinding or quite often turning, can produce tensile stresses at or near the surface of the workpiece [32–34]. These tensile stresses will reduce the fatigue performance even further.

The turned base metal specimens have a surface geometry consisting of closely spaced grooves perpendicular to the loading direction. Therefore this is not beneficial for the fatigue performance and as a consequence, Series A and B have the lowest S-N curves in Fig. 7. In addition, the tensile residual stresses caused by turning (cf. Table 7), was an additional detrimental factor.

The fatigue results for the uncoated specimens show that surface compressive stress increases the fatigue resistance of the sample. This can be noticed when comparing the S-N curves in Fig. 7. Both grit blasting (G Series) and grinding/polishing (P Series) increases fatigue performance compared to the situation for the turned base metal specimens (A and B Series). In the case of polished specimens, relatively high compressive stresses were measured in the sample surface. However, it might is not only the increased surface compressive stress but also radical smoothening of the surface, which would positively affect fatigue resistance. Grinding/polishing of the turned surface produces a surface structure that is much less prone to crack initiation (Series P). In addition, this surface treatment appears to ensure that the initial surface stress state involves compression (cf. Table 7). The overall effect is a reduced slope of the S-N curve compared to those pertaining to the turned-only material (Series A and B). In Fig. 7 it can also be seen that grit blasting (Series G) leads to better fatigue performance compared to turned-only material at higher cycles despite the rough surface micro-geometry. On the other hand, in the high load and lower cycle regime (below some 90,000 cycles) one can assume, based on the slope of the S-N curve of Series G in comparison to those of Series A and B, that the adverse effect of the rough surface will outweigh the beneficial effect of the compressive stresses.

The results show that the applied coating process had a clearly stronger beneficial effect on the fatigue performance compared to only a treatment of the substrate metal surface, even if the final surface was

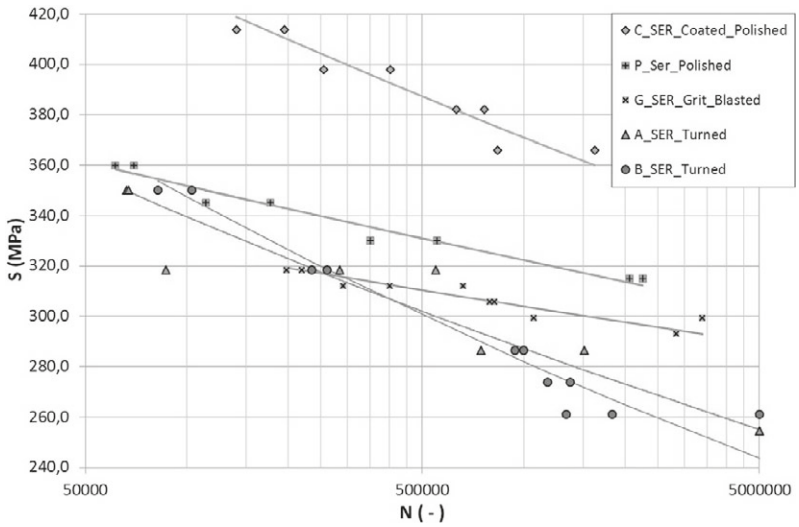

Fig. 7. S-N curves corresponding to each of the axial fatigue tests series A, B, C, G, and P.

Table 8
Estimated fatigue limits and information relating to stair case tests.

Test series[a]	Fatigue limit[b] (MPa)	Stress increment (MPa)	Lowest stress level (MPa)	No of stress levels (−)	No of specimens (−)
A	255	12.7	267	3	7
B	227	12.7	248	3	7
C	313	15.9	350	2	7
P	265	15.0	300	2	7

[a] Fatigue limit was not estimated for grit blasted specimens (G Series) as this was only an intermediate state of fabrication.
[b] With a confidence level of 90%, 95% of the outcomes observed in tests are expected to exceed the fatigue limit.

of similar quality in both cases. The good fatigue resistance of the C Series specimens was naturally a consequence of both surface treatment and coating, but it appears that the coating plays the leading role. After coating the C Series specimens were belt ground and polished to a surface quality relevant for the end product (sealing surface of hydraulic cylinder rods). The P Series specimens received a similar surface finish after a sequence of grinding and polishing steps with emery papers. In Table 8 it can be seen that polishing only somewhat increases the fatigue limit of the turned base metal (10 MPa), while the combined effect of coating and polishing results in a significant increase (86 MPa). While belt grinding and polishing as such will influence fatigue performance positively, the good performance of Series C cannot be explained solely by these last surface treatment steps. The HVOF coated specimens were in a class of their own, mainly due to the compressive residual surface stress state caused by the coating process.

It has been presented that fatigue failures in the coated specimens usually start at the interface of coating and substrate at the locations where highest tensile stress concentrations are generated [9,13,14]. As discussed before, tensile residual stresses and surface irregularities and residue alumina particles [10] are not beneficial. Many authors [5,6,9–12,17] have reported that HVOF coating reduces the fatigue resistance, mainly due to those mentioned flaws at the interface. However, compared to CJS D coating, the processes they have used usually produces more tensile stresses similarly as coating DJH. In our study we saw a significant increase in fatigue performance of coated specimens, which is seldom reported. It has been earlier clearly shown that compressive stresses due to peening effects positively on the coating fatigue performance. Voorwald et al. [9] showed that by shot peening of the specimen surface prior to coating deposition the fatigue life can be increased to the same level as it was without coating. The compressive stress impedes crack initiation and propagation and thereby increases the fatigue life [8]. In our case, we propose that the compressive state of the coating and especially the substrate caused by *spray particle peening*, plays an important role in preventing the crack initiation. The peening effect in CJS process is high due to the high kinetic energy of this particular deposition process and this effect seems to be even higher than compressive stress produced by shot blasting procedure. As can be seen in Fig. 8b, a uniform thin layer of compressive residual stress can be seen to be produced on the steel substrate similarly as presented by Ibrahim et al. [8]. This effects on the crack propagation orientation and also presumably, on the growth velocity.

To understand the good performance on the coated (and polished) samples, its residual stresses needs to be discussed in more detail. High compressive stresses in the coating were confirmed in our study by both X-ray for round bar (−652.3 MPa in Table 7) and curvature techniques for flat specimen (−698.5 MPa in Table 6). Difference in the results can be explained by the different shapes of the specimens measured and characteristics of the measurements techniques. Curvature technique and calculation of stresses based on curvature data are the average stresses in the coating. On the other hand, X-ray technique shows the stresses at the very thin layer on the surface of the coating and this surface layer might be at a different stress level than layers beneath. Bolelli et al. [35] have shown, that surface layer is different, because it has not been subjected to peening by the particles.

Unfortunately, it was not possible to get data of the residual stress at the coating-substrate interface, from where the cracks most definitely initiates. However, based on the residual stress formation mechanisms some further discussions can be done. The residual stresses generated in the coating during the deposition process derive from three origins [22], which all can be detected from beam curvatures: CTE difference of coating and substrate, peening effect and quenching of the individual particles. Stress from the CTE difference is well understandable. Cr_3C_2—NiCr-coating has lower CTE than steel, which pushes the coating layer towards the compressive stress during the cooling of the sample from about 180 °C to room temperature. (It is necessary to note, that mentioned temperature was the temperature of the coating surface and underlying substrate remains well below that during the deposition process. Substrate temperature was therefore low enough, that relaxation of residual stresses was not significant.) When coating is in compression force balance requires the substrate material to be in tension. As the tensile stresses are not beneficial for fatigue life the role of the other stress components on the good fatigue behaviour of coated sample seems evident. It is important to note that quenching stress is always tensile for the spray particles but quenching of first deposition layer enforces the underlying substrate towards more compressive stress. Thus quenching stresses are preventing the crack initiation from the substrate interface. Due to the small size of the spray particle and relatively thin layer thickness (thickness/pass in Table 5), quenching stresses are supposed to effect only on the thin layer under the first layer and cannot affect deep in the substrate. Peening of the particles effects compressively and seems to influence the underlying layers more deeply. As a result, we propose that due to the combination of the peening and quenching, the substrate surface has locally relatively high compressive stress, which improves the fatigue performance of the CJS D coating. It is also important, like in the CJS case, that coating itself is in compressive stress and thus cracks cannot initiate easily from inside the coating and neither from the surface of the coating.

Finally, it is important to note that coating increases the stiffness of the component and thus can carry a larger portion of the applied load as described by Ibrahim et al. [8]. It is also essential that coating needs to be excellent quality as can be achieved by CJS and needs to be well adhered to be able to increase stiffness and prevent the crack growth at the interface and thus avoid the delamination of the coating.

5. Conclusions

The results showed that the applied CJS coating process had a clearly stronger beneficial effect on the fatigue performance compared to only a surface quality-improving treatment of the substrate metal, even if the final surface was of similar quality in both cases. Even if the good fatigue performance of the coated specimens was naturally a consequence of both surface treatment and the coating process, the main influence can be attributed to the latter. The high kinetic manufacturing process

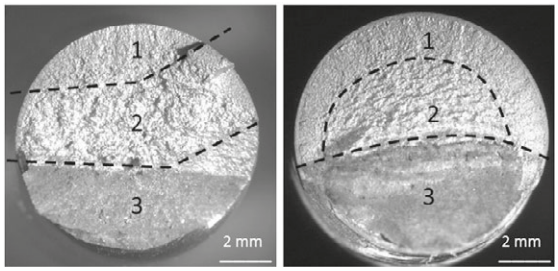

Fig. 8. Fracture surfaces of a) uncoated and b) coated specimen showing the regions of 1) slow crack growth, 2) fast crack growth and 3) final fracture.

has high impact energy to produce a relatively deep compressive residual stress layer on the substrate, which hinders crack initiation and growth. Due to this spray particle peening effect, one could expect a clear increase in fatigue performance by CJS coating the mild steel specimens. Such was indeed the case, as the HVOF coated specimens were clearly superior to other treatments in the fatigue tests.

It should be noted that residual stresses of thermally sprayed Cr_2C_3—NiCr are relatively sensitive to the spray process used and the selected spray parameters. The coating for the fatigue tests was produced by using one out of six different HVOF spray parameter sets that were used to evaluate the optimal spray condition. The selected high kinetic HVOF-sprayed Cr_3C_2—NiCr coating had a hardness of 1177 HV and was very dense and well adhered to the substrate.

In conclusion, HVOF Cr_2C_3—NiCr coating produced by using high kinetic thermal spray process can be considered a very promising solution for improving fatigue performance of structural steel components in several industrial applications, as well as a good candidate for hard chrome replacement on sealing and bearing surfaces in fluid power components.

Acknowledgements

The research was partly done under the auspices of the DEMAPP research program organized by FIMECC (Finnish Metals and Engineering Competence Cluster). The financial support of Aalto University to finalize the fatigue tests is greatly appreciated. The authors want to thank Mr. Mika Jokipii at VTT for performing the grit blasting and coating of the fatigue specimens as well as Ms. Suvi Santa-aho and Mr. Jarkko Kiilakoski at Tampere University of Technology for residual stress measurements.

References

[1] J. Tuominen, J. Näkki, H. Pajukoski, J. Miettinen, T. Peltola, P. Vuoristo, Wear and corrision resistant laser coating for hydraulic piston rods, J. Laser Appl. 27 (no. 2) (2015) (022009-1-022009-12).
[2] J.A. Picas, A. Forn, G. Matthäus, HVOF coatings as an alternative to hard chrome for pistons and valves, Wear 261 (2006) 477–484.
[3] J.M. Guilemany, N. Espallargas, P.H. Suegama, A.V. Benedetti, J. Fernandez, High-velocity Oxyfuel Cr3C2—NiCr replacing hard chromium coatings, J. Therm. Spray Technol. 14 (3) (2005) 335–341.
[4] D. Dudzinski, P. Au, J. Legoux, S. Simard, Salt fog corrosion resistance of HVOF WC-CoCr coated and electrolytic hard chromium plated AerMet 100 and 300 M steel alloys, Proc. Int. Therm. Spray Conf. 1 (2002) 686–692.
[5] A. Aguero, F. Camon, J. Garcia de Blas, J. del Hoyo, R. Muelas, A. Santaballa, S. Ulargul, P. Valles, HVOF-deposited WCCoCr as replacement for hard Cr in landing gear actuators, J. Therm. Spray Technol. 20 ((6), no. December) (2011) 1292–1309.
[6] R.C. Souza, H.J.C. Voorwald, M.O.H. Cioffi, Fatigue strength of HVOF sprayed Cr3C2—25NiCr and WC-10Ni on AISI 4340 steel, Surf. Coat. Technol. 203 (3–4) (2008) 191–198.
[7] S. Watanabe, T. Tajiri, N. Sakoda, J. Amano, Fatigue cracks in HVOF thermally sprayed WC-Co coatings, Journal of Thermal Spray Technology 7 (no. 1) (1998) 93.
[8] A. Ibrahim, C.C. Berndt, The effect of high-velocity oxygen fuel, thermally sprayed WC-Co coatings on the high-cycle fatigue of aluminium alloy and steel, J. Mater. Sci. 33 (1998) 3095.
[9] H.J.C. Voorwald, R.C. Souza, W.L. Pigatin, M.O.H. Cioffi, Evaluation of WC–17Co and WC–10Co–4Cr thermal spray coatings by HVOF on the fatigue and corrosion strength of AISI 4340 steel, Surf. Coat. Technol. 190 (2005) 155–164.
[10] W.A. Gonzalez-Hermosilla, D. Chicot, J. Lesage, J.G. La Barbera-Sosa, I.C. Gruescu, M.H. Staia, E.S. Puchi-Cabrera, Effect of substrate roughness on the fatigue behavior of a SAE 1045 steel coated with a WC-10Co-4Cr cermet, deposited by HVOF thermal spray, Mater. Sci. Eng. A 527 (2010) 6551–6561.
[11] K. Padilla, A. Velasquez, J.A. Berrios, E.S. Puchi Caberra, Fatigue behavior of a 4140 steel coated with a NiMoAl deposit applied by HVOF thermal spray, Surf. Coat. Technol. 150 (2002) 151–162.
[12] E.S. Puchi-Cabrera, M.H. Staia, M.J. Ortiz-Mancilla, J.G. La Barbera-Sosa, E.A. Ochoa Pérez, C. Villalobos-Gutiérrez, S. Bellayer, M. Traisnel, D. Chicot, J. Lesage, Fatigue behavior of a SAE 1045 steel coated with Colmonoy 88 alloy deposited by HVOF thermal spray, Surf. Coat. Technol. 205 (2010) 1119–1126.
[13] N.E. Frost, K.J. Marsh, L.P. Pook, Metal Fatigue, Dover, 1999.
[14] J. Schijive, Ch 2 fatigue as a phenomenon in the material, Fatigue of Structures and Materials, Kluwer 2004, pp. 7–44.
[15] J.R. García, J.E. Fernández, M. C. J., F.G. Costales, Fatigue effect of WC coatings thermal sprayed by HVOF and laser treated, on medium carbon steel, Eng. Fail. Anal. 18 (2011) 1750–1760.
[16] D.M. Zhu, R.A. Miller, Investigation of thermal high cycle and low cycle fatigue mechanisms of thick thermal barrier coatings, Mat. Sci. Eng. A-Struct. 245 (2) (1998) 212–223.
[17] H.J.C. Voorwald, L.F.S. Vieira, M.O.H. Cioffi, Evaluation of WC-10Ni thermal spraying coating by HVOF on the fatigue and corrosion AISI 4340 steel, Procedia Eng. 2 (2010) 331–340.
[18] S. Suresh, Y. Sugimura, L. Grondin, Fatigue crack growth at arbitrary angles to bimaterial interfaces, Scr. Metall. Mater. 33 (12) (1995) 2007–2012.
[19] S. Kuroda, T.W. Clyne, The quenching stress in thermally sprayed coatings, Thin Solid Films 200 (1991) 49–66.
[20] T.W. Clyne, S.C. Gill, Residual stresses in thermal spray coatings and their effect on interfacial adhesion: a review of recent work, J. Therm. Spray Technol. 5 (4) (1996) 401–418.
[21] J. Matejicek, S. Sampath, Intrinsic residual stresses in single splats produced by thermal spray processes, Acta Mater. 49 (11) (2001) 1993–1999.
[22] S. Kuroda, Y. Tashiro, H. Yumoto, S. Taira, H. Fukanuma, Peening action and residual stresses in HVOF thermal spraying of 316L stainless steel, 15th International Thermal Spray Conference, vol. 1, 1998, pp. 569–574.
[23] T. Suhonen, T. Varis, S. Dosta, M. Torrell, J.M. Guilemany, Residual stress development in cold sprayed Al, Cu and Ti coatings, Acta Mater. 61 (2013) 6329–6337.
[24] J. Matejicek, S. Sampath, In situ measurement of residual stresses and elastic moduli in thermal sprayed coatings: part 1: apparatus and analysis, Acta Mater. 51 (3) (2003) 863–872.
[25] G.G. Stoney, The tension in metallic films deposited by electrolysis, Proc. R. Soc. Lond. A82 (1909) 172–175.
[26] M. Ohring, Materials Science of Thin Films, 2nd Ed, p. 413, Academic Press, San Diego, 2002.
[27] A. Brenner, S. Senderoff, Calculation of stress in electrodeposits from the curvature of a plated strip, J. Res. Natl. Bur. Stand. 42 (1949) 105–123.
[28] ASTM, Standard E466-07, "Standard Practice for Conducting Force Controlled Constant Amplitude Axial Fatigue Tests of Metallic Materials", ASTM International, West Conshohocken, PA, 2007.
[29] Y.-L. Lee, D. Taylor, Ch 4 stress-based fatigue analysis and design, in: P. J. H. R. B. M. Lee Y-L (Ed.), Fatigue Testing and Analysis - Theory and Practice, Elsevier, 2005.
[30] J. Cuban, O. Calonius, M. Pietola, J. Jersák, Fatigue life and surface integrity measurements of EN S355J2 steel used in hydraulic components, Manuf. Technol. 11 (11) (2011) 5–11.
[31] N.A. Alang, N.A. Razak, A.K. Miskam, Effect of surface roughness on fatigue life of notched carbon steel, Int. J. Eng. Technol. 11 (1) (2011) 160–163.
[32] D. Novovic, R.C. Dewes, D.K. Aspinwall, W. Voice, P. Bowen, The effect of machined topography and integrity on fatigue life, Int. J. Mach. Tools Manuf. 44 (2004) 125–134.
[33] M.H. El-Axir, A method of modeling residual stress distribution in turning for different materials, Int. J. Mach. Tools Manuf. 42 (2002) 1055–1063.
[34] E. Capello, Residual stresses in turning. Part II. Influence of the machined material, J. Mater. Process. Technol. 172 (2006) 319–326.
[35] G. Bolelli, I. Hulka, H. Koivuluoto, L. Lusvarghi, A. Milanti, K. Niemi, P. Vuoristo, Properties of WC–FeCrAl coatings manufactured by different high velocity thermal spray processes, Surf. Coat. Technol. 247 (2014) 74–89.